Regional traffic and trip characteristics simulation and applications for MFD models calibration

Anna Takayasu

N°d'ordre NNT : 2022LYSET007

THÈSE de DOCTORAT DE L'UNIVERSITÉ DE LYON
opérée au sein de
l'École Nationale des Travaux Publics de l'État

École Doctorale N° 162
MEGA (Mécanique, Energétique, Génie Civil et Acoustique)

Spécialité / discipline de doctorat :

Anna Takayasu

Simulation des caractéristiques du trafic et des déplacements régionaux et applications pour l'étalonnage des modèles MFD

Devant le jury composé de :

Zargayouna, Mahdi	CR MTES and HDR/Universite Gustave Eiffel	Rapporteur
Haddad, Jack	Associate Prof. and HDR/Technion University	Rapporteur
Solnon, Christine	Prof./INSA	Présidente
Kouvelas, Anastasios	Assistant Prof. and Director/ETHZ	Examinateur
Leclercq, Ludovic	Prof. and HDR/Universite Gustave Eiffel	Directeur de thèse
Geroliminis, Nikolas	Prof./EPFL	Co-directeur de thèse

Thèse préparée au LICIT-ECO7

N°d'ordre NNT : 2022LYSET007

A THESIS OF THE UNIVERSITE OF LYON

Prepared at

École Nationale des Travaux Publics de l'État

In international cotutelle with

École polytechnique fédérale de Lausanne

Doctoral school N° 162

MEGA (Mécanique, Energétique, Génie Civil et Acoustique)

Doctoral specialty / discipline: Civil Engineering

Defended on March 24, 2022 by:

Anna Takayasu

Regional Traffic and Trip Characteristics Simulation and Applications for MFD models calibration

---

In front of the following examination committee:

Zargayouna, Mahdi	CR MTES and HDR/Universite Gustave Eiffel	Reviewer
Haddad, Jack	Associate Prof. and HDR/Technion University	Reviewer
Solnon, Christine	Prof./INSA	Committee chair
Kouvelas, Anastasios	Assistant Prof. and Director/ETHZ	Examiner
Leclercq, Ludovic	Prof. and HDR/Universite Gustave Eiffel	Supervisor
Geroliminis, Nikolas	Prof./EPFL	Co-supervisor

Abstract

This thesis investigates how the setting of large-scale dynamic models based on the Macroscopic Fundamental Diagram (MFD) influences prediction accuracy. It mainly focuses on trip length representation and network partitioning. We used an unprecedented set of trajectory data from the pNEUMA experiment (https://doi.org/10.1016/j.trc.2019.11.023) to carry out in-depth analyses of regional trip length behaviors, considering several spatial partitionings of the road network (single region vs. multiple regions). These investigations define different resolutions when calibrating trip lengths that have been cross-compared in simulation using the different primary expressions of accumulation and trip-based MFD models. This extensive benchmarking process provides solid guidelines for calibrating MFD models concerning trip lengths and network partitioning.

Network-level aggregated models based on MFD have received much attention in the literature because they can predict traffic states over large networks with short computation times. Traffic prediction based on classic MFD models using real data consists of three main steps:

1. Estimating traffic variables, i.e., traffic flow, density, and speed, and calibrating MFD settings;
2. Calibrating trip length;
3. Predicting traffic states based on calibrated parameters.

MFD shape and trip length play an essential role in prediction results. On the other hand, the calibration accuracy of these parameters may depend on data availability and network representation. For example, many studies have shown that the heterogeneous state inside a region leads to scattered MFDs. Network partitioning methods for dividing large areas into multiple smaller areas have been proposed to reduce heterogeneity in each region. However, complex partitioning makes trip length calculation difficult since the individual complete trajectories in all regions are necessary for calculating trip length; however, typical trajectory data sources such as probe vehicles cannot track these trajectories because of missing data and automatic changes of vehicle ID. Also, trip length aggregation methods, e.g., average or distribution, may affect the prediction results differently according to the MFD models used. Therefore, it is necessary to analyze the impacts of data availability and network representation on model accuracy. However, no comprehensive investigation has yet been conducted to propose the best model calibration design according to data availability due to

the lack of real data. It requires long-term data sets from several data sources from the same network to test the different data availabilities, and sufficient trajectory data to test several trip length aggregations in the partitioned network. Loop and probe data from the Lyon network and the complete trajectory data of all vehicles obtained by drone experiments in Athens have been used in this thesis to circumvent these limitations.

This thesis consists of two main parts: 1) the investigation of the effect of data availability and network representation on the estimation of traffic states and trip characteristics, and 2) the assessment of how MFD model settings influence prediction accuracy. In the first part, we also study the magnitude of errors when estimating density at the local and regional levels, as it is a core variable for MFD models. We also focus on the effects of network partitioning on MFD shapes and trip lengths. In particular, we address the case of non-convex partitioning that makes each region more homogeneous although to the detriment of trip length representation. We introduce the concept of path sequence to track vehicles that may go back and forth between two close and interlaced regions. Such information appears crucial when simulating a network with interlaced areas using MFD models. For the second part, the prediction accuracy of classic MFD models is assessed by comparing different MFD and trip length settings. An extension of the accumulation-based MFD framework to deal with path sequence is proposed and compared with more classical approaches. It is shown to be more efficient when predicting flow exchanges between regions.

RÉSUMÉ

Chapitre 1: Introduction

La congestion routière dans et autour des zones urbaines pendant les heures de pointe est un problème mondial important du point de vue économique et environnemental. Les stratégies de contrôle du trafic en temps réel et la gestion du trafic ont reçu beaucoup d'attention en tant que solutions pour réduire la congestion urbaine. Pour que ces stratégies puissent fonctionner correctement, des prédictions robustes et précises de l'état du trafic basées sur des données réelles sont nécessaires. La prédiction de l'état du trafic à partir de données comprend trois étapes : 1) Estimation de l'état du trafic et des propriétés des déplacements sur la base de la conception du réseau et des données de trafic, 2) Calibrage des paramètres du modèle sur la base des variables de l'état du trafic et des propriétés des déplacements estimées, 3) Prédiction des propriétés de l'état du trafic à l'aide de modèles basés sur les paramètres calibrés. Ainsi, la précision de la prédiction du modèle peut dépendre à la fois de la méthode de calibrage des paramètres et de la conception du modèle elle-même. En outre, la précision de l'estimation de l'état du trafic et des propriétés des déplacements, qui dépend de la disponibilité des données et des propriétés du réseau, peut affecter de manière significative la calibration des paramètres. Par conséquent, une étude complète de la calibration du modèle prenant en compte la disponibilité des données et les propriétés du réseau est essentielle pour améliorer la précision de la prédiction de l'état du trafic.

Dans cette thèse, nous nous concentrons sur les modèles MFD, qui permettent de reproduire la dynamique du trafic à l'échelle urbaine et sont très utiles pour envisager des stratégies de contrôle à l'échelle urbaine. Les modèles MFD classiques nécessitent deux paramètres essentiels : le MFD et la longueur du trajet. Les variables fondamentales de l'état du trafic qui composent le MFD sont principalement la densité, le débit et la vitesse agrégés, moyennés sur tous les liens de la région. Ces variables peuvent être estimées à partir de données typiques telles que les boucles et les sondes. Cependant, étant donné que ces données ont des couvertures et des propriétés différentes et que la disponibilité des données peut varier, il peut être assez difficile d'estimer les variables, en particulier pour la densité et l'accumulation. D'autre part, de nombreuses études ont mentionné que les formes des MFD affectent considérablement les résultats de simulation obtenus avec les modèles MFD. La longueur agrégée des trajets pour le paramètre du modèle MFD est calculée à partir des données de trajectoire des trajets individuels complets. Les modèles MFD typiques requièrent différentes agrégations des longueurs de trajet pour éviter des erreurs importantes. Ainsi, une calibration précise des paramètres du modèle est importante pour améliorer la précision de la prédiction du modèle MFD. Cependant, nous manquons d'une analyse empirique de la relation entre la disponibilité des données et la calibration des paramètres et la

précision de la prédiction des modèles MFD.

De plus, les modèles MFD reposent sur l'hypothèse forte que l'état du trafic dans chaque région urbaine est homogène puisque les mêmes variables d'état du trafic sont utilisées pour caractériser tous les véhicules en mouvement à un moment donné. Des méthodes de partitionnement du réseau ont été développées pour déterminer la répartition d'un réseau urbain en régions homogènes. Les modèles MFD ont également été étendus pour prendre en compte l'échange de flux entre deux ou plusieurs régions. En outre, les autres modes de circulation, tels que les bus et les motos, ont des effets différents sur l'état du trafic, alors que les modèles MFD précédents ne prennent en compte que les voitures. Le modèle MFD étendu utilisé pour prendre en compte les différents modes de circulation a récemment fait l'objet d'une attention considérable. Ces modèles étendus ont souvent été considérés dans le contexte du contrôle et des opérations avec la simulation numérique. Cependant, aucun modèle conçu pour améliorer la précision des prévisions à l'aide de données réelles en tenant compte de la calibration des paramètres n'a encore été proposé dans un cadre multirégional ou multimodal.

Ici, le principal objectif de recherche de cette thèse est d'étudier comment ajuster les paramètres du modèle MFD et les méthodes de calibration pour obtenir la meilleure précision de prédiction. Cet objectif est lié à trois défis : 1) Estimer les principales variables du modèle et définir les meilleures méthodes de calibration, y compris la résolution appropriée pour les principaux paramètres, 2) Évaluer la précision du modèle MFD par rapport aux réglages du modèle et des paramètres, 3) Tester de nouvelles extensions du modèle MFD avec des longueurs de trajets hétérogènes et des descriptions de séquences de trajets. Les chapitres 2 et 3 ont abordé le défi 1. Les chapitres 4, 5 et 6 ont résolu le défi 2. Le défi 3 a été abordé dans les chapitres 5 et 6.

Chapitre 2: Évaluation expérimentale de l'estimation de la densité du trafic au niveau des liens et du réseau avec des données éparses

La surveillance des réseaux de transport urbain est un défi car les données sont généralement éparses : les détecteurs de boucles ne couvrent qu'une fraction limitée du réseau routier et les véhicules sondes ont un faible taux de pénétration. Ce chapitre étudie la précision de l'estimation de la densité moyenne à partir de la détection directe à différentes échelles urbaines, principalement aux niveaux du lien et du réseau. Des études antérieures ont montré que la densité des liens est difficile à estimer car (i) les capteurs ponctuels comme les boucles ne peuvent pas fournir une image complète de l'état du trafic des liens dans un contexte dynamique, et (ii) les véhicules sondes fournissent une meilleure couverture spatiale dans les liens, mais les taux de pénétration souffrent de grandes divergences tout en étant nécessaires aux observations d'échelle.

Ici, différentes méthodes de calcul sont comparées en fonction du type de données et de leur disponibilité afin de quantifier l'ampleur des erreurs attendues. Il apparaît que les données de sonde sont essentielles pour réduire l'ampleur de l'erreur au niveau du lien, mais l'estimation précise de la densité nécessite des taux de pénétration élevés, ce qui n'est guère vrai en pratique. Dans cet article, nous améliorons la méthode du taux de pêche

pour estimer la densité lorsque la couverture spatiale du détecteur de boucle et les taux de pénétration des sondes sont faibles. Le taux de pêche est le rapport entre les sondes détectées à l'emplacement des boucles et le débit des boucles. La méthode combine les observations des sondes et des boucles au même endroit pour déterminer les flux de liaison. Lorsque ces données ne sont pas disponibles en temps réel, nous pouvons toujours utiliser des informations historiques où le taux de pêche est déterminé sur la journée au même endroit ou en moyenne sur l'ensemble du réseau. Les données des sondes sont également précieuses pour mieux caractériser la longueur des véhicules électriques détectés par les boucles. Cela permet d'améliorer la relation entre l'occupation et la densité lorsque seules les données des boucles sont disponibles en temps réel.

Au niveau du réseau, il est possible d'obtenir des estimations précises de la densité en combinant les observations des boucles et des sondes, même si peu de liens capturent les deux sources de données. En particulier, la nouvelle méthode qui considère explicitement la covariance entre le temps de déplacement total calculé par les données de sonde et le taux de pêche conduit à des erreurs très faibles. Cependant, le besoin initial de données pour estimer correctement cette covariance est important. L'utilisation du taux de pêche au niveau du réseau, qui est calculé à partir des liens avec des boucles pour l'estimation de tous les liens, est une méthode plus raisonnable avec une faible erreur. Les résultats montrent que, en utilisant la méthode d'estimation appropriée en fonction de la disponibilité des données, c'est-à-dire en définissant soigneusement les taux de pêche à cette échelle, nous pouvons obtenir une bonne précision d'une densité moyenne qui représente la charge globale de la région.

Ainsi, ce chapitre propose des indications claires sur l'ampleur de l'erreur à laquelle nous pouvons nous attendre compte tenu de la méthode de calcul et de la disponibilité des données. Nous pouvons, par exemple, utiliser ces résultats pour spécifier quel taux de pénétration et quelle couverture de boucle sont nécessaires pour atteindre un niveau d'erreur ciblé. De telles indications seraient très utiles lors de la conception de systèmes de surveillance sur le terrain, tant au niveau des liaisons que des réseaux.

Chapitre 3 : Enquête sur les propriétés du voyage en considérant le partitionnement du réseau

La longueur des trajets et le diagramme fondamental macroscopique (MFD), c'est-à-dire la relation entre le débit, la densité et la vitesse au niveau du réseau, sont des paramètres clés des modèles de trafic macroscopiques. Des études antérieures ont précisé que l'étalonnage du MFD moins dispersé nécessite le partitionnement du réseau en plusieurs petites régions présentant un état de trafic homogène. Cependant, le calibrage de la longueur du trajet dans de petites régions nécessite des données de trajectoire détaillées qui peuvent être difficiles à obtenir à partir de sources de données de trajectoire typiques telles que les sondes. Ce chapitre étudie l'effet de la granularité du partitionnement sur la précision de la calibration du MFD et de la longueur du trajet et découvre la méthode d'agrégation de la longueur du trajet appropriée avec des données limitées.

Tout d'abord, une méthode statique simple pour séparer le réseau en deux zones d'état du trafic, c'est-à-dire les poches congestionnées et les poches moins congestionnées, avec différents poids sur l'homogénéité de la vitesse dans les zones, est proposée pour tester les

différentes granularités du partitionnement du réseau. Pour le calibrage MFD, nous confirmons que l'écart type de la vitesse moyenne des liaisons dans la zone peut être assez faible selon le partitionnement du réseau. D'autre part, ce partitionnement du réseau conduit à un nombre élevé de longueurs moyennes de séquences de chemins, c'est-à-dire le nombre moyen de zones traversées par tous les trajets, ce qui rend le calcul de la longueur des trajets difficile avec une disponibilité limitée des données.

Pour le calibrage de la longueur des trajets, différentes méthodes d'agrégation pour deux paramètres typiques de longueur des trajets à adapter dans les modèles MFD, à savoir la moyenne et la distribution, en fonction de la disponibilité des données de trajectoire, sont comparées à la vérité terrain, qui est calculée à partir des données de trajectoire détaillées de tous les véhicules du réseau capturées par l'expérience de drone à Athènes. En conséquence du calibrage de la longueur moyenne du trajet, si aucune information sur la séquence de la trajectoire n'est disponible, l'estimation précise de la longueur du trajet est assez difficile. C'est notamment le cas lorsque seules des trajectoires partielles sont disponibles en raison d'un changement d'identification du véhicule sonde ou de données manquantes. D'autre part, si même quelques échantillons des trajectoires régionales ou des informations sur la séquence du trajet sont disponibles, la précision de l'estimation s'améliore considérablement. Suite au calibrage de la distribution de la longueur du trajet, l'utilisation d'une distribution conjointe entre la longueur du trajet régional des poches ou entre la longueur du trajet et la séquence du trajet est nécessaire pour obtenir une estimation précise des longueurs du trajet régional et du trajet complet. Cependant, le volume des données de trajectoire affecte énormément l'estimation de la longueur du trajet avec la distribution conjointe, et il est nécessaire d'avoir un plus grand nombre de trajectoires pour obtenir de meilleurs résultats.

Chapitre 4 : Calibrage des modèles MFD considérant une seule région

La calibration précise des paramètres du modèle est essentielle pour la prédiction de l'état du trafic dans le cadre du modèle macroscopique. Cependant, l'effet du réglage des paramètres n'a jamais été clarifié dans la littérature car il nécessite des données de trajectoire détaillées avec un bon taux de pénétration, ce qui est difficile par les sources de données typiques telles que les sondes. Ce chapitre évalue la précision de la prédiction par les modèles de trafic macroscopiques en fonction des réglages des paramètres clés, c'est-à-dire le diagramme fondamental macroscopique (MFD) et la longueur du trajet, sur la base des données de trajectoire complètes collectées par les expériences de drone à Athènes (Barmpounakis & Geroliminis (2020)).

Pour évaluer la prédiction du modèle MFD, nous avons besoin d'un ensemble de données continues pendant toute une période afin de travailler avec un horizon de prédiction suffisamment large. Cependant, les expériences de drone ont quatre temps d'arrêt dans une période de temps totale de 2,5 heures pour changer les batteries du drone. Par conséquent, nous proposons tout d'abord une méthode pour compléter les trajectoires des véhicules pendant cette période sans données en nous basant sur la dynamique globale du trafic que nous observons.

Des études antérieures mentionnent que deux modèles classiques de MFD, c'est-à-dire le modèle basé sur l'accumulation et le modèle basé sur les trajets, nécessitent des paramètres

de longueur de trajet différents, et l'utilisation de paramètres inappropriés peut entraîner une énorme erreur dans les résultats de prédiction. Nous comparons d'abord les résultats de prédiction de deux modèles MFD utilisant des paramètres de longueur de trajet typiques, c'est-à-dire la moyenne et la distribution, avec l'état du trafic de base calculé directement à partir des données de trajectoire après imputation des données. Pour éviter les erreurs causées par les paramètres MFD et se concentrer sur l'effet de la longueur du trajet, des valeurs de vitesse réelles ont été utilisées au lieu d'utiliser le MFD. En conséquence, le modèle basé sur l'accumulation utilisant la longueur moyenne du trajet était une méthode efficace avec une grande précision et peu d'exigences de calibration des paramètres par rapport au modèle basé sur le trajet. Cependant, la précision de l'estimation de la longueur moyenne des trajets peut affecter de manière significative les résultats de prédiction des deux modèles, et les petites erreurs de calibration peuvent conduire à d'énormes erreurs de prédiction. Si la précision de l'estimation de la longueur du trajet est insuffisante, le modèle basé sur le trajet utilisant la distribution de la longueur du trajet peut conduire à des résultats meilleurs et plus stables.

Pour étudier l'effet des paramètres du MFD, les résultats de prédiction sont comparés en fonction des paramètres variables du MFD approximé. Il en résulte que la production critique, c'est-à-dire le débit maximal du réseau, joue un rôle important dans les résultats de perdition. De plus, comme les meilleurs réglages de variables sont différents selon les modèles, il a été nécessaire de procéder à un calibrage séparé.

Chapitre 5 : Calibrage des modèles MFD en tenant compte des régions multiples et des séquences de parcours

Une extension multirégionale des modèles MFD a été développée pour prédire plus précisément l'état du trafic dans le réseau partitionné avec un état du trafic régional homogène. Comme les flux de trafic régionaux interagissent les uns avec les autres, le réglage des paramètres peut affecter les résultats de la prédiction différemment des modèles à région unique. En particulier, la séquence des chemins, c'est-à-dire l'ordre des régions traversées par un véhicule, y compris les trajets de retour vers la région, peut jouer un rôle important, notamment lorsque nous considérons le partitionnement non compact en petites régions non connectées, par exemple les poches congestionnées et moins congestionnées expliquées au chapitre 3. Cependant, un modèle MFD capable de prendre en compte l'effet de telles trajectoires sur la base d'informations sur la séquence des chemins n'a pas encore été proposé.

Dans un premier temps, ce chapitre propose une méthode étendue pour prendre en compte la séquence des trajectoires dans le cadre des modèles MFD classiques. Pour le modèle basé sur l'accumulation, la séquence des trajets est considérée comme un processus binomial, et seule la valeur moyenne du nombre de retours dans les régions est nécessaire comme information agrégée sur la séquence des trajets. Pour le modèle basé sur les déplacements, l'extension est simple car les longueurs des déplacements et les séquences de trajets correspondantes peuvent être attribuées individuellement.

Nous comparons les résultats de prédiction entre les cas avec et sans prise en compte de la séquence des trajets basés sur les modèles basés sur l'accumulation et les trajets selon deux paramètres de longueur de trajet, c'est-à-dire la moyenne et la distribution. Pour éviter

les erreurs causées par les paramètres MFD et se concentrer sur l'effet de la longueur du trajet, des valeurs de vitesse réelles ont été utilisées au lieu d'utiliser le MFD. Par conséquent, la prise en compte de la séquence des trajets améliore considérablement la précision du débit sortant régional. La précision de l'accumulation était légèrement meilleure ou peu différente par rapport au cas sans considération de la séquence des trajets lorsque la longueur moyenne des trajets partiels est utilisée dans les deux modèles. Lors de l'utilisation de la distribution conjointe entre la séquence des trajets et la longueur des trajets régionaux, la précision de l'accumulation prédite pourrait se détériorer par rapport au cas sans séquence des trajets puisque l'estimation de la distribution conjointe nécessite plus de données individuelles que la distribution normale de la longueur des trajets. Ainsi, la calibration globale des différentes longueurs de trajet par séquences de sillons inclut plus d'erreurs qui ont un impact sur les résultats de la simulation.

Chapitre 6 : Calibrage des modèles MFD en tenant compte des modes multiples

Les modèles MFD dans le cadre multimodal, qui prennent en compte les différents comportements de déplacement de chaque mode et l'interaction entre les flux de trafic modaux, ont récemment fait l'objet d'une grande attention. Il est essentiel d'étudier l'effet des paramètres modaux sur la précision de la prédiction, mais aucune étude n'a jamais été réalisée en raison du manque de données sur les trajectoires modales dans le même réseau. Dans ce chapitre, les données de trajectoire complètes de tous les véhicules dans plusieurs modes de l'expérience du drone d'Athènes (Barmpounakis & Geroliminis (2020)) permettent d'étudier l'effet des paramètres, c'est-à-dire le MFD et la longueur du trajet, sur les résultats de la prédiction dans le cadre du modèle MFD multimodal.

Avant de considérer le modèle MFD multimodal, l'effet du paramétrage de la longueur du trajet avec différentes agrégations, c'est-à-dire la moyenne et la distribution, a été comparé pour les voitures, les bus et les motos sur la base des modèles monomodaux en utilisant la vitesse moyenne réelle au lieu d'utiliser le MFD. En conséquence, les résultats de la prédiction pour les bus et les motos pourraient avoir des erreurs plus importantes que pour les voitures, car la vitesse individuelle avait une plus grande plage alors qu'une seule valeur était donnée pour chaque mode de véhicule. De plus, l'accumulation des bus et des motos étant un peu plus faible que pour les voitures, la petite différence par rapport à la vérité terrain entraînerait des erreurs considérables.

La principale différence entre les modèles multimodaux et monomodaux est que l'étalonnage du MFD étendu 3D, qui représente la relation entre le débit, la densité et la vitesse dans deux modes différents, est nécessaire pour les modèles MFD multimodaux. Nous examinons ici deux méthodes différentes de calibrage de la MFD 3D, à savoir " l'approximation basée sur le V-MFD ", utilisée par plusieurs études précédentes, et " l'approximation basée sur le P-MFD ", que nous venons de proposer. L'approximation V-MFD est une approximation linéaire basée sur la relation entre l'accumulation et la vitesse moyenne des voitures et d'un autre mode. L'approximation basée sur P-MFD est une approximation trapézoïdale pour la relation entre l'accumulation et la production de voitures ou d'un autre mode.

En raison de la précision de la prédiction selon les différentes méthodes de calibration 3D MFD, l'utilisation de l'approximation basée sur V-MFD entraîne des erreurs as-

sez importantes dans la prédiction des accumulations modales. La meilleure option est l'approximation proposée basée sur le P-MFD, et nous pouvons obtenir des prédictions plus précises qu'en utilisant le MFD monomode. D'autre part, les petites erreurs de calibration des paramètres peuvent conduire à des erreurs de prédiction significatives pour l'état de trafic très encombré.

Chapitre 7 : Conclusions

Les principales conclusions de cette thèse peuvent être résumées en quatre points.

1. L'estimation précise de la densité du trafic est presque impossible au niveau du lien, sauf si les données de sonde en temps réel et les données de boucle historiques capturent des sondes à chaque lien au moment concerné. En revanche, l'estimation de la densité du trafic au niveau du réseau peut conduire à une bonne précision, notamment en utilisant les taux de pêche au niveau du réseau. Lorsque les données de sonde en temps réel ne sont pas disponibles, l'utilisation d'une relation historique entre l'occupation et l'EVL est utile.

2. Le partitionnement du réseau avec une faible compacité du réseau améliore l'homogénéité de la vitesse, ce qui conduit à une bonne forme de MFD, mais conduit également à une plus grande complexité de l'estimation de la longueur du trajet, qui nécessite des données plus détaillées. Si aucune information sur la séquence du trajet n'est disponible, l'estimation de la moyenne et de la distribution de la longueur du trajet est difficile. L'utilisation de la distribution conjointe entre la longueur du trajet régional des deux poches ou entre la longueur du trajet et la séquence des trajets est nécessaire pour estimer avec précision la longueur du trajet régional et complet.

3. Le modèle basé sur l'accumulation avec la longueur moyenne des trajets est une méthode efficace avec une précision similaire à celle du modèle basé sur les trajets avec un temps de calcul inférieur. Cependant, la précision de la calibration de la longueur moyenne du trajet affecte le modèle basé sur l'accumulation de manière plus significative que le modèle basé sur le trajet, et le modèle basé sur l'accumulation nécessite une calibration plus précise de la longueur du trajet. L'utilisation de la distribution de la longueur des trajets est plus stable et meilleure pour le modèle basé sur les trajets si la précision de la calibration de la longueur des trajets est insuffisante.

4. Dans le cadre multirégional, l'accumulation régionale peut être prédite avec précision sans séquence de trajets. Cependant, la prédiction du flux sortant régional nécessite des informations sur la séquence des chemins. Le calibrage global de la distribution de la longueur des trajets par séquence de trajets peut inclure plus d'erreurs pour introduire une moins bonne précision de prédiction que lorsque la séquence de trajets est considérée séparément de la longueur des trajets. Dans le cadre multimodal, l'extension 3D de l'approximation trapézoïdale basée sur la P-MFD peut fournir des prédictions plus précises que l'utilisation de la MFD monomodale et de l'approximation linéaire de la V-MFD 3D.

Cette thèse élargit les perspectives pour les recherches ultérieures. Certaines d'entre elles sont présentées ci-dessous. Par exemple, l'extension multirégionale des modèles MFD multimodaux peut encore améliorer la précision des prédictions. D'un autre côté, étant donné que l'extension multirégionale nécessite des données de trajectoire plus détaillées pour le calibrage de la longueur du trajet, et que l'extension multimodale nécessite un calibrage 3D-MFD qui est beaucoup plus compliqué que le MFD d'un seul mode, les modèles multimodaux multirégionaux peuvent nécessiter beaucoup plus de données et de calibrage pour le réglage des paramètres afin de prédire des états de trafic précis. Dans un autre exemple, l'utilisation de l'assimilation de données pour calibrer les paramètres peut améliorer les résultats de la prédiction. L'assimilation de données en temps réel dans les cadres de modèles MFD a récemment reçu beaucoup d'attention de la part de nombreux chercheurs. Il est possible de développer davantage ce cadre en fonction des résultats de cette thèse.

DECLARATION

This these has been prepared in collaboration between LICIT-ECO7 in École Nationale des Travaux Publics de l'État (ENTPE) and Urban Transport Systems Laboratory (LUTS) in École Polytechnique Fédérale de Lausanne (EPFL) and co-supervised by Prof. Ludovic Leclercq from ENTPE/Université Gustave Eiffel and Prof. Nikolas Geroliminis from EPFL. This research project is co-funded by Univ. Gustave Eiffel and EPFL.

ACKNOWLEDGEMENTS

It was a big challenge for me to stay abroad more than three years to complete my doctoral research. Also, the last two years from 2020 were exceptional and complex, with 6 months of lockdown in total and a lot of new rules because of the world-class pandemic of Covid19. It would have been impossible to finalize my thesis without the support of my two great supervisors, Professor Ludovic Leclercq, director of the LICIT lab (ENTPE, Univ. Gustave Eiffel), and Professor Nikolas Geroliminis, director of the LUTS lab (EPFL). Prof. Leclercq took care of me even before arriving in Lyon for my new life abroad. Discussing with him always made me excited to consider new research problems ideas. In addition, our discussions helped me mentally during the lockdown. Prof. Geroliminis always made me find new exciting research perspectives during discussions and in his comments on the research reports. My only regret was that the plan to stay at Lausanne every year had been canceled due to Covid19, and I could visit only once in the first year. The most impressive moments were the discussions with both professors, which were always interesting and stimulating with a harmonious atmosphere. I would therefore first of all like to express my deep gratitude towards both Prof. Leclercq and Prof. Geroliminis for taking care of me a lot and providing me with an amazing research experience.

I would also like to thank the committee members of my thesis. Professor Mahdi Zargayouna (Universite Gustave Eiffel) and Professor Jack Haddad (Technion University) reviewed my manuscript and gave a lot of exciting and detailed comments and advice to improve my thesis. Together with Prof. Zargayouna and Prof. Haddad, Professor Christine Solnon and Professor Anastasios Kouvelas provided me with critical questions during the Ph.D. defense that broadened my perspective and made interesting discussion about the prospects of this research. It was my honor to have such high-level and internationally recognized professors as committee members.

The warm atmosphere at both the LICIT and LUTS labs helped me a lot to improve my research without stress. I would especially like to thank Professor Nour-Eddin El Faouzi (Universite Gustave Eiffel), Sonia Cenille, and Anne-Christine Demanny, the two secretaries of the lab, for their respective support of research circumstances and related administrative tasks. Also, I would like to thank all my colleagues in LICIT and LUTS. Lunch and coffee break time with LICIT members were some of the most fun moments. Besides these enjoyable moments, I learned many interesting things not only related to research techniques but also about French and international cultures. LUTS members broke the ice easily and welcomed me for the three months that I stayed at Lausanne. It was sad that I missed the

opportunity to work together with them again because of the lockdown. Thank you very much to all members of both laboratories, and I believe that we can keep in contact and see each other often.

In the first place, I got the motivation to start this challenge, i.e., doing doctoral research abroad, due to Professor Masao Kuwahara (Tohoku university). His advice, based on his own studying experience abroad, made me motivated to leave Japan and ask Prof. Leclercq and Prof. Geroliminis to be my supervisors. Also, Prof. Yusuke Hara (Tohoku university) provided me with many tips to do research abroad and took care of me at the beginning of my doctoral life. 桑原先生，原さん，本当にお世話になりました

Also, I appreciate my friends who supported my life in Lyon and Lausanne. I could refresh and enjoy the music, exchange languages, discover food and bars in Lyon, hike in the nature in Lausanne, and travel in Europe. リヨンで仲良くしてくださった皆様，ありがとうございました！ Merci beaucoup à mes amis et amies de Lyon et Lausanne ! Ευχαριστώ πολύ, ελληνική μου οικογένεια ! Tusind tak, min snuske!

Finally, I would like to thank my loving family. It was too long not to see them in person during the Covid period. But they always cheer me up over the telephone and take care of me the most. いつも応援してくれて，励ましてくれて，本当にありがとう．これからも頑張るよ！

TABLE OF CONTENTS

1. General Introduction

1.1 Background

Road congestion in and surrounding urban areas during peak commuting hours is an important global issue from the economic and environmental standpoints. Heavy congestion is expensive for the economy due to the time lost and it increases air pollution emissions. Real-time traffic control strategies, e.g., road pricing and dedicated lanes, and traffic management, e.g., route guidance and traffic information announcement, have received much attention as solutions to decrease urban congestion. So that such strategies can function properly , robust and accurate traffic state predictions based on real data are necessary. In this thesis, we focus on one specific class of traffic model based on the MFD concept, e.g., Daganzo (2007) and Geroliminis & Daganzo (2008). Such models permit reproducing traffic dynamics at the large urban scale and are very useful when considering control strategies acting at the full urban scale.

Traffic prediction using data consists of three steps, as shown in Figure 1.1:

1. Estimating traffic state and trip properties based on network design and traffic data
2. Calibrating model parameters based on estimated traffic state variables and trip properties
3. Predicting traffic state properties using models based on calibrated parameters.

Thus, model prediction accuracy may depend on both the parameter calibration method and on the model design itself (resolution, settings, etc.). In addition, traffic state and trip property estimation accuracy dependent on data availability and network properties may sig-

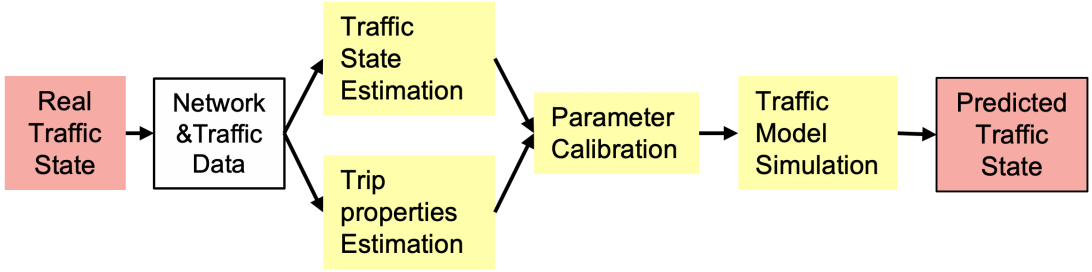

FIG. 1.1 – *Traffic Prediction Steps*

nificantly affect parameter calibration. Therefore, a comprehensive investigation of model calibration considering data availability and network properties is essential to improve traffic state prediction accuracy. In the following subsections, we present classical traffic data properties in Section 1.1.1 and the MFD models in Section 1.1.2. In Section 1.1.3, the essential traffic state variables and model parameters are presented. In Section 1.1.4, we link the main objective of this thesis to the components presented previously .

1.1.1 Traffic Data Properties

Due to the development of sensor technologies, several types of data are available in real-time. Traditional data sources for capturing vehicle traffic states are loop detectors and probe vehicles. The loop detector provides the number of vehicles observed per period of observations and local information on vehicle speed. Probe vehicles provide the vehicle's trajectory information, i.e., time and location. Recently, aerial video data that can track the complex behavior of vehicles are becoming available due to the development of drones.

Each type of data has different advantages and disadvantages when used for traffic simulation. For example, we can easily obtain an accurate local flow level by counting the number of vehicles on loops. However, for monitoring traffic in a larger area, the number of existing loops is usually not large enough to provide a complete picture. Because of the huge cost related to adding new loop sensors, not many cities can have high coverage with loops, e.g., around 7% of the total network in Lyon, France. Probe data usually covers a huge area according to individual trips. On the other hand, if there are only a few probe vehicles in some links, they may not be numerous enough to obtain accurate local traffic state estimations. For example, if there is only one probe vehicle that drives slowly in the road link with, the traffic state estimated from the data can be considered "congested." Thus, it is necessary to know the probe vehicle penetration rate, i.e., the ratio of the probe vehicles over total number of vehicles in the area. However, it is impossible to obtain the total number of vehicles number using probe data. Also, individual complete trajectories are sometimes unavailable because of missing spatial and temporal data and changes of vehicle ID. Aerial video data can provide complete trajectories of all the vehicles in the area. However, the time duration is often short, and the area monitored is quite limited.

The difference in coverage of these data is summarized in Figure 1.2. The red color shows where the data sources can detect all the vehicles, and blue color shows where they can detect some vehicles. As shown in Figure 1.2, the coverage of all data is quite different. Therefore, we need to carefully estimate traffic and trip characteristics according to the

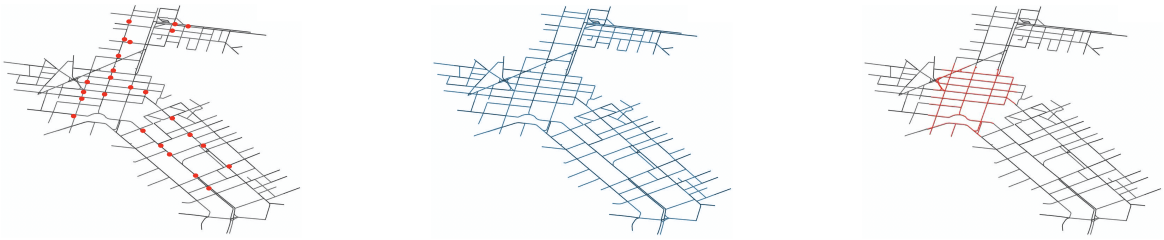

(a) Loop Detector (b) Probe Vehicles (c) Aerial Videos (Drones)

FIG. 1.2 – *Example of Coverage of Each Data Source in the network (Red: possible to detect all vehicles, Blue: possible to detect some vehicles)*

properties of the available data.

1.1.2 Network-level Aggregated Traffic Simulation Model

For decades, the traffic simulation model has been developed for traffic state prediction at the link and network levels. In particular, the aggregated network-level model based on the Macroscopic Fundamental Diagram (MFD) has received lot of attention for calculating the traffic state of a large network with short computational time in line with the works of Daganzo (2007), and Geroliminis & Daganzo (2008). The idea of this model is to express the traffic as regional flows by using MFD that shows the relationship between the mean traffic flow and density in the network. This model does not require calculating the local traffic state at the link level whereas the other traditional traffic models do. Therefore, a much shorter computational time is required for network-level traffic estimation and prediction; besides, MFD can provide network-level traffic trends. The facility of using MFD models has already led to their implemention in studies on control and operations. Keyvan-Ekbatani *et al.* (2012) and Haddad & Mirkin (2017) implemented a perimeter control and gating system and showed promising results to decrease congestion in urban areas. Yildirimoglu *et al.* (2015) and Sirmatel & Geroliminis (2017) proposed route guidance methods at a large scale by using MFD models to improve traffic conditions.

MFD models rely on the strong assumption that the traffic state in each urban region is homogeneous since the same traffic state variables are used to characterize all moving vehicles at a given time. Network partitioning methods have been developed to determine the break down of a urban network into homogeneous regions, e.g., Ji & Geroliminis (2012), Saedi *et al.* (2020), An *et al.* (2018), and Saeedmanesh & Geroliminis (2016). MFD models have also been extended to consider the exchanging flows between two or multiple regions, e.g., for two regional models: Geroliminis *et al.* (2013) and for multiregional models: Aboudolas & Geroliminis (2013), Hajiahmadi *et al.* (2013), Yildirimoglu & Geroliminis (2014), Mariotte & Leclercq (2019), based on the idea of the first two regional models by Geroliminis & Daganzo (2007). Furthermore, according to Boyaci & Geroliminis (2011) and Barmpounakis *et al.* (2016), the other traffic modes, such as buses and motorcycles, have different effects on the traffic state while the previous MFD models only consider cars. The extended MFD model used to consider different traffic modes has received considerable attention recently, e.g., Ampountolas *et al.* (2017) and Dakic *et al.* (2019), based on the idea of bi-modal MFD (3D-MFD) proposed by Geroliminis *et al.* (2014). These extended models have often been considered in the context of control and operations with numerical simulation. However, no model designed to improve prediction accuracy using real data by considering parameter calibration has yet been proposed within multiregional or multimodal frameworks.

1.1.3 Variables and Parameters for MFD Models

Classical MFD models require two essential parameters: MFD and trip length. The fundamental traffic state variables that compose MFD are mainly aggregated density k_r, flow q_r, and speed v_r averaged over all the links in region r. Accumulation n and production P are useful variables to calculate the network-level total amounts straightforwardly by summing up these variables of all the vehicle modes in the regions as $n = \sum n_{r,m}$ and $P = \sum P_{r,m}$ where r expresses the regions and m expresses the vehicle modes. The aggregated density and flow

can be easily transformed into these variables as $n_{r,m} = l_{r,m} * k_{r,m}$ and $P_{r,m} = l_{r,m} * q_{r,m}$, where $l_{r,m}$ is the total link length of mode m vehicles in region r. These variables can be estimated based on typical data such as loop and probe. However, since such data have different coverages and properties and the availability of the data may differ, it can be quite challenging to estimate the variables, especially for density and accumulation. On the other hand, many studies, e.g., Leclercq *et al.* (2015) and Xue *et al.* (2016), mentioned that MFD shapes considerably affect the simulation results obtained with MFD models, in particular an MFD that is scattered or unstable over time may lead to large errors. The aggregated trip length for the MFD model parameter is calculated from the trajectory data of complete individual trips. Typical MFD models require different aggregations of trip lengths. For example, the initial MFD model called the "accumulation-based model" proposed by Daganzo (2007) and Geroliminis & Daganzo (2008) uses an average trip length value for all individuals. The "Trip-based model" was proposed to consider trip length variety, and trip length distribution was adapted easily by Lamotte & Geroliminis (2017). Batista *et al.* (2019) mentioned that using an average value for all individuals in the trip-based model may cause significant errors in prediction results. Thus, accurate model parameter calibration is important to improve MFD model prediction accuracy.

In the multiregional and multimodal frameworks, calculating model parameters with good accuracy can be tricky as it depends on data availability. For example, network partitioning into multiple regions is useful to observe highly scattered MFD. On the other hand, trip length calculation requires the complete individual trajectories in every region. This can be quite challenging in the case of sparse data such as probe data. Furthermore, Batista *et al.* (2019), and Paipuri *et al.* (2020) suggested calibrating trip length parameters considering path sequence, i.e., ordering regions crossed by a vehicle, which requires even more detailed and sequencing trajectory data. Also, multimodal MFD models require multimodal traffic and trajectory data for parameter calibration that may be available in a few limited areas.

Thus, the accuracy of model parameter calibration according to data availability may strongly affect prediction accuracy. However, we lack an empirical analysis of the relation between data availability and parameter calibration and the accuracy of MFD model prediction.

1.1.4 The Structure of Chapter 1

This chapter has five sections. In Section 1.2, we explain the final research goal in this thesis and three main challenges to achieve the goal. In Section 1.3, six research questions to address the challenges and the methods used to answer the questions are described. The relationship between all the challenges and research questions is summarized in Figure 1.3. In Section 1.4, the main contributions of this thesis are summarized in two main parts: 1) the estimation of traffic and trip characteristics, and 2) the application of the method to the MFD model. Finally, the outline of the following chapters is presented in Section 1.5.

1.2 Research Goal and Challenges

The research goals of this thesis are listed below:

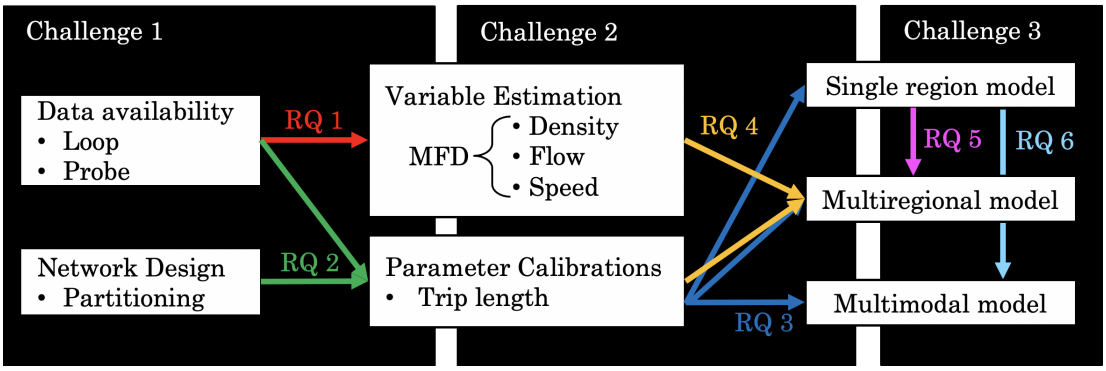

FIG. 1.3 – *Outline of Sections in Chapter 1 (RQ: Research Question)*

Research Goal Investigating how to adjust the MFD model settings and calibration methods to achieve the best prediction accuracy.

This goal is related to three main challenges.

1.2.1 Challenge 1

Challenge 1

Estimating the main model variables and defining the best calibration methods including the proper resolution for the main parameters.

The proper calibration of two key MFD model parameters, i.e., MFD and trip length, is essential for accurate prediction. However, parameter calibration has several issues that depend on the available data.

MFD calibration requires accurate traffic state variables, while the traffic state estimation, especially for traffic density, can be challenging because of technical and scaling issues of available data. When using loop data, density cannot be directly calculated from observation, and loop detectors observe only a narrow local area of the road link. Therefore, it is necessary to transform the local variables observed into link-level density, which is technically hard to estimate correctly. Also, probe data is quite sparse temporally and spatially. The penetration rate, which is impossible to estimate in general, is required to scale up the probe vehicle density to represent all vehicles.

MFD parameters should be calibrated in a region with a stable and homogeneous state once the traffic state has been estimated accurately. However, network partitioning that results in smaller homogeneous regions can decrease trip length calibration accuracy since it requires more detailed trajectory data that is often challenging to obtain with probe data. Also, since each MFD model uses trip length differently for traffic state prediction, different trip length aggregation granularities are required.

Thus, it is important to calibrate model parameters by carefully estimating and aggregating traffic and trip characteristics according to data availability. However, analysis of the empirical effect of data availability on model parameter calibration has not yet been accomplished because of the lack of real data sets such as long-term data from several typical data sources in the same network. These sets can be used to test the different data available and

the detailed trajectory data to obtain accurate and variable trip length aggregations.

1.2.2 Challenge 2

Challenge 2

Assessing MFD model accuracy with respect to the model and parameter settings.

Considering the two main kinds of MFD models, i.e. the accumulation-based and trip-based models, different trip length aggregations are required, as described in Section 1.1.3. Furthermore, trip length and MFD settings may affect prediction results in a more complicated way when considering a multiregional or multimodal setting than for a more classical single regional approach. Since data availability and network design may affect parameter calibration, it is important to clarify the effect of parameter calibration accuracy and settings on the prediction results by MFD models in single-region, multiregional, and multimodal configurations.

However, few studies have investigated the effect of parameter settings on MFD model prediction, and those that have are theoretical or based on numerical simulations of the real network. The empirical analysis of MFD model parameter settings using real traffic data has not been accomplished since it requires data to provide the real traffic state and detailed trajectories to test trip length aggregations in multiple regions and for multiple modes. In this thesis, an unprecedented dataset of the complete trajectories of all vehicles will for the first time allow investigation by empirical analysis to assess the concrete effect of parameter and model settings.

1.2.3 Challenge 3

Challenge 3

Testing new MFD model extensions with heterogeneous trip lengths and path sequence descriptions.

In the multiregional framework, path sequence, i.e., the order of regions that a vehicle crosses, can be an important parameter in addition to MFD and trip length, as affects trip length calibration. In particular, when only partial trajectories in a region can be tracked for individual trips by probe data, aggregated information to complete a whole trip, such as path sequence information, is necessary. Also, Batista *et al.* (2019) suggested using path sequence information in the MFD model, especially in the trip-based model, to obtain an accurate prediction.

MFD models considering trip OD and regional routes to a destination have been developed in the multiregional framework. However, these models are used for control applications, while routes optimizing the traffic state and corresponding trip length are defined by dynamic traffic assignment. The route assigned in the previous models cannot cross the same regions multiple times, although with real data vehicles can return to the same region several times. To improve prediction accuracy in a multiregional framework, it is necessary to consider more accurate trip information such as path sequence information. However, a

method for calibrating path sequence information, and MFD models that take such information into account have not yet been proposed. This gap will be filled in this thesis.

1.3 Research Questions and Scopes

To address the challenges in Section 1.2, we defined the six research questions below.

1.3.1 Research Question 1: Accurate Traffic Density Estimation for MFD calibration

Research Question 1

What is the best method to estimate traffic density when the available data are limited? What is the level of accuracy of all the existing methods to estimate link and network density?

This research question is directly linked with Challenge 1, described in Section 1.2.1. Since typical data, e.g., loop and probe, have different technical and scaling issues, as mentioned in Section 1.2.1, different data aggregation procedures and estimation approaches are required to obtain accurate estimation for density. However, no comprehensive comparison of methods for a real test case has been proposed.

To determine the best traffic density estimation method and the expected estimation accuracy, we introduce two variables for scaling up local observations: loop coverage and probe penetration according to real-time and historical data availability. First, when real-time probe data are available, the fishing rate proposed by Geroliminis & Daganzo (2008) is useful. The fishing rate is the ratio of probes detected at the loop locations over the loop flows. Secondly, when real-time loop data are available, the length of the vehicle detected by the loop (called electric vehicle length here – EVL) can be used to improve the relationship between occupancy and density. When these variables are not available in real-time, we can still use historical information in which these variables are determined over the day at the same location or as an average over the whole network.

The assessment of density estimation accuracy requires the loop and probe data in the same network on multiple days. We select road links that have both probe and loop data in Lyon to define a subnetwork. The best method of estimating traffic density is when we use both probe and loop data of every time and location, whereas both probe and loop data are generally sparse in time and location. Therefore, we use this case as the reference of the accuracy assessment, and other cases using data aggregations are compared with this reference.

1.3.2 Research Question 2: Proper Trip Length Calibration according to Network Partitioning

Research Question 2

To what extent does network partitioning affect the MFD shape and trip length estimation accuracy? What is the proper trip length aggregation method for a partitioned network with limited data?

Challenge 1 can be addressed directly by investigating the proper MFD and trip length calibration. Several studies have already proved that network partitioning can create homogeneous states inside regions with less scattered MFD. On the other hand, it can complicate trip length estimation because of the increasing need for trajectory data, but no study clarifies the effect of network partitioning on trip length estimation accuracy. Also, Batista *et al.* (2019) and Paipuri *et al.* (2020) mentioned that path sequence information plays an important role in trip length estimation. However, the trajectory data of complete trips are necessary to obtain path sequence information, which is often difficult to get from typical data sources such as probe vehicles. Therefore, to investigate proper parameter calibration, we first need to clarify the effect of the network partitioning design on the MFD and the accuracy of trip length estimation. Finally, Challenge 1 can be addressed by a comparative accuracy assessment of trip length calibration according to data availability and network design.

To analyze the network partitioning effect on the speed homogeneity and complexity of trip length estimation, we propose a simple static method that separates the network into two traffic state areas, i.e., congested and less-congested pockets that are not necessarily connected. Partitioning with different weights on speed homogeneity versus the compactness of the region can be considered by using this partitioning method. Note that less compact regions will make trip length calculation difficult because they require more detailed trajectory data to track regional trips. We compare the variables representing speed homogeneity and trip length estimation complexity according to network partitioning settings. The standard deviation (STD) of link mean speed and the MFD shapes represent speed homogeneity. Correlations between individual path sequence length, i.e. the number of times vehicles pass through different pockets, and trip length and between the regional trip lengths of both pockets, are used as variables to show the difficulty of trip length and path sequence estimation.

To assess trip length estimation accuracy, we need to compare the real trip length from the complete trajectories and estimated trip length from typical sparse data. Athens drone data from Barmpounakis & Geroliminis (2020) provides all complete vehicle trajectories in the urban area. Using these data, we can calculate the real trip length as the reference of the assessment of trip length estimation accuracy. Also, the real path sequence of all the trajectories can be calculated from data to analyze the effect of path sequence information on trip length estimation accuracy. Proper methods for two typical aggregations of trip length, i.e., average and distribution, are investigated by comparing the reference and estimation with different data availabilities and trip length aggregation granularities, e.g., the availability of complete, regional, or partial trip length, and the availability of path sequence information.

1.3.3 Research Question 3: MFD Model Prediction Accuracy in a Single Region according to Parameter Settings

Research Question 3

To what extent do parameter settings affect the prediction accuracy of classical MFD models in a single region?

Research Question 3 directly addresses Challenge 2 in Section 1.2.2. Certain studies, e.g., Batista *et al.* (2019), Paipuri *et al.* (2020), Yildirimoglu & Geroliminis (2014), and Kouvelas *et al.* (2017), mentioned that trip length settings greatly impact the prediction results of MFD models. Also, since MFD is another key parameter in MFD models, many studies have developed proper MFD approximation. However, a few studies, i.e., Mariotte *et al.* (2017), analyzed the impact of these parameters on prediction results, considering different versions of MFD models. The comparative analysis of MFD models using real data according to different parameter settings can provide new insights into how to improve model predictions.

As Section 1.3.2, we can consider the various trip length aggregation settings by using drone data that includes the most detailed trajectory information. However, the trajectories are captured for 11-13 minutes every 30 minutes because of the need to change the drone's batteries, and each period is too short to analyze the changing dynamics of the traffic state. Therefore, we first complete trajectories during no-data periods to fit with the real observed traffic state.

By using the completed trajectory data, we compare the prediction results based on accumulation-based and trip-based models in a single region according to different parameter settings. We consider two classical settings for the trip length setting, i.e., using trip length average value and distribution. For the MFD settings, we consider two variables, i.e., the maximum throughput of the network (critical production) and the corresponding accumulation (critical accumulation), which are important for deciding the congested state of the MFD shapes and are often the hardest to define.

1.3.4 Research Question 4: New Extension of Multi-regional MFD Models Considering Path Sequence Information

Research Question 4

How can path sequence information in the classical MFD model framework be considered?

This research question is directly related to Challenge 3. Batista *et al.* (2019) and Paipuri *et al.* (2020) mentioned that path sequence information may have a major impact on MFD model prediction accuracy. However, a multiregional MFD model that can use the aggregated path sequence information as an input parameter has not been proposed. To improve the prediction accuracy of the multiregional MFD models, extensions that take into account path sequence information are necessary.

We propose new extensions to the MFD frameworks by considering path sequences based on the idea of the accumulation-based model that take into account regional routes

proposed by Yildirimoglu & Geroliminis (2014) and the trip-based model as the extension proposed by Mariotte *et al.* (2017) of the model developed by Yildirimoglu & Geroliminis (2014) model. The path sequence is more accurate trip information that can consider returning trips to the same region. The extension that considers path sequence information is straightforward for the trip-based model since the trip length and corresponding path sequence can be assigned individually. On the other hand, we need the aggregated path sequence information for all the vehicles inside the region for the accumulation-based model. We solve this problem by considering the path sequence that includes returning to one region or ending in the region as a binomial process, i.e. returning means failing and ending means success. According to this mathematical solution of considering the path sequence, this extended model requires only the average value of the number of returns to the region as the aggregated path sequence information.

1.3.5 Research Question 5: MFD Model Prediction Accuracy in Multiple Regions according to Parameter Settings

Research Question 5

To what extent do the parameter settings affect the prediction accuracy of the multi-regional MFD model?

This research question is related to Challenge 2 as the multiregional extension of Research Question 3 in Section 1.3.3. The effect of parameter settings on prediction accuracy can be different from the single region models since the traffic states in regions interact with each other. Therefore, the comparative analysis of the parameter setting effect using real data is also necessary for the multiregional framework. No study has investigated the effect of parameter settings on MFD model results using real data, since it requires more detailed trajectory data than for a single region, as shown in Section 1.3.3. In particular, the effect of path sequence information on prediction results may be significant, as described in Section 1.3.4, although it has never been investigated.

The same method employed to analyze the effect of trip length and MFD settings on the prediction accuracy of MFD models and used for answering Research Question 3 in Section 1.3.3 can be adapted for solving this research question in the multiregional framework based on drone data. Additionally, to investigate the effect of path sequence information, we compare all trip length setting cases and MFD models between with and without path sequence information, using the new extended model. Aggregated path sequence information is calculated as path sequence distribution from all the complete trajectories of the drone data.

1.3.6 Research Question 6: MFD Model Prediction Accuracy in Multiple Modes according to Parameter Settings

Research Question 6

To what extent do the trip length and MFD settings affect the prediction accuracy of the multi-modal MFD model?

This research question is related to Challenge 2 as the multimodal extension of Research Question 3 in Section 1.3.3. Paipuri & Leclercq (2020) mentioned that trips behave differently according to the impact of modes. For example, buses stop several times in a shorter period than normal vehicles in order to allow passengers enter. Also, since different modes often share the same roads, the traffic states of each mode can interact with each other. Therefore, parameter settings may affect the MFD model prediction differently compared to the single-region model. The multimodal extension of the MFD model has been undergoing development since Loder *et al.* (2017) proposed the empirical study of 3D-MFD and is now attracting much attention. The investigation of parameter setting effects on predicted accuracy is required for both single-region and multiregional models, although no study has addressed this topic yet.

For this investigation, trips are segregated by modes when calculating trip length. This thesis uses Athens drone data which includes modal information for all vehicles.

To address Challenge 2 in the multimodal framework, the traffic dynamics and trip characteristics of several modes, e.g., motorcycles and buses, are first compared with normal vehicles. Then, we compare the prediction accuracy based on the single region bimodal model proposed by Paipuri & Leclercq (2020), itself based on estimated 3D-MFD according to the different settings of trip lengths.

1.4 Main Contributions

The main contributions of this thesis can be categorized into two categories: 1) estimation of traffic and trip characteristics, and 2) application for the MFD model.

1.4.1 Estimation of Traffic and Trip Characteristics

- Summarizing the proper real-time estimation methods of link-level and network-level traffic density according to the availability of historical and real-time typical data, e.g., loop and probe data.
- Enhancing the fishing rate method to estimate density when both loop detector spatial coverage and probe penetration rate are small.
- Proposing the density estimation method by characterizing the length of the vehicle (EVL) detected by loops to improve the relationship between occupancy and density when only loop data are available in real-time.
- Providing clear guidance of the expected accuracy of streaming density estimation according to data availability and data aggregation granularity.
- Proposing the simple network partitioning method for two traffic state pockets that can be used to adjust the balance between speed homogeneity and network compactness, and which can be easily adapted to the multiple-region system.
- Proving that network partitioning leads to high homogeneity and low trip length tractability, using full trajectory data.
- Proposing the best trip length aggregation method according to data availability.

- Investigating the necessity of path sequence information or the correlation between regional trip lengths to estimate trip length accurately.

1.4.2 Application for the MFD Model

- Describing the detailed data imputation methods for trajectory data with the gap times (times during which the drones do not supply data) according to the type of missing data.
- Investigating the effect of trip length and MFD settings on the predicted results by classical MFD models in a single region.
- Extending the multiregional accumulation-based and trip-based models to use the aggregated path sequence information as an input parameter.
- Investigating the effect of parameter settings, especially path sequence information, on the results predicted by multiregional MFD models.
- Investigating the effect of parameter settings on the results predicted by multimodal MFD models.

1.5 Thesis Outline

The visual outline of this thesis, which is divided into two parts, is presented in Figure 1.4. Part 1 presents the estimation of traffic and trip characteristics for traffic variable and model parameter calibration in the MFD framework. In Chapter 2, different traffic density estimation methods using loop and probe data are compared to determine the accuracy at the link and network levels. This chapter is related to Research Question 1 in Section 1.3.1. The contents in this chapter are based on a journal publication. The effect of network partitioning on mean speed homogeneity and trip length estimation accuracy are analyzed in Chapter 3. Also, the proper methods to aggregate the trip lengths are investigated according to data availability. This chapter is related to Research Question 2 in Section 1.3.2.

Part 2 presents the application of calibrated parameters for MFD models. In Chapter 4, the prediction accuracy of classical MFD models, e.g., accumulation-based model and trip-based model, is assessed according to the trip length and MFD settings in a single region. This chapter is related to Research Question 3 in Section 1.3.3. The single region models are extended to multiregional models in Chapter 5. In particular, the path sequence information is introduced in classical MFD model frameworks. Prediction accuracy according to parameter settings is also assessed in Chapter 5. This chapter is related to Research Questions 4 and 5 in Section 1.3.4 and 1.3.5. In Chapter 6, the accuracy of extended MFD models, which can consider different traffic modes, is assessed according to trip length aggregation and MFD settings. This chapter is related to Research Question 6 in Section 1.3.6.

Finally, Chapter 7 presents the conclusions, discussions, and future perspectives of this dissertation.

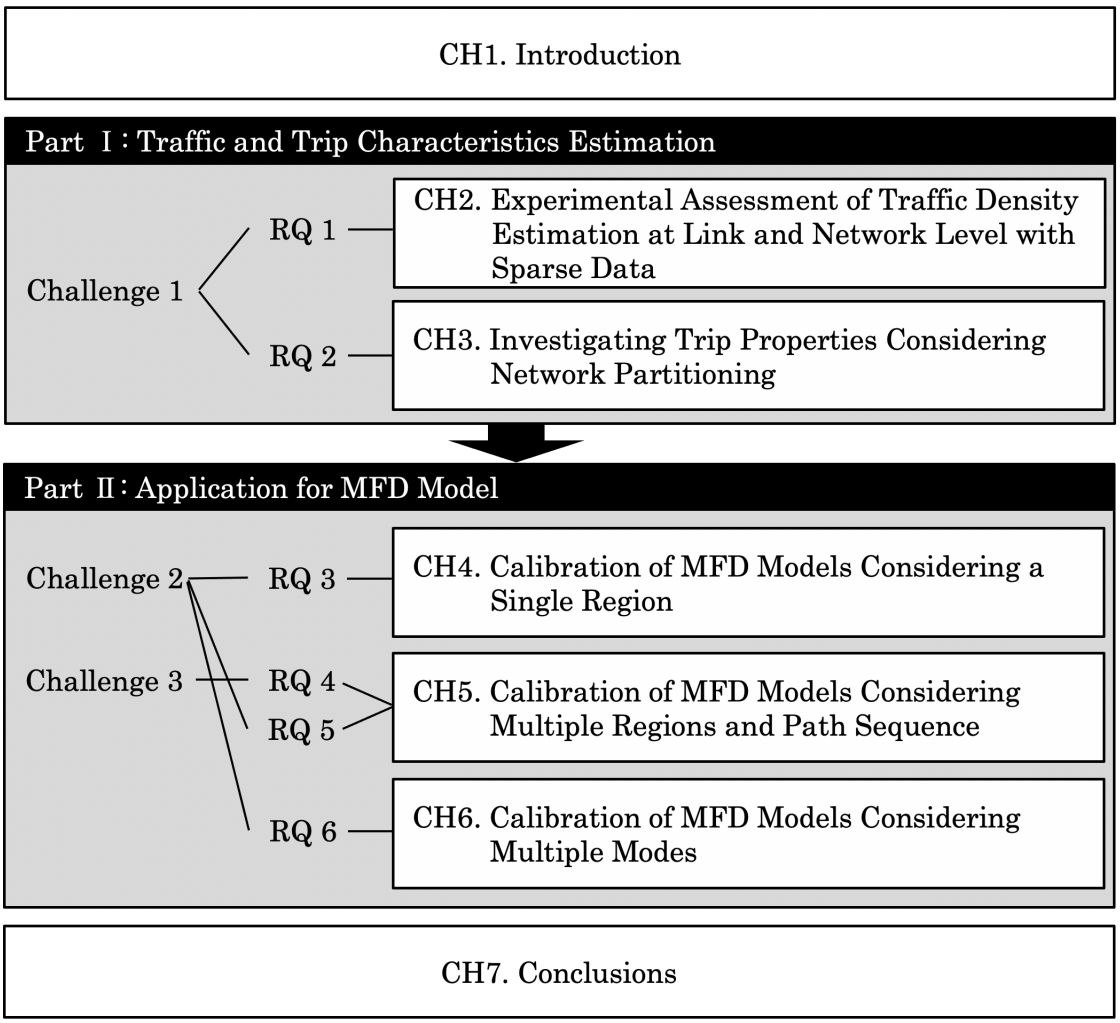

FIG. 1.4 – *Visual outline of the thesis (RQ: Research Questions described in Section 1.3, CH: Chapaters in the thesis)*

2 EXPERIMENTAL ASSESSMENT OF TRAFFIC DENSITY ESTIMATION AT LINK AND NETWORK LEVEL WITH SPARSE DATA

This chapter is an updated version of the paper:

Takayasu, A., Leclercq, L. & Geroliminis, N. (2021). Experimental assessment of traffic density estimation at link and network level with sparse data. *Transportmetrica B: Transport Dynamics*, 101:245–267, doi:10.1080/21680566.2021.2002738

2.1 Introduction

Accurate traffic state estimation, at both the link and the network levels, is crucial for network monitoring and management, e.g., local-level signal control, network-level perimeter control, traffic information. Traffic data availability has greatly improved over the last decades, which should result in improving density estimation. However, these data contain measurement errors, temporal and/or spatial gaps, depending on the sensors location and number. In heterogeneous traffic states, these data limitations can lead to huge gaps between reality and estimation. Thus, it is essential to consider traffic state estimation approaches according to the data availability. To our best knowledge, it exists no study that provides a complete benchmark of all possible estimation methods when considering the most commonly available data, i.e., loop detectors and probe vehicles. It is important to carefully compare those methods on the same dataset while considering the impacts of both data coverage and availability. This gives a clear vision of the level of errors we can expect when estimating densities by different methods and scales (link and network). Such information can be very important when designing or implementing new monitoring or control systems as the quality of density estimates directly impact their efficiency.

In the literature, the methods developed to improve accuracy and save computational time have attracted a great deal of attention. Seo *et al.* (2017) described three categories of traffic state estimation approaches: *model-driven approach*, *data-driven approach*, and *streaming data-driven approach*. The *model-driven approaches* are based on physical traffic flow models fused with data. The Lighthill–Whitham–Richards (LWR) model (Lighthill & Whitham (1955), Richards (1956a)) is very popular in this context. Most of the methods that have a high level of accuracy require additional information such as traffic signal settings, signal offsets or detailed detector actuations vehicle per vehicle (Skabardonis & Geroliminis (2005), Skabardonis & Geroliminis (2008), Wu *et al.* (2011)). To improve the accuracy of model parameters, data assimilation techniques are often used with real-time data especially at the link level, e.g., Mazaré *et al.* (2012), Yuan *et al.* (2012), Nantes *et al.* (2016), or at the platoon level, e.g., Yuan *et al.* (2015), Wang *et al.* (2019). Also, at the network level, *model-driven approaches* have recently received more attention such as Kawasaki *et al.* (2018), Saeedmanesh *et al.* (2019). Such approaches may prove very efficient for estimating traffic states but are strongly dependent on the quality of the embedded model.

On the other hand, *data-driven approaches* and *streaming data-driven approaches* currently appear very appealing due to increases in data quality and availability. In the *data-driven approaches*, a large amount of historical data is necessary to train models using statistical or machine learning methods. Since strong theoretical assumptions are not required, the quality and quantity of data greatly impact the accuracy of estimation. Example of *data-driven approaches* include those by Kong *et al.* (2009), Anuar *et al.* (2015), Lu *et al.* (2018) and Aljamal *et al.* (2019). As missing data can negatively affect the outputs, several previous studies, e.g., Chen *et al.* (2003), Xu *et al.* (2015), and Herring *et al.* (2010), specifically focus on this issue. The *data-driven approaches* usually have low computational costs once the training stage has been completed. Furthermore, the results may not be accurate when disruptions or rare events occur.

The *streaming data-driven approaches* need only real-time data combined with simple physical assumptions such as vehicle conservation. Therefore, the calculation is fast compared to the *model-driven approaches* and the *data-driven approaches*. It is also more robust and ver-

satile as it can immediately adapt to new traffic conditions that may not have been foreseen when considering historical observations, i.e., consequences of major incidents or changes in mobility behaviors. Astarita *et al.* (2006) and Qiu *et al.* (2010) mention that the *streaming data-driven approaches* can take advantage of combining loop and probe data to improve traffic state estimation. Seo & Kusakabe (2015) estimated the traffic state by using position and spacing information of probe vehicles based on the conservation law of the traffic flow. Bekiaris-Liberis *et al.* (2016) combined these methods with Kalman Filter to improve the estimation of the connected vehicle penetration rate. However, these methods require high coverage or a large amount of real-time data. Time availability and space coverage can significantly harm accuracy. Thus, it is important to quantify precisely how these two factors influence the estimation errors. Therefore, in this paper, we focus on assessing the accuracy of traffic state estimation using the *streaming data-driven approach*.

When working on traffic state estimation with real-time data, it is essential to design an adequate method related to the targeted variables. There are three fundamental variables at the link level, i.e., flow, mean speed, and density. It is already known that flow can be directly calculated by counting vehicle numbers at one unit time by the lane loop detectors of the road link. Additionally, since methods used to compensate the missing data of loop detectors have been developed extensively, the accuracy of flow estimation by using loop detector data is now quite high, e.g., Oh *et al.* (2002), Maghrour Zefreh & Torok (2018). Nevertheless, these flow estimates are usually averaged over a period of a few signal cycles, and information that can help accurately estimate queue lengths and link density is missing, according to Ramezani & Geroliminis (2015).

Mean speed estimation approaches also attract much attention. Techniques that use probe vehicles are simple and straightforward to implement as the only requirement is to observe a sufficient number of vehicles per time period to obtain accurate results, e.g., Lee & Coifman (2012), Chaudhuri *et al.* (2011), Zhai (2013). Van Erp *et al.* (2017) prescribed the error distribution of mean speed estimation relating to traffic conditions using several sensing data, e.g., loop detector and probe vehicle data, considering different estimation approaches. Finally, mean speed estimation using loop detector or/and probe vehicle data appears quite accurate in both free flow and congested conditions.

These past works enable real-time estimation and prediction of other crucial traffic variables. For example, travel time is important not only for considering route choice decisions but also for calculating accumulation and density. Lopez *et al.* (2017b) proposed a travel time estimation on an urban network using network clustering from a 3D speed map. This method makes it possible to treat the spatial heterogeneity of congestion with reduced computational time. To treat the heterogeneity of congestion, Zhang & Rice (2003) proposed the linear regression model, which considers the relation between instantaneous and experienced travel time for freeway networks. Kwak & Geroliminis (2020) extended this linear regression model for the real-time estimation and prediction of travel time.

The hardest variable to estimate from existing data is certainly the density. There are several technical and scaling issues involved both at the link and network levels. We can calculate mean density from total accumulation divided by area size. In the case of using loop detector data, the total number of vehicles in the area under consideration might not be available, so we usually derive density from occupancy, i.e., the percentage of the time that vehicles occupy the detector. Occupancy is related to density through electric vehicle lengths. But the location of the detector might influence the result as density is not uniform

neither across links or over time. Because the detection of the individual electric length for each vehicle is technically difficult, a constant value is usually used in practice for every road links and all time periods. However several researchers such as Zefreh *et al.* (2017), Leclercq (2005) and Kockelman (1998) mentioned that this assumption may lead to significant errors in traffic density estimation because electric lengths can be locally different and change with traffic conditions.

Furthermore, loop detectors only capture local information. Thus, to obtain mean density at the link level, accumulation at the local level should be scaled-up to the link level. Leclercq *et al.* (2014) and Knoop & van Zuylen (2009) clarified theoretically and empirically that traffic observation in a loop detection area is not adequate to estimate density over a full link. Also, to estimate mean density at the network level, the total density of each link with loops should be scaled up to all network links. However, because the number of loop detectors is usually quite small compared to the number of links, it is not obvious that mean density for a few links is representative for all links.

Density estimation by using probe vehicle data has also some scaling issues. We need to quantify the penetration rate to scale up the observed probe vehicle accumulation into the total vehicle accumulation. This factor is hard to estimate in general and can undergo spatial and/or temporal variation according to Lu *et al.* (2018), Mazaré *et al.* (2012). Geroliminis & Daganzo (2008) proposed to use the fraction of probe vehicles captured over loop detectors (the fishing rate) instead of the spatial penetration rate to scale up the probe vehicle accumulation. However, the validity of the estimation may rely on the coverage of loop detectors used to capture the probe vehicles. The empirical verification in Yokohama contained a very small number of probe vehicles ($\sim$150) that didn't allow for wide validation of the method at the link level. In addition to the issues mentioned above, the accuracy of density estimation in the *streaming data-driven approach* is influenced by the data processing method. In short, the accuracy of mean density estimation at the link and network levels depends on the data source and availability, and the estimation method. Those factors have not yet been comprehensively investigated on the same network and dataset.

In this chapter, we assess the accuracy of mean density calculation in the *streaming data-driven approach* from the most usual data sources, i.e., loop detector and probe vehicle data. We consider the technical and scaling issues, including the time- and space- sparseness at the link and network levels. Our objectives are to: 1) characterize the magnitude of expected errors for each estimation method, and 2) identify the best compromise between data requirements and density estimation accuracy. In this chapter, we mainly use a comprehensive dataset from Lyon that contains both loop detectors and probe data. Section 2.2 describes the features of the Lyon network and the raw traffic data. Also, a complete trajectory dataset for a small urban area captured by a drone experiment in Athens, Greece, is utilized to determine the accuracy of the reference method we defined in the case of Lyon, which covers a much larger area, but with sparser information. Section 2.3 provides an explanation of all the definitions of variables and mean density estimation approaches at the link level, and at the network level in section 2.4. Section 2.5 shows that the comparison of traffic density estimation results of the proposed methods at the link level, and at the network level in section 2.6. Finally, we discuss the application and present the conclusion in section 2.7.

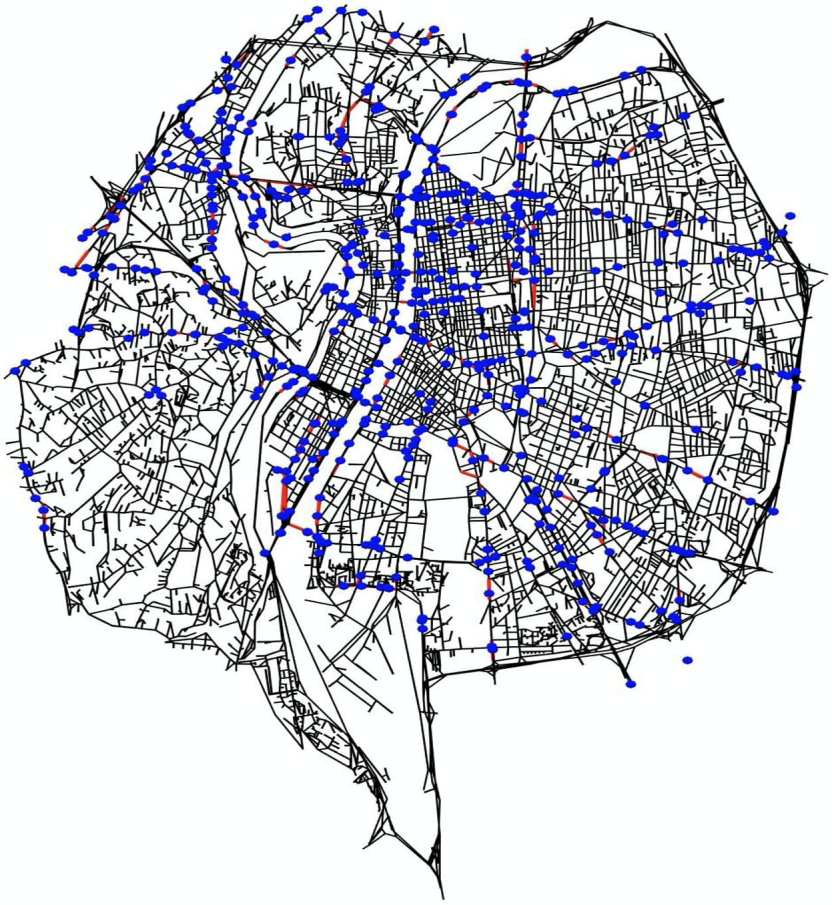

FIG. 2.1 – *The Lyon network used in this study and the location of loop detectors (Black line: all links (19967 links), Red line: chosen links (250 links), i.e., network in this study, Blue dots: location of loop detectors (673 loops))*

2.2 Network and Traffic Data

Lyon is the third-largest city in France and has its second-largest urban area. Around 2 million residents live in the metropolitan area. The Lyon authorities provided us with the road network, including street names, longitude and latitude of edge nodes of road links, speed limits, lane numbers, link length of road links, and the locations of loop detectors on the link. This area covers $80km^2$ with around 20000 links, and the total link length of this network is around $1900km$. 673 links are now equipped with loop detectors, as shown by the blue dots in Figure 2.1. The spatial coverage of links equipped with loops corresponds to 7% of the network total link length. The loop detector data are composed of average flow and occupancy at each loop every 6 minutes. Traffic signal settings were not provided.

Mediamobile, a French company specialized in real-time traffic data, provides the probe vehicle information used in this paper. These data are composed of observation ID, link ID, the trajectory coverage of one link, timestamp, average speed, vehicle ID, and observation ID list. These data are created based on the trajectory data of each probe vehicle every 10 seconds. The space coverage of probe vehicle data, i.e., the ratio of total traveled distance by probes every 6 minutes over the total network link length, is represented by black plots

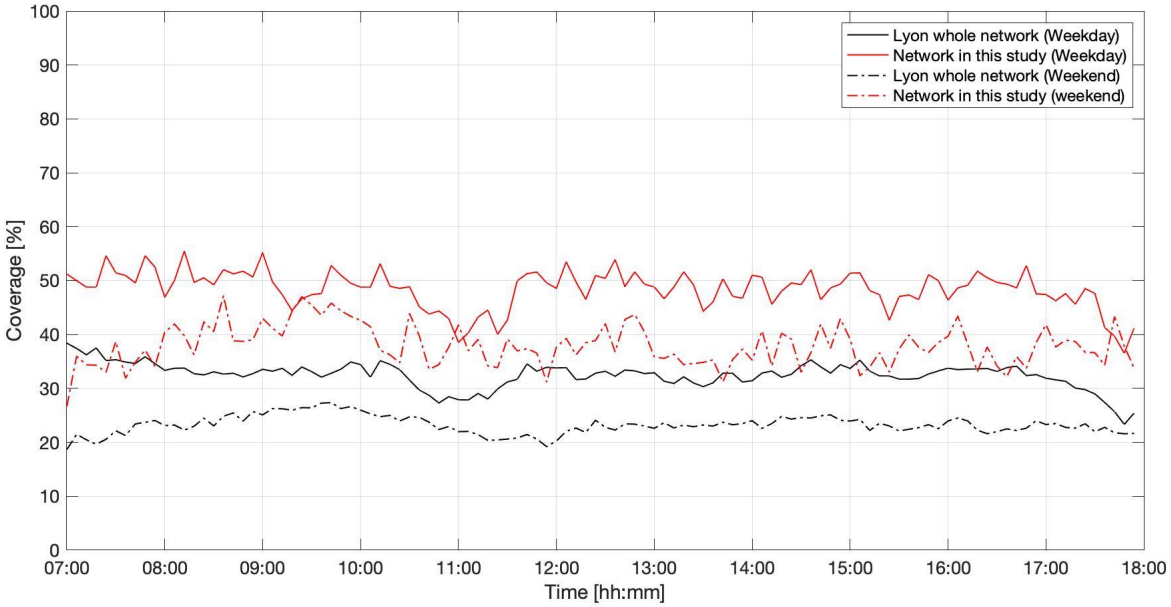

FIG. 2.2 – *Fraction of the Lyon network passed by probes every 6 min*

in Figure 2.2. Probe space coverage is about $30-40\%$ on a weekday and around 20% on a weekend.

Figure 2.3 shows the spatial correlation of traffic flow on the network to compare loop (a) and probe data (c) features. At this time, each average flow over the whole day duration $Q[veh/s]$ is colored using a six-level scale depending on the flow volume. Also, Figure 2.3 (b) and (d) show the link flow distribution from loop and probe data during the morning rush hours (7:00-10:00) and the daytime (12:00-15:00). From these distributions, we can see that both data capture both high and low link flows during the rush and non-rush hours. According to Figure 2.3 (a), the loop data capture flow only with limited spatial coverage. Conversely, Figure 2.3 (c) shows that the probe data provide more extensive coverage. Also, we have high probe flow at the loop locations. Thus, it is possible to investigate how density estimation methods can benefit from both data sources.

Information for probes is given in their own mapping system. We used street names and directions to identify common links and map loop detectors in the probe data network. As the links in the probe network appeared small, we gather links locally around loops to define a subnetwork of the city of Lyon with both probe and loop information at the link level. Finally, the average link length is around $170m$ (standard deviation is $111m$), which is similar to the loop data network around $134m$ (standard deviation is $99m$).

To carefully assess the estimation accuracy of the different methods, links with both loops and probe observations are required. In the Lyon network, 250 links satisfy such a condition but they do not define a connected component of the topological graph that represents the road network, see the red lines in Figure 2.1. Nevertheless, this is not an issue as density estimation methods do not resort to the network topology but rather data aggregation considering independent links. We use these selected links as the subnetwork in this study. The total link length of the selected links is around 58 lane-km. We use the loop and the probe

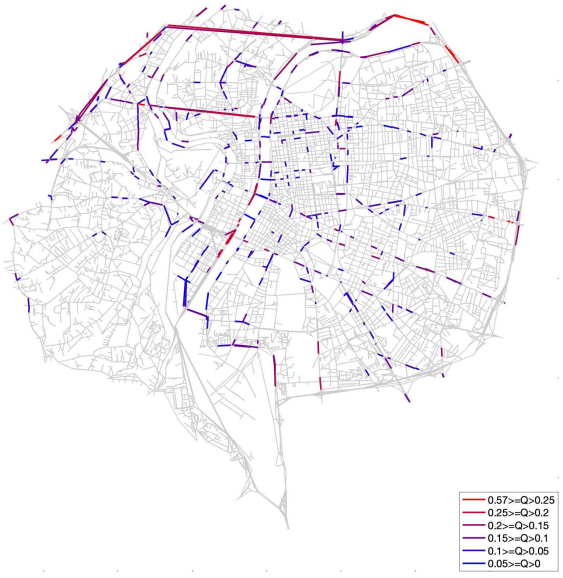

(a) Average flow map over the whole period (7:00-18:00) from loop data

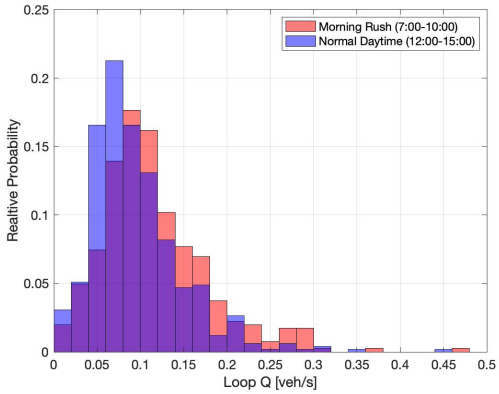

(b) Link flow distribution during morning rush hour (7:00-10:00) and normal daytime (12:00-15:00) from loop data

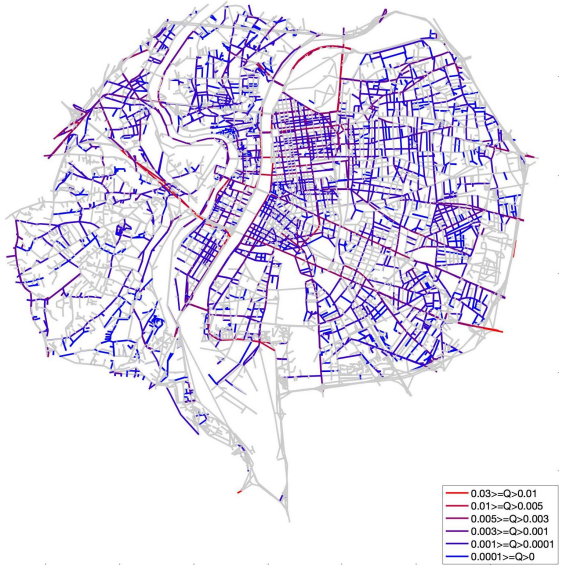

(c) Average flow map over the whole day (7:00-18:00) from probe data

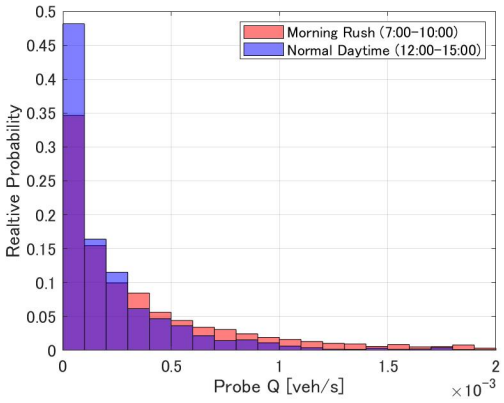

(d) Link flow distribution during morning rush hour (7:00-10:00) and normal daytime (12:00-15:00) from probe data

FIG. 2.3 – *Spatial correlation between loop data and probe data of Lyon network. Q shows the average flow of each link [veh/s]*

data from 7:00 to 18:00 of all the days in April 2018, as monthly data, of April 3rd as weekday data, and of April 7th as weekend data. All these days were sunny and did not have any special events. The space coverage of the probe data over the network in this study is around 50% on a weekday and around $35-45\%$ on the weekend.

Given the sparse amount of probe data, the limited coverage of loop detectors together with the coarse temporal aggregation and the lack of signal settings, it is difficult to know the groundtruth or estimate with high confidence accurate link level information. For this reason, drone data taken from the pNEUMA experiment by Barmpounakis & Geroliminis (2020) are used to perform an initial screening of the reference method we choose for density estimation. This dataset is quite unique as all vehicle trajectories are available for a (small) urban region making it possible to calculate the true density values in all links. We utilize part of the data of this experiment, more specifically from 8:00 to 10:30 in the morning on October 30th, 2018, at the congested intersection of the Alexandras and 28th Oktovriou avenues in Athens, Greece. The total number of vehicles during this time period is 2040 vehs, and the link length of this street is $140.69m$. The drone data are based on pictures taken by drones with a 0.04 second time-frequency. These data consist of the track ID, vehicle type, travel distance, vehicle location, vehicle speed, and time stamp of each vehicle at each time period. According to Barmpounakis & Geroliminis (2020), the tracking algorithm that reconstructs vehicle trajectories from the drone footages has an accuracy level of 98.8%; see the original paper for further details. Therefore, these drone data are quite reliable for estimating real traffic states. Nevertheless, the pNEUMA dataset covers a small part of the full Athens network ($1.3km^2$ vs. $80km^2$ of the Lyon network) and as the experiment took place during the peak hour, the network density and speed variation is quite small (see Paipuri *et al.* (2020)). For the reasons above, Athens data is utilized to evaluate the accuracy of the different methods at the link level for various penetratin rates vs. an accurate groundtruth, while the Lyon data is utilized both at the link and network level.

2.3 Mean Density Estimation approaches at the Link Level

We describe different *streaming data-driven approaches* of mean density estimation at the link level considering three levels of availability for vehicular data in real-time: 1) all trajectories, 2) only probe vehicle information, 3) no data. In all cases, link flow is monitored with loop detectors. All variables in this section are shown in Table 2.1.

2.3.1 Definition of traffic density

Let us define a subsection of length Δx_s for a link and n_s the number of vehicles (accumulation) in this subsection. Traffic density is defined as $k_s = n_s/\Delta x_s$. When Δx_s is small, we call it *local-level density*. This is the case when the density is estimated in the vicinity of a loop detector. When Δx_s is equal to the link length, we call the average density over the link *link-level density*. Both the local- and link-level densities are always estimated per lane.

If all trajectories are available for one link, it is the ideal situation. $k_i(t)$ on a link i during time period $[t, t+\Delta t]$ can be precisely estimated by Edie's formula (Edie (1963)), as shown in Eq. (2.1).

$$k_i(t) = \frac{ttt_i(t)}{l_i * \Delta t} \tag{2.1}$$

Variables	
$i \in I$	i is a link. I is a set of all links in the network
l_i	link length of a link i
t	time
Δt	time duration for calculation
$d \in D$	d is a day. D is a set of all days in the data set
k_i	link-level traffic density at link i
ttt_i	total travel time of all vehicles at link i
ttd_i	total travel distance of all vehicles at link i
n_i	the number of vehicles at link i
q_i	the traffic flow at link i
v_i	space mean speed at link i
$*^P$	a variable $*$ calculated over the data set of probes
p_i	probe penetration rate at link i
$\gamma_i(t)$	the dynamic fishing rate at link i between time t and $t + \Delta t$
o_i	loop occupancy at link i
$\alpha_i(t)$	the dynamics electric vehicle length EVL at link i between time t and $t + \Delta t$
$\alpha_i(o_i)$	a functional form between EVL and occupancy
$*_{UD}$	a variable $*$ averaged over all days
$*_{UL}$	a variable $*$ averaged over all links
$\bar{*}$	a constant variable $*$ averaged over a day

TAB. 2.1 – *Lists of Variables in Section 3*

$ttt_i(t)$ is the total travel time for all vehicles, and l_i is the link length. $ttt_i(t)$ can be calculated by summing the travel time of each vehicle in the link during the time period Δt. For example, a vehicle that was in the link before t and that is still there at time $t + \Delta t$ counts for Δt. In practice, it is difficult to achieve such completeness except for specific data acquisition processes, e.g., the drone footage from the pNEUMA experiment in Athens.

In the following subsections, we focus on different and more practical methods to estimate the link-level density using probes, loops, or a combination of both. The main difference between the methods is the completeness of the data (full or partial availability) and the availability of historical patterns to fit certain parameters.

2.3.2 Case 1: Real-time probe trajectories and real-time loop data are available

Usually, we cannot access real-time data for all the trajectories but only a fraction of them (probes). When only probe vehicle data are available, the temporal scaling factor, i.e., the penetration rate of the probe vehicles, is necessary to estimate the traffic density at the link-level. The probe penetration rate ($p_i(t)$) is defined as the ratio of the number of probe vehicles (n_i^P) over the total number of vehicles (n_i) in the link i between t and $t + \Delta t$. This factor is impossible to estimate in practice. Geroliminis & Daganzo (2008) proposed to use as a proxy the ratio of the probe flow q_i^P over the total flow q_i between t to $t + \Delta t$. When a loop exists in a link, the total flow q_i can be measured. We call this ratio q_i^P over q_i the fishing rate ($\gamma_i(t)$)

as probe vehicles are caught along with all the vehicles in the loop. This ratio corresponds to the estimated probe penetration rate for the link i. Note that the actual probe penetration rate $p_i(t)$ and the fishing rate $\gamma_i(t)$ between t to $t + \Delta t$ are equal when the probe and other vehicles exhibit the same speed, which is a reasonable assumption at the link level.

$$p_i = \frac{n_i^P/\Delta t}{n_i/\Delta t} = \frac{ttt_i^P}{ttt_i};\ \gamma_i = \frac{q_i^P}{q_i} = \frac{ttd_i^P/(l_i*\Delta t)}{ttd_i/(l_i*\Delta t)};$$
$$p_i = \frac{ttt_i^P}{ttt_i} = \frac{ttd_i^P/v_i^P}{ttd_i/v_i} = \gamma_i \frac{v_i}{v_i^P} \approx \gamma_i \tag{2.2}$$

ttd_i is the total travel distance for all the vehicles, and v_i is the space-mean speed in the link i. Index P means that the variable is calculated over the restrictive set of probes.

By using the fishing rate, traffic density can be approximated as

$$k_i(t) = \frac{ttt_i^P(t)}{l_i * \Delta t} * \frac{1}{\gamma_i(t)} \tag{2.3}$$

2.3.3 Case 2: Real-time probe trajectories and historical loop data are available

The fishing rate cannot be calculated when loop detector data in a link are not available at time t as term $q_i(t)$ from Eq. (2.2) cannot be measured. Alternatively, $\gamma_i(t)$ can be approximated by using historical or other location data. To calculate the estimated fishing rate, three types of aggregations are considered depending on the data availability. First, if $q_i^P(t)$ and $q_i(t)$ of other days are available, the aggregation of the fishing rate by day (United data of all Days, UD) is possible: $\gamma_{UD,i}(t) = \sum_{d \in D} \gamma_{d,i}(t)/|D|$. D is a set of dates. Second, link aggregation (United data of all Links, UL) can be useful data if fishing rates of other links are available: $\gamma_{d,UL}(t) = \sum_{i \in I} \gamma_{d,i}(t)/|I|$. I is a set of all links. Third, a constant approximation may be required if not enough data are available to calculate the dynamic fishing rate: $\gamma_{\bar{d},i}$. However, the fishing rate distribution over all links and all time periods in Figure 2.4 shows significant differences over links and between time periods, especially during morning and evening peak hours. From 7:00 to 9:00 a.m. on a weekday, the traffic flow increases because of commuting hours, and it leads to a smaller fishing rate. On the contrary, at this time period on a weekend, the flow is quite low. Therefore, the ratio of the number of probe vehicles can be high. These differences can lead to massive estimation errors when the probe data of a link are not available in real-time and average values are utilized instead. Therefore, assessing the validity of using spatial and temporal approximations and combinations of them is important.

2.3.4 Case 3: Trajectories at a link are not available

Sometimes no trajectory is observed for certain links at several time periods because probe vehicle data are sparse in time. In this case, we may have to estimate the link-level density from loop detector measurements only. However, loop detectors provide occupancy instead of density. Therefore, two levels of transformation are necessary, i.e., occupancy to local-level density and local-level density to link-level density. For the first transformation, it is known that local-level density can be calculated by dividing occupancy by electric vehicle

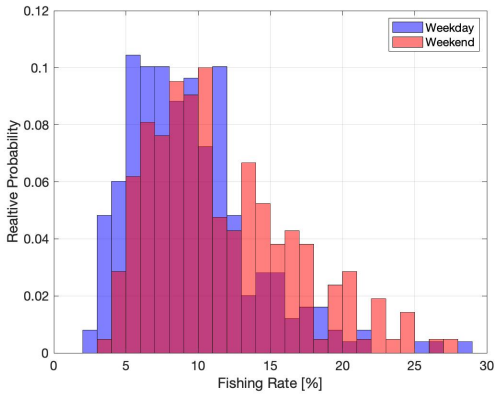

(a) Distribution of fishing rate across links over the whole time period

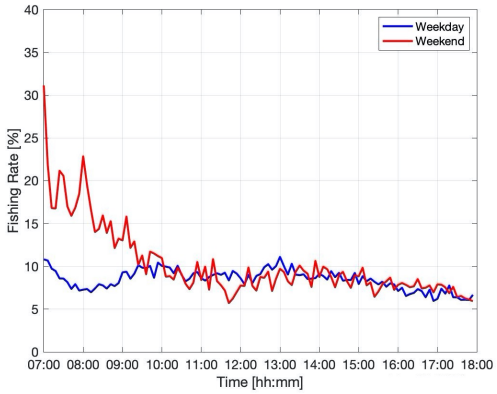

(b) Average dynamics of fishing rate calculated every 6 minutes over weekdays/weekends

FIG. 2.4 – *Features of fishing rate $g_i(t)$ of the Lyon network*

length (EVL), i.e., the length that is detectable by the loop. Because it is difficult to obtain these values from data, EVL is usually considered constant for every loop detector and time period in many previous studies. Lee & Coifman (2012) recommended using the aggregate value of daily EVL at each loop detector to avoid excessive sensitivity. Note that the detection size may vary from loop to loop, depending on the physical loop features and road pavement conditions. On the other hand, Zefreh *et al.* (2017) mentioned that setting a single average EVL for the entire day may lead to large errors.

A second transformation is necessary to solve the scaling issue according to the difference between local-level density and link-level density. Figure 2.5 is the time-space diagram at link i during the time period $[t + \Delta t]$ with signals downstream of the link. Let us denote l_i is the length of link i. The link-level density is calculated by $k_i = n_i/l_i$ where n_i is the vehicle accumulation at the link-level area represented by the number of blue lines inside the black-dotted pattern zone. On the other hand, the local-level density is calculated by $k_s = n_s/\Delta x_s$ where x_s is the length of the loop detection area and n_s is the vehicle accumulation at the local-level area represented by ones inside the pink zone. According to this figure, k_d can be different when the loop is either upstream or downstream of the link. Thus, the location of the loop can create some bias in the estimates as mean density over a cycle is higher for loops located upstream rather than downstream of traffic lights (see for further example Skabardonis & Geroliminis (2008)). Leclercq *et al.* (2014) theoretically clarified that it is impossible to use observations from loop detectors directly as estimations for the full link density. However, as mentioned in Coifman (2001), if we can access to the mean speed over the link, it is possible to directly determine the transformation factor between occupancy and link-level density. Such a factor is the electric vehicle length (EVL) $\alpha_i(t)$ in the link i at time t:

$$\alpha_i(t) = \frac{o_i(t)}{k_i(t)} = \frac{v_i(t)}{q_i(t)} * o_i(t) = \frac{v_i^P(t)}{q_i(t)} * o_i(t) \tag{2.4}$$

$o_i(t)$ and $q_i(t)$ are the occupancy and traffic flow calculated directly from loop detector data. According to Leclercq *et al.* (2014), it is possible to estimate mean speed with a good accuracy

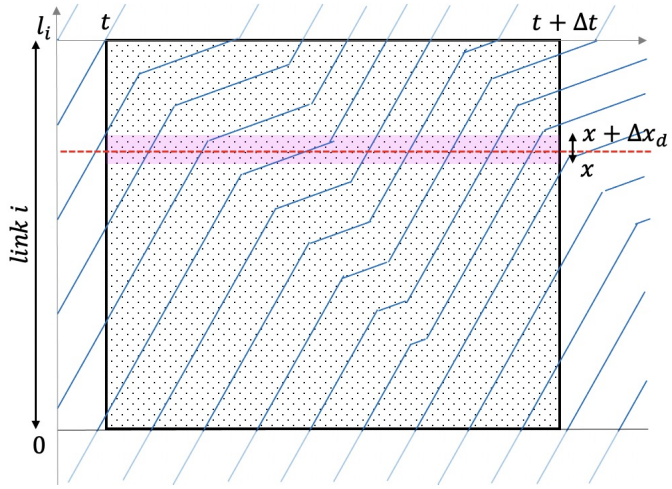

FIG. 2.5 – *Difference between local-level density and link-level density (Time-Space diagram which x-axis shows location and y-axis shows time. The signal is located in downstream of link location. Blue lines show vehicle trajectories. The red line shows the loop location and the pink zone shows the local-level area. The black-dotted pattern zone shows the link-level area.)*

from 5% of probes. As we assume that the mean speed exhibits regular dynamic patterns in time for all weekdays/weekends, the actual mean speed $v_i(t)$ can be estimated based on probe vehicle observations from historical data, i.e., $v_i(t) = v_i^P(t)$ where t would be the same time of the day in the historical observations. The flow value is the same over a period of one cycle at any location of a link, the local effect of occupancy and speed over a loop can be scaled up by using the mean speed of probe vehicles over a full link. Thus, the scaling issue between the local-level and the link-level is already taken into account.

In the Lyon network, the difference of $\alpha_i(t)$ according to Eq. (2.4) depends on location and the time-series is shown in Figure 2.6. Figure 2.6 shows that $\alpha_i(t)$ is different regarding time and location, especially on weekdays, as mentioned in the previous studies. Also, the relation between occupancy obtained from the loop data, velocity from the probe data, and $\alpha_i(t)$ calculated by Eq. (2.4) are shown in Figure 2.7. Note that the lengths of all loop detectors in Lyon is around $1m$. In this figure, we present five representative links by different colors. According to the Figure 2.7(a), the relation between $v_i^P(t)$ and $\alpha_i(t)$ is positive and linear, while most engineering textbook assume EVL to be constant whatever traffic states are. Kockelman (1998) and Leclercq (2005) reached the same conclusion and showed that EVL usually follows a linear relation in speed. The reason is the correlation between vehicle lengths and speeds but also a natural technical bias from the detectors: a loop is supposed active when a given threshold for the induced current is reached. However, the detected signal for the same vehicle changes with the vehicle speed. It is then important to consider the dependency of EVL to traffic conditions when estimating link density. As link spatial speed is only available with probes, we can try to directly fit the relation between $\alpha_i(t)$ and the occupancy $o_i(t)$. We adapt linear regression to fit with the plots of $\alpha_i(t)$ and $o_i(t)$ in that case. It is not ideal as the variation of $\alpha_i(t)$ for a given occupancy is large but at least it helps to capture the overall trend and improves the usual constant approximation. Consequently, the estimation of this relation is difficult; however, this observation is crucial to estimate the link-level density from the loop when probe data are missing. If we obtain a decent estima-

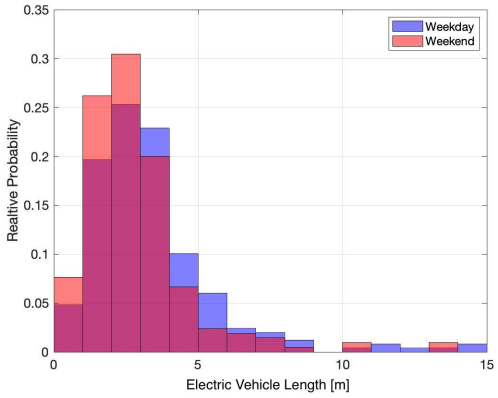

(a) Distribution of $\alpha_i(t)$ across links over the whole time period

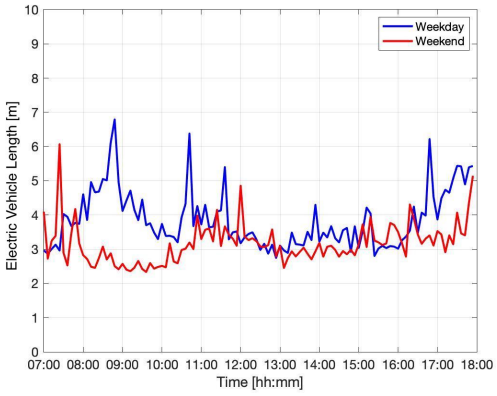

(b) Average dynamics of $\alpha_i(t)$ over weekdays/weekends

FIG. 2.6 – *Features of dynamic electric vehicle length $\alpha_i(t)$ of the Lyon network*

tion for this relation, we can calculate a functional form between EVL and occupancy at the local level, i.e., $\alpha_i(o_i)$, and then directly apply it to estimate k_i.

$$k_i = \frac{o_i}{\alpha_i(o_i)} \tag{2.5a}$$

A minimum requirement is to have access to probe information from historical data to fit this functional form. Otherwise, we can only restrict ourselves by using a constant EVL value for all the loops, which leads to large discrepancies in density estimation. Therefore, the definition of $\alpha_i(t)$ in Eq.(2.4) can be useful to estimate mean density at the link-level, and it can be shown in Eq. (2.5b).

$$k_i(t) = \frac{o_i(t)}{\alpha_i(t)} \tag{2.5b}$$

If real-time information for $v_i^P(t)$ in the link is available, the estimated density is exactly the same as the one obtained by using the fishing rate in Eq. (2.3). As already mentioned, when historical $v_i^P(t)$ of the same time period is available, we can estimate density by using day aggregation: $\alpha_{UD,i}(t) = \sum_{d\in D} \alpha_{d,i}(t)/|D|$. When probe trajectories in other links are available, we can use link aggregation: $\alpha_{d,UL}(t) = \sum_{i\in I} \alpha_{d,i}(t)/|I|$. When we can obtain historical $v_i^P(t)$ in other links at other time periods, we can use Eq. (2.5a). When no historical trajectories are available, using a constant value is necessary: $\bar{\alpha_{d,i}}$. According to previous studies and Figure 2.6, both link and time aggregations can lead to large estimation errors. Clarifying the validity of this approach by using different aggregation combinations is necessary.

2.4 Estimating Density at the Network Level

Links equipped with loops are only a small fraction of all the links in the network. The question is if such a sparse sampling is sufficient to provide an accurate estimation of the overall network density. To answer this question, we compare different estimation methods

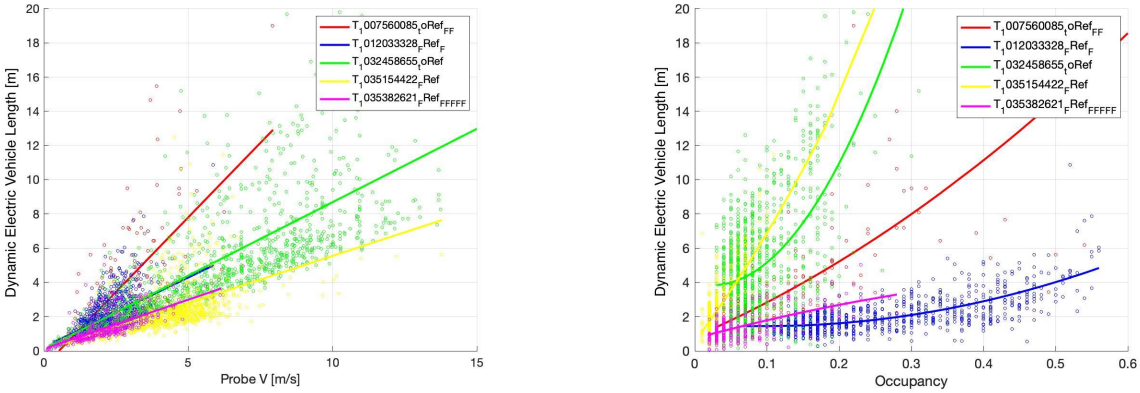

(a) Between $v_i^P(t)$ and $\alpha_i(t)$. R square of each link is: red link=0.41, blue link=0.29, green link=0.62, yellow link=0.26, pink link=0.59.

(b) Between $o_i(t)$ and $\alpha_i(t)$. R square of each link is: red link=0.46, blue link=0.50, green link=0.50, yellow link=0.90, pink link=0.32

FIG. 2.7 – *Relation between probe speed $v_i^P(t)$, loop occupancy $o_i(t)$ and dynamic electric vehicle length $\alpha_i(t)$ of the Lyon network. Plots shows the value every 6 minutes over the whole time period. Plain lines represent linear (a) and quadratic (b) regressions. The different colors correspond to 5 randomly selected links as an example.*

Variables	
r, $\|r\|$	r is a set of all links in a network. $\|r\|$ is the total number of links in the network
l_r	total link length of the network
K_r	network level density of the network
Γ_r	network-level fishing rate of the network
$E[.]$	mathematical expectation (mean)
$cov[.]$	covariance
r_1	a set of links with loops in the network
r_0	a set of links without loops in the network

TAB. 2.2 – *Lists of Variables used in Section 4*

that include links both with and without loops to the reference when all links are monitored. Therefore, we first describe the reference estimation of the network-level density in the case where all the links have loops. Then, we compare different estimation approaches, including a new method that explicitly considers the aggregation bias related to the link-level fishing rate. All the variables we use in the equations in this section are shown in Table 2.2. Note that in the current stage, we cannot repeat the network level estimation for the Athens data because the trajectory data have not been map matched to links for the whole network (only contain GPS coordinates at the moment). This is a tedious ongoing task, and it is expected to be reported in the near future.

2.4.1 Case 1: Probe trajectories and loop data in all links are available

When we have probe trajectories and loop data in all links at every time period, the network-level density $K_r(t)$ for a given time period between t and $t + \Delta t$ can be calculated as the average of link-level density calculating with the link-level fishing rate, as shown in Eq. (2.6).

$$K_r(t) = \frac{\Sigma_{i \in r}(ttt_i^P(t)/\gamma_i(t))}{l_r * \Delta t} \tag{2.6}$$

l_r is the total link length of the network as $l_r = \Sigma_{i \in r} l_i$. This reference method is the most accurate but is only available when probes and loops are available in all links.

When missing data happen for some time periods, we can use the network-level fishing rate as a proxy for the link fishing rates. We define the harmonic mean of the link-level fishing rate $\gamma_i(t)$ in Eq. (2.2) as the network-level fishing rate $\Gamma_r(t)$, as shown in Eq. (2.7).

$$\frac{1}{\Gamma_r(t)} = \frac{\sum_{i \in r}(1/\gamma_i(t))}{|r|} \tag{2.7}$$

$|r|$ shows the total number of links in the network. If we assume that all link-level fishing rates in Eq. (2.6) can be replaced by this network-level fishing rate, i.e., $\gamma_i = \Gamma_r \ \forall i$, the network-level density is given by Eq. (2.8).

$$K_r = \frac{1}{l_r * \Delta t} * \frac{\Sigma_{i \in r} ttt_i^P(t)}{\Gamma_r(t)} \tag{2.8}$$

This formula is simple but includes a bias that can be highlighted by an exact transformation of Eq. (2.6):

$$\begin{aligned} K_r(t) = & \ \frac{|r|}{l_r * \Delta t} * \frac{\Sigma_{i \in r}(ttt_i^P(t)/\gamma_i(t))}{|r|} \\ = & \ \frac{|r|}{l_r * \Delta t} * E[\frac{ttt_i^P(t)}{\gamma_i(t)}] \end{aligned} \tag{2.9}$$

where E is the mathematical expectation (mean). Here we have to calculate the expectation of the ratio between two random variables, the total travel time $ttt_i^P(t)$ and the link-level fishing rate $\gamma_i(t)$. These two variables are distributed over space (the link). The expectation of a ratio can be transformed into the ratio of expectations and a covariance term:

$$\begin{aligned} K_r(t) = & \ \frac{|r|}{l_r * \Delta t} * \{E[ttt_i^P(t)] * E[\frac{1}{\gamma_i(t)}] + cov[ttt_i^P(t), \frac{1}{\gamma_i(t)}]\} \\ = & \ \frac{1}{l_r * \Delta t} * \{\Sigma_{i \in r} ttt_i^P(t) * E[\frac{1}{\gamma_i(t)}] + |r| * cov[ttt_i^P(t), \frac{1}{\gamma_i(t)}]\} \\ = & \ \frac{1}{l_r * \Delta t} * \frac{\Sigma_{i \in r} ttt_i^P(t)}{\Gamma_r(t)} + \frac{|r|}{l_r * \Delta t} * cov[ttt_i^P(t), \frac{1}{\gamma_i(t)}] \end{aligned} \tag{2.10}$$

A natural estimation for Eq. (2.6) using aggregated variables would be the first term of Eq. (2.10), but the above formula shows that it would be a biased estimation. To derive an unbiased estimation, it is necessary to take into account the second term. We will confirm this result numerically by showing the results of the biased and unbiased estimation methods.

2.4.2 Case 2: Probe trajectories and loop data in loop equipped links are available

Let us now consider the case when only a fraction of the links is equipped with loops. We denote the fraction of links with loops as f, a set of links with loops as r_1, and a set of all links in a network as r. The number of links in each set is shown as $|.|$. Thus, $f = |r_1|/|r|$.

In this case, we have three options to estimate the network-level density:

Option 1) Network-level fishing rate over all links: When $\Gamma_r(t)$ can be estimated with reasonable accuracy, we use Eq. (2.10) directly. However, it is normally challenging to get such a network-level fishing rate since it requires high loop coverage, which is almost 100%, or spatially homogeneous $\gamma_i(t)$ for all links.

Option 2) Network-level fishing rate over loop-equipped links for non-equipped links: We use the loop-equipped links to estimate $\Gamma_{r_1}(t)$ (the harmonics mean of $\gamma_i(t)$ over the loop-equipped links). We can separate the sum of total travel time in Eq. (2.6) from the group of loop-equipped links $i \in r_1$ and non-equipped ones $j \in r_0$, as shown in Eq. (2.11).

$$K_r(t) = \frac{1}{l_r * \Delta t} * \{\Sigma_{i \in r_1} \frac{ttt_i^P(t)}{\gamma_i(t)} + \Sigma_{j \in r_0} \frac{ttt_j^P(t)}{\gamma_j(t)}\} \tag{2.11}$$

The first term can be directly calculated using the same definition as Eq. (2.6). To calculate the second term, Eq. (2.10) can be applied, as shown in Eq. (2.12)

$$K_r = \frac{1}{l_r * \Delta t} * \Sigma_{i \in r1} \frac{ttt_i^P(t)}{\gamma_i(t)} + \frac{1}{l_r * \Delta t} * \Sigma_{j \in r0} ttt_j^P(t) * E[\frac{1}{\gamma_j(t)}] + \frac{|r_0|}{l_r * \Delta t} * cov[ttt_j^P(t), \frac{1}{\gamma_j(t)}] \tag{2.12}$$

Note that in the second and third terms of the above equation, $E[\frac{1}{\gamma_j(t)}]$ and $cov[ttt_j^P(t), \frac{1}{\gamma_j(t)}]$ should have been calculated over the non-equipped links, which is obviously not possible. Therefore, we use the network-level fishing rate $\frac{1}{\Gamma_{r_1}(t)}$ and covariance $cov[ttt_i^P(t), \frac{1}{\gamma_i(t)}]$ over the equipped links.

Option 3) Network-level fishing rate over loop-equipped links for all links: When it is impossible to obtain a good estimation for $\Gamma_r(t)$ independently, we can use Eq. (2.10) by replacing $\Gamma_r(t)$ by $\Gamma_{r_1}(t)$ and $cov[ttt_j^P(t), \frac{1}{\gamma_j(t)}]$ by $cov[ttt_i^P(t), \frac{1}{\gamma_i(t)}]$.

Furthermore, when there are not enough probe trajectories in links with loops to estimate the network-level fishing rate, we need to find an alternative. When historical data at the same time period are available, day aggregation may be effective: $\Gamma_{UD,r}(t) = \Sigma_{d \in D} \Gamma_{d,r}(t)/|D|$, $cov[ttt_i^P(t), \frac{1}{\gamma_{UD,i}(t)}]$. Otherwise, we have no choice than using a constant value: $\bar{\Gamma_{d,r}}$, $cov[ttt_i^P(t), \frac{1}{\bar{\gamma_{i,d}}}]$.

2.4.3 Case 3: Trajectories are not available in all links

If no probe vehicle trajectory is available in all links in certain time periods, we can calculate network-level density by using $\alpha_i(t)$ given in Eq. (2.4) as shown in Eq. (2.13).

$$K_r(t) = \frac{\Sigma_{i \in r1}(o_i(t) * l_i/\alpha_i(t))}{l_{r1}} \tag{2.13}$$

where l_{r1} is the total link length with loops. We emphasize that this equation requires the availability of historical probe trajectories in the same time period. For example, we can

calculate it by using day aggregation $\alpha_{UD,i}(t)$. When not enough historical data for this time period are available, we can use $\alpha_{d,i}(o_i)$ as Eq. (2.5a). However, historical data are also required to estimate the relation $\alpha_i(o_i)$ for each link. Otherwise, we need to use constant value $\bar{\alpha_{d,i}}$.

2.5 Assessing the accuracy of the link-level density estimation

The main objective of this paper is to evaluate the accuracy of urban density estimation using loop and probe data at the link and network level with empirical data. One important challenge is that the ground-truth values are usually not available due to (i) lack of high penetration rates and (ii) measurement errors. The pNEUMA dataset allows having a penetration rate close to 100% with high resolution measures (position every $0.025sec$) and very little measurement error (in the range of a few cm). Thus, by installing virtual loops, we can emulate loop detector data, and by sampling trajectories, we can emulate various penetration rates. Thus, in section 2.5.1, we investigate the accuracy of link-level density estimation for the Athens dataset, while in sections 2.5.2-2.5.3, we analyze the Lyon data, which cover a much larger area, but without ground-truth information.

2.5.1 Using real-time probe and real-time loop data (Case 1)

When all trajectories are available, we can calculate the true value of traffic density by Eq. (2.1). When loop and probe data are available, the method in Eq. (2.3), i.e., combining probe information and the fishing rate, provides a descent estimation of Eq. (2.1). Despite the fact that loops provide only local information in their proximity and the spatiotemporal evolution of queues is not fully captured, spatial mean speed can be accurately estimated with the probes and the flow with the loops meaning that using the ratio between the flow over the mean spatial speed should give a tight estimate of the real density. We will use the latter as the reference for the global analysis with the Lyon data, but we first aim to confirm that Eq. (2.3) indeed provides a tight estimation corresponding to Eq. (2.1) results. We first test this method with the drone experiment in Athens. This unprecedented dataset provides almost all vehicle trajectories for loop time periods of $15min$ in inner-city links. The experiment includes significant congestion.

True traffic density is derived from all trajectories of the drone data. Also, we estimate traffic density from Eq. (2.3) at 20 links whose length is longer than $80m$ as shown in Figure 2.8, using virtual loop data, located at the edge of the all links, and virtual probe data, chosen randomly among all trajectories for a given penetration rate. For now, we assume that the noise/error is not included in virtual data to focus on the effect of probe penetration. To clarify the effect of the time span of the loop data, we use different aggregation periods of 1 minute, 3 minutes, and 6 minutes. We calculate relative errors by dividing the absolute value of the difference between true density and estimated density by the true density. The mean value of the relative errors over a whole period for each link is first calculated. This calculation is repeated 25 times with different probe penetrations. The overall average (over all links) along with the 25/75 percentiles are plotted on Figure 2.9 (a) for different mean fishing rates. As a result, the relative errors are small and around 2-4 %, regardless of the

FIG. 2.8 – *Selected links location in Athens network (grey links: all links in the network, red links: selected links for assessment)*

fishing rate when the fishing rate is lower than 50%, which confirms that Eq. (2.3) provides a narrow estimation of link-level density. A longer time span of loop data leads to better accuracy. According to Figure 2.9 (b), where each plot represents the mean value of relative errors with respect to the true density over a whole time period of each link, the relative error can be significant when the traffic density is low, but in terms of absolute errors, the values are quite small. However, taking longer time aggregation periods leads to smaller errors. When we compare the relative error between 3 minutes and 6 minutes of time aggregation periods, we cannot find a large difference either according to the fishing rate or the true density. For Athens data, a time aggregation of 3 minutes looks sufficient when estimating the link-level density.

When we consider the same setting as for the Lyon data, i.e., a time span for loop detectors equal to 6 minutes, and fishing rates around 10%, the relative error is very small, e.g., around $2 - 4\%$ in most cases. Therefore, we can confirm considering the Athens data that the estimation method using the real-time probe vehicle data with the real-time fishing rate is accurate enough to be considered as the reference method for the link-level density assessment. We will then use this method to calculate the reference density values for the Lyon data. It is not possible to carry the full analysis on the Athens data because the space and time coverages are too limited (the total link length is 20 lane-km and the experiment duration is only 75 minutes). It is not sufficient to investigate the effect of data aggregation and to determine how historical observations of previous days can help to improve the density estimation of a new current day. Therefore, in the following section, we compare this reference case, i.e., calculated from both real-time probe and loop data according to Eq. (2.3), on the Lyon network with different methods or data aggregation cases on the same data set.

2.5.2 Using real-time probe data and historical loop data (Case 2)

When the fishing rate in a link in the time period is not available, we can estimate it by using three types of aggregation methods and a combination of them. Using historical data for the time period, we can estimate the fishing rate by day aggregation (UD). In this study, we used all the weekday/weekend data of April 2018 in 250 links. If no real-time and historical data in the link are available, link aggregation (UL) may be useful. For link aggregation, we

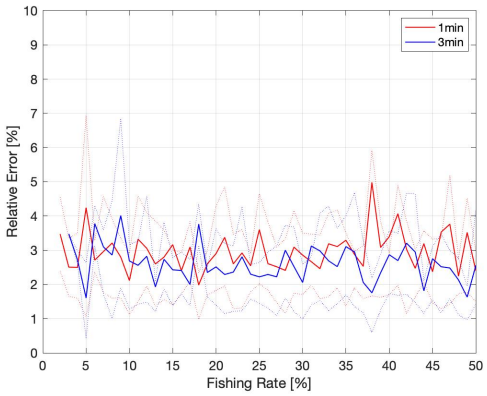

(a) Mean and 25/75 percentiles of relative error over all links according to fishing rate and time aggregation periods

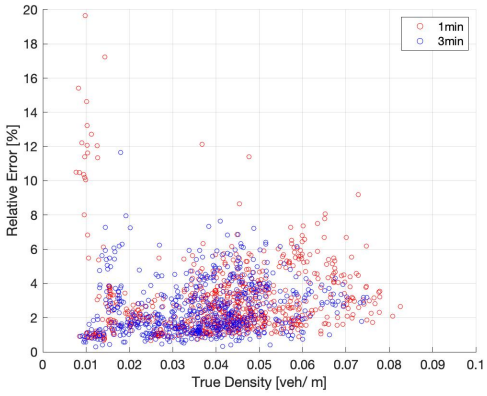

(b)Mean value of relative error over a whole time period of a whole time period of each link according to true density and time aggregation period (1 minute and 3 minutes)

FIG. 2.9 – *Relative error of density estimation between true density and reference case of this study based on the drone data of Athens*

calculate the average over the links in our network. When no real-time and historical data in a time period is available, we have to use a constant value over a day (Static). In the latter case, we calculate an average for a time over a day. We define the cases without day, link, and time aggregation as 1D, 1L, and Dynamic. We use one set of weekday/weekend data and each set of link data, which is the same as the reference case for 1D and 1L. The reference case, as shown in Eq. (2.3), uses the fishing rate without any aggregations (1D, 1L, Dynamic). We compare the estimation using all aggregation combinations with the reference in every link at every time period to determine the most adequate combination according to data availability. The result is shown as the mean and distribution of the error, i.e., calculated by subtracting the reference from the estimation using the aggregation in every link at every time period, and mean of the relative error.

According to the result shown in Figure 2.10, the error is positive, and the relative error is high, larger than 29% for weekdays and all the aggregation levels. In particular, link aggregation leads to quite large relative errors even in the case of using a real-time fishing rate (1D, Dynamic) such as close to 50% on a weekday and 40% on a weekend. It is derived from the significant difference in the fishing rate in each link, as shown in Figure 2.4 (a). Since some links can have a quite high fishing rate randomly at the link level and a lot of links have lower fishing rates than the mean of all links, it leads to positive and high error and significant relative errors which are close to 50%. In Figure 2.11 (a), we see the large relative errors, which are over than 70%, especially of link aggregation when traffic density is low (less than $0.05 veh/m$). Thus, link aggregation can lead to heterogeneous results depending on the traffic state and should be avoided at the link-level. Secondly, the comparison between Static and Dynamic cases shows that using a constant value over a day leads to larger errors around 35% of the relative error (UD, 1L, Static) compared to 30% in the Dynamic case (UD, 1L, Dynamic). Since the difference between Static and Dynamic cases is small in the case of using link aggregation (UL), we find that the impact of time aggregation is smaller

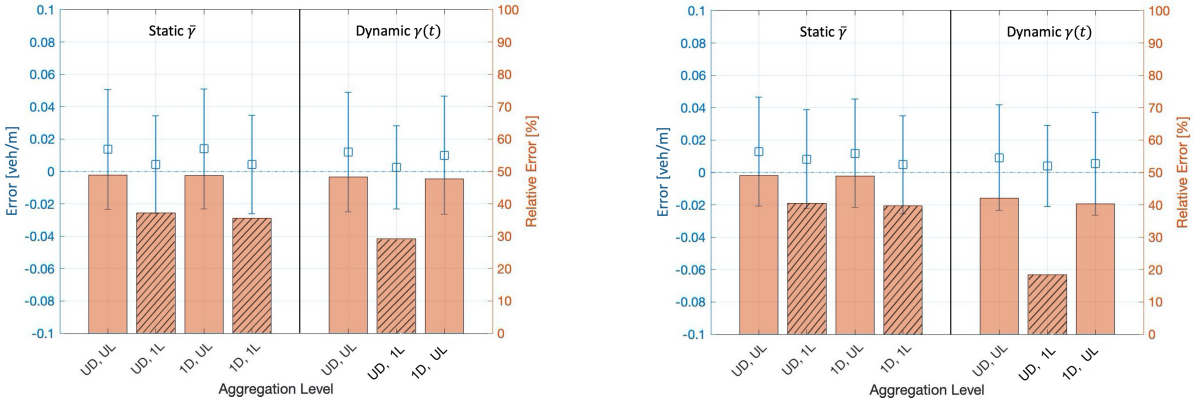

(a) One Weekday (b)One Weekend

FIG. 2.10 – *Errors and relative errors between the reference and estimated density using the aggregated fishing rate at the link-level of the Lyon network. The aggregation level used to calculate the fishing rate is UD (using one month data), 1D (using the data of one day), UL (using the data all the links), 1L (using the data of one link)*

than that of link aggregation. Also, Figure 2.11 (b) shows that time aggregation leads to slightly smaller errors when the traffic density is small. However, the relative error of using the time aggregation (1D, 1L, Static) case is quite large: average $35 - 40\%$. Therefore, it is evident that using a constant value also leads to significant errors (which is the state of practice for loop detector data). By comparing the results with and without day aggregation (UD/1D), the difference of the relative error according to day aggregation is almost zero. The result of using day aggregation (UD, 1L, Dynamic) leads to a relative error of 30% on the weekday. This error is smaller than that obtained using other aggregations with errors around 35% to 50%. Also, as shown in Figure 2.11 (a), the relative error is not affected by the traffic density. When the density is lower than 0.05 veh/m, the relative error sometimes goes up to 80%. According to Figure 2.11 (b), those high relative error comes from low reference density values. In any cases, the relative errors can be seen as large (over than 70%) leading to poor density estimates. This is because the fishing rate estimation is not robust, mainly because there are not enough available probe trajectories at the link-level.

As a result, we clarify quantitatively that using data in other links or a static value to estimate the fishing rate leads to quite large errors close to 50% of relative errors on weekdays at the link level. Using historical data in a link at each time period is better than other aggregation methods. However, the errors obtained using all of these aggregations are substantial around 30% to 50% of relative errors on weekdays at the link level. This study helps to quantify the magnitude of such errors and clearly show that it can be as high as 50%.

2.5.3 Using real-time loop data without real-time probe data (Case 3)

When there is no real-time probe trajectory in a link in the time period, we can estimate density from $o_i(t)$ and $\alpha_i(t)$ per Eq. (2.5b). According to Eq. (2.4), the calculation of $\alpha_i(t)$ requires probe trajectories that are impossible to obtain in this case. For this period, we can

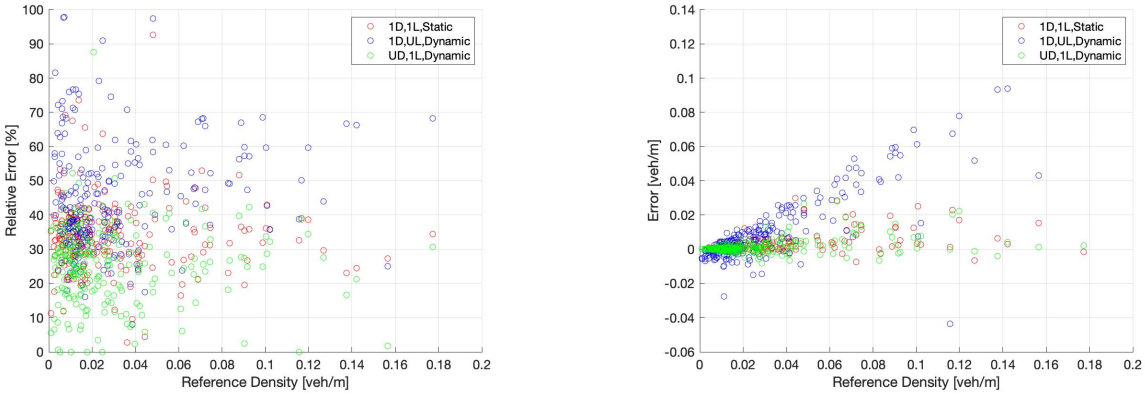

(a) Relative error (b) Error

FIG. 2.11 – *Mean value of the relative error and error at each link according to the traffic density of the reference case and aggregation level of the fishing rate based on the Lyon data. The aggregation level used to calculate the fishing rate is UD (using one month data), 1D (using the data of one day), UL (using the data all the links), 1L (using the data of one link)*

use four types of proxy to estimate EVL based on data availability. When historical probe trajectories are available, we can use day aggregation (UD). For this calculation, we used all the weekday/weekend data of April 2018 in 250 links. When no historical data in a link is available, we can use link aggregation (UL). If we obtain historical data without aggregation in the same time period, or $\alpha_i(o_i)$ can be used per Eq. (2.5a). Otherwise, we need to choose a constant value over a day (Static). In this study, we use the average value of every time period and also use $\bar{\alpha}_i = 5m$ based on the values of previous studies, which are between $5m$ to $10m$ (Leclercq (2005), Lee & Coifman (2012), Zefreh *et al.* (2017)). We calculated the mean and distribution of the errors but also the mean of relative errors according to the comparison between the reference and the estimation by using aggregation in every link at every time period.

According to the results shown in Figure 2.12, each combination is worse than the case of using the fishing rate. This is especially the case when using link aggregation; the relative errors of almost all combinations are more than 50%, and the errors are positive and huge. This clearly shows that link aggregation leads to large errors because the range of link specific $\alpha_i(t)$ values is very large as shown in Figure 2.6 (a). It can reach up to $20m$ for some links mainly those experiencing high speeds, see Figure 2.7 (a) but also go down to $2.5m$. So, when we replace $\alpha_i(t)$ by a dynamic mean value over links such as around $2.5m$ to $7m$ as shown in Figure 2.6 (b), it is no surprise that errors on density can be very large. Comparing dynamic and static states, the relative error in the case of using static EVL $\bar{\alpha}$ is somewhat greater than when using dynamic EVL $\alpha(t)$, especially in the case of 1L, which is around 50% for $\bar{\alpha}$ against around 40% for $\alpha_i(t)$ on a weekday, and around 40% for $\bar{\alpha}$ against around 20% for $\alpha_i(t)$ on a weekend. Even in the case without any aggregations (1D,1L), the relative error is around 40% on a weekday/weekend. In the case of using $\alpha_i(o_i)$, the error of every combination is smaller than when using static $\bar{\alpha}$. Especially in the case of (UD, 1L), the relative errors of both cases are quite high, around 40% for $\alpha_i(o_i)$ and around 50% for $\bar{\alpha}$. Therefore, historical data are useful even if no data for the same time period are available. However, even in the static case without any other aggregations (1D,1L), the relative error

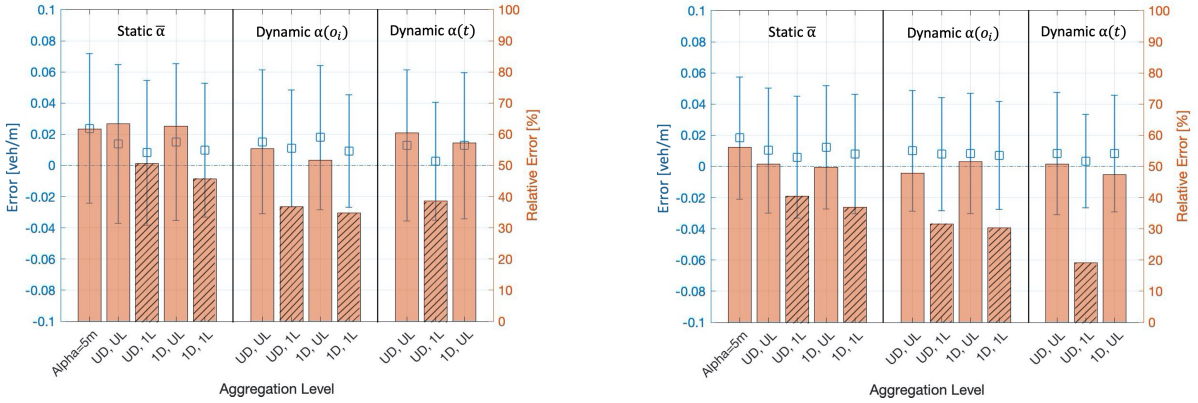

(a) One Weekday (b) One Weekend

FIG. 2.12 – *Errors and relative error between the reference and estimated density by using α at the link-level of the Lyon network. The aggregation level used to calculate the fishing rate is referred as UD (using one month data), 1D (using the data of one day), UL (using the data all the links), 1L (using the data of one link)*

is higher than 30%. This large error is derived because $\alpha_i(o_i)$ is different in each link and the real-time $\alpha_i(t)$ at the link level is too sensitive to fit with $\alpha_i(o_i)$, also, there are not enough probe trajectories in a link in the time period. By comparing the cases with and without day aggregation (UD/1D), the difference obtained is quite small (less than 5% of relative errors). Therefore, using historical data does not give a more pronounced effect than other aggregations. However, when we look at the case with day aggregation (UD, 1L, Dynamic) on a weekday, the relative error is high, reaching 40%. This shows that day aggregation makes EVL robust, but it cannot adapt to the sensitivity of real-time $\alpha_i(t)$ at the link-level. Thus, using the historical data is an effective approximation to improve the estimation accuracy when space- and time-dependent fishing rates are not available. We quantify precisely the accuracy level we can get when resorting to historical data only. However, because real-time $\alpha_i(t)$ is too sensitive, every aggregation leads to vast deviations from the reference such as ranging from 35% to 63%. Therefore, more advanced methods introducing traffic models would be necessary to improve the density estimation (e.g., Skabardonis & Geroliminis (2008), Liu *et al.* (2009), Ban *et al.* (2011), Ramezani & Geroliminis (2015)). However, those methods are not straightforward to implement in practice and may require data that are not easily available, e.g., signal settings including offsets.

2.6 Assessing the accuracy of Network Level Density Estimation

2.6.1 Probe trajectories and loop data are available in all links (Case 1)

Before considering the case that only a few links have loops, we confirm the accuracy of the estimation by using the accurate network-level fishing rate according to Eq. (2.10). We have selected the subnetwork of Lyon with loops in all links, so it can represent a case study with

100% loop coverage. The estimation result is compared with the reference case, which is the average of the link-level estimation in Eq. (2.6). We calculate the covariance of $ttt_i^P(t)$ and $1/\gamma_i(t)$ by using the Minimum Covariance Determinant (MCD) method, which is known as a highly robust estimator of the covariance (Rousseeuw (1984) and Rousseeuw (1985)) to treat the time period for which there are few probe trajectories. The relative error is quite small, 9.92%, while in the case of biased estimation without covariance, as in Eq. (2.8), the relative error is 15.9%. Thus, we confirm that the validity of the network-level fishing rate method even when the bias is quite high compared to the link-level fishing rate. By comparing the results at the link-level with the network-level, we observe that link-level errors cancel out during the spatial aggregation and the relative error decreases from 48% to around 20%.

2.6.2 Probe trajectories and loop data are available in limited links (Case 2)

In reality, only a subset of links is equipped with loops. In this case, we can use only two of the options described in section 2.5.2, (options 2 and 3) as explained in Eq. (2.11) and Eq. (2.12). We determine the network-level fishing rate over links equipped with loops and use it as a proxy for all links. Also, the same is done to estimate $cov(ttt_i^P(t), 1/(\gamma_i(t))$. First, we assess the accuracy of option 2, by using the average of the reference link-level estimation for links with loops and use the network-level fishing rate for the other links. To compare the accuracy of the network-level fishing rate according to loop coverage, we also calculate the density estimation by using the accurate network-level fishing rate and covariance calculated over all links in Eq. (2.11). This estimation is not perfect since we need the network-level fishing rate over the links without loops, which is impossible to measure directly. The result in the case of using the network-level fishing rate and covariance over all the links, e.g., Γ_r and cov_r, and links with loops, e.g., Γ_{r1} and cov_{r1}, is compared with the reference case by relative errors shown as the red and blue plots in Figure 2.13. At this point, we consider the loop coverage to be 10%, 30%, 50% and 100% for the chosen subnetwork with loops, as mentioned in section 2.2. When the loop coverage is about 10%, which is close to what is observed for the real Lyon network (7%), we do not have enough combined observations of loops and probes to accurately estimate the covariance term cov_{r1}. In such a case, the estimation method without considering the covariance term gives better results than when the covariance is considered (27.5% compared to 37%).However, large deviations can be observed when calculating the covariance for low loop coverage, which jeopardizes the overall density estimation. Fortunately, both estimation methods (with and without the correlation term) lead to reasonable relative errors, starting from 27.5% for 10% loop coverage, quickly dropping with higher loop coverage (19% for 30% loop coverage without the correlation term, and 17% for 30% loop coverage with cov_{r1}).

When we cannot estimate the network-level fishing rate from the real-time data, we can use the aggregated fishing rate by using historical data as in the link-level estimation. We consider day aggregation by using the data of all the weekdays in April to calculate the network-level fishing rate and time aggregation by using the average on time over a day. If we use these aggregations, we cannot estimate covariance accurately because there is higher uncertainty between the total travel time of probe vehicles and the aggregated link-level fishing rate. Therefore, we calculate only the estimation without considering covariance. As

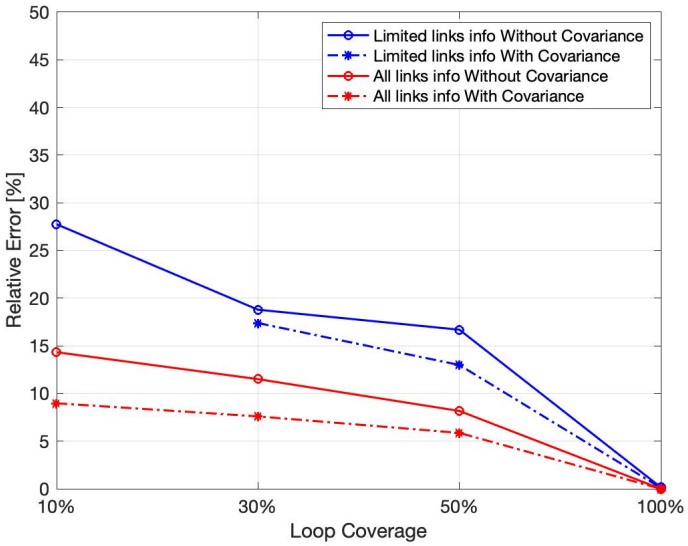

FIG. 2.13 – *The effect of covariance according to 1D Dynamic calculation in Option2 (Case 2) based on the Lyon data*

shown in Figure 2.14 (a), using day or/and time aggregation makes the estimation robust with quite small relative errors, around 18% with 5% loop coverage and less than 15% in 10% loop coverage.

Next, we assess the accuracy of option 3, using the network-level fishing rate for all the links. The result is shown in Figure 2.14 (b). When a small number of links is equipped with loops (loop coverage below 10%), the result is similar to option 2, and accuracy decreases with higher covariance. Therefore, we can say option 3 is a robust and straightforward option that we can recommend for low loop coverage.

In brief, the results show that we need around only 7% of loop coverage to reach relative errors below 15% when using options 2 and 3. To reach lower relative errors (below 10%), we need to use option 2 with a loop coverage higher than 30%, which is not yet possible in many cities around the world.

Also, it is important to investigate whether the errors depend on the density value when applying the network-level estimation to the control. It can be crucial for many applications like traffic perimeter control to guarantee that the error magnitude is not different in free-flow and congested situations. Figure 2.15 shows the relative error according to the estimated density of the reference case when the loop coverage is 10%. It appears that the error range is stable over all density values when we use the fishing rate method. The average (and the standard deviation) of relative errors over a whole density, 27.2% (7.0) in Option 2 and 27.9% (7.5) in Option 3 when the fishing rate aggregation level is Dynamic-1D, and 13.4% (6.2) in Option 2 and 14.2% (7.2) in Option 3 when the aggregation level is Static-UD. Thus, we confirm that we can get similar accuracy by using Option 2 and 3 when loop coverage is 10%, and the accuracy is not affected by the density.

Until now, the calculation has focused on a day with a complete or partial streaming loop and probe data set. We propose a more challenging test with fewer data to assess the validity of learning the fishing rate for a case in which we have no loop data during a month, so we cannot adjust the fishing rate. In this study, we use all the weekday data of April to

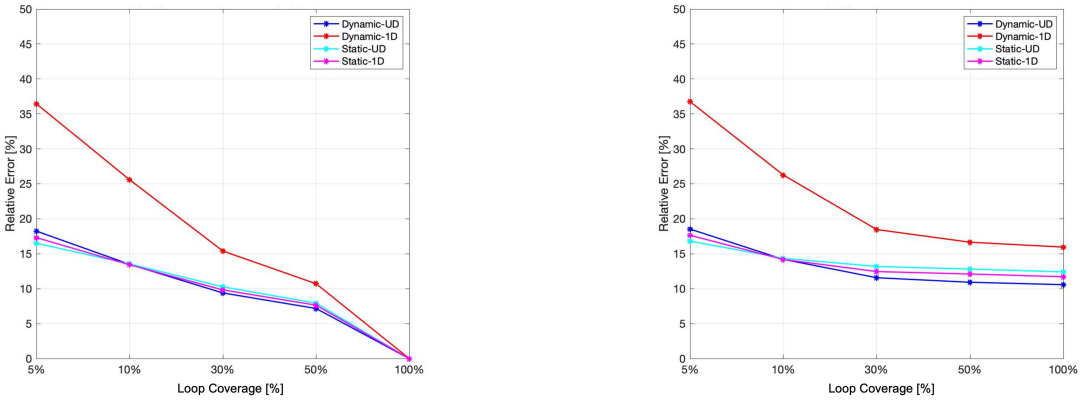

(a) Option 2: using Γ_{r1} for links without loops (b) Option 3: using Γ_{r1} for all links

FIG. 2.14 – *Relative error by using the network-level Fishing Rate over equipped links depends on loop coverage (Case 2) based on the Lyon data. The aggregation level used to calculate the fishing rate is UD (using one month data), 1D (using the data of one day)*

learn the fishing rate, apply it to estimate density on five weekdays in May and assess the uncertainty of the estimation. The estimation based on historical data is compared with the estimation when the probe and loop data are available in real-time. Since the difference in accuracy between the fishing rate with and without time aggregation using multiple-day data is small, we use a fishing rate averaged over time to compare the accuracy of the estimation. According to the result shown in Figure 2.16 (a) and (b), there is no significant difference over five days when using options 2 or 3. With option 2, the relative error is less than 15% when loop coverage is 10% and reduces even further when the coverage gets higher. With option 3, the relative error is constant and equal to $11 - 13\%$ regardless of loop coverage, which can be considered as small. These results are quite similar to those shown in the case with time and data aggregation (Static UD) of Figure 2.14. Therefore, it is clear that using historical data to estimate the fishing rate is valid in particular when we do not have enough loop data.

2.6.3 No real-time trajectory is available (Case 3)

Last, we assess the accuracy of the network-level density estimation in the case where we cannot obtain any trajectories in real-time. This time, we rely on historical probe data according to Eq. (2.13). For the comparison, we calculate the case for which we can obtain the real-time EVL of all the links with loops (Dynamic-1D) as shown in Figure 2.17. In comparison to the result using the fishing rate, as shown in Figure 2.14, the relative error is high at around 32% when loop coverage is 10%. It quickly drops when the loop coverage gets higher. However, even in the case of 10% loop coverage, the relative error is smaller ($25 - 40\%$ in the all cases) than the link-level estimation as shown in Figure 2.12 (over 50% in all cases with link aggregation).

When we cannot obtain real-time trajectories, we have to estimate EVL using historical probe data with the link-level estimation. Using historical data (Dynamic-UD) to estimate dynamic EVL is the almost same result, e. g., the difference of the relative error is less than

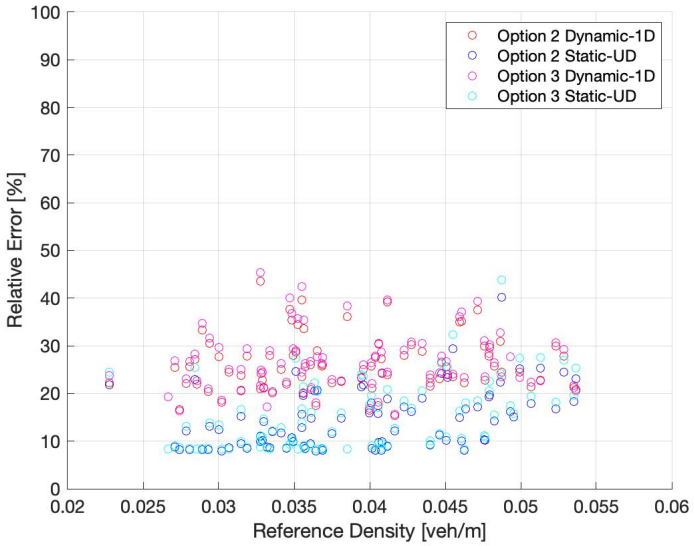

FIG. 2.15 – *Mean value of the relative error at the network level according to the traffic density of the reference case and aggregation level of the fishing rate based on the Lyon data with 10% loop coverage. The aggregation level used to calculate the fishing rate is UD (using one month data), 1D (using the data of one day). Option 2 is using Γ_{r1} for links without loops, and Option 3 is using Γ_{r1} for all links*

1%, as using real-time data (Dynamic-1D) in the case of 10% loop coverage. However, if the loop coverage is more than 15%, using historical probe data leads to a much larger error as 22% for 30% loop coverage and 20% for 50% loop coverage compared to using real-time data, e. g., rates of increase for each loop coverage are 43% and 80%. Historical data make a robust estimation even when the loop coverage is low (10%). On the other hand, it is less flexible to the sensitive traffic behavior of each day, and the accuracy does not improve a lot along with the loop coverage.

If we cannot estimate dynamic EVL with historical probe data, we can use the relation $\alpha_i(o_i)$ of each link according to Eq. (2.5a). In the case of estimating this relation by using the day data (Occ-1D), the result is better than all the other cases, including using the real-time data (Dynamic-1D), when the loop coverage is below 15% since using $\alpha_i(o_i)$ relation leads to a robust estimation. Even when loop coverage is over 30%, the result is almost the same as that of using dynamic EVL by historical data (Dynamic-UD). Using historical data for estimating $\alpha_i(o_i)$ makes estimation with similar accuracy, e. g., the difference of the relative error is around 1%, as using dynamic EVL when 10% loop coverage. Since the accuracy of this case does not improve when the loop coverage is over 30%, the accuracy gets worse compared to one by Dynamic-UD case. However, the maximum difference is around 5% from Dynamic-UD case, and the relative error is always less than 25%. Since this method does not require data as much as estimating dynamic EVL by historical data, it can be quite an effective method if only limited data are available.

We must use a static value over a day when we cannot obtain any real-time or historical trajectories. We calculated the value by an average of the day (Static-1D) and historical days (Static-UD). We found that using a static value over a day leads to large errors, as high as 40% in the case of 10% loop coverage and around 30% in the case of 100% loop coverage. This shows that we need more than 35% loop coverage and a reasonable estimation of real-

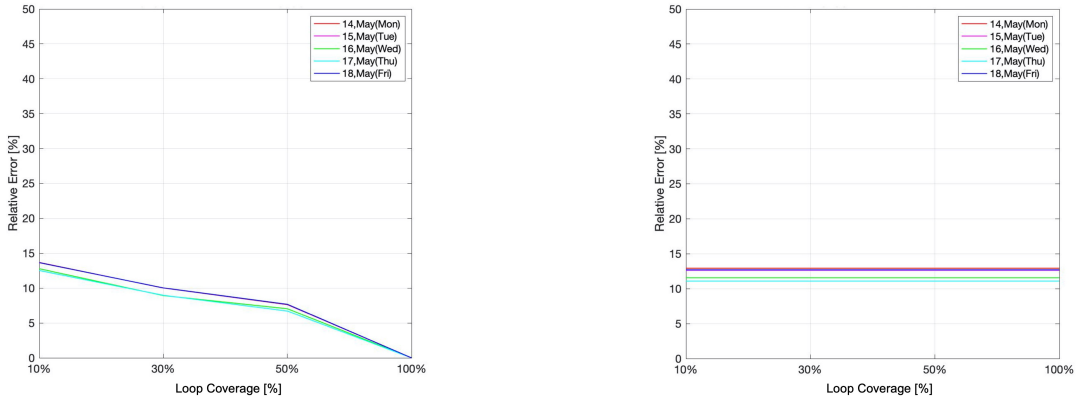

(a) Option 2: using Γ_{r1} for links without loops (b) Option 3: using Γ_{r1} for all links

FIG. 2.16 – *Relative error by using static network-level fishing rate derived from historical data (Case 2) of Lyon network*

time EVL to fall below a relative error of 15%.

Figure 2.18 shows the relation between the relative errors and the density values. It appears that errors increase with density. When using $\alpha_i(o_i)$ as Eq. (5a) (Occ-UD), the relative error is less than 30% when the density is less than $0.03veh/m$ but it exceeds 40% when the density is more than $0.05veh/m$. Therefore, we need to be careful about using EVL when the density is high (congested situations).

2.7 Conclusion

This study provides the first overall thorough quantitative assessment of the density estimation errors depending on the method, the data type, and the penetration rate by using real data from two different experiments in Lyon and Athens. Also, we provide a detailed analysis about how link-level data should be properly aggregated at the network level. In the case where probe trajectories are available in real-time, we could estimate the link-level and network-level density using the fishing rate. If no trajectory is available, we could use occupancy from the loop data and the dynamic electric vehicle length (EVL).

We calculate the relative errors compared to the reference case of the results obtained from the real-time probe and loop data of all links. Main data aggregation cases are summarized in Table 2.3 for the link-level estimation and Table 2.4 for the network-level estimation. The data requirement levels in these tables are the total points of required data detailedness of each day, each link, or each time equal to 1 point. For example, the data requirement level is 5 when we use the link-level fishing rate dynamics of a link aggregated over a month (denoted as $\gamma_{UD,i}(t)$ in Table 2.3). For the network-level estimation by using the network-level fishing rate, we introduce two options when loop coverage is below 30% such as Option 2, i. e., using the link-level fishing rate for links with loops and using the network-level fishing rate for links without loops, and Option 3, i.e., using the network-level fishing rate for all links. Option 2 needs to calculate the link-level fishing rate of links with loops, which requires at least real-time probe data and loop data with the day or time aggregations. Therefore, we define adding 0.5 points of the data requirement level for Option 2. Each case's

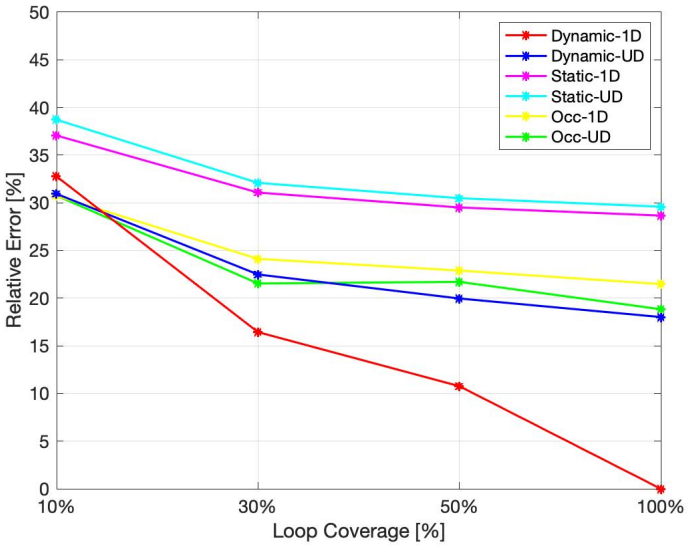

FIG. 2.17 – *Relative error using α at the network level depends on loop coverage (Case 3) based on the Lyon data. The aggregation level used to calculate α is UD (using one month data), 1D (using the data of one day). Occ uses the relation between occupancy and α.*

results on the weekday are summed up according to data requirement level in Figures 19 and 20 for the link- and network-level estimations.

At the link level, relative errors can be kept below 30%, only when we can obtain probe trajectories and loop data of each link at the moment concerned of past many days ($\gamma_{UD,i}(t)$). The time aggregation of the fishing rate, i. e., $\bar{\gamma}_{UD,i}$ or $\bar{\gamma}_{d,i}$, leads to large relative errors around 35% to 40%. Furthermore, using the global fishing rate (UL) makes the relative errors over 45%. Therefore, time aggregation cannot be recommended, and link aggregation for using the link-level fishing rate should be avoided. All cases using EVL lead to considerable relative errors, such as over 35%. When using only the day aggregation or/and using $\alpha_i(o_i)$ relation instead of the static value, i. e., $\alpha_{UD,i}(t)$, $\alpha_{d,i}(o_i)$, and $\alpha_{UD,i}(o_i)$, the relative errors are around 35% to 45%. All the other cases lead to the larger errors, around 45% to 65%. Thus, it is almost impossible to get accurate results at the link level except if the historical fishing rate at each link at the moment concerned is available and if we can reach a very high penetration rate (a fishing rate higher than 10%).

At the network level, using either the fishing rate or EVL lead to better accuracy, i.e., the highest relative error is below 30% by using the fishing rate and below 40% by using EVL when loop coverage is 10%, compared to the link-level estimation since errors are canceling out due to spatial aggregation. Especially, the new method that explicitly considers the covariance term $cov[ttt_i^p(t), \frac{1}{\gamma_i(t)}]$ when aggregating link-level fishing rate ($\Gamma_d^{op2}(t) + Cov$) leads to very low relative errors, below 18% when loop coverage is over 30%. However, the initial data requirement to properly estimate this term is large. We need enough probe data (at least average 10% of fishing rate) and a loop coverage higher than 30% for the Lyon network. The difference between Option 2 and 3 of using network-level fishing rate is quite small as less than 3% when loop coverage is below 30%. Since Option 3 requires only the network-level fishing rate calculated from links with loops for estimation of all links, it is a more reasonable method. Day and/or time aggregation of the fishing rate calculation led to

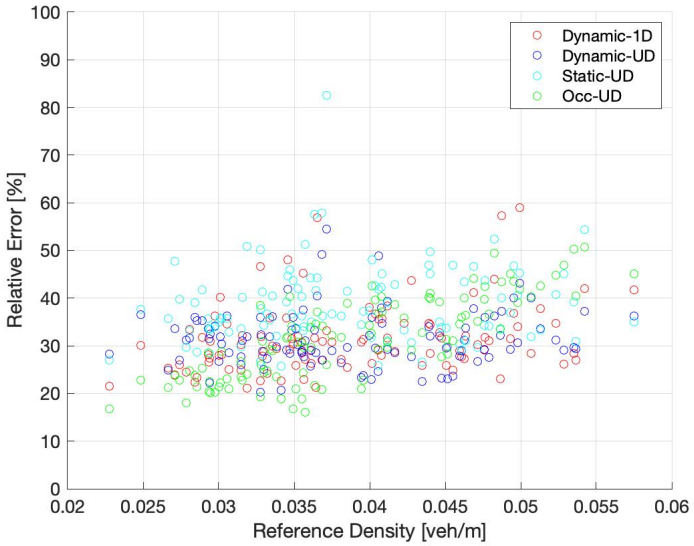

FIG. 2.18 – *Mean value of the relative error at the network level according to the traffic density of the reference case and aggregation level of α based on the Lyon data with 10% loop coverage. The aggregation level used to calculate α is UD (using one month data), 1D (using the data of one day). Occ is the case with using the relation between occupancy and α.*

robust results below 20% even when loop coverage is 10%. In all cases of using EVL, the accuracy is lower than when we use the network-level fishing rate. In particular, using a constant value for EVL led to a considerable relative error higher than 30% even when the loop coverage is over 30%. On the other hand, using the relationship between occupancy and EVL is useful when no trajectory is available, i. e., the relative error is around 25% to 35% when loop coverage is 10% and below 25% when the loop coverage is over 30%. These results clearly show that, by using the proper estimation method according to data availability, i.e., using fishing rate when the real-time trajectory data is available and using EVL when no real-time trajectory data is available, we can get good accuracy of an average density that represents the overall loading of the region.

Thus, this chapter proposes clear guidance about the error magnitude we can expect considering the calculation method and the data availability. We can for example use these results to specify which penetration rate and loop coverage are required to achieve a targeted relative error level. Such insights would be of great value when designing on-field monitoring systems both at the link and network level.

Device	Probe			Loop					
Requirement	day	link	time	day	link	time	other	Level	Index
Using Fishing Rate (Case 2)	Y	Y	Y	-	Y	Y	-	5	$\gamma_{UD,i}(t)$
				Y	Y	-	-	5	$\bar{\gamma}_{d,i}$
				Y	-	Y	-	5	$\gamma_{d,UL}(t)$
				-	Y	-	-	4	$\bar{\gamma}_{UD,i}$
				-	-	Y	-	4	$\gamma_{UD,UL}(t)$
				Y	-	-	-	4	$\bar{\gamma}_{d,UL}$
				-	-	-	-	3	$\bar{\gamma}_{UD,UL}$
Using EVL (Case 3)	-	Y	Y	Y	Y	Y	-	5	$\alpha_{UD,i}(t)$
	Y	Y	-				$\alpha_i(o_i)$	5	$\alpha_{d,i}(o_i)$
	Y	Y	-				-	5	$\bar{\alpha}_{d,i}$
	Y	-	Y				-	5	$\alpha_{d,UL}(t)$
	-	Y	-				$\alpha_i(o_i)$	4	$\alpha_{UD,i}(o_i)$
	-	Y	-				-	4	$\bar{\alpha}_{UD,i}$
	-	-	Y				-	4	$\alpha_{UD,UL}(t)$
	Y	-	-				$\alpha_i(o_i)$	4	$\alpha_{d,UL}(o_i)$
	Y	-	-				-	4	$\bar{\alpha}_{d,UL}$
	-	-	-				$\alpha_i(o_i)$	3	$\alpha_{UD,UL}(o_i)$
	-	-	-				-	3	$\bar{\alpha}_{UD,UL}$

TAB. 2.3 – *Data Requirements and Index of All Cases at the Link-Level Traffic Density Estimation in This Study (Y: required, -: not required, Level: Data Requirement Level)*

Device	Probe				Loop				
Requirement	day	time	γ_i	other	day	time	other	Level	Index
Using Fishing Rate (Case 2)	Y	Y	Y	$cov(\gamma_i, tt_i)$	Y	Y	-	4.5	$\Gamma_d^{op2}(t) + Cov$
			Y	-	Y	Y	-	4.5	$\Gamma_d^{op2}(t)$
			-	-	Y	Y	-	4	$\Gamma_d^{op3}(t)$
			Y	-	-	Y	-	3.5	$\Gamma_{UD}^{op2}(t)$
			-	-	-	Y	-	3	$\Gamma_{UD}^{op3}(t)$
			Y	-	Y	-	-	3.5	$\bar{\Gamma}_d^{op2}$
			-	-	Y	-	-	3	$\bar{\Gamma}_d^{op3}$
			Y	-	-	-	-	2.5	$\bar{\Gamma}_{UD}^{op2}$
			-	-	-	-	-	2	$\bar{\Gamma}_{UD}^{op3}$
Using EVL (Case 3)	Y	Y	-	-	Y	Y	-	4	$\alpha_{d,i}(t)$
	Y	-	-	-			$\alpha_i(o_i)$	3	$\alpha_{d,i}(o_i)$
	Y	-	-	-			-	3	$\bar{\alpha}_{d,i}$
	-	Y	-	-			-	3	$\alpha_{UD,i}(t)$
	-	-	-	-			$\alpha_i(o_i)$	2	$\alpha_{UD,i}(o_i)$
	-	-	-	-			-	2	$\bar{\alpha}_{UD,i}$

TAB. 2.4 – *Data Requirements and Index of All Cases at the Network-Level Traffic Density Estimation in This Study (Y: required, -: not required, Level: Data Requirement Level, γ_i: the link-level fishing rate)*

3. Investigating Trip Properties Considering Network Partitioning

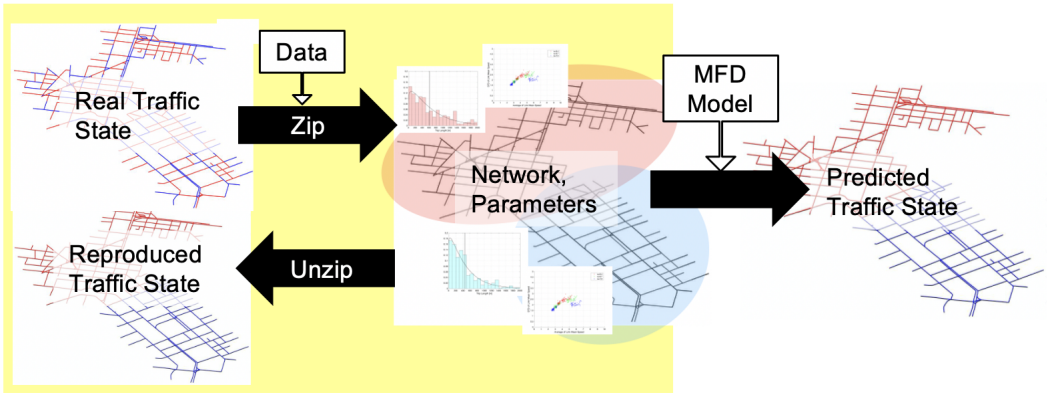

FIG. 3.1 – *Framework of assessing the proper design of network partitioning and parameter estimation for traffic prediction by using an MFD model*

3.1 Introduction

Aggregate traffic models have attracted considerable attention as a good compromise between the resolution of traffic dynamics and low computational cost for traffic prediction in a large network. In particular, the Macroscopic Fundamental Diagram (MFD) model has received much attention since Geroliminis & Daganzo (2008) observed the relationship between vehicle accumulation and mean speed in the network on the basis of real traffic data. In traffic prediction, many things, e.g., data availability, aggregation, the network, and parameter design may greatly affect prediction accuracy. The design of network partitioning and parameters are the core element of any MFD model. Therefore, the partitioned network and estimated parameters should represent the real traffic state with good accuracy. In this chapter, we first carry out network partitioning and estimate parameters based on data. Then, we reproduce the traffic state from the partitioned network and estimated parameters. In other words, we zip the real traffic state by data in the form of a partitioned network and estimated parameters and unzip them to reproduce the traffic state, as shown in Figure 3.1. By comparing a reproduced traffic state with a real traffic state, we discuss the proper designs of the network and parameters to be used for MFD models.

However, it can be challenging in practice to conduct both the proper network partitioning and parameter estimation since both are strongly related to data availability. To explain this relation in a comprehensible way, we compare reproducing the traffic state from the partitioned network and estimated parameters to drawing a realistic painting. The process of drawing a realistic painting is similar to reproducing the traffic state, like reproducing the real scenery according to the color variance in the palette, and deciding the resolution. As shown in Figure 3.2 (a), if you want to draw a high-quality painting, you need a palette with many colors and time to draw all the details, a task that may normally be difficult. On the contrary, the painting strays far from the real scenery if you draw with less color variance or less resolution. Now, we compare color variance to parameter design granularity and compare resolution to network partitioning granularity, as shown in Figure 3.2 (b). A huge amount of data is required to obtain high granularity for network partitioning and the parameters necessary to reproduce the traffic state with good accuracy. Therefore, it is essential to design network partitioning and parameters with a good balance according to data availability.

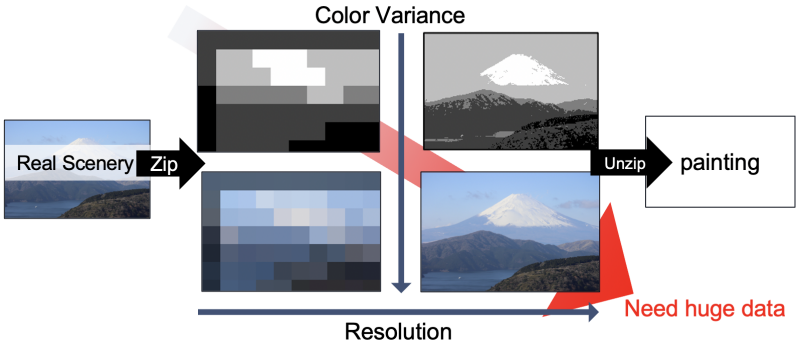

(a) Drawing a realistic painting

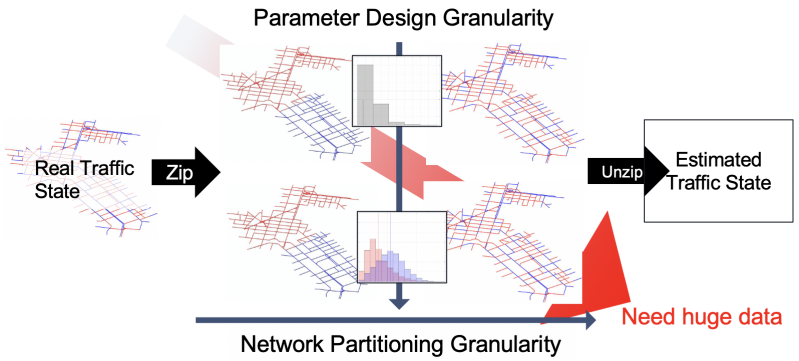

(b) Traffic state estimation

FIG. 3.2 – *Image of the balance between high reproductivity and the amount of data required.*

Key parameters of the MFD models are the speed-MFD, i.e., the relationship between average space-mean speed and vehicle accumulation of a region, and aggregated information on trip lengths, i.e., the average or distribution of total travel distance of each vehicle in a region calculated from vehicle trajectories. Since these parameters are the same for all links in a region, traffic state homogeneity is required in each region to improve the accuracy of the estimation. Partitioning a whole heterogeneous network into homogeneous regions is a well-known problem. Therefore, speed homogeneity inside the region, which is essential to calculate the speed-MFD with reasonable accuracy, increases along with partitioning granularity. However, detailed partitioning may make it harder to estimate trip lengths according to data availability. We define high "trip length tractability" when most of the required information, e.g., entry- and exit time and trip lengths of each vehicle at every time it moves to the different regions, is available. Typical trajectory data, e.g., probe data, often have missing data at certain locations and times and vehicle ID may change before completing a trip. Missing data make regional trip lengths non-tractable when the partitioning granularity is too high compared to the availability of trajectory data in the partitioned region. When the vehicle ID changes, tracking the complete trip length is impossible. It may lead to an estimated trip length that is much shorter than the real one and making it impossible to obtain the regional path sequence. Thus, both issues may lead to low trip length tractability and huge errors in the trip length estimation according to the partitioning granularity. Therefore, clear indications of the effect of partitioning on the parameters of the MFD model, i.e., speed-MFD and trip length, and proper data aggregation methods to estimate the average and distribution of trip length according to data availability, are necessary.

3.1.1 Literature Review

A network level aggregated traffic model, i.e., the idea of MFD, was initially introduced by Godfrey (1969). Daganzo (2007) proposed the theoretical foundation of MFD, which is a well-defined relation between the mean flow or the mean speed and the accumulation. The existence of MFD was verified first by Mahmassani (1984) and Mahmassani (1987) from microscopic simulation studies and by Geroliminis & Daganzo (2008) from real data from Yokohama, Japan. Since then, the literature has confirmed its existence all over the world, such as by Buisson & Ladier (2009) in Toulouse, France, Ji (2014) in Shenzhen, China, by Tsubota (2014) in Brisbane, Australia, and by Loder *et al.* (2017) in Zurich, Switzerland. Despite these findings relating to the existence of well-defined MFD, networks with temporal or spatial heterogeneous congestion may exhibit excessively scattered MFD. Buisson & Ladier (2009), Geroliminis & Sun (2011), Saberi *et al.* (2014), Daganzo *et al.* (2011) and Gayah & Daganzo (2011) showed the hysteresis phenomena that occur at the onset or offset of traffic congestion. Buisson & Ladier (2009), Geroliminis & Sun (2011), Mazloumian *et al.* (2010), Daganzo *et al.* (2011) and Knoop & Hoogendoorn (2013) presented a highly scattered MFD when the congestion of the network is spatially heterogeneous. To solve these problems, Ji & Geroliminis (2012) introduced partitioning based on the Ncut method which divides the network into smaller subregions with well-defined MFD.

Following Ji & Geroliminis (2012), various partitioning methods have been developed and assessed the homogeneity inside regions. For example, Saeedmanesh & Geroliminis (2016) proposed a method to search for a connected homogeneous area with the lowest density variance around each road, called 'snake', by starting from a single road and adding

one adjacent road based on similarity. Saedi *et al.* (2020) assessed homogeneity and travel time reliability by using this 'snake' partitioning. An *et al.* (2018) proposed a robust and efficient partitioning algorithm by using link connectivity and regional growth technology to manage partial data and incomplete information. Lopez *et al.* (2017a) and Lopez *et al.* (2017b) investigated the partitioning methods based on the 'snake' algorithm developed by Saeedmanesh & Geroliminis (2016) and classical methods such as DBSCAN and Growing Neural Gas from the data-mining field to construct 3D speed clusters of road links. Lin & Xu (2020) proposed a method to overcome the shortcomings of the Kmeans algorithm based on Canopy-Kmeans clustering, which can manage the difficulty of estimating the K value. For cases for which stationary sensors have a strong bias and where existing partitioning approaches are not applicable, Ambühl *et al.* (2019) suggest a Monte-Carlo-like partitioning algorithm which is independent of the sensor's positions. Based on studies on network partitioning, we can obtain a fairly accurate MFD in each region.

On the other hand, most MFD models require that trip length distribution is characterized in each region in addition to the MFD. There are two well-known modeling frameworks: the accumulation-based model and the trip-based model. In the accumulation-based model, the outflow function is defined as the ratio between the MFD and the average trip length whereas, in the trip-based model, MFD dynamics is centered on the individual trip length. Lamotte *et al.* (2018) presented a simple method to implement trip length distribution in this framework.

MFD models are based on the premise that trip length reproductivity, i.e., the index of how the trip lengths reproduced from the parameter estimated are close to the real trip lengths, is high enough to represent the real traffic state. However, Batista *et al.* (2019), who analyzed the impact of trip length setting on the accuracy of MFD model estimation based on the real network topology, mentioned that estimating trip length properly for the applications of MFD models is generally difficult with multi-regions. Also, Paipuri *et al.* (2020) confirmed this by using partial trips obtained from probe data. Therefore, it is important to obtain clear indications of trip length reproductivity with different levels of aggregation according to partitioning design and data availability, a dimension that has not been studied before. Thus, it is necessary to perform an experimental investigation into the impact of partitioning and data availability on trip length reproductivity using real data and clarifying the proper aggregation methods needed to estimate trip length.

3.1.2 Research Objectives

The purpose of this study is to: 1) analyze the impact of partitioning on the estimation of two crucial parameters for MFD models, i.e., Speed-MFD and trip lengths; and 2) assess the accuracy of trip length estimation as a function of data availability, and clarify the proper aggregation granularity of the trajectory data. These investigations are essential to improve the predictability of the MFD model. However, as yet such an experimental study with real data has not been performed since it requires good quality trip trajectory data. However, the drone data from the pNEUMA experiment in Athens, which have the complete trip trajectories of all the vehicles in the area, makes it possible here to achieve the abovementioned objectives.

In Section 3.2, the drone data of Athens are explained in detail. In Section 3.3, we introduce a simple static partitioning method that can consider different weights on speed ho-

mogeneity and analyze the balancing tendency between speed homogeneity and trip length tractability according to the partitioning weight. The effect of partitioning on speed homogeneity and MFD shape is confirmed compared to the results of previous studies in Section 3.4. In Section 3.5, the interaction between trip length tractability and trip length value is analyzed, and the adequate methods for estimating the average trip length and trip length distribution according to data availability and aggregation granularity are investigated. Then, all the conclusions and contributions are summarized in Section 3.6. The insight gained from this study will be an important indicator of the improvement of traffic prediction accuracy using MFD models.

3.2 Drone Data in Athens

The pNEUMA experiment conducted by Barmpounakis & Geroliminis (2020) used 10 drones to capture urban traffic in the congested area of a $1.3km^2$ area with more than 100 km-lanes in Athens. Drones took aerial videos and vehicle trajectories were detected every 0.04 s of the time-frequency. Thus, drone data can provide all trajectories during the flight time of drones in the area. These data make it possible to investigate parameter calculation according to aggregation scales regardless of data penetration and availability in this study.

We use the morning peak data (8:00 - 10:30) of one working day from drone data. Because drone batteries must be changed every 30 minutes, these data have 4 break times of 10 to 15 minutes over the full 2.5 hours.

The original data include several modes of vehicles, i.e., cars, taxis, buses, medium vehicles, heavy vehicles, and motorcycles. Figure 3.3 (a) shows the relation between the travel time and the travel distance of each vehicle mode. According to this figure, the motorcycles have a shorter travel time than the other modes when they have similar travel distances because motorcycles are less affected by traffic queues. Also, motorcycles can pass through narrow roads that drones cannot detect. Thus, these trajectories sometimes split and have relatively short travel times and distances. Figure 3.3 (a) shows that some vehicles have quite a long travel time for short travel distances. Since buses stop many times and have dedicated lanes in several roads, they behave quite differently from the other vehicles. Those vehicle modes can lead to errors when calculating the aggregated parameters. Therefore, we remove buses and motorcycles from our data set.

Furthermore, some vehicles that park several times have long travel times with short travel distances in these data. We disregard parking when the vehicle stops longer than 5 minutes, based on signal red light time in Athens and separate one trajectory as before parking and after parking.

After this data cleaning phase, the relation between travel time and travel distance of each trip is changed to red plots from blue plots in Figure 3.3 (b). Cleaned drone data are used for investigating speed homogeneity and trip length tractability in this study.

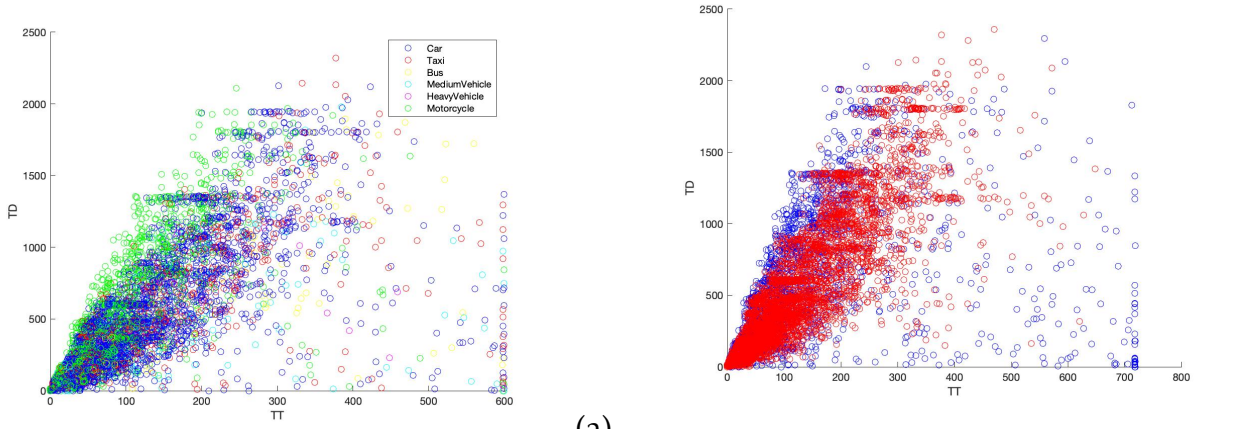

(a) Vehicle Modes

(b) The original data (Blue) and the data of this study (Red))

FIG. 3.3 – *Travel Time(TT) and Travel Distance (TD) of each mode for the first 15 minutes of data observed period.*

3.3 Partitioning to Investigate the Effect of Speed Homogeneity and Trip Length Tractability

Accuracy of speed MFD and trip length estimations have a huge impact on traffic prediction by MFD models. Speed homogeneity inside the area is known as an important factor to calculate accurate speed-MFD. Ji & Geroliminis (2012) asserted that partitioning the area into multiple regions is an effective solution to achieve homogeneity. However, complex partitioning may make trip length calculation more difficult since it requires detailed trajectory data, difficult to obtain using general data sources with low penetration, e.g., probe vehicles, to provide enough data in each region. For example, we need at least entry and exit timing and location to calculate trip lengths for each region. Therefore, if a vehicle passes through many regions, trip length calculation requires as many entry and exit conditions as the lengths of the regional passage sequences of the vehicle. Probe data usually have low penetration and missing data. Since the required information is not available for all no-probe vehicles and for probe vehicles at several times and locations, they may lead to low trip length tractability in low density networks with complex partitioning in which the vehicles may pass through many regions. Thus, high trip length tractability is necessary to calculate accurate trip length. Therefore, we need to investigate the best balance for partitioning between speed homogeneity and trip length tractability.

In this section, we introduce a simple static partitioning method which can consider different weights on speed homogeneity against region density. Then, two indicators, e.g., variance of link mean speed in the region which represents speed homogeneity and the length of regional path sequence which represents trip length tractability, are compared along with the partitioning weight to investigate the balance of speed homogeneity and trip length tractability.

	$w = \infty$	$w = 6.7$	$w = 1$
Link Amount	(272, 184)	(288, 168)	(320, 136)
Total Link Length [m]	(18780, 11030)	(17870, 11930)	(19040, 10770)

TAB. 3.1 – *Number of links and total link length of pockets according to the weight on speed of the network partitioning (Congested, Less-congested Pocket).*

3.3.1 Simple static partitioning into two states of regions

From the beginning, we apply simple static partitioning which shows two types of traffic states according to link space-mean speed and a road network topology. We call the link groups of these traffic states "congested pockets" and "less-congested pockets". In this partitioning, links belonging to the same pocket do not have to be connected to each other. In other words, a pocket does not necessarily form a connected component.

The space-mean speed v_l of a link $l \in L$ whose length is l_l is calculated by total travel time ttt_l and the total travel distance ttd_l of each link during a time period Δt according to Edie's definition (Edie (1963)): $v_l = q_l/k_l = (ttd_l/(\Delta t * l_l))/(ttt_l/(\Delta t * l_l))$ where q_l and k_l are the flow and density of the link. We calculate the link space mean speed every $1 minute$ and then average the whole time period to estimate $\bar{v_l}$.

To consider a road network topology, we calculate the distance d_{lm} between neighboring link centers l and m. At this time, the center location of each link is calculated by the middle of the longitude and latitude of link edge nodes. Then, the distance of two links is calculated by considering the large circle arcs on the surface of a sphere.

By using the space-mean speed and the distance between links, the element of similarity matrix $S = [s_{lm}]_{|L|\times|L|}$ of each link pair $(l, m) \in L$ is calculated as $s_{lm} = \sqrt{w * (\bar{v_l} - \bar{v_m})^2 + d_{lm}^2}$ when w is a weight on the space-mean speed versus the distance. We note that weighting this distance leads to the high compactness of the region. The dimension of the similarity matrix is reduced by Multiple Dimensional Scaling (MDS), c.f., a well-known method for producing a representation in a small dimension using data with many variables proposed by Seber (1984), to create a similarity vector. Finally, we apply partitioning into two pockets by using the K-mean algorithm (Lloyd (1982)) with the similarity vector. It is noteworthy that the computational cost of this partitioning is quite low, even for dynamic calculation.

Figure 3.4 and Table 3.1 show the location of pockets and network features of three partitioning examples according to the weight on speed. In Figure 3.4 (a), each pocket is quite scattered when we apply partitioning without considering the network topology. In contrast, Figure 3.4 (c) shows that the pockets are decided ultimately regardless of traffic state when the weight on speed is insufficient. According to Table 3.1, the number of links and total link length inside each pocket do not have marked features corresponding to the weight. Therefore, our partitioning leads to lower network compactness and higher speed homogeneity inside the region when we place a heavier weight on speed, and vice versa.

3.3.2 The Balance between Speed Homogeneity and Trip Length Tractability

We perform a simple analysis on the effect of partitioning on speed homogeneity and trip length tractability. The average and standard deviation (STD) of mean speed over all the

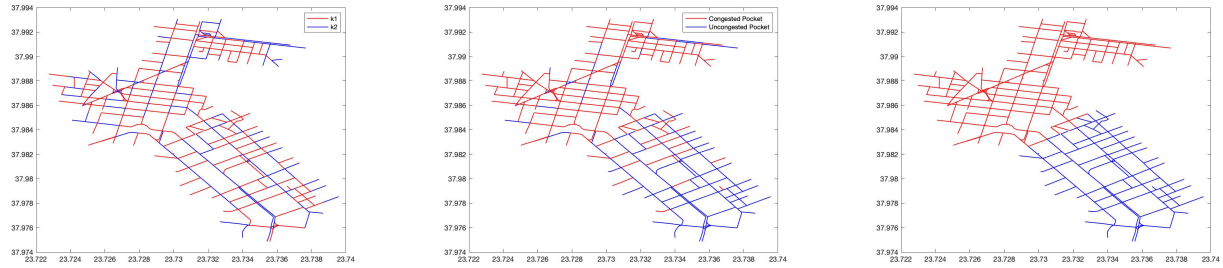

(a) $w = \infty$ (b) $w = 6.7$ (c) $w = 1$

FIG. 3.4 – *Congested pocket map according to the weight on speed of the network partitioning (Red: congested pocket, Blue: less-congested pocket)*

links in each region provide indicators of speed homogeneity. The mean speed of each link is calculated using the same method as the partitioning, which is a temporal average over a whole time period of mean speed calculated every 1 minute. Trip length tractability is represented by regional path sequence complexity, such as average, STD, and percentiles of the pockets switching numbers of vehicles (PSN). PSN is calculated for each vehicle by counting the entry number into another pocket in a whole trajectory. A high value of PSN means low trip length tractability because we require the entry/exit time and location information at every pocket. These indicators are compared along with the partitioning weight on speed w.

Figure 3.5 shows the average (a) and STD (b) of the link mean speed of each pocket. The difference of the average value between the two pockets is small when the weight is less than 6.4. However, its size quickly increases, and it becomes very large and almost stable after the weight reaches 7.0. Figure 3.5 (b) shows that the STD of speed over links is quite considerable until the weight is around 6.6 and drops quickly. After the weight reaches 7.0, STD also becomes low and stable. In the less-congested pocket, the STD increases from 2.0 to 2.2 until the weight reaches 6.6. Thus, an insufficient increase of the weight on speed may lead to further heterogeneity inside a pocket. The STD decreases by around 40% in the congested pocket and around 30% in the less-congested pocket when $w = 7.0$ compared to when $w \leq 6.0$. When $w = 6.7$, the STD in the congested pocket decreases by around 25%, meanwhile that in the less-congested pocket is the same as when $w = 6.0$. Therefore, a value higher than $w = 7.0$ is the first best weight, and $w = 6.7$ is the minimum limit for considering homogeneity.

Regarding trip length tractability, Figure 3.6 shows the average (a) and the percentiles (b) of PSN according to the weight on speed. From Figure 3.6 (a), the number is quite low such that most vehicles do not change pocket when the weight is less than 6.4. However, the average value and STD quickly become larger until the weight reaches 6.9. When the weight is larger than 6.9, the average value of PSN is around 3, and the STD is quite large and stable. Furthermore, Figure 3.6 (b) shows more than 50% of vehicles pass one region until the weight reaches 6.5. However, PSN increases and more than 70% of vehicles pass through more than two pockets, and 50% of vehicles pass through more than three pockets when the weight exceeds 6.8. Thus, when considering tractability, the first best weight is less than 6.5, and the maximum limit of weight is 6.8.

Thus, we clarify that the detailed partitioning, which significantly improves speed ho-

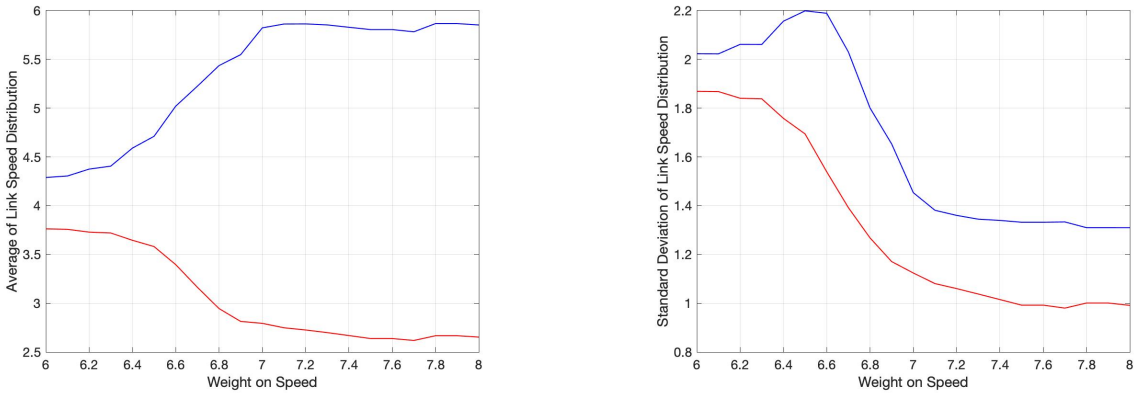

(a) Average of Link Mean Speed (b) STD of Link Mean Speed

FIG. 3.5 – *The homogeneity of link mean speed according to the weight on speed of the network partitioning (Red: congested pocket, Blue: less-congested pocket).*

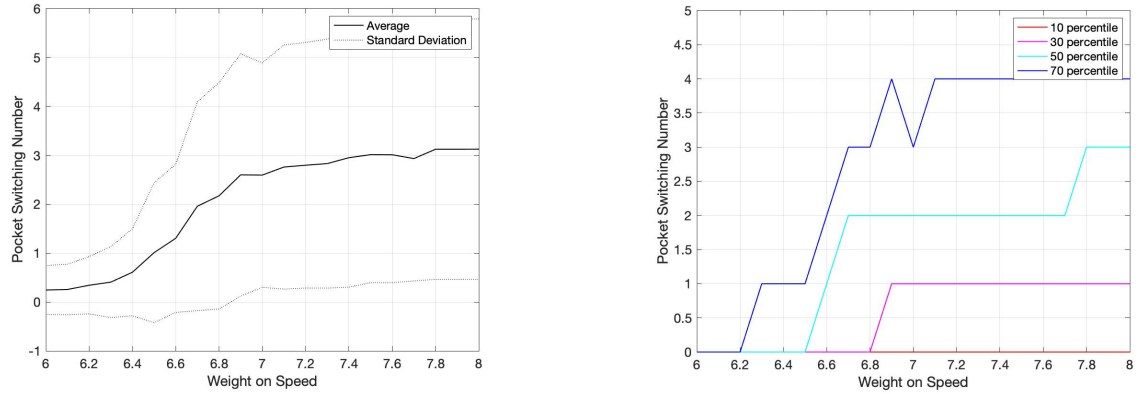

(a) Average and STD of PSN (b) Percentiles of PSN

FIG. 3.6 – *The tractability of trajectories according to the weight on speed.*

mogeneity, leads to a drop in trip length tractability. Based on the above results, we perform further analyses on speed homogeneity and trip length tractability in the following sections by using three values of weight, i.e., 1) 6.4, 2) 6.7 and 3) 7.0 which represent the cases of: 1) placing priority on trip length tractability, 2) considering the balance of both, and 3) placing priority on speed homogeneity.

3.4 The Effect of Partitioning on Speed Homogeneity and Speed-MFD shape

According to many previous studies such as that of Buisson & Ladier (2009), spatial heterogeneous congestion leads to highly scattered MFD. Correspondingly, many studies have shown that partitioning is an effective solution for obtaining homogeneity and producing a well-defined MFD.

In this section, we confirm the effect of partitioning on speed homogeneity and speed-MFD shape. In particular, we compare the average and STD of link mean speed and the scatter of speed-MFD with and without partitioning. We note that the noise produced from sampling the number of vehicles, which is usually included when we use low penetration data resources such as probe data, can be omitted when using drone data to supply all the trajectories of vehicles. Additionally, the effect of partitioning weight w is discussed using several indicators inspired by previous studies.

3.4.1 State of the Art

From the beginning, we see the behaviors of speed dynamics, e.g., average link speed dynamics and speed-MFD, and speed homogeneity, e.g., STD of link speed, of the Athens network in the case without partitioning. Also, to confirm the traffic state, production-MFD, i.e., the relation between accumulation [veh] and production [veh*m/s], is calculated. Link speed is calculated with the same method as in Section 3.1. To calculate the Speed-MFD, the mean speed is calculated as TTD/TTT when TTD and TTT are the total travel distance and total travel time of all the links, and the accumulation is calculated as $TTT/\Delta t$ when the time period Δt is 1 minute. Production is calculated as $TTD/\Delta t$.

Figure 3.7 (a) shows the average dynamics of space mean speed over the links. For around $140 minutes$ of the data period, we did not obtain data during four time periods due to the charging life of the drones' batteries. Except for these durations, the mean speed becomes slower, falling from around $4-5$ m/s to $3-3.5$ m/s.

The Speed MFD is shown in Figure 3.7 (b). The shape of the speed MFD is similar to that in many previous studies: the mean speed decreases linearly versus the increase in accumulation and the plots are not very scattered in this network which has a maximum speed gap around 1.5 m/s at the same accumulation. However, according to the speed-MFD in Figure 3.7 (b) and the production-MFD in Figure 3.7 (c), we find that the trend of the MFD shape is stable and the difference of the congested state is not clear without partitioning.

Figure 3.7 (d) shows the STD of the link mean speed. It characterizes speed heterogeneity over the network for the accumulation values. The speed heterogeneity is already low, 2.1 to 2.7 of STD in this network, and it gets lower as the accumulation gets higher.

Saeedmanesh & Geroliminis (2017) found a fundamental relationship (similar to Production-MFD) between the spatial heterogeneity of congestion, e.g., STD of the traffic state indicator that is the density in the literature, and the average congestion level, e.g., the average of the indicator from a large number of clustering results. They mentioned that we observe only the top point of the functional form when clustering is of low quality. In Figure 3.7 (e), we observe only the partial shape of the top point of the relationship from the average and STD of the mean speed without partitioning. It also shows that the difference in the traffic state is not clear without partitioning.

3.4.2 Comparison of dynamic speed behavior and homogeneity according to the partitioning weight

To analyze the effect of partitioning, the same indicators as the previous subsection, which represent dynamic speed behavior and homogeneity at each pocket, are compared with the state of the art in Figure 3.7 and the cases of different partitioning weights on speed, e.g., $w = 6.4$, 6.7, and 7.0.

From the beginning, we can see the clear difference of the average of the link mean speed between the pockets in Figure 3.8 (a). When the weight is 7.0, the difference in speed between pockets is quite significant, about 3 m/s , compared to the difference when the weight is 6.4, which is around 1 m/s.

Figure 3.8 (b) shows the Speed-MFD where the round plots and the cross plots represent the values in the congested and less-congested pockets. Each pocket has a quite different accumulation range from 300 veh to 500 veh in the less-congested pocket and from 450 veh to 700 veh in the congested pocket. In the case of $w = 6.4$, there is no large gap in mean speed around 3.5 m/s to 4.0 m/s between two pockets at the same accumulation $n = 500$ veh. On the other hand, when $w = 7.0$, the mean speeds at the same accumulation around 450 veh in two pockets are clearly different, as the value is around 3.0 m/s in the congested pocket and more than 4.0 m/s in the less-congested pocket. In the case of $w = 6.7$, the difference between pockets is naturally less than $w = 7.0$. However, the result is quite close to the case of $w = 7.0$. Also, the slopes of the plots between congested and less-congested pockets are clearly different when w is higher. This difference is clarified in Figure 3.8 (c). In this figure, two different traffic states in the pockets are obvious when $w = 7.0$: traffic state between free-flow and congested in the less-congested pocket, in which we can observe the curve with the critical accumulation around 400 veh, and the saturated state in the congested pocket which has almost the same production as when the accumulation ranges from 450 veh to 700 veh.

Speed heterogeneity is lower with partitioning, as shown in Figure 3.8 (d), than without partitioning, as shown in Figure 3.7. In particular, when we place a heavier weight on speed such as $w = 7.0$, the STD is reduced by more than 0.5 when the accumulation is high compared to the case without partitioning. Furthermore, the linear decreasing trend in the less-congested pocket and the stable trend in the congested pocket are evident when the weight is heavy. For example, when $w = 7.0$, the STD of the link mean speed decreases from around 2.5 to 1.7 when the accumulation increases from around 300 veh to 500 veh, and it becomes stable around 1.5 when the accumulation is more than 500 veh. This result shows that when the total accumulation in a whole region is low, free-flow links leads to traffic state heterogeneity since the mean speed at the free-flow links can change depending

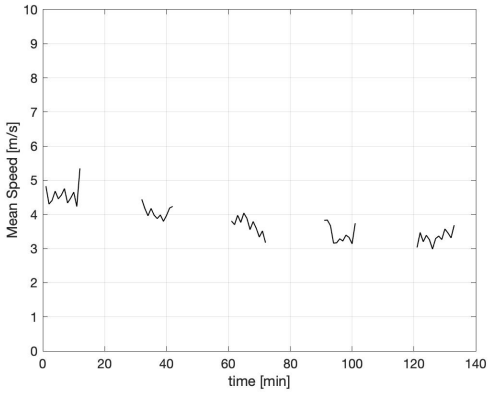

(a) Average Link Mean Speed

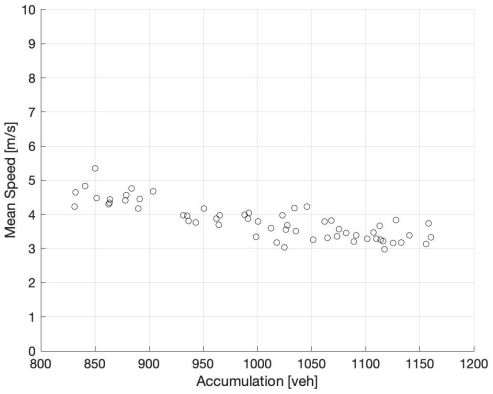

(b) Speed MFD

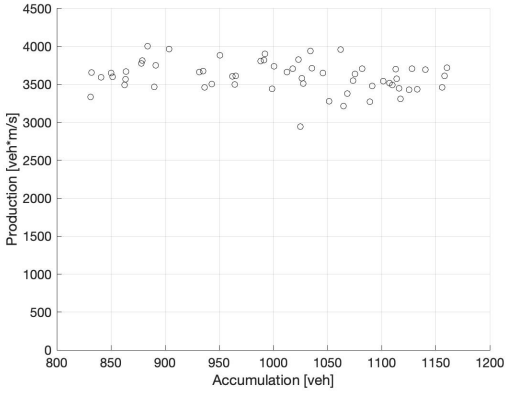

(c) Production MFD

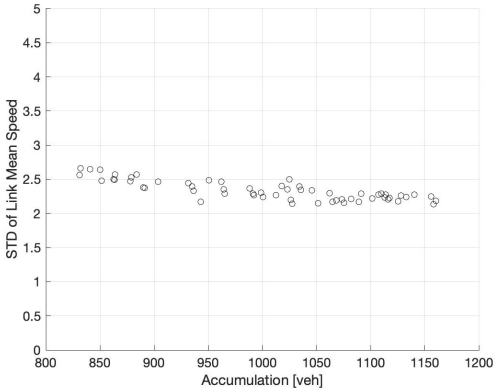

(d) STD of Link Mean Speed and Accumulation

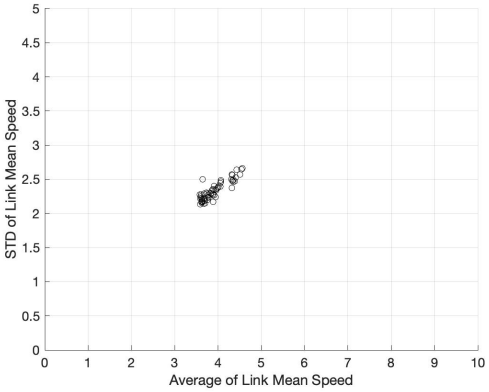

(e) Average and STD of Link Mean Speed

FIG. 3.7 – *The homogeneity of link mean speed and the shape of speed-MFD in the state of the art.*

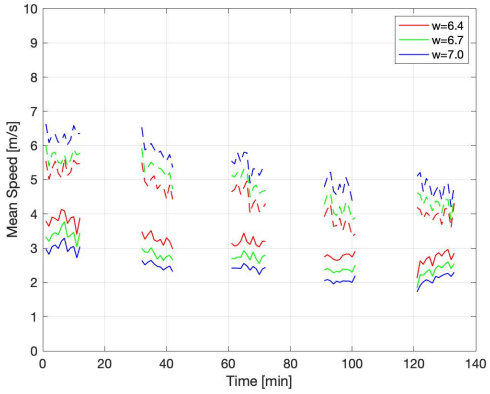

(a) Average Link Mean Speed

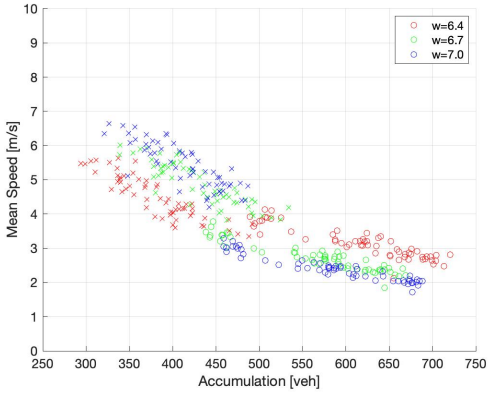

(b) Speed MFD

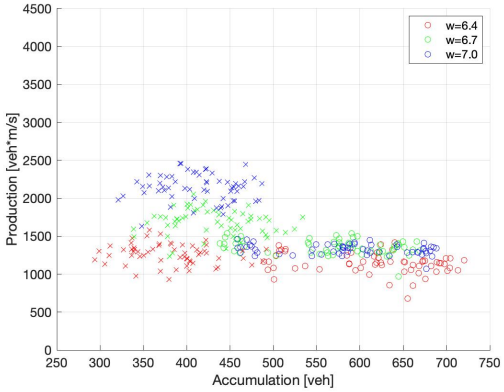

(c) Production MFD

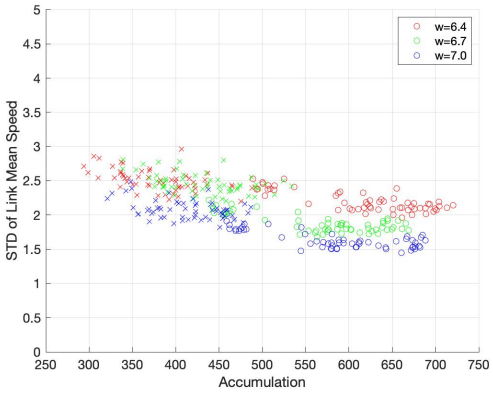

(d) STD of Link Mean Speed and Accumulation

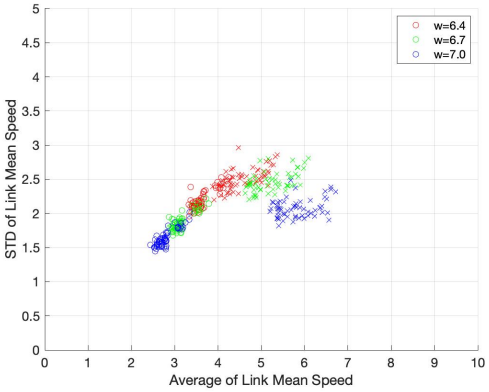

(e) Average and STD of Link Mean Speed

FIG. 3.8 – *The homogeneity of link mean speed by partitioning (w is the value of weight on the speed homogeneity. The round plots show the result of the congested pocket and the cross plot shows the result of the less-congested pocket in (b), (c), (d) and (e).)*

on individual vehicle behaviors. On the contrary, when the region reaches saturated state, the STD of the link mean speed remains stable whatever the accumulation because the mean speed of the congested links is not much different compared to the free-flow links. Thus, we can detect the area with saturated congestion by partitioning. The heterogeneity of congestion in the case of $w = 6.7$ is similar to $w = 6.4$ in the less-congested pocket. However, it is close to that of $w = 7.0$ in the congested pocket. As a result, we can observe that partitioning has a significant effect, especially on the homogeneity in the congested area.

In Figure 3.8 (e), we can see the MFD-like relationship between the average and the STD of the link mean speed, as mentioned by Saeedmanesh & Geroliminis (2017) regarding density. In the congested pocket, the STD increases along with the average value. However, in the uncongested pocket, the plot is scattered over the average value at the same STD. This shows when we place a considerable weight on speed for partitioning, the heterogeneity of the link mean speed is low and relatively stable even between the free-flow links, which usually have an extensive range of speeds.

Therefore, we confirm the positive effect of partitioning on regional homogeneity, especially when the heavier weight is placed on speed more than compactness. Also, we verify the relationship between the average and the STD of the mean speed experimentally.

3.4.3 Comparison of speed homogeneity by using previous indicators from the literature

Additionally, we calculate indicators that represent the homogeneity and compactness of partitioning in the previous literature. Normalized Total Variance TVn, which is defined as the ratio between total variance of a partitioned and non-partitioned network, is utilized to evaluate the performance of partitioning by many studies on the effect of partitioning, e.g., Saeedmanesh & Geroliminis (2016), Lopez *et al.* (2017a) and Saedi *et al.* (2020). Normalized Total Variance for the link means speed in 2 pockets, the congested pocket (c) and the less-congested pocket (u), is calculated as shown below:

$$TVn = \frac{N_c * var(V_c) + N_u * var(V_u)}{N * var(V)} \tag{3.1}$$

where N_c and N_u denote the number of links in each pocket, and $var(V_c)$ and $var(V_u)$ denote the variance of speed of all links in each pocket while N and $var(V)$ are the total link number and speed variance in a whole region. Note that, when this value is smaller, the improvement gained for homogeneity versus compactness is bigger. Normalized Total Variance is 0.744 when partitioning into two clusters in the Shenzen network according to Saeedmanesh & Geroliminis (2016) (Table 5) and around 0.86 to 0.98 in the Chicago metropolitan network according to Saedi *et al.* (2020) (Figure 5 (b)). As shown in Figure 3.9 (a), Normalized Total Variance is quite high, close to 1 when the weight on speed is insufficient, as with $w = 6.4$. When $w = 6.7$, this value is around 0.9, which is similar to the case of Saedi *et al.* (2020). The biggest improvement is $TVn \approx 0.75$ when we put the heavy weight on speed such as $w = 7.0$.

Another indicator is 'NcutSilhouette' (NS) which is utilized to evaluate the homogeneity and estimate the optimal number of clusters by Ji & Geroliminis (2012) and An *et al.* (2018).

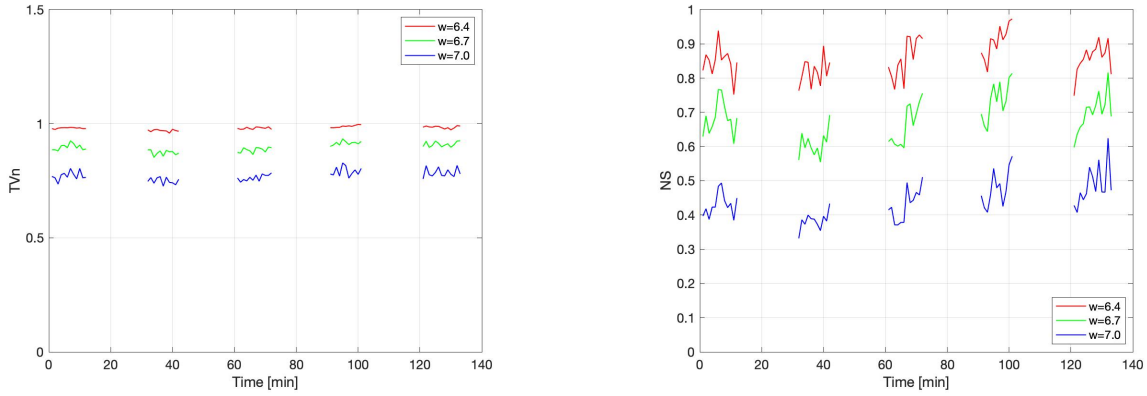

(a) Normalized Total Variance (TVn) (b) NS

FIG. 3.9 – *Speed homogeneity according to the weight on speed of the network partitioning based on the homogeneity indicators of previous studies.*

NS for the link mean speed in 2 pockets is calculated as below:

$$NS = \frac{\sum_{r\in[c,u]} NS(V_r)}{2}; NS(V_r) = \frac{2Var(V_r)}{Var(V_c) + Var(V_u) + (\bar{V}_c - \bar{V}_u)^2} \tag{3.2}$$

where $\bar{V}_c$ and $\bar{V}_u$ denote the average of link mean speed in each pocket. The NS value obtained is 0.8117 by N-cut partitioning into two clusters in the San Francisco network according to Ji & Geroliminis (2012) (Table 1). As shown in Figure 3.9 (b), NS is around 0.75 to 0.95 when $w = 6.4$. This value drops significantly when we place a heavier weight on speed. When $w = 7.0$, NS is quite low, e.g., from around 0.4 to 0.6. Even when $w = 6.7$, this value is small enough, e.g., around 0.6 to 0.8, compared to the two clusters in the previous studies.

As a result, from the point of view of speed homogeneity, the best case is obviously when $w = 7.0$. However, in comparison with previous studies, the link mean speed in the pockets is also homogeneous enough when $w = 6.7$.

3.5 The Impact of Data Availability and Aggregation Granularity on Trip Length Estimation

Trip length is a crucial parameter in MFD models besides mean speed, and the quality of trip length estimation significantly affects the accuracy of traffic prediction, according to Batista *et al.* (2019). However, as shown in the results of Section 3.3.2, if the sub-networks are not compact after partitioning, it can harm trip length tractability, as each single loop trips multiple times between regions. In such a situation, data availability and aggregation methods may significantly impact trip length estimation. Therefore, it is essential to assess the accuracy of trip length estimation based on data availability and specify the proper method to aggregate trajectory data. This aspect has not received much attention from the previous literature. This section analyzes the correlation between trip length and path sequence according to partitioning weight w, firstly to verify that the trip length tractability can have a

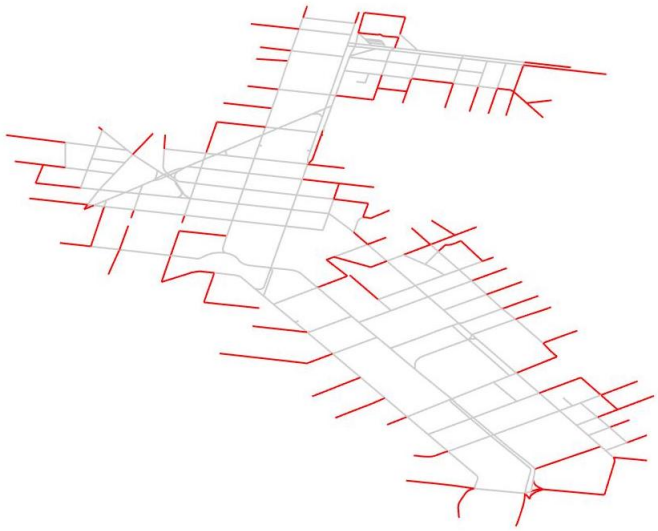

FIG. 3.10 – *Edge links of the network (black, all links, red: edge links).*

considerable impact on trip length estimation. We then assess the impact of data availability and aggregation granularity on the average trip length estimation, which is necessary for the accumulation-based MFD model. Finally, we analyze the accuracy of the approaches for estimating trip length distribution according to data availability and aggregation granularity by comparing them with the trip length distribution directly derived from trip lengths of all the vehicles in the data. Also, we clarify the proper approach to estimate trip length distribution, which is an essential parameter for the trip-based model.

3.5.1 Trajectory Chosen for Trip Length Calculation

To assess trip length tractability, we use only the trajectories for which the trip start/end timing inside the region or the entry/exit timing into/from the region is available. The vehicles already inside the region during the first or last 5 seconds of the data duration are removed because these vehicles may have a longer trip length than the observations. Exceptionally, if the vehicles are at the edge links shown as red lines in Figure 3.10 at the first or last seconds of the duration and they pass through other links from the edge links, we regard them as vehicles which only enter/exit at the beginning/ending of the duration and we use their trip length.

In Figure 3.11, the black plots show the travel time and trip length of all the vehicles, and the red plots show those of the vehicles for which we have trajectories of a whole trip. The black plots that have long travel times represent vehicles inside the region at the beginning or the ending of the data duration, and those with fairly short travel times represent vehicles that pass through only the edge links. Therefore, we use the vehicles with start/enter and end/exit trip times, as shown in the red plot for the following trip length calculation.

3.5.2 The Effect of Partitioning on Trip Length Tractability

We found that partitioning weighted on speed more than on compactness was effective to obtain speed homogeneity in Section 3.4. However, this partitioning may make trip length

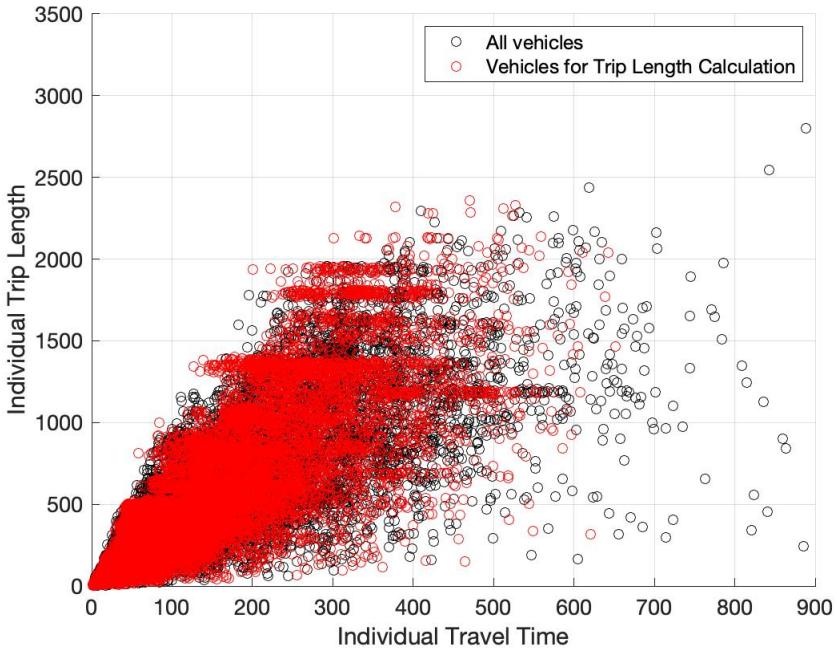

FIG. 3.11 – *Travel Time(TT) and Travel Distance (TD) of the vehicles used for trip length calculation*

calculation more difficult because of low trip length tractability, since more complex partitioning requires more detailed trajectory data which is hard to obtain from a traditional data resource, such as probe data. Therefore, to clarify the interaction between trip length tractability and trip length, we analyze the correlation between PSN, i.e., the percentiles of the pockets switching numbers of vehicles, and the trip length of each vehicle, and the correlation between the trip length of each pocket according to the partitioning weight w.

To calculate the real individual trip length of each pocket and path sequence, we utilize the cases of $w = 7.0$ and $w = 6.4$, which have less and better connectivity between the links at each pocket. The real path sequence is calculated by the location of the individual vehicle trajectory. The real trip length is calculated as the sum of trip lengths over a whole individual trajectory inside each pocket according to the path sequence.

The relation between PSN and total trip length is shown in Figure 3.12 (a). We can see the positive correlation between the trip length and PSN, where the R-square value is 0.761. On the other hand, when the connectivity of links inside pockets is high, such as $w = 6.4$, this correlation gets weaker, as shown in Figure 3.12 (c). In this case the R-square value is 0.414. Also, the vertical axis shows trip length tractability, and it is much lower compared to the case of $w = 7.0$. Thus, when we put a heavier weight on speed regardless of network compactness, trip length tractability impacts trip length calculation more because the path sequence gets more complex.

Figure 3.12 (b)(d) shows the correlation between the trip length of each pocket. In the case of $w = 7.0$, as shown in Figure 3.12 (b), we can recognize the positive correlation between the trip lengths of each pocket while it is not found in the case of $w = 6.4$, as shown in Figure 3.12 (d). Also, the R-square value is relatively low when $w = 6.4$, i.e. 0.058 compared to when $w = 7.0$, for which it is 0.411. This shows that the trip lengths of each pocket have a non-negligible impact on each other, especially when we place a heavy weight on speed

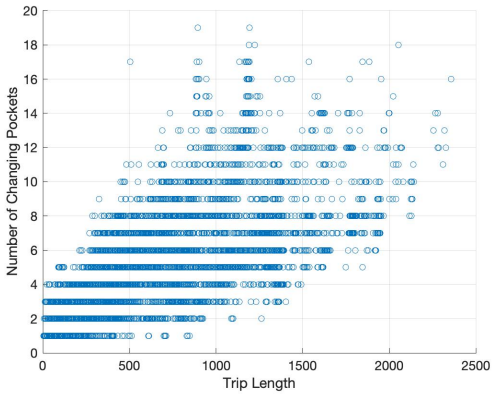

(a) Individual PSN and Trip Length ($w = 7.0$)

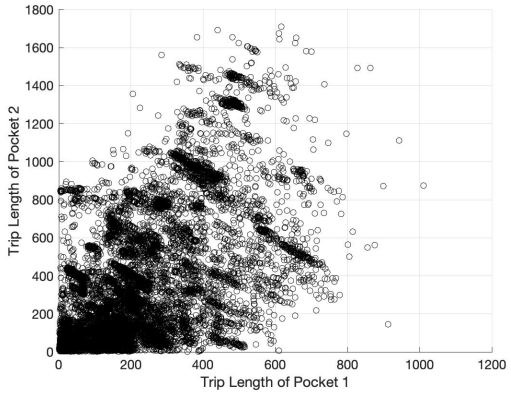

(b) Individual rip length of congested pocket and less-congested pocket ($w = 7.0$)

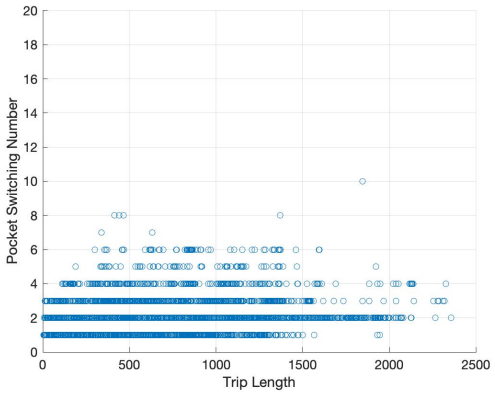

(c) Individual PSN and trip length ($w = 6.4$)

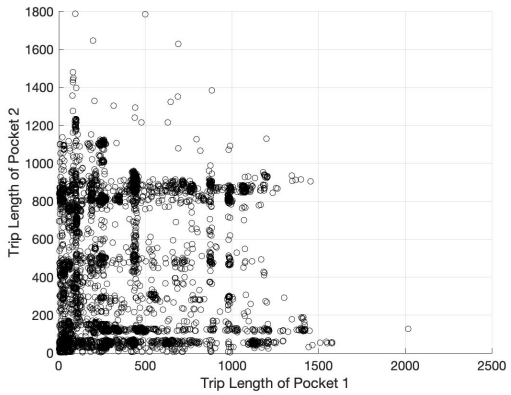

(d) Individual trip length of congested pocket and less-congested pocket ($w = 6.4$)

FIG. 3.12 – *Correlation between trip length and PSN according to the weight on speed w of the network partitioning ((a) and (b):$w = 7.0$, (c) and (d):$w = 6.4$)*

homogeneity.

Consequently, we confirm that trip length tractability may have a huge impact on trip length calculation, especially when partitioning weights speed more than connectivity. At the same time, the trip lengths in each region, which are harder to calculate when trip length tractability is low, interact with each other. Therefore, the availability of path sequence information or correlation between trip lengths in regions must be an essential key for trip length calculation.

3.5.3 Average Trip Length Calculation according to Data Availability and Aggregation Granularity

When trip length tractability is lower, we need more detailed information on each trajectory or the correlation between the trip lengths of pockets according to section 3.5.2. In addition, using virtual trips in the Lyon network Batista *et al.* (2019) showed the average trip length of a whole network without considering that each vehicle's regional path is not representative of all the possible average trip lengths estimated according to the path sequence. Thus, they mentioned that it is essential when estimating trip length distribution to consider all the paths or at least the previous and the next regions traveled by the trips. However, typical data resources such as probe vehicles often lead to several issues for providing detailed information: 1) data missing in certain time periods at certain locations, 2) change of vehicle ID during a trip. The first issue can make it difficult to calculate the trip length of each pocket because of the lack of necessary information when the pocket covers a small area. The second issue can lead to shorter trip lengths and make it difficult to obtain the path sequence information. For example, the returning vehicles in a region that may be identified as separate in the trip length estimation. Therefore, it is important to investigate the effect of data availability and data aggregation granularity according to trip length tractability on the trip length estimation. Here, we assess the reproducibility of trip length by comparing average trip length in a whole network to the sum of the regional trip length in each pocket calculated according to the different data availabilities and aggregation granularities. In particular, the average trip length is an important parameter in the accumulation-based model.

Four data aggregation cases for regional average trip length (TL_r) calculation according to the availability of full trajectory and path sequence information are prepared. We define that TL denotes average complete trip length in a whole network. The four cases are explained below:

Case 1-1 We only have the partial trajectories of individual i in each pocket r. This is the case when the full individual trajectories are not available, e.g., changing vehicle ID. The trip length of the partial trajectory is denoted $l_{i,r}$, thus TL_r can be calculated by the average of these partial trajectories $< l_{i,r} >$.

Case 1-2 We have some full individual trajectories in each pocket, which are the sum of individual partial trajectories in the same pocket. The trip length of the full trajectory in each pocket is denoted $L_{i,r}$, thus TL_r can be calculated by the average of these full individual trajectories $< L_{i,r} >$.

Case 1-3 We have partial individual trajectories in each pocket and the average path sequence of some vehicles. The average path sequence is represented by the average

	Case1-1		Case1-2		Case1-3		Case1-4	
TL_r definition	$< l_{i,r} >$		$< L_{i,r} >$		$< n_{i,r} > * < l_{i,r} >$		$< L_{i,r}/L_i > *TL$	
	Dif	Rel	Dif	Rel	Dif	Rel	Dif	Rel
$w = 6.4$	101	20	204	40	-0.04	0.007	-0.14	0.03
$w = 6.7$	-174	34	112	22	-0.04	0.007	-0.14	0.03
$w = 7.0$	-231	45	50	10	-0.04	0.007	-0.14	0.03

TAB. 3.2 – *Difference (Dif) [m] and Relative Difference (Rel) [%] of average trip length calculation (Case 1) ($< . >$ denotes the average value)*

number of vehicles that pass through the pocket in certain full trajectories $< n_{i,r} >$. TL_r can be calculated by $< n_{i,r} > * < l_{i,r} >$. We note that PSN of vehicle $i = \sum_r n_{i,r} - 1$.

Case 1-4 We have several full individual regional trajectories $L_{i,r}$ and individual complete trajectories in a whole network L_i. We note that $L_{i,r}$ is sum of $l_{i,r}$ of the same vehicle in the same pocket. In this case, we can calculate the ratio between TL_r and TL using $L_{i,r}$ and L_i as $\rho_r =< L_{i,r}/L_i >$. $\rho_{i,r}$ can be 0 when the vehicle with a full trajectory in a whole network does not pass through one pocket. TL_r can be calculated by $\rho_r * TL$.

The trip length reproducibility of each case is characterized by the difference between TL and the sum of TL_r, i.e., $\Sigma_r TL_r - TL$, and the relative difference, i.e. $|\Sigma_r TL_r - TL|/TL$, according to the different weights w. The ground-truth value TL is 515 m. We note that when w is small, trip length tractability increases according to the result in previous sections.

The results are shown in Table 3.2. When neither path sequence information nor correlation between trip lengths in regions is available (Case 1-1 and 1-2), the difference is quite large, around 10 to 45% of relative difference. This especially so when we have only partial trajectories (Case 1-1), the difference takes a huge negative value, as much as -230, and the relative difference drastically increases, i.e., from 20 to 45%, along with the partitioning weight on speed. This is derived from the fact that the long trip length of vehicles that return to the same pocket several times cannot be considered only with partial trajectories. Thus, in this case, the partitioning with low network compactness to obtain a homogeneous state inside regions makes estimated trip length quite smaller than the real one and trip length reproducibility is quite low, for example 0.45 of the relative difference when $w = 7.0$. The difference is positive only when $w = 6.4$, since we simply sum up TL_r to calculate the estimated TL without path sequence information while the average PSN is less than 1, as shown in Figure 3.6 (a). When we have the full trajectories of each pocket (Case 1-2), the differences are positive values and decrease as w increases. In this case, long trips with a large PSN can be considered. On the contrary, vehicles that stay in one pocket cannot be treated without path sequence information or the correlation between trip lengths in regions. Thus, as network compactness increases with larger w and the number of vehicles that pass through only one pocket decreases, the difference and the relative difference become lower, i.e. falling from 40% to 10% (relative difference).

Table 3.3 shows the results of Case 1-1' and 1-2' which are restricted versions of Cases 1-1 and 1-2 calculated only from vehicles that pass through both pockets. For Case 1-1, the relative difference becomes even worse than the result in Table 3.2, i.e., the relative difference reaches 0.50 when w is over 6.7, due to the removal of the vehicles with short trips that are the only vehicles detectable from partial trajectories. On the other hand, Case 1-2 is

	Case1-1′		Case1-2′	
Definition of TL_r	$< l_{i,r} >$		$< L_{i,r} >$	
	Difference	Relative	Difference	Relative
$w = 6.4$	-170	22	-0.05	0.006
$w = 6.7$	-352	52	-0.04	0.005
$w = 7.0$	-310	52	-0.03	0.005

TAB. 3.3 – *Difference [m] and Relative Difference [%] of average trip length calculation (Case 1) only with the vehicles which pass through both pockets ($< . >$ denotes the average value).*

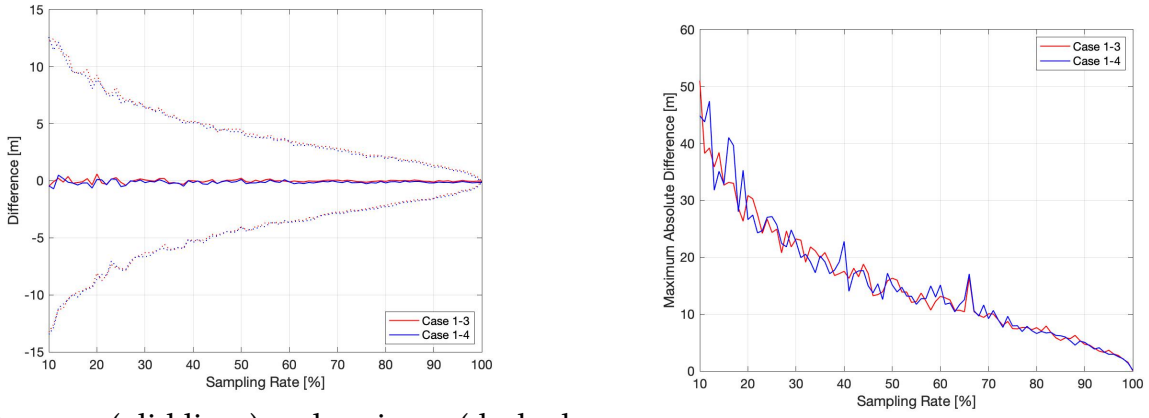

(a) Average (olid lines) and variance (dashed lines)

(b) Maximum absolute difference

FIG. 3.13 – *Errors of TL average estimation according to the sampling rate of $n_{i,r}$ (Case 1-3) and $\rho_{i,r}$ (Case 1-4). (The network partitioning weight on speed is $w = 6.7$).*

a significant improvement compared to the result in Table 3.2, i.e. the relative errors are below 0.0001. Therefore, if the full trajectories are available in each region, we can estimate trip length for long trips with good accuracy by partitioning with low network compactness.

In cases 1-3 and 1-4, the relative differences are quite small, i.e. 0.00007 in case 1-3 and 0.0003 in case 1-4, compared to Cases 1-1 and 1-2 in Table 2. Using $< n_{i,r} >$, Case 1-3 can deal aggregately with the issue of Case 1-1 in which the returning vehicles into the pocket cannot be considered. When ρ_r is available (Case 1-4), the difference becomes smaller than in Case 1-2 and close to Case 1-2′ in Table 3.3, by considering the vehicles which stay in one region. It shows that even the aggregated information of path sequence or trip length correlation can help get to obtain an accurate TL_r estimation. Also, the results of these cases are not significantly affected by the partitioning weight.

In Table 3.2, the aggregated information of path sequence $< n_{i,r} >$ or trip length correlation ρ_r is calculated by all the vehicle trajectories. However, in reality, it is difficult to get complete detailed trajectories to calculate the number of switching pockets by individual vehicle $n_{i,r}$ or the ratio between complete trip length in the network and total trip length in each region $\rho_{i,r}$. Therefore, we check the difference according to the sampling rate of the complete trajectories, i.e. from 10% to 100% of all vehicles. Vehicles whose complete trajectories we presume known are randomly chosen based on the sampling rate, and the calculation of difference is repeated 1000 times for each sampling rate. Figure 3.13 (a) shows

that the average values of the differences of both cases are constant regardless of the sampling rate. The variances are larger when the sampling rate is low in both cases, i.e. around 10 m when the Sampling Rate is 10%. However, in Figure 3.13 (b), the maximum absolute differences in both cases are quite smaller even when the sampling rate is low, i.e. less than 51 m in both Case 1-3 and Case 1-4 with 10% of the sampling rate, compared to the differences in Cases 1-1 and 1-2 (-174 and 112 when $w = 6.7$).

Thus, obtaining reliable trip length is quite difficult if any information about path sequence is not available, This especially the case when only partial trajectories are available, as it is almost impossible to get an accurate estimation. On the other hand, when the complete regional trajectories are available, we can improve estimation accuracy by partitioning using low compactness. Even if a few samples of $\rho_{i,r}$ or $n_{i,r}$ are available, the estimation accuracy of average trip length improves significantly.

3.5.4 Estimating Trip Length Distribution

Now, we analyze the effect of data availability and aggregation granularity on the trip length distribution estimation. Trip length distribution is essential for the trip-based model. However, it can be quite complicated to get an accurate estimation from the available data, c.f., Batista *et al.* (2019). To assess the accuracy, we first reproduce the complete trip length L_i, regional trip length $L_{i,r}$, and PSN_i as the representation of the path sequence according to the different aggregation methods and availability of the distribution generated by the original data, i.e. $P(L_i)$, $P(L_{i,r})$, $P(PSN_i)$. Then, we compare the distribution of reproduced trip lengths and path sequence with the original distribution.

We prepare 6 cases with different data availabilities and aggregate granularities. When the complete trip length distribution $P(L_i)$ is available, which is the case when the trajectory data cover a large temporal and spatial range with data missing at certain locations or times, we consider the two cases below:

Case 2-1 We have the complete trip length distribution $P(L_i)$ and also the ratio ρ_r between average complete trip length TL and average regional trip length TL_r. This case is equivalent to the Case 1-4 in Section 3.5.3. PSN_i equal to 1, i.e., every vehicle pass through both pockets once, since path sequence is not available in this case. L_i is chosen randomly from the distribution $L_i \sim P(L_i)$, and $L_{i,r}$ is calculated as $L_{i,r} = L_i * \rho_r$.

Case 2-2 We have the joint distribution of complete trip length and the path sequence length, i.e., the number that each vehicle pass though the same pocket, as $P(L_i, n_{i,r})$. L_i and $n_{i,r}$ are randomly chosen from the distribution $P(L_i, n_{i,r})$. PSN_i is calculated by $\sum_r n_{i,r} - 1$, and $L_{i,r}$ can be calculated by $L_i * n_{i,r} / \sum_r n_{i,r}$.

When the regional trip length distribution $P(L_{i,r})$ or partial trip length $P(l_{i,r})$ is available, which is the case when vehicle ID changes and complete trips are not tractable for many vehicles, we can consider the four aggregation methods according to data availability.

Case 3-1 We have only the regional trip length distribution $P(L_{i,r})$. This case is equivalent to Case 1-2 in Section 3.5.3. PSN_i is set to 1. $L_{i,r}$ is chosen randomly from the distribution $L_{i,r}$ $P(L_{i,r})$, and L_i is calculated by $\sum_r L_{i,r}$.

	L_i	$L_{i,r}$	$n_{i,r}$
Case 2-1	$L_i \sim P(L_i)$	$L_{i,r} = L_i * \rho_r$	1
Case 2-2	$L_i \sim P(L_i, n_{i,r})$	$L_{i,r} = L_i * n_{i,r} / \sum_r n_{i,r}$	$n_{i,r} \sim P(L_i, n_{i,r})$
Case 3-1	$L_i = \sum_r L_{i,r}$	$L_{i,r} \sim P(L_{i,r})$	1
Case 3-2	$L_i = \sum_r L_{i,r}$	$L_{i,c}, L_{i,u} \sim P(L_{i,c}, L_{i,u})$	1
Case 3-3	$L_i = \sum_r L_{i,r}$	$l_{i,r} \sim P(l_{i,r}, n_{i,r})$ $L_{i,r} = l_{i,r} * n_{i,r}$	$n_{i,r} \sim P(l_{i,r}, n_{i,r})$
Case 3-4	$L_i = \sum_r L_{i,r}$	$L_{i,r} \sim P(L_{i,r}, n_{i,r})$	$n_{i,r} \sim P(L_{i,r}, n_{i,r})$
Fitting Error	$L_i \sim P(L_i)$	$L_{i,r} \sim P(L_{i,r})$	$n_{i,r} \sim P(n_{i,r})$

TAB. 3.4 – *The settings of complete trip length (L_i) and regional trip length ($L_{i,r}$) distributions and pocket switching number ($n_{i,r}$) of test cases.*

Case 3-2 We have the joint distribution of regional trip lengths of both pockets $P(L_{i,c}, L_{i,u})$ where c denotes the congested pocket and u denotes the less-congested pocket. PSN_i is set to 1. $L_{i,r}$is randomly chosen from the distribution $P(L_{i,c}, L_{i,u})$. L_i is calculated by $\sum_r L_{i,r}$.

Case 3-3 We have the joint distribution of the partial trip length of each pocket and the path sequence length $P(l_{i,r}, n_{i,r})$. This case is equivalent to Case 1-3. $l_{i,r}$ and $n_{i,r}$ are randomly chosen from the distribution $P(l_{i,r}, n_{i,r})$. PSN_i is calculated by $\sum_r n_{i,r} - 1$, and $L_{i,r}$ can be calculated by $l_{i,r} * n_{i,r}$. L_i is calculated by $\sum_r L_{i,r}$.

Case 3-4 We have the joint distribution of the regional trip length of both pockets and the path sequence length $P(L_{i,r}, n_{i,r})$. $L_{i,r}$ and $n_{i,r}$ are randomly chosen from the distribution $P(L_{i,r}, n_{i,r})$. PSN_i is calculated by $\sum_r n_{i,r} - 1$. L_i is calculated by $\sum_r L_{i,r}$.

In this study, we prepare two different aggregations to calculate distributions $P(L_i)$ and $P(L_{i,r})$: 1) discrete distribution, 2) Weibull distribution. The discrete distribution is calculated by the vehicle numbers counted based on the trip length every 100 m. The Weibull distribution is calculated by fitting the complete and regional trip lengths of all the vehicles. These distributions are also used for joint distributions. $P(PSN_i)$ is a discrete distribution based on the pocket switching numbers. Also, to consider the distribution fitting errors, we compare the case in which L_i, $L_{i,r}$ and PSN_i are chosen directly from the distributions of $P(L_i)$, $P(L_{i,r})$ and $P(PSN_i)$. The parameters used in each case are summing up in Table 3.4.

According to the aggregation methods of each case, we reproduce the distributions of $P(L_i)$, $P(L_{i,r})$ and $P(PSN_i)$ from 15000 samples to make the comparison with the original distribution, which is constructed from 14981 vehicles.

3.5.4.1 Trip length aggregated by discrete distribution

The estimated distribution based on the discrete distribution is shown in red in Figure 3.14, while the original distribution is shown in black.

From the beginning, we can see the estimated distributions (Fitting Error case) are quite similar to the original distribution according to Figure 3.14. The T-test result, i.e. from a well-known statistical hypothesis test, is shown in Table 3.5. The test decision shows 0 if the estimated and original distributions have the same statistical populations at a 5%

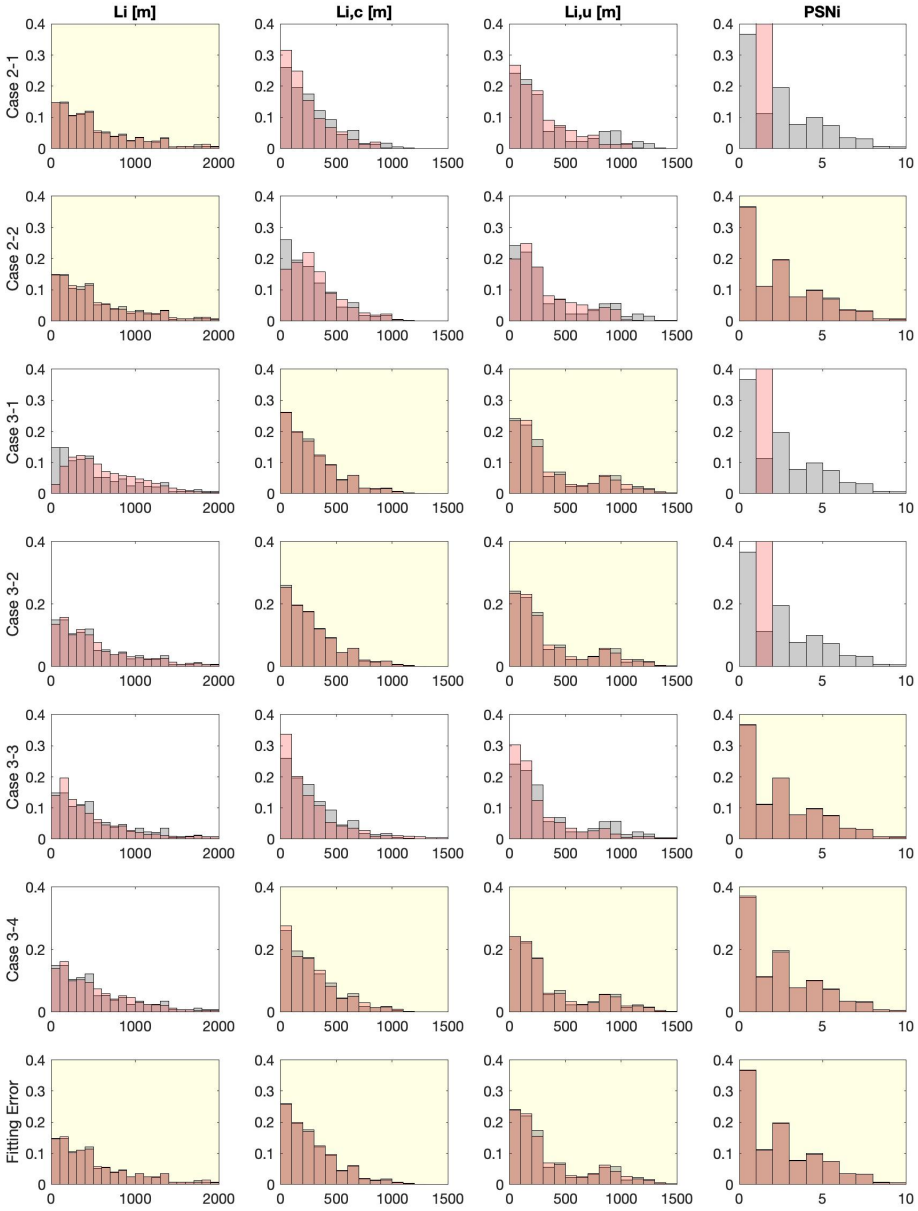

FIG. 3.14 – *Distribution reproductivity of complete trip length L_i, regional trip length $L_{i,r\in c,u}$ and path sequence PSN in all cases (w=6.7) (Black: Original distribution, Red: Estimated distribution (Discrete) of each case, Yellow box: Distributions calculated directly from the original distribution).*

	L_i	$L_{i,c}$	$L_{i,u}$	$n_{i,r}$
Case 2-1	0(0.69)	1(1e-76)	1(6e-77)	1(0)
Case 2-2	0(0.77)	1(7e-22)	1(8e-14)	0(0.75)
Case 3-1	1(2e-123)	0(0.97)	0(0.09)	1(0)
Case 3-2	0(0.42)	0(0.21)	0(0.74)	1(0)
Case 3-3	0(0.32)	0(0.67)	0(0.09)	0(0.71)
Case 3-4	0(0.46)	0(0.39)	0(0.86)	0(0.42)
Fitting Error	0(0.96)	0(0.97)	0(0.14)	0(0.82)

TAB. 3.5 – *T test decision and p-value inside (.) of the trip length and pocket switching number distribution calibration accuracy based on discrete distribution.*

	L_i	$L_{i,c}$	$L_{i,u}$	$n_{i,r}$
Case 2-1	0.41(0.54)	17.54(12.96)	18.72(27.30)	50.80(100)
Case 2-2	0.29(0.25)	10.15(4.06)	8.10(21.93)	0.39(0.42)
Case 3-1	22.74(9.02)	0.04(0.55)	1.96(0.35)	50.80(100)
Case 3-2	0.81(0.57)	1.37(1.14)	0.40(1.71)	50.80(100)
Case 3-3	1.16(29.46)	0.57(40.45)	2.53(46.64)	0.46(0.81)
Case 3-4	0.72(4.01)	0.93(1.12)	0.22(0.76)	0.98(0.34)
Fitting Error	0.04(0.43)	0.04(0.54)	1.70(0.37)	0.28(0.44)

TAB. 3.6 – *Relative difference [%] of moments between the estimated distribution (Discrete) of each case and original distribution. Each value shows Mean and Variance inside (.).*

significance level and shows 1 otherwise. The p-value ($[0, 1]$) shows the probability that the estimated distribution can be created from the same population as the original distribution. According to Table 3.5, all the parameters are accepted by the T-test for the Fitting Error case. Table 3.6 shows the relative difference of distribution moments, i.e. calculated as the absolute difference between the mean and variance of estimated and original distributions divided by the mean and variance of the original distribution. The relative differences of the mean and variance are very small, below 0.30% for the mean and below 0.55% for the variance, except for $P(L_{i,u})$. For the less-congested pocket, trip lengths vary with a longer tail and a double hump distribution than the congested pocket according to the original distribution. Therefore, it requires more samples to reduce the errors.

When only the complete trip length distribution $P(L_i)$ is available for estimating the regional trip length $P(L_{i,r})$ (Case 2-1), the estimated $P(L_{i,r})$ gets a shorter tail than the original distribution. Due to the calculation using the same trip length ratio $\rho_{i,r}$ for all vehicles without any path sequence information, the short complete trip length by the vehicles which pass through only one pocket leads to the increment of shorter regional trip lengths. When we use joint distribution between the complete trip length and PSN (Case 2-2), the peak of the distribution of $P(L_{i,c})$ is $200 - 300$ m while the peak of the original distribution is $0 - 100$ m, and the distribution tail of $P(L_{i,u})$ is shorter, i.e., $1000 - 1100$ m, than the original, i.e., $1200 - 1300$ m. Thus, it is difficult to reproduce the different features of the regional trip length distribution shape of each pocket using complete trip length distribution, even with path sequence information. In Table 3.5, in both cases complete trip length distribution is available, the results of the estimated regional trip length distributions are denied. By com-

paring the results of the regional trip length distribution between Cases 2-1 and 2-2 in Table 3.6, the relative differences in Case 2-2 of both the mean and variance become smaller, e.g., 42% for the mean and 69% for the variance in the congested pocket, than in Case 2-1. Thus, it is challenging to estimate the regional trip length from the complete trip length. However, aggregated path sequence information can improve estimation accuracy.

When only the regional trip length is available (Case 3-1), the estimated complete trip length distribution becomes larger than the original distribution, as shown in Figure 3.14. This results from the same reason as for Case 1-2 in the previous section. The vehicles which stay in one pocket cannot be considered without a path sequence. When we have the correlation between regional trip lengths in both pockets, such as joint distribution $P(L_{i,c}, L_{i,u})$ (Case 3-2), the estimated complete trip length becomes more similar to the original distribution than for Case 3-1. The T-test results in Table 3.5 show this significant improvement, i.e. the complete trip length estimation in Case 3-1 is denied, and the estimation in Case 3-2 is accepted. The relative difference of $P(L_i)$ in Case 3-2 shown in Table 3.6 decreases by 96% for the mean from 22.74% in Case 3-1 and 94% for the variance from 9.02% in Case 3-1 using the joint distribution. When we have the joint distribution of partial trip length and PSN (Case 3-3), complete trip length and regional trip lengths are estimated as being smaller than the original distribution. Since the partial trip length distribution is much smaller than the regional trip length distribution, as shown in Figure 3.15, it leads to smaller estimation results even with joint distribution between partial trip length and the path sequence. Although the T-test result is accepted for all the parameters, the p-values are smaller than in the Fitting Error case, e.g., 0.32 for $P(L_i)$ versus 0.96 in the Fitting Error case, and the relative differences of variance are very large, around 30% for $P(L_i)$ and over 40% for $P(L_{i,r})$. Thus, this calculation method is effective for estimating average trip length, c.f. Section 3.5.3, but not for estimating trip length distribution. If we have the joint distribution of regional trip length and PSN (Case 3-4), all the distributions become very close to the original distributions. Not only the T-test results are accepted for all the distributions, but also the relative differences are small compared to the estimation results of all the other cases: 0.72% for the mean and 4.01% for the variance of the complete trip length distribution estimation. According to these results, the joint distribution between regional trip lengths and path sequence can provide a quite accurate estimation for all the parameters. Even if PSN is not available, we can obtain an acceptable estimation of complete and regional trip length distributions by using the correlation between the regional trip lengths of each pocket.

To analyze the effect of the number of vehicles of the sample when reproducing the distribution on the accuracy of the estimation, we compare the relative differences of the mean and variance of complete and regional trip length distribution in Cases 2-2 and 3-4, which may be affected by the amount of data used to calculate aggregated distribution, to the Fitting Error case based on the number of vehicles of the sample. The average value of 100 times each number of vehicles of the sample from 1000 to 30000 veh is shown in Figure 3.16. According to Figure 3.16 (a), the relative differences of the mean of complete and regional trip length distribution in the Fitting Error case decreases exponentially. In particular, the relative difference of the regional trip length of the less-congested pocket $P(L_{i,u})$ decreases from 0.94% when the sample number is 5000 to 0.53% when the sample number is 30000. Also, in Figure 3.16 (b), the relative differences of variance of complete and regional trip length distributions decrease exponentially, e.g., $16\% - 55\%$ lower for 5000 samples than for 30000 samples. In Case 2-2, the relative difference of both the mean and variance of

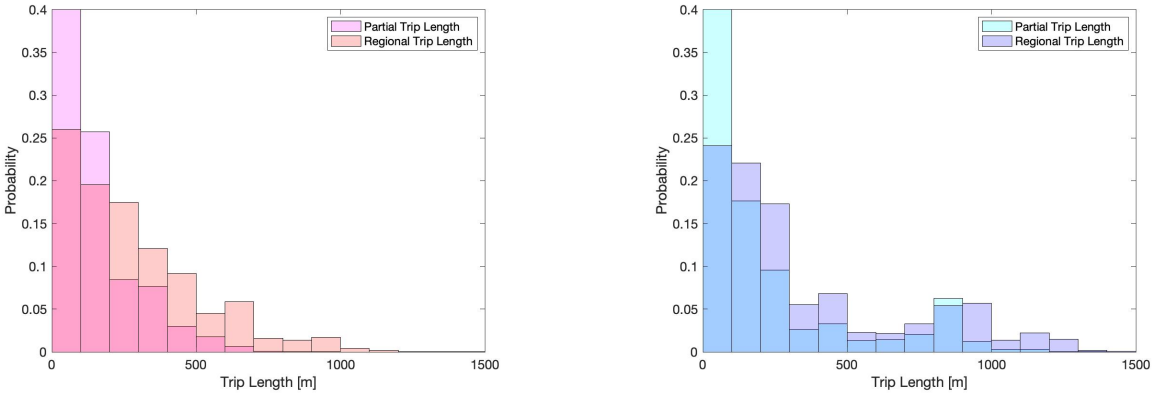

(a) Congested Pocket (b) Less-Congested Pocket

FIG. 3.15 – *Comparison between Partial and Regional Trip Length Distributions in each pocket*

the complete trip length, which is chosen from the joint distribution with PSN, is decreased from 1.01% to 0.40% when the number of vehicles of the sample increases from 5000 veh to 30000 veh for the mean, and from 0.85% to 0.40% when the number of vehicles of the sample increases from 5000 veh to 30000 veh for the variance. Notably, when the samples are fewer than 5000 veh, the relative difference increases exponentially up to 1.91%. On the other hand, the relative differences of regional trip length distribution are quite high and constant, e.g., around 8% and 11% for the mean and 4% and 22% for the variance. Thus, the accuracy of regional trip length estimation cannot improve even with a huge sample number. The relative differences of both the mean and variance of the regional trip length distribution in Case 3-4 decrease exponentially from $11-50\%$ along from 5000 to 30000 samples. Compared to the other cases except for $P(L_{i,r})$ in Case 2-2, the relative difference of the complete trip length distribution in Case 3-4 decreases more gradually, e.g., decreasing by 21% for the mean and by 2% for the variance from 5000 to 30000 samples. Therefore, the number vehicles in the sample affects the distribution estimation of the element parameter of the joint distribution but not the other estimated parameters.

3.5.4.2 Trip length aggregated by Weibull distribution

Trip length distributions estimated using the fitted Weibull distribution of original trip length are shown in Figure 3.17. PSN is the discrete distribution, as in the previous section, and Case 3-2 is excluded from this analysis since the calculation of the joint Weibull distribution is quite difficult. All the estimated distributions, colored red, are smoother, and the details of the original distribution shape are lacking in comparison to Figure 3.14. However, the T-test results shown in Table 3.7 are the same as those in Table 3.5. By comparing the relative difference of distribution moments when using the Weibull distributions in Table 3.8 with the cases of using discrete distributions in Table 3.6, most of the results of the estimated distribution chosen directly from the Weibull distribution, e.g., $P(L_i)$ in Case 2-1 and the Fitting Error case and $P(L_{i,r})$ in Case 3-1 and the Fitting Error case, get worse, e.g., increasing from around $2\%-93\%$ for the mean and from around $80\%-93\%$ for the variance. On the other hand, many of the estimated distributions calculated by each aggregation method, e.g., $P(L_{i,r})$ in Case 2-1 and $P(L_i)$ in Cases 3-1 and 3-4, obtain better results, from around

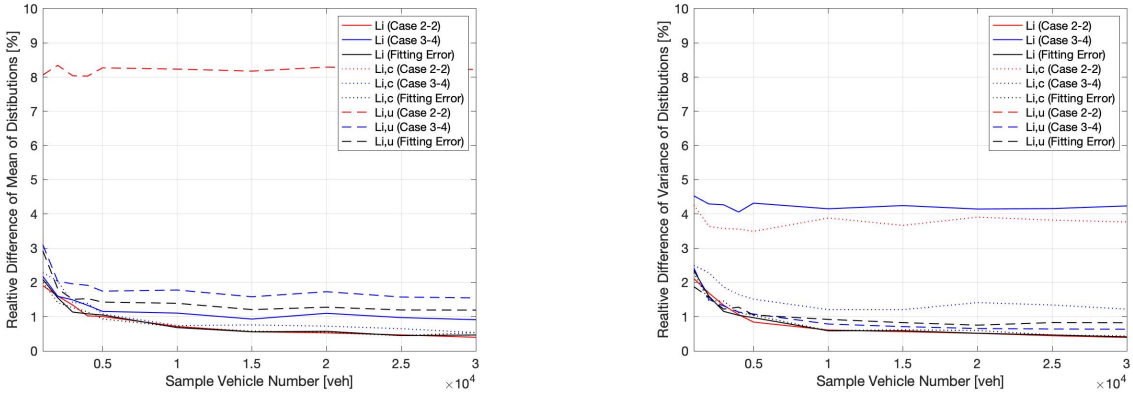

(a) Mean ($L_{i,c}$ in Case 2-2 is around 11%) (b) Variance ($L_{i,u}$ in Case 2-2 is around 22%)

FIG. 3.16 – *Relative difference [%] of moments between the estimated distribution (Discrete) of Case 2-2, Case 3-4, and the Fitting Error and the original distribution according to the number of vehicles of the sample.*

	L_i	$L_{i,c}$	$L_{i,u}$	$n_{i,r}$
Case 2-1	0(0.68)	1(1e-67)	1(3e-69)	1(0)
Case 2-2	0(0.53)	1(5e-33)	1(7e-13)	0(0.33)
Case 3-1	1(2e-112)	0(0.57)	0(0.37)	1(0)
Case 3-3	0(0.89)	0(0.82)	0(0.78)	0(0.59)
Case 3-4	0(0.76)	0(0.97)	0(0.78)	0(0.79)
Fitting Error	0(0.84)	0(0.30)	0(0.44)	0(0.67)

TAB. 3.7 – *T test decision and p-value inside (.) of the trip length and pocket switching number distribution calibration accuracy based on Weibull distribution.*

3% – 58% for the mean and from around 5% – 76% for the variance. Since the continuous distribution is more robust for adapting the model and the estimation results obtained can be better than in the cases using discrete distribution, the proper aggregation method proposed is useful as an input parameter of MFD models.

3.6 Conclusion

This experimental study investigated the effect of partitioning granularity on speed-MFD shape and trip length tractability using Athens drone data. Also, the reproductivity of estimated trip length was analyzed according to data availability and aggregation granularity compared to the average and distribution of trip length calculated directly from the data.

Thus, we confirmed that detailed partitioning, which significantly improves speed homogeneity and leads to low trip length tractability, while trip length tractability has a huge impact on trip length estimation. Also, if any information on the path sequence or correlation between regional trip lengths is not available, the estimated trip length may be quite far from the real trip length. This is especially the case when only partial trajectories are available due to a change of probe vehicle ID, as the reproductivity of trip length decreases. Also, the amount of data affects the trip length estimation with the joint distribution between the

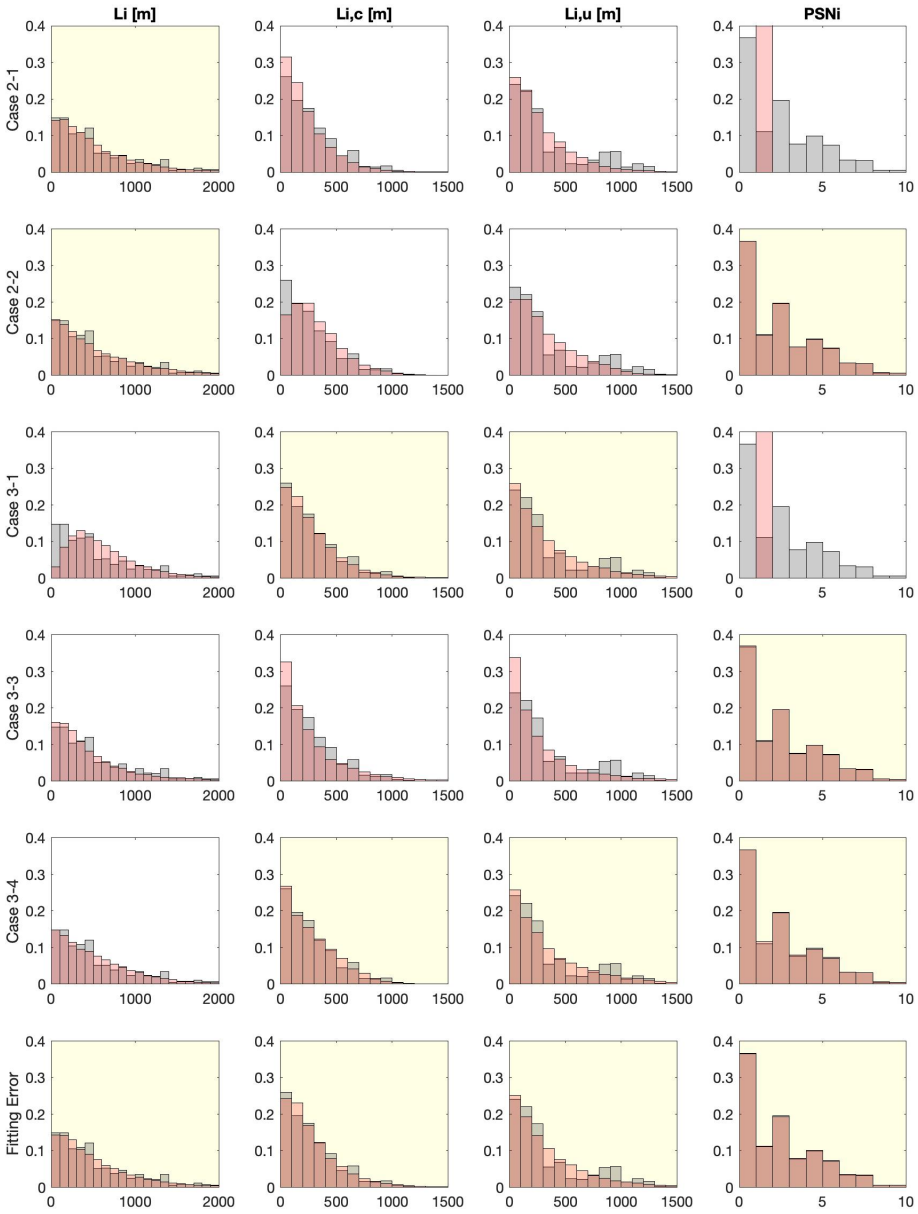

FIG. 3.17 – *Distribution reproductivity of complete trip length L_i, regional trip length $L_{i,r\in c,u}$ and path sequence PSN in all cases (w=6.7) (Black: Original distribution, Red: Estimated distribution (Weibull) of each case, Yellow box: Distributions calculated directly from original distribution).*

	L_i	$L_{i,c}$	$L_{i,u}$	$n_{i,r}$
Case 2-1	0.42(4.36)	16.86(8.67)	18.04(23.71)	50.80(100)
Case 2-2	0.63(0.97)	12.79(2.51)	7.75(22.45)	1.20(0.93)
Case 3-1	22.10(5.12)	0.60(3.61)	1.07(5.28)	50.80(100)
Case 3-3	0.17(30.79)	0.29(35.44)	0.42(48.48)	0.67(0.23)
Case 3-4	0.30(3.81)	0.04(1.76)	0.34(0.97)	0.33(0.63)
Fitting Error	0.20(2.15)	1.08(3.35)	0.92(2.93)	0.53(0.03)

TAB. 3.8 – *Relative difference [%] of moments between the estimated distribution (Weibull) of each case and the original distribution. Each value shows the Mean and the Variance inside (.).*

regional trip length of both pockets or between trip length and path sequence, especially for the element parameter of the given joint distribution. Using the continuous fitted distribution, e.g., the Weibull distribution, instead of the discrete distribution, the estimated accuracy of most of the distributions for which data are available decreases. However, the estimation accuracy of the parameter for which the data are not available can be improved by certain of the proposed aggregation methods based on the fitted Weibull distribution. These investigations are useful for improving traffic prediction accuracy using MFD models.

4. Calibration of MFD Models Considering a Single Region

4.1 Introduction

Accurate traffic state prediction is necessary for traffic operation and control. Traffic flow models that predict traffic states have been developed at both the micro and macro scales. Microscopic models, e. g., the car-following models and the lane-changing models, deal with traffic flows by considering the interactions between successive vehicles. However, since such models are complex and require high computational costs, they were rarely been used for traffic state prediction in the past. Macroscopic models describe the traffic stream at the large urban scale as a continuous flow using the conservation law of fluid dynamics. The Lighthill Whitham-Richards (LWR) model proposed by Lighthill & Whitham (1955) and Richards (1956b) is the best-known framework for macroscopic models. In the LWR model, local traffic states are represented by an equilibrium as the link flow-density relation, the Fundamental Diagram (FD). FD is defined as $q_l = v_l * k_l$ where q_l is the link flow, k_l is the link density, and v_l is the space mean speed at link l. Newell (1993) proposed a simple triangular approximation of FD.

Network-level models based on the macroscopic fundamental diagram (MFD), i.e., the FD-like relationship between network-level flow, density, and mean speed, have received attention recently to deal with network-level traffic prediction. The first MFD model was introduced by Daganzo (2007) and Geroliminis & Daganzo (2007). Since the principle of this model was to describe the urban network traffic state by the aggregated accumulation of a whole region, this model is often called the "accumulation-based model." The accumulation-based model calculates traffic states such as the aggregated outflow and accumulation based on an MFD function, average trip length, and the conservation equation. It has only a few parameters and can be easily implemented for the purposes of simulation with time and vehicle composition. However, since the model is based on the strong hypothesis of homogeneous steady state in the region, errors can occur when the inflow drops suddenly, according to Leclercq *et al.* (2015) and when the network does not have a homogeneous state, according to Xue *et al.* (2016). Also, the model by Daganzo (2007) and Geroliminis & Daganzo (2008) used a constant average complete trip length within a whole region. However, Yildirimoglu & Geroliminis (2014) and Kouvelas *et al.* (2017) showed that a single average trip length inside a region may introduce significant errors since trip lengths change in practice. Furthermore, Yildirimoglu & Geroliminis (2014) mentioned the importance of considering the dynamic variation of trip length inside a region. However, there is still a lack of extensive experimental studies able to better characterize trip length behavior with time.

To deal with the variance of trip lengths, the "trip-based model" was introduced by Lamotte and Geroliminis (2017), based on an idea of trip definition by Arnott (2013), Fosgerau (2015), and Daganzo & Lehe (2015). The principle of the trip-based model is to assign individual trip lengths for all vehicles with speed based on MFD. Mariotte *et al.* (2017) and Lamotte *et al.* (2018) developed an easy method to implement trip length distribution in this framework using an event-based scheme. This model can consider the variation of trip lengths, although more parameters are required. A higher computational load than the accumulation-based model is observed since the model tracks the trip of each individual vehicle.

Thus, trip length and MFD are key parameters in both models. The aggregation method of trip lengths and MFD shape may have a huge impact on prediction accuracy. On the other

hand, estimating the average trip length and trip length distribution can be hard depending on data availability, as mentioned in Chapter 3. In particular, validating trip length distribution for a whole region is not possible when data on time and location are sparse, and the complete trip lengths of vehicles are not available. Although parameter settings such as trip length aggregation and MFD approximation may affect prediction accuracy, several studies compared the effect of parameter scaling according to model formulation. Mariotte *et al.* (2017) compared the estimation accuracy of accumulation-based and trip-based models according to different inflow profiles and initial conditions with numerical simulation. Lamotte *et al.* (2018) compared the result of both models theoretically according to the different shapes of trip length distribution. Since the empirical MFD model assessment requires the ground truth traffic state and detailed trajectory data to calculate real trip length distribution, no study up to now has provided a complete empirical investigation, mainly due to a lack of large databases of vehicle trajectories in urban environments.

Our purpose in this chapter is to investigate the effect of trip length estimation and MFD approximation on the prediction accuracy of traffic state dynamics by using classical MFD models. This is the first comparative analysis of MFD models with full trajectory data collected by a drone experiment (Barmpounakis & Geroliminis (2020)). The real traffic state calculated by drone data is used as ground truth to assess the prediction accuracy of MFD models. However, drone data have several break times because of battery changes, and each period captured by drones is too short to observe the complete dynamics of a full peak hour. Therefore, we first need to compensate for the break times of the drone data to obtain the long-term dynamics. Section 4.2 explains the data imputation method and shows the parameter dynamics after data imputation. They are used as ground truth and for calculating the parameters of the MFD model assessment. In Section 4.3, the two classical MFD models, i. e., the accumulation-based model and the trip-based model, in a single region are described. The effect of trip length estimation on the accuracy of traffic state prediction by MFD models is shown in Section 4.4. Finally, we analyze the impact of MFD approximation in Section 4.5. The conclusion and contributions are summarized in Section 4.6.

4.2 Data Imputation of Athens Drone Data

The Athens drone experiments described in Chapter 3, c.f., Barmpounakis & Geroliminis (2020), have four break times in a whole time period of 2.5 hours (8:00-10:30) to change the drone batteries. Therefore, we usually have drone data during 11-13 minutes and then no drone data during 18-19 minutes every 30 minutes. We call the time period with drone data as drone period and without drone data as no-drone period. Figure 4.1 shows the dynamics of mean speed and accumulation based on drone data in a whole time period. Mean speed v is calculated from the total travel time ttt and total travel distance ttd of all vehicles as $v = ttd/ttt$. Accumulation n is calculated as $n = ttt/dt$ where dt is the calculation unit time. 8:00 denotes 0 min in the x-axis of Figure 4.1. As shown in the figures, the traffic state in Athens changes during a whole period, especially during the morning commuting period around 9:00-10:00 a.m., i.e., $60 - 120min$ in the x-axis of the figures, but this dynamic is not very significant during one short drone period. To assess the predictions from the MFD model, we need a continuous data set during a whole period in order to work with a large enough prediction horizon. Therefore, we need to complete the vehicle trajectories

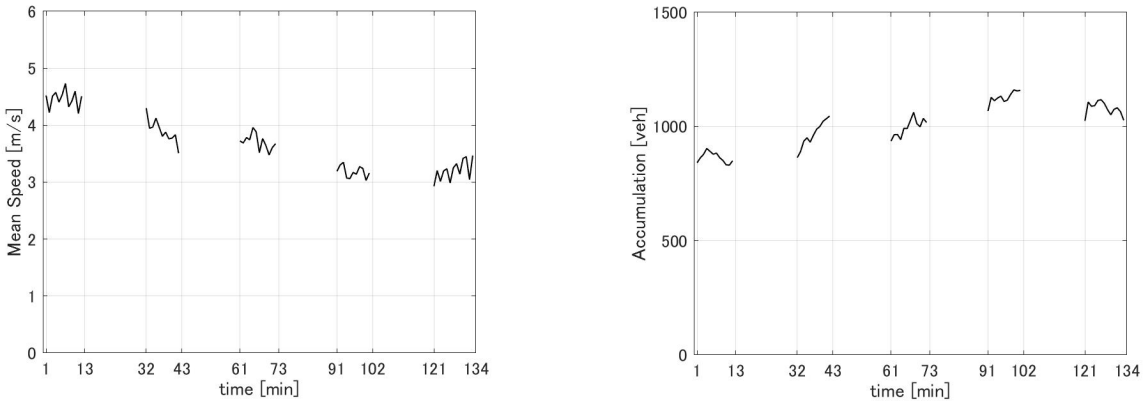

(a) Mean Speed (b) Accumulation

FIG. 4.1 – *Traffic state dynamics in Athens (calculated every 1 minute)*

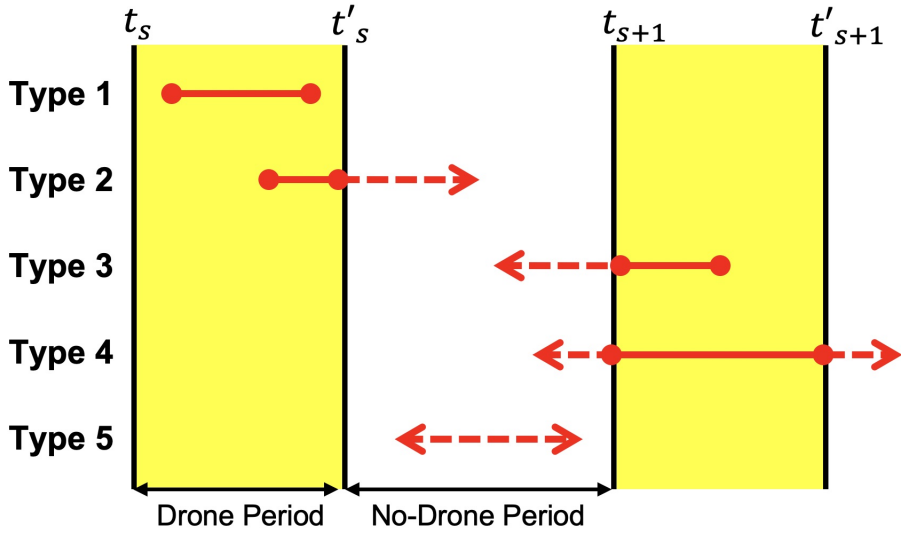

FIG. 4.2 – *The 5 trip types. (Yellow zone: the drone period, white zone: no-drone period, red solid lines: observed periods of each trip, red dashed lines: estimated periods of each trip)*

during the no-drone period based on the overall traffic dynamics we observe during the drone period.

First, we categorize the vehicle trajectories into five trip types according to the level of missing data. In Figure 4.2, the yellow zone started from time t_s and ended at t'_s, shows the drone period where s is the number of drone periods from 1 to 5, and the white zone shows no-drone period. The red lines show the period when each type of vehicle appears: the solid lines show when data is observed, and the dashed lines show when data is missed. As shown in Figure 4.2, the five types are categorized as below:

Type 1 A trip begins and ends during a drone period (no data is missing),

Type 2 A trip begins during a drone period and ends during a no-drone period (missing exit time and final trip length),

Type 3 A trip begins during a no-drone period and ends during a drone period (missing

entry time and initial trip length),

Type 4 A trip begins during a no-drone period before a drone period and ends during a no-drone period after a drone period (missing entry and exit time and initial and final trip length),

Type 5 A trip begins and ends during a no-drone period and never occurs during a drone period (missing all).

Then, we try to estimate the missing information for all vehicle trajectories, e.g., entry/exit time, trip length, according to trip types. There are also cases that due to occlusion in the view from the drone or limited visibility (due to trees or shadows), a trajectory of a vehicle might not be continuous and break into multiple trajectories. However, since there is no full re-identification method, matching and completing those trajectories is quite challenging. Moreover, it is not the issue for the following investigations of prediction accuracy according to parameter settings based on MFD models. Therefore, we do not deal with these cases.

The detailed trip categories of real vehicle trajectories according to the missing data level are explained in Section 4.2.1. Then, we explain the data imputation method for assigning entry/exit times and trip lengths according to trip types in Section 4.2.2. Estimations are compared with observations from a distribution perspective to ensure consistency in data imputation, see Section 4.2.3. When considering the network partitioned into more than two regions, path sequence is also important information that significantly impacts trip length calibration, as described in Chapter 3. The data imputation method for assigning path sequences between regions is described in Section 4.2.4, and the regional parameter comparison is given in Section 4.2.5.

4.2.1 Categorizing Trajectories to 5 Trip Types

Ten drones observed the traffic state with a slightly different start and end timing in the Athens drone experiments. From the beginning, we decided the start and end of the drone period as the beginning and end of when all the drones provided data. Thus, all observed trajectories start and end during the drone period. However, the real trips of the observed trajectories, when they start at t_s or/and end at t'_s in Figure 4.2, may start or/and end during the no-drone period. Therefore, we need to categorize these observed trajectories according to trip types to complete the missing parts of all trajectories.

When the trajectory begins at least 5 seconds after the beginning of drone period t_s and ends at least 5 seconds before the end of drone period t'_s, we assume that we have the time and location data of the whole trajectory of this vehicle. We categorize this vehicle as a Type 1 (no data is missing) vehicle. Exceptionally, if the trip begins in the first 5 seconds and/or ends in the last 5 seconds of the drone period at the perimeter link of the network, we assume that this vehicle enters into/exits from the network at this timing and regard it as a Type 1 vehicle. The perimeter links are chosen manually when the link edge connects with the links outside of the network, as shown in Figure 4.3. When the trajectory begins more than 5 seconds after t_s and ends 5 seconds before t'_s, the vehicle's entry time is observed, but this vehicle may end its trip during the no-drone period. This vehicle is categorized as a Type 2 (missing exit time and final trip length) vehicle. When the trajectory begins 5 seconds after t_s and ends more than 5 seconds before t'_s, the vehicle's exit time is observed, but this

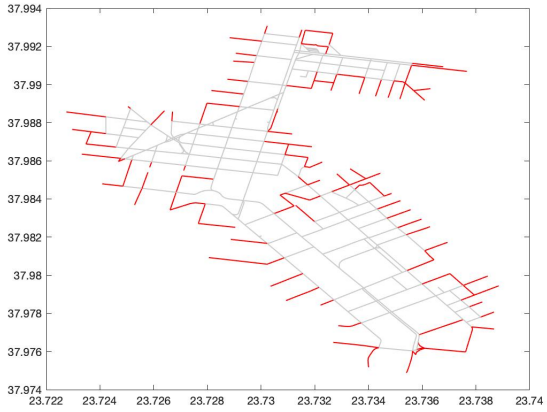

FIG. 4.3 – *Perimeter links of the network (Red: perimeter links, gray: all other links in the network*

vehicle may begin its trip during the no-drone period. This vehicle is categorized as a Type 3 (missing entry time and initial trip length) vehicle. When the trajectory begins and ends 5 seconds after t_s and before t'_s, the vehicle is observed during the drone period, but this vehicle may begin and end its trip during the no-drone period. We categorize this vehicle as a Type 4 (missing entry and exit time and initial and final trip length) vehicle. The Type 5 (missing all) vehicle never appears during the drone period. Therefore, we cannot obtain any information from the data but we still need to estimate such vehicle parameters if we want to have a complete vision of the traffic dynamics over the prediction horizon when comparing with the MFD models.

In Figure 4.2, the solid circles show the beginning and ending times of the trajectories observed, and the solid lines show the trip observed. The dashed lines are the missing parts of trips that need to be compensated and arrows show the actual starting and ending time of the unobserved part. Figure 4.4 shows the entry and exit times of 500 observed trajectories that are chosen randomly from the data and sorted by entry time. The red lines show Type 1 vehicles, and the blue and green lines show Type 2 and 3 vehicles. Since each drone starts and ends the observation at slightly different timing, some Type 2 and 3 vehicles have been observed even during no-drone periods. Type 4 vehicles are few, i.e., about 0.04% of the all vehicle number, so these do not appear in the figure. Obviously, Type 5 vehicles cannot be seen in this figure. Sample observed trajectories of each trip type are shown in Athens' network map in Figure 4.5. Round plots at the edge of colored lines show where the observed trips start, and cross plots show where the trip ends. Type 4 vehicles have longer trajectories than other types, as shown in Figure 4.5. Trajectories of Type 2 and 3 vehicles are quite similar. Many Type 1 vehicles have shorter trajectories than Type 2 and 3 vehicles. Some short trajectories of Type 1 may be caused by a trip being broken in two because a vehicle is lost for a few seconds by drone observation. However, there is no method to identify those trips. Trip length differences in each type can be clearly seen in Figure 4.6. The average trip length of Type 1 vehicles is around 500 m, while one of Type 2 and 3 is around 700 m. Only Type 4 vehicles have trip lengths longer than 2500 m.

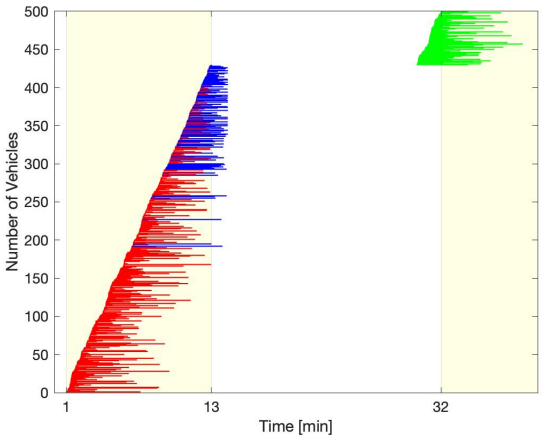

FIG. 4.4 – *Entry and exit time of sample vehicles of each trip type (Yellow zone: drone period, white zoned: no-drone period, red lines: Type 1 vehicles, blue lines: Type 2 vehicles, green lines: Type 3 vehicles)*

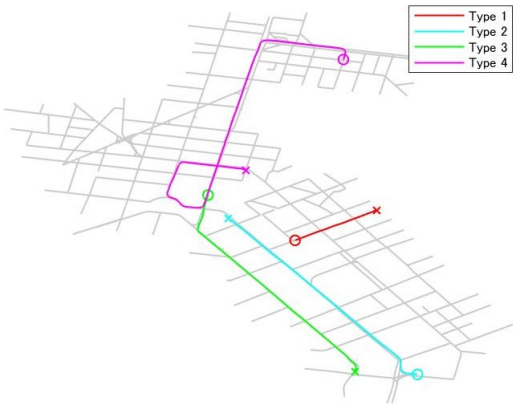

FIG. 4.5 – *Sample trajectories of each trip type (round plot: origin location of the trajectory, cross plot:destination location of the trajectory)*

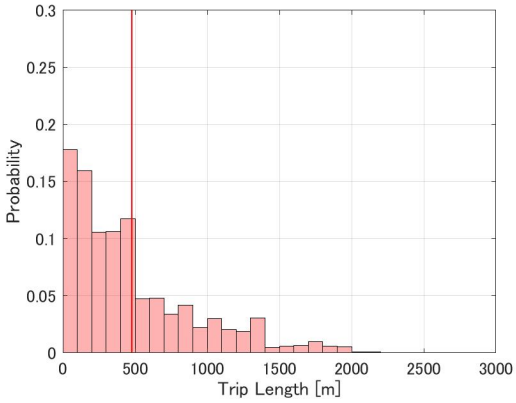

(a) Type 1: No data is missing

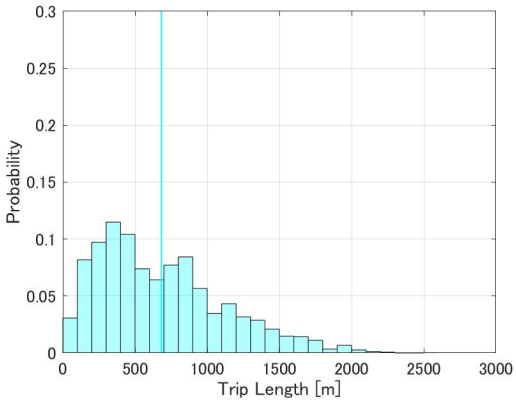

(b) Type 2: Missing exit time and final trip length

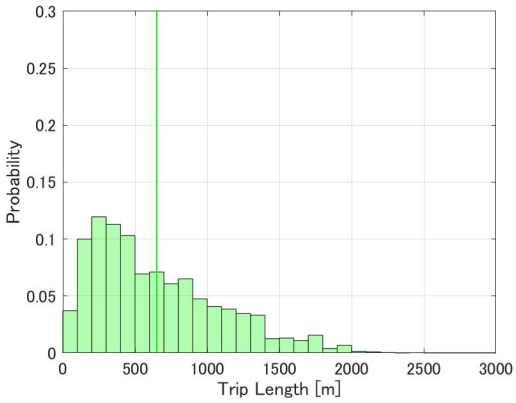

(c) Type 3: Missing entry time and initial trip length

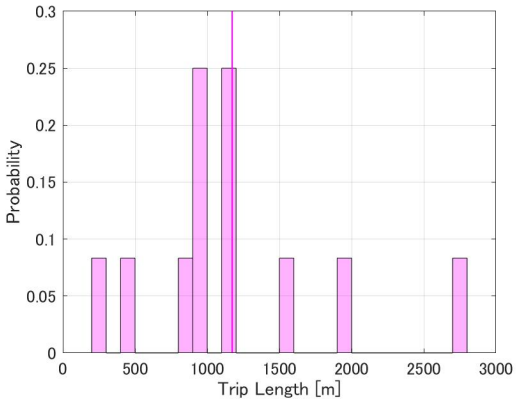

(d) Type 4: Missing entry and exit time and initial and final trip length

FIG. 4.6 – *Original trip length distribution according to trip types (vertical lines: average trip length)*

4.2.2 Assignment of Entry- and Exit-Times, and Trip Length

The vehicle trajectory information necessary for calculating the MFD model parameters is entry time into the network, exit time from the network, and complete trip length. Therefore, we need to assign this information for the vehicle trips during the no-drone period. Extrapolating the inflow observed, i.e., accumulation of vehicles which enter the network par time period, and outflow values, i.e., accumulation of vehicles which exit from the network per time period, during the drone period over the neighboring non-drone time periods, is an easy way to estimate entry and exit times during the non-drone period. Also, complete trip lengths can be assigned from a complete trip length distribution calculated by data during the drone period. However, there are some issues: 1) the in- and outflow during the no-drone period may not be constant between each drone period since the accumulation is changed dynamically, as shown in Figure 1 (b), and 2) the complete trip length distribution, including the long trips which exists during a whole drone period, i.e., Type 4 vehicles, is not available. Thus, we first need to estimate those parameters based on data. At the same time, the accumulation of Type 2, 3, and 4 vehicles in both of the no-drone periods calculated based on the estimated parameters and the drone period calculated from the data should be

Variables	
Tin_i	entry time in the network of vehicle i
$Tout_i$	exit time from the network of vehicle i
L_i	a complete trip length of vehicle i
Tin_i^*	entry time in the network of vehicle i obtained from the data
$Tout_i^*$	exit time in the network of vehicle i obtained from the data
L_i^*	a complete trip length of vehicle i obtained from the data
t_s	the beginning of the drone period $s \in [1, 2, ..., 5]$
t'_s	the end of the drone period $s \in [1, 2, ..., 5]$
qin'_s	the average inflow over 3 minutes before the end of drone period t'_s and after the beginning of the next drone period t_{s+1}
$qout'_s$	the average outflow over 3 minutes before the end of drone period t'_s and after the beginning of the next drone period t_{s+1}
N_{type}	the accumulation of each type
V_i	the individual space-mean speed of vehicle i
tt_i	travel time of vehicle i during the drone period
tdi	travel distance of vehicle i during the drone period
v'_s	the average mean speed over 3 minutes before the end of drone period t'_s and after the beginning of the next drone period t_{s+1}
L'_i	trip length chosen from trip length distribution

TAB. 4.1 – *Lists of Variables used in Section 4.2.2*

equal. Since estimating all traffic state variables and trip characteristics of the no-drone period fitted with the real traffic state during the drone period is challenging, we must choose either using in- and outflow equations calculated by data in drone periods for no-drone periods or keeping the complete trip length distribution of drone periods for no-drone periods and modify the other accordingly. When we keep the complete trip length distribution calculated in drone periods for no-drone periods, the accumulation and outflow dynamics have sudden rises and drops, especially at the beginning and the end of each drone period. A detailed explanation of the method and result of this case is described in the Appendix A. The following sections explain the method that uses the in- and outflow equation calculated from drone periods for no-drone periods and the estimated variables and parameters. All the indexes that appear in this section are summarized in Table 4.1.

For Type 1 (no missing) vehicles, all the trajectory information is available from the data, and we have $Tin_i = Tin_i^*$, $Tout_i = Tout_i^*$, and $L_i = L_i^*$.

To assign the entry and exit times of the other types of vehicles, inflow and outflow dynamics during the no-drone period should connect smoothly with those during the drone period. Therefore, we first calculate the average inflow and outflow over 3 minutes before the end of the drone period and after the beginning of the next drone period by counting the numbers of entry and exit vehicles. In Figure 4.7, the x-axis and y-axis show the time and number of vehicles. The yellow zones before t'_s and after t_{s+1} show the drone period, and the white zone from t'_s to t_{s+1} shows the no-drone period. Average inflows and outflows are calculated from observed entry and exit times from $t'_s - 3min$ to t'_s and from t_{s+1} to $t_{s+1} + 3min$ separately, as shown in Figure 4.7 (b) and (a). Then, we calculate the inflow and outflow during the no-drone period, i.e., qin'_s and $qout'_s$, as the average value of inflows and

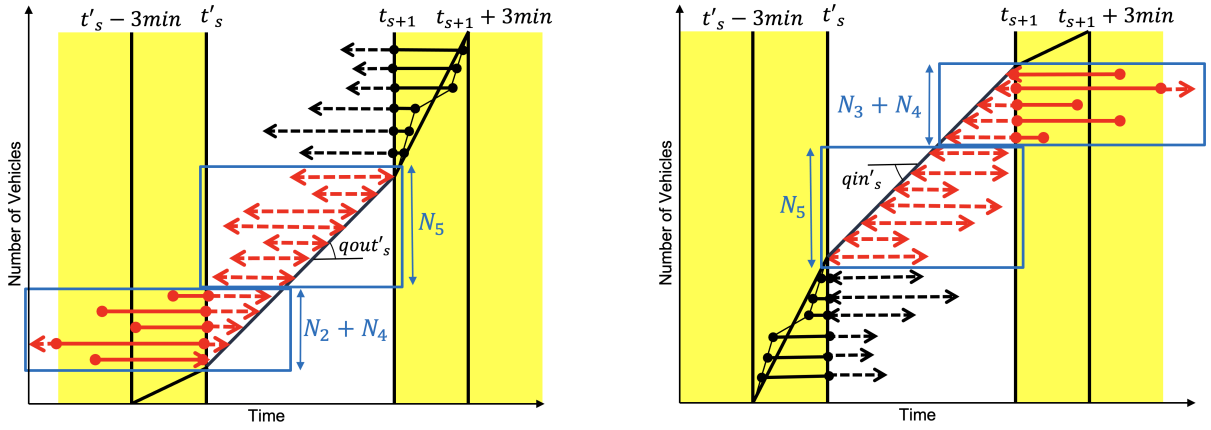

(a) Outflow and Exit Time (b) Inflow and Entry Time

FIG. 4.7 – *Entry and exit time assignment based on inflow and outflow according to trip types (Yellow zone: drone period, white zoned: no-drone period)*

outflows for 3 minutes before and after the drone period.

Based on the inflow qin'_s and outflow $qout'_s$, we create the entry and exit time list of all the vehicles during this no-drone period denoted $\mathbf{Tin}_s$ and $\mathbf{Tout}_s$. The entry time list $\mathbf{Tin}_s$ starts from t'_s and ends just before t_{s+1} ordered by every $1/qin'_s$, i.e., $Tin_s = [t'_s, t'_s + 1/qin'_s, t'_s + 2/qin'_s, \dots]$. $\mathbf{Tin}_s$ will be assigned to the entry time of Type 3 (missing entry time), 4 (missing entry and exit time) and 5 (missing all) vehicles from t'_s to t'_{s+1}. Therefore, the list length of $\mathbf{Tin}_s$, i.e., $|\mathbf{Tin}_s|$, should be the same as the accumulation sum of Type 3, 4 and 5 vehicles, such that $|\mathbf{Tin}_s| = N_3 + N_4 + N_5$ where N_{type} denotes the accumulation of each type. Th exit time list $\mathbf{Tout}_s$ starts from t_{s+1} and ends just after t'_s ordered by every $-1/qout'_s$, i.e., $\mathbf{Tout}_s = [t_{s+1}, t_{s+1} - 1/qout'_s, t_{s+1} - 2/qout'_s, \dots]$. $\mathbf{Tout}_s$ will be assigned to the exit time of Type 2 (missing exit time), 4 and 5 vehicles from t_s to t_{s+1}. Therefore, the list length of $\mathbf{Tout}_s$, i.e., $|\mathbf{Tout}_s|$, should be the same as the accumulation sum of Type 2, 4, and 5 vehicles, such that $|\mathbf{Tout}_s| = N_2 + N_4 + N_5$. Note that N_2, N_3, and N_4 can be calculated from the data by counting vehicles of each type. Since Type 5 vehicles should enter and exit during a no-drone period, $|\mathbf{Tin}_s| - N_3 - N_4$ has to equal $|\mathbf{Tout}_s| - N_2 - N_4$. We choose the smallest value of each as N_5 and recalculate another value of $|\mathbf{Tin}_s|$ or $|\mathbf{Tout}_s|$ based on N_2, N_3, N_4, and modified N_5 values. For example, if $|\mathbf{Tin}_s| - N_3 - N_4 > |\mathbf{Tout}_s| - N_2 - N_4$, we keep $\mathbf{Tin}_s$ and recalculate $qout'_s$ by $qout'_s = (|\mathbf{Tin}_s| - (N_3 + N_4) + (N_2 + N_4))/(t_{s+1} - t'_s)$ and $\mathbf{Tout}_s$ based on modified $qout'_s$. In Figure 4.7, red and black horizontal lines show each vehicle's travel time. In Figure 4.2, the solid parts of lines and round plots show available values. In Figure 4.7 (a), the red lines show the Type 2, 4, and 5 vehicles whose exit times are ordered based on $qout'_s$, and the black lines show the Type 3 vehicles. In (b), the red lines show Type 3, 4, and 5 vehicles whose entry times are ordered based on qin'_s, and the black lines show the Type 2 vehicles. The red dashed parts of lines show the travel time that we have to assign based on $\mathbf{Tin}_s$ and $\mathbf{Tout}_s$. The dashed red lines in a whole part are Type 4 vehicles whose number should be the same in Figure 4.7 (a) and (b).

Using $\mathbf{Tout}_s$, we assign exit times to Type 2 and 4 vehicles. For Type 2 (missing exit time) vehicles, the entry times are available from the data. Therefore, we can assign this real value directly to the entry time as $Tin_i = Tin^*_i$. As shown in Figure 4.7 (a), we assume that

Type 2 and 4 vehicles that travel during the drone period exit earlier than Type 5 vehicles that enter during the no-drone period. Therefore, the first $N_2 + N_4$ vehicles of $\mathbf{Tout}_s$, i.e., $\mathbf{Tout}_s^{1:N_2+N_4}$, are randomly assigned to Type 2 and 4 vehicles. Thus, the exit time of the Type 2 and Type 4 vehicles are $Tout_i \sim \mathbf{Tout}_s^{1:N_2+N_4}$. The complete trip length of the Type 2 vehicle is calculated as $L_i = V_i * (Tout_i - Tin_i)$ when V_i shows the individual space-mean speed of vehicle i. V_i is calculated from travel time tt_i and travel distance td_i during the drone period as tt_i/td_i. We assume the individual speed is constant during the drone and no-drone period when $td_i >= 100m$. However, when td_i is shorter than $100m$, V_i values during the drone period may have errors because the observation finished just after the vehicle's departure. Therefore, when $td_i < 100m$, we calculate the vehicle speed during the drone period as tt_i/td_i. Then, the vehicle speed during the no-drone period from t'_s to t_{s+1} is calculated as the average mean speed of the network over 3 minutes before t'_s and after t_{s+1}, i.e., v'_s. The mean speed of the network is calculated by dividing the total travel distance of all vehicles by the total travel time of all vehicles. Thus, the individual space-mean speed is shown as $V_i = (tt_i/(tt_i/td_i) + (Tout_i - Tin_i - tt_i)/v'_s)/(Tout_i - Tin_i)$.

We assign entry times to Type 3 and 4 vehicles from $\mathbf{Tin}_s$. As shown in Figure 4.7 (b), we assume that Type 3 and 4 vehicles that exit during or after the next drone period enter at later times in the no-drone period than Type 5 vehicles that exit during the no-drone period. Therefore, the last $N_3 + N_4$ vehicles of $\mathbf{Tin}_s$, i.e., $\mathbf{Tin}_s^{end-N_3+N_4:end}$, are randomly assigned to Type 3 and 4 vehicles. Thus, the entry times of Type 3 and 4 vehicles can be explained as $Tin_i \sim \mathbf{Tin}_s^{end-N_3+N_4:end}$. For Type 3 (missing entry time) vehicles, the exit times are available from the data. Therefore, we can assign the real data values directly to the exit time as $Tout_i = Tout_i^*$. The complete trip length is calculated as the same as Type 2 vehicles, i.e., $L_i = V_i * (Tout_i - Tin_i)$.

For Type 4 (missing entry and exit time) vehicles, we assign entry and exit times as the same method as Type 2 and 3 vehicles, i.e., $Tout_i \sim \mathbf{Tout}_s^{1:N_2+N_4}$ and $Tin_i \sim \mathbf{Tin}_s^{end-N_3+N_4:end}$. The complete trip length is calculated by the same method as Type 2, i.e., $L_i = V_i * (Tout_i - Tin_i)$.

For Type 5 (missing all) vehicles, entry times Tin_i during the no-drone period are assigned by the rest of $\mathbf{Tin}_s$. Since Type 5 vehicles only appear during the no-drone period, we assume that individual mean speed is $V_i = V'_s$. To assign the exit time, two methods can be considered: 1) assigning exit time randomly from the rest of $\mathbf{Tout}_s$, and 2) assigning exit time according to the complete trip length chosen from trip length distribution. For the first method, we randomly choose exit time $Tout_i$ from the rest of $\mathbf{Tout}_s$ with the limitation that the exit time should be later than the assigned entry time as $Tout_i > Tin_i$. The complete trip length is calculated as $L_i = (Tout_i - Tin_i) * V_i$. For the second method, we choose the $Tout_i$ from the rest of $\mathbf{Tout}_s$ by considering trip length L'_i chosen from trip length distribution and V_i. We assume that the trip length distribution does not change in every drone period, and we use the one trip length distribution derived from the trips of all the drone periods. The trip length distribution is normally created by all the complete trips, i.e., Type 1 vehicles. However, the beginning and end of the drone period lead to a bias for the ratio of long trips because the complete trip lengths of the vehicles that enter the network before or exit after the drone period should have long trip lengths but are not available. The red horizontal lines in Figure 4.8 show the travel time (left figure) and trip length (center figure) of Type 1 vehicles which appear at the beginning and in the middle of the drone period, i.e., the

yellow zone in Figure 4.8 (a) and (b). The blue horizontal lines show the other Type 1 vehicles during the drone period. The right side of the figures show the trip length distribution based on the trips over the target time period shown as red lines in the left and center of the figures. By comparing Figure 4.8 (a) and (b), the ratio of long trips at the beginning of the drone period is somewhat lower than that in the middle of the drone period because the long trips entering before the drone period cannot be observed as complete trips. Therefore, we calculate the trip length distribution based on the vehicles that are in the network for a minute in the middle of each drone period, as shown in Figure 4.8 (b). However, since the drone period is short, some vehicles such as Type 2,3 and 4 vehicles with longer trip lengths than Type 1 vehicles cannot be considered. Therefore, we modify the trip length distribution by considering Type 2, 3, and 4 vehicles. In Figure 4.9 (a), the black curve shows the fitted cumulative distribution function (CDF) of Type 1 vehicle trip lengths by using a Weibull distribution, while the orange line shows the real CDF without fitting. From the beginning, we calculate the accumulation ratio of Type 1 vehicles, i.e., N_1, and all the vehicles that exist during the drone period, i.e., $N_1 + N_2 + N_3 + N_4$. This ratio shows the number of observed complete trip lengths versus all trip numbers. To consider the long complete trip length that we cannot observe in the data, we first scale down the fitted CDF of Type 1 vehicles by the ratio shown by the horizontal dashed line at 0.88 in Figure 4.9 (a). Now, the original CDF shown as a black solid curve becomes the black dashed line with a maximum limitation of 0.88. Since the amount of the short trip should be similar to N_1, we keep the dashed black curve smaller than $1000m$ and create 50000 sample trip lengths based on this limited CDF to recalculate the modified CDF by using the Weibull distribution. The blue curve in the figure shows the modified CDF. Figure 4.9 (b) shows the trip length distribution based on Type 1 vehicles as black bars and the modified distribution, which is derived from the 50000 sample trip lengths based on the modified CDF, as blue bars. The curves show the fitted Weibull distribution, and vertical lines show the average values of each distribution. Based on L_i' chosen from the modified distribution, as shown in Figure 4.9 (b), the closest value to $Tin_i + L_i'/V_i$ is assigned to $Tout_i$ from $\mathbf{Tout}_s$. Finally, the complete trip length is modified as $L_i = V_i * (Tout_i - Tin_i)$.

4.2.3 Parameter Comparison of a Whole Network Before and After Data Imputation

Here, we verify that the dynamics of parameters after data imputation are stable, e.g., without a sudden drop or rise in the values, by comparing them with the parameters calculated by the original data. Between the two methods for assigning exit time of Type 5 vehicles mentioned in Section 4.2.2, the inflow, outflow, mean speed, and accumulation dynamics do not differ. However, the results of the trip length distribution and trip length dynamics are quite different. Therefore, we first describe the results of the parameters except for trip length distribution and dynamics based on method 2, which assigns exit time according to the complete trip length chosen from trip length distribution. Then, we compare the results of the trip length distribution and trip length dynamics between method 1, which assigns exit time randomly from the rest of $\mathbf{Tout}_s$, and method2.

In Figure 4.10, the black lines show the parameters calculated directly from the original data for the drone period. For the inflow, outflow, and mean speed shown in Figure 4.10 (a), (b), and (c), the black lines during the no-drone period show the input value of data

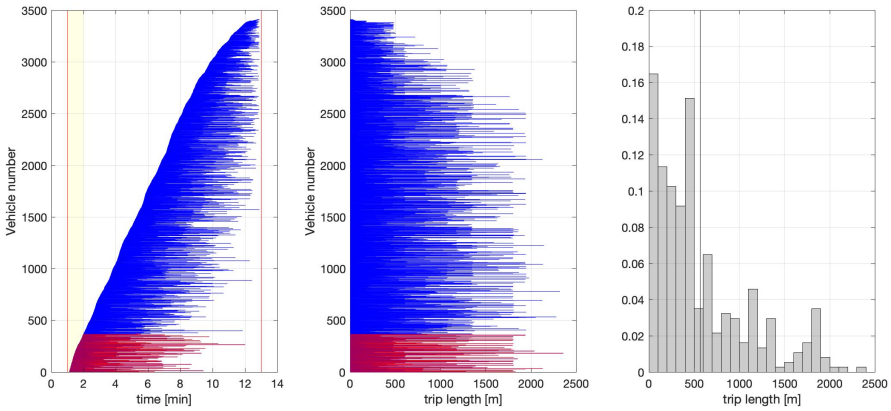

(a) using the first 1 minute of drone period

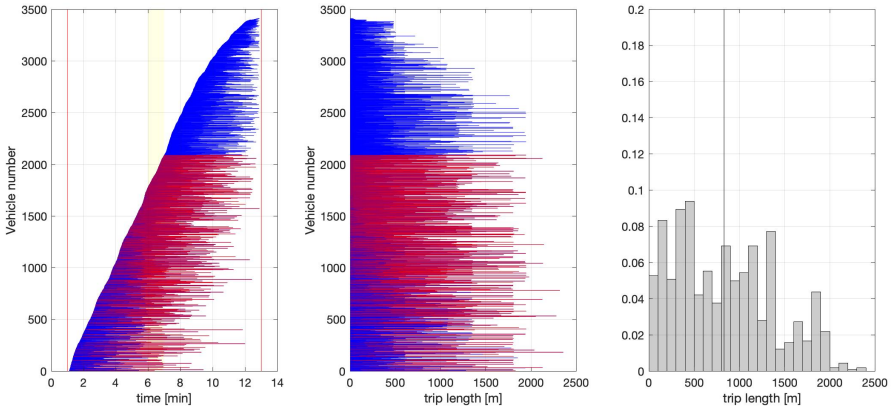

(b) using the middle 1 minute of the drone period

FIG. 4.8 – *Travel time (left) and Trip length (center) of vehicles, and trip length distribution (right) according to the concerned time period. (yellow zone: the time period for trip length distribution calculation, red horizontal lines: Type 1 vehicles appeared in the concerned time period, blue horizontal lines: Type 1 vehicles do not appear in the concerned time period)*

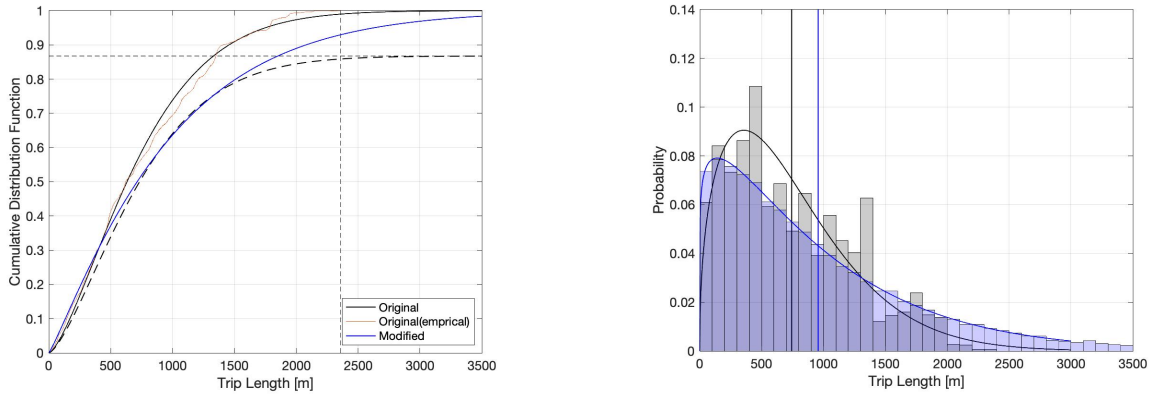

(a) Cumulative Distribution Function

(b) Trip Length Distribution

FIG. 4.9 – *Modification of Trip Length Distribution (Black: original data, Blue: after modification)*

imputation, which are qin'_s, $qout'_s$, and v'_s. For the accumulation in Figure 4.10 (d), the black lines are not shown during the no-drone period since it is not available from the original data alone, and we do not use the average value as the input value. The red lines show the parameters calculated by trajectories after data imputation. The inflow and outflow are calculated by counting the vehicles which enter and exit the network every minute. The mean speed is calculated by the total travel time divided by the total travel distance of all the vehicles inside the network every minute. Each vehicle's travel time and distance during the drone periods are calculated every minute based on the real trajectories of the original data. During the no-drone period, the travel time is calculated from the assigned entry and exit times as $Tout_i - Tin_i$. However, detailed travel distances every minute are not available since we assign only entry, exit time, and the complete trip length. Therefore, we assume travel distance as constant and divide the complete trip length L_i by travel time. Accumulation is calculated based on Edie's formula, i.e., the total travel time of all the vehicles during one minute divided by one minute.

As shown in Figure 4.10 (a), the inflow after data imputation completely fits with the original data for most of the time during the drone period. Only at the beginning of each drone period does the inflow become lower after data imputation because Type 3 vehicles are considered as entering the network or starting their trips at the beginning of the drone period in the original data whereas they are assumed as entering the network or starting trips during the no-drone period after data imputation. During the no-drone period, the inflow after data imputation is slightly different from the black lines, i.e., qin'_s. This difference is derived from adjusting the link length of $\mathbf{Tin}_s$ with the length in $\mathbf{Tout}_s$ to fit the amount of Type 4 vehicles in both lists. The outflow after data imputation also completely fits with the original data except at the end of the drone period and during the no-drone period, as shown in Figure 4.10 (b). At the end of each drone period, the outflow decreases after data imputation because of the Type 2 vehicles which are considered as exiting the network or ending their trips at the end of the drone period in the original data. These vehicles are assumed to exit the network or end their trips during the no-drone period after data imputation. The difference between the red and black lines during the no-drone period is derived from the same reason as the inflow since both the inflow and outflow during the no-drone period are obtained using the same method, c.f., see Section 4.2.2. In Figure 4.10 (c), the mean speed after data imputation follows the dynamics of original data. The values are not entirely the same even during the drone period because the travel time and travel distance of Type 2, 3, and 4 vehicles are changed after data imputation. The accumulation after data imputation is exactly the same as that of the original data during the drone period, as shown in Figure 4.10 (d). Also, the values between each drone period are smoothly connected without any sudden drop or rise after data imputation. The total accumulation of Type 1, 2, 3, and 4 vehicles during a whole period are the same before and after data imputation, i.e., Type 1: 16833 veh, Type 2: 5204 veh, Type 3: 4793 veh, and Type 4: 12 veh. There are 24051 Type 5 vehicles after data imputation. The accumulation dynamics of each missing data type before and after imputation are shown in Figure 4.11 (a) and (b). At the beginning and the end of the drone period, the accumulation of Type 1 vehicles is low whereas the accumulation of Type 2 and 3 vehicles increases considerably. The accumulation dynamics of Type 2 and 3 vehicles expand at the beginning and at the end of the no-drone period after data imputation. Type 4 vehicles are quite numerous. However, the accumulation dynamics expand at the beginning and at the end of the no-drone period. The accumulation dynamics of Type

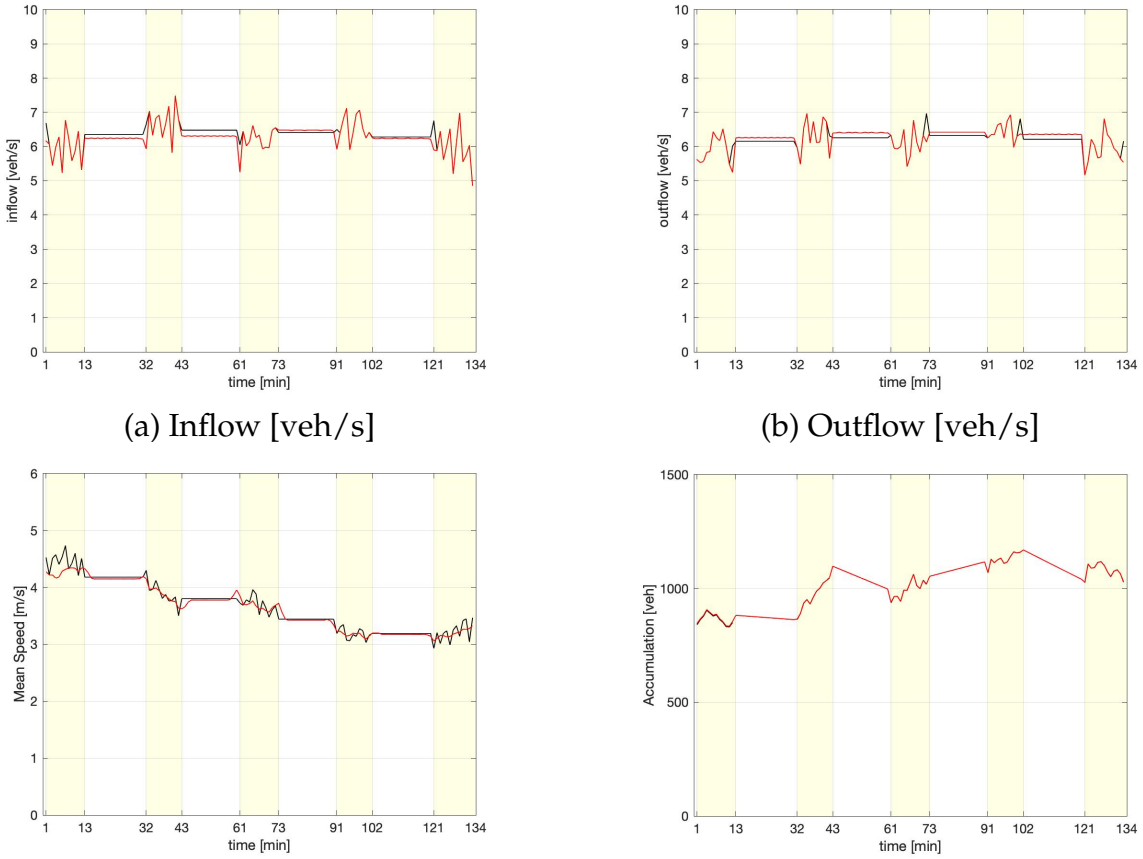

(a) Inflow [veh/s]

(b) Outflow [veh/s]

(c) Mean Speed [m/s]

(d) Accumulation [veh]

FIG. 4.10 – *Traffic state dynamics before (black lines) and after data imputation (red lines). (yellow zone: drone period, white zone: no-drone period)*

5 vehicles only appear during the no-drone period after data imputation. At the beginning and at the end of the no-drone period, the accumulation of Type 4 vehicles is low while the accumulation of Type 2 and 3 vehicles increases considerably.

Figures 4.12 and 4.13 show the trip length distribution (a) and trip length dynamics (b) according to two methods for assigning the exit times. In (a) of the figures, the black bars show the trip length distribution based on Type 1 vehicles, which is the same as the original data and as the black bars in Figure 4.9 (b), while the red bars show the trip length distribution based on all the vehicles after data imputation. The curves show the fitted Weibull distribution, and the vertical lines show the average values of each distribution. In (b) of the figures, the black line shows the trip length dynamics of the Type 1 vehicles of the original data. The trip length dynamics are calculated every minute by averaging the complete trip lengths of vehicles that exist at the time. As mentioned in Section 4.2.2, the ratio of vehicles with long trip lengths decreases at the beginning and end of the drone period before data imputation, as shown in Figure 4.8. Therefore, the average value of the trip length gets lower at the beginning and the end of the drone period. The red line shows the dynamics after data imputation. As shown in Figure 4.12 (a), method 1 provides smooth trip length distribution, e.g., whose form is close to the fitted Weibull distribution, with more very short trip lengths,

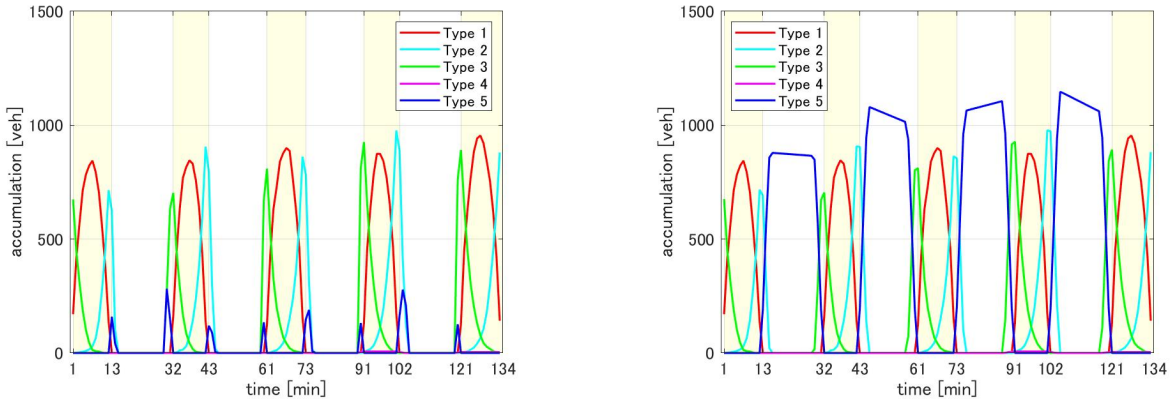

(a) original data (b) after data imputation

FIG. 4.11 – *Accumulation of each trip type (yellow zone: drone period, white zone: no-drone period)*

e.g., less than $200m$, than the distribution before data imputation. Since exit times are chosen randomly from $\mathbf{Tout}_s$ without any limitation of trip lengths, some entry times at the end and exit times at the beginning of the no-drone period are assigned to the Type 5 vehicles with very short trip lengths. This fact is clearly shown by the drop at the beginning and at the end of the no-drone period in Figure 4.12 (b). On the other hand, the Type 5 vehicles which enter at the beginning of the no-drone period can have very long trip lengths when the exit times are assigned at the end of the no-drone period. Therefore, the trip length of these vehicles can be longer depending on the length of the no-drone period, leading to a higher average value at the middle of the no-drone period, as shown in Figure 4.12 (b). At the beginning and the end of the drone period, the average trip length dynamics after data imputation is around $100m$ larger than the original one because Type 2 and 3 vehicles are assigned longer trip lengths to exit or enter during the no-drone period. Even in the middle of the drone period, the values after data imputation are slightly higher because of Type 2, 3, and 4 vehicles that are not used to calculate trip length distribution and dynamics before data imputation. By using method 2, the trip length distribution after data imputation has a peak point around from 700 to $900m$ instead of the lower amount for long trip lengths over $1000m$, as shown in Figure 4.13 (a). This is because we assign a maximum limitation for trip length of Type 5 vehicles to make them exit before the end of the no-drone period to maintain the outflow dynamics. Although the trip length distribution is not smooth when we use method 2, the average trip length dynamics is smoother than with method 1, as shown in Figure 4.13 (b), e.g., the gap value between at the beginning or end of the drone period and during the no-drone period is less than $150m$ in Figure 4.13 (b) while it is around $200 - 300m$ in Figure 4.12 (b). Thus, we can have smooth trip length distribution, but the average dynamics fall significantly and rise when we use method 1, whereas when we use method 2 we can have smooth average dynamics, but the high peaks of the trip length distribution differ from those of the original distribution. In the MFD model comparison in the following sections, we use static trip length distribution as the input parameter of the models. Trip length distribution built on average trip length dynamics with huge gaps may lead to additional errors in the prediction results affecting the accuracy of the MFD model. Therefore, we decided to use the discrete trip length distribution calculated by method 2,

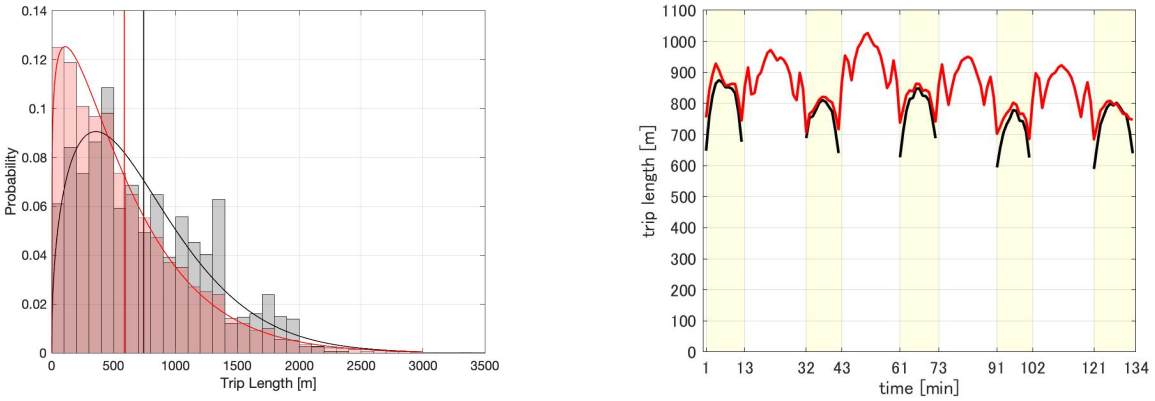

(a) Trip Length Distribution (b) Average Trip Length Dynamics

FIG. 4.12 – *Trip Length before (black) and after (red) data imputation by Method 1, i.e., assigning exit time randomly from the rest of* $\mathbf{Tout}_s$. *(yellow zone: drone period, white zone: no-drone period in (b))*

because its trip length dynamics is more stable than with method 1.

Thus, the parameters of the network during the no-drone period are compensated, and we obtain the continuous vehicle information for a whole 2.5 hours. In the following sections, we use these parameters after data imputation calculated by method 2 as the input of the MFD models.

4.2.4 Path Sequence Definition

The path sequence showing the order of the regions passed in the network by individual vehicles is useful information when considering MFD models for several regions. In addition to the path sequence, regional trajectory information such as the entry and exit time and trip lengths of each region according to the path sequence is necessary to estimate the ground truth regional traffic state. Therefore, we determine the path sequence, regional entry and exit time, and trip length in each region for all the trajectories for which we assign the entry and exit time of the network and complete trip length in Sections 4.2.2 and 4.2.3. All the new indexes in this section are explained in Table 4.2.

From the beginning, we define path sequence PS_i as a vector of regions r ordered by the timing which the vehicle i passes through. It can be denoted as $PS_i = [r_{i,1}, r_{i,2}, \ldots, r_{i,p}, \ldots r_{i,|PS_i|}]$ while $r_p = r \in R$ where p is the ordering number in the path sequence and R is the group of regions in the network. We denote the entry time of vehicle i in each region at pth of PS_i as $tin_{i,p}$, and the exit time as $tout_{i,p}$. Note that the entry time of the beginning of the path sequence and the exit time of the end of the path sequence should be the same as the entry and exit times of the network, e.g., $tin_{i,1} = Tin_i$, and $tout_{i,|PS_i|} = Tout_i$. The trip length in each region is denoted $l_{i,p}$, and the sum of these partial trip lengths should equal the complete trip length, e.g., $\sum_{p=1:|PS_i|}(l_{i,p}) = L_i$.

For Type 1 vehicles, regional trajectory information can be derived directly from observations. Therefore, we use the real path sequence and real values of entry, exit time, and trip length of each region as $PS_i = PS_i^* = [r_{i,1}^*, r_{i,2}^*, \ldots, r_{i,p}^*, \ldots r_{i,|PS_i|}^*]$, $tin_{i,p} = tin_{i,p}^*$, $tout_{i,p} = tout_{i,p}^*$, and $l_{i,p} = l_{i,p}^*$.

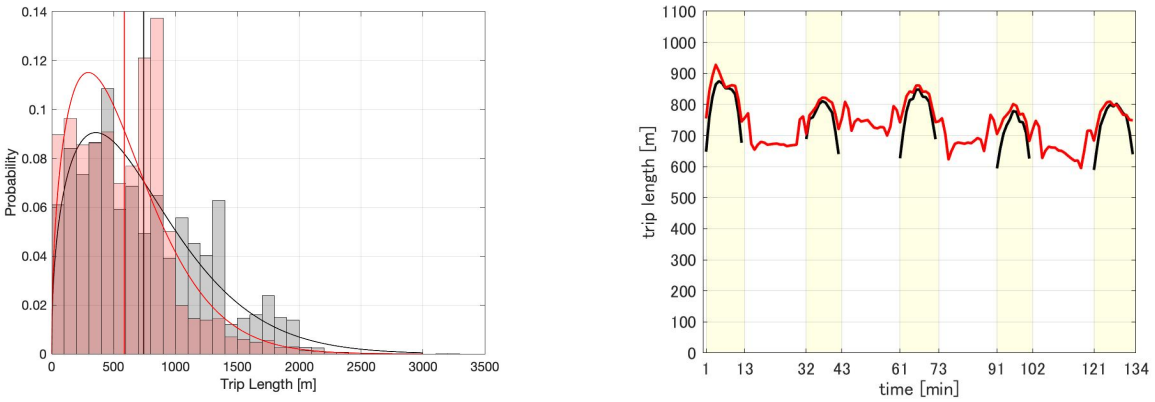

(a) Trip Length Distribution (b) Average Trip Length Dynamics

FIG. 4.13 – *Trip Length before (black) and after (red) data imputation by Method 2, i.e., assigning exit time and trip length according to trip length distribution. (yellow zone: drone period, white zone: no-drone period in (b))*

For the vehicles of the other types, the entry, exit time, and the complete trip length of a whole network are already assigned in Section 4.2.2. Therefore, we need to define which path sequence to assign in a consistent manner with existing information and in particular the actual network entry and exit time. Firstly, the conditional path sequence distribution according to the complete trip length of a whole network $P(PS_i^*|L_i^*)$ is calculated based on real path sequences and the complete trip lengths of Type 1 vehicles.

For Type 2 vehicles, regional information on the beginning of the path sequence is available from data as PS_i^*. We need to complete the following part of the path sequence PS_i^* until the vehicle exits at the assigned exit time $Tout_i$. Also, the entry time at the end of PS_i^*, i.e., $tin_{i,|PS_i^*|}$, is available from the data, but the exit time is not available from the data since we only have the assigned exit time from the network during the no-drone period. Therefore, we keep the regional trajectory information of data from the beginning of the path sequence $p = 1$ until that before the end of the observed path sequence $p = |PS_i^*| - 1$. When we express $()'$ for the remaining part of regional information from $p = |PS_i^*| - 1$ until the end of the trip at $Tout_i$, the path sequence of the remaining part can be labeled as $PS_i' = [r_1', r_2', \dots r_{p'}', \dots r_{|PS_i'|}'$ where p' is the ordering number of the remaining part and $r_{p'}' = r \in R$. Also, the sum of the trip length and travel time of the remaining part is denoted L_i' and TT_i', and the regional entry and exit time of the remaining part p' is denoted $tin_{i,p'}'$ and $tout_{i,p'}'$. Note that the entry time and the region at the beginning of the remaining path sequence $p' = 1$ should be the same as at the end of the path sequence from data $p = |PS_i^*|$, i.e., $tin_{i,1}' = tin_{i,|PS_i^*|}^*$ and $r_{i,1}' = r_{i,|PS_i^*|}$. We firstly assign the remaining path sequence PS_i' which starts from $r_{i,1}'$ by choosing from the conditional path sequence distribution according to L_i', i.e., $PS_i' \sim P(PS_i^*|L_i', r_{i,1}')$. The list length of the pass sequence PS_i', i.e., the number of passing regions at the remaining part, is $NS_{i,r}'$. L_i' and TT_i' are calculated by using the regional information from the data, the assigned complete trip length L_i, and the assigned exit time $Tout_i$ as $L_i' = L_i - \sum(l_{i,1}^*, \dots l_{i,|PS_i^*|-1}^*)$ and $TT_i' = Tout_i - tin_{i,1}'$. For the individual

Variables	
p	the ordering number in the path sequence
R	the group of regions in the network
PS_i	a vector of regions $r \in R$ ordered by the timing which the vehicle i passes through
$tin_{i,p}$	Entry time of vehicle i into the region at the ordering number p
$tout_{i,p}$	Exit time of vehicle i from the region at the ordering number p
$l_{i,p}$	the partial trip length of vehicle i at the ordering number p
$P(PS_i^*\|L_i^*)$	conditional path sequence distribution according to the complete trip length of a whole network
$v'_{s,r}$	the average mean speed of each region r over 3 minutes before the end of drone period t'_s and after the beginning of the next drone period t_{s+1}
p'	the ordering number of the path sequence during no-drone period
L'_i	total trip length during no-drone period
TT'_i	total travel time during no-drone period
$tin'_{i,p'}$	the entry time of vehicle i at p'
$r'_{i,p'}$	the region that vehicle i passes through at p'
$NS'_{i,r}$	the number of regions r passed through in the pass sequence PS'_i
$NS_{i,r}$	the number passing regions r passed through in the pass sequence PS_i

TAB. 4.2 – *Lists of Variables used in Section 4.2.4*

speed at the remaining part $v'_{i,p'}$ during the no-drone period from t'_s, we assume that the individual speed is constant at the average mean speed of each region r, i.e., $v'_{s,r}$, which is calculated over 3 minutes before the end of the drone period t'_s and after the beginning of the next drone period t_{s+1}. We also assume that the partial trip length and travel time of each vehicle in each region are always the same in the path sequence. We can then denote all the partial trip lengths and travel times of vehicle i in the remaining path sequence as $l'_{i,r}$ and $tt'_{i,r}$ where $r'_{p'} = r$. Under these assumptions, L'_i, TT'_i, and $v'_{i,p'}$ can be expressed by using $l'_{i,r}$, $tt'_{i,r}$, and $NS'_{i,r}$, as below:

$$\begin{aligned} TT'_i &= \sum_r (tt'_{i,r} * NS'_{i,r}) \\ L'_i &= \sum_r (l'_{i,r} * NS'_{i,r}) \\ v'_{i,p'} &= v'_{s,r} = tt'_{i,r}/l'_{i,r} \end{aligned} \tag{4.1}$$

If $l'_{i,r}$ and $tt'_{i,r}$ are fully negative when applying Eq. (4.1), we sample the remaining path sequence PS'_i again until we obtain the positive values. Finally, we add the remaining path sequence PS'_i after the path sequence from data PS_i^* to obtain the assigned path sequence as $PS_i = [r_1^*, \ldots, r^*_{|PS_i^*|-1}, r'_1, \ldots, r'_{|PS'_i|}]$. The partial trip length pth, the entry-, and the exit times of PS_i are $l_{i,p} = l_i^*$, $tin_{i,p} = tin_{i,p}^*$, and $tout_{i,p} = tout_{i,p}^*$ while $p <= r^*_{|PS_i^*|-1}$, and $l_{i,p} = l'_{i,r}$, $tin_{i,p} = tout_{i,p-1}$, and $tout_{i,p} = tout_{i,p-1} + tt'_{i,r}$ where $r = r_p$ while $p > r^*_{|PS_i^*|-1}$.

For Type 3 vehicles, regional information on the end of the path sequence is available from the data as PS_i^*. We need to assign the path sequence which starts from the assigned

entry time Tin_i and connects with the following PS_i^*. The exit time at the beginning of PS_i^*, i.e., $tout_{i,1}$, is available from data, but the entry time is not available since it passes during the no-drone period. Therefore, we keep the regional information on that after the beginning of the path sequence $p = 2$ until the end $p = |PS_i^*|$. We denote $()'$ as the remaining part, which we need to assign in the path sequence as Type 2 vehicles. Now, the remaining part is from the beginning of the trip at Tin_i until the beginning of PS_i^*. The exit time and the region at $p' = |PS_i'|$ should be the same as the exit time and the region at the beginning of PS_i^*, i.e., $tout'^{i,|PS_i'|=tin_{i,1}^*}$ and $r'_{i,|PS_i'|} = r_1^*$. Similarly, for Type 2 vehicles, we assign the path sequence PS_i' from the conditional path sequence distribution to make it end in the same region at the beginning of the path sequence from the data, i.e., $r'_{i,|PS_i'|} = r^*_{i,1}$. Therefore, the remaining path sequence can be shown as $PS_i' \sim P(PS_i^*|L_i', r'_{i,|PS_i'|})$. By using the assigned complete trip length L_i and entry time Tin_i, the sum of trip length L_i' and travel time TT_i' of the remaining part is calculated as $L_i' = L_i - \sum(l^*_{i,2}, \dots l^*_{i,|PS_i^*|})$ and $TT_i' = tout'_{i,|PS_i'|} - Tin_i$. To calculate $tt'_{i,r}$ and $l'_{i,r}$ of Type 3 vehicles, we solve the simultaneous equations in Eq. (4.1) in the same way as for Type 2 vehicles. Finally, the path sequence of vehicle i is shown by adding PS_i' before PS_i^* as $PS_i = [r'_{i,1}, \dots, r'_{i,|PS_i'|}, r^*_{i,2}, \dots, r^*_{i,|PS_i^*|}]$. The pth partial trip length, the entry-, and the exit time of PS_i are $l_{i,p} = l'_{i,r}$, $tin_{i,p} = tout_{i,p-1}$, and $tout_{i,p} = tout_{i,p-1} + tt_{i,r}$ where $r = r_p$ while $p < r_{i,|PS_i'|}$, and $l_{i,p} = l_i^*$, $tin_{i,p} = tin^*_{i,p}$, and $tout_{i,p} = tout^*_{i,p}$ while $p >= r_{i,|PS_i'|}$. Note that $tin_{i,1} = Tin_i^*$.

For Type 4 vehicles, the beginning of the path sequence is not available as Type 3 vehicles and the end as Type 2 vehicles. Therefore, we complete the beginning and end parts of the path sequence by using the same methods as for Type 2 and Type 3 vehicles.

For Type 5 vehicles, no regional trajectory information is available. Therefore, the whole path sequence is chosen directly from the conditional path sequence distribution according to the assigned complete trip length L_i as $PS_i \sim P(PS_i^*|L_i)$. Under the assumption that the partial travel time and trip length are constant in each region as Type 2, 3, and 4 vehicles, we denote all travel times and trip lengths in the region r in the path sequence PS_i as $tt'_{i,r}$ and $l'_{i,r}$. Also, we assume the speed of vehicle i in region r is the same as $v_{s,r}$. When $NS_{i,r}$ shows the number of region passed r in the pass sequence PS_i, $tt'_{i,r}$ and $l'_{i,r}$ can be calculated by the simultaneous equations below:

$$\begin{aligned} &\sum_r (tt'_{i,r} * NS_{i,r}) = Tout_i - Tin_i \\ &\sum_r (l'_{i,r} * NS_{i,r}) = L_i \\ &tt'_{i,r}/l'_{i,r} = v'_{s,r} \end{aligned} \tag{4.2}$$

By using $tt'_{i,r}$ and $l'_{i,r}$ from Eq. (4.2), the partial trip length at pth in the path sequence PS_i can be expressed as $l_{i,p} = l'_{i,r}$, and the entry time and exit times are $tin_{i,p} = tout_{i,p-1}$ and $tout_{i,p} = tout_{i,p-1} + tt_{i,r}$ when $r = r_p$.

4.2.5 Comparison of Regional Parameters Before and After Data Imputation

To verify that the variables representing the regional traffic state after data imputation are stable, i.e., no sudden value drop and rise observed in the real normal situation, we use the two region network explained in Chapter 3, i.e., congested and less-congested pockets when the partitioning weight on speed is $w = 6.7$. The regional inflow and outflow of each pocket are calculated by counting the vehicles entering and exiting each pocket every minute. Regional mean speed is calculated every minute by the total travel time divided by the total travel distance of all the vehicles inside the pocket. The regional accumulation is calculated based on Edie's formula using the total travel time of each pocket. In Figure 4.14, the black lines show the parameters calculated directly from the original data for the drone period and the average values over 3 minutes before the end of the drone period and after the beginning of the next drone period for the no-drone period. The solid and dashed lines show the parameters in the congested pocket and less-congested pocket. The solid red lines show the variables after data imputation in the congested pocket, and the blue dashed lines show the variables in the less-congested pocket. Figures 4.14 (a) and (b) indicate that the regional inflow and outflow after data imputation are almost the same values as the original data in both pockets during the drone period. At the beginning and the end of the drone period, the values are sometimes slightly different because of Type 2,3 and 4 vehicles for which we have modified the regional entry and exit times from the drone period to the no-drone period. This is clarified in Figure 4.14, which shows the regional starting inflow, i.e., the inflow of the vehicles which start their trips or enter into the network, and the transferring inflow, i.e., the inflow of the vehicles which come from another pocket. At the beginning of the drone period, the starting inflow after data imputation, especially in the congested pocket, i.e., the red line in Figure 4.14 (a), is sometimes lower than the original starting inflow, i.e., the black line in the figure, and the transferring inflow after data imputation is higher than the original transferring inflow. Thus, the modification of Type 3 and 4 vehicles reflect the regional inflow dynamics. During a whole period, the inflow and outflow in the congested pocket are around 1 to 3 veh/s less than in the less-congested pocket, both before and after data imputation. Also, there is no sudden drop or rise in values in either pocket after data imputation during the no-drone period. Figure 4.14 (c) shows that the regional mean speed in the congested pocket after data imputation (the solid red line) follows the dynamics from the original data (the solid black line). The mean speed in the less-congested pocket after the data imputation (the dashed blue line) is around 0.3 to 0.8 m/s lower than the original data (the dashed black line) since the regional trip length and travel time were changed because of the modification of path sequences for Type 2, 3, and 4 vehicles, especially at the beginning and the end of the original path sequence. The regional accumulation is shown in Figure 4.14 (d). The values after data imputation in both pockets are almost the same as from the original data during the drone period. The value is lower in the congested pocket and higher in the less-congested pocket, or vice versa, only for the 1st minute of the beginning and the last minute at the end of certain drone periods,. It is also derived from our assignment method for the path sequence of Type 2, 3, and 4 vehicles for which the beginning and the end of the path sequence of original data are modified to adapt the complete trip length and total travel time as a whole network. Note that the sum of accumulations in both pockets is the same as the dynamics shown in Figure 4.10 (d).

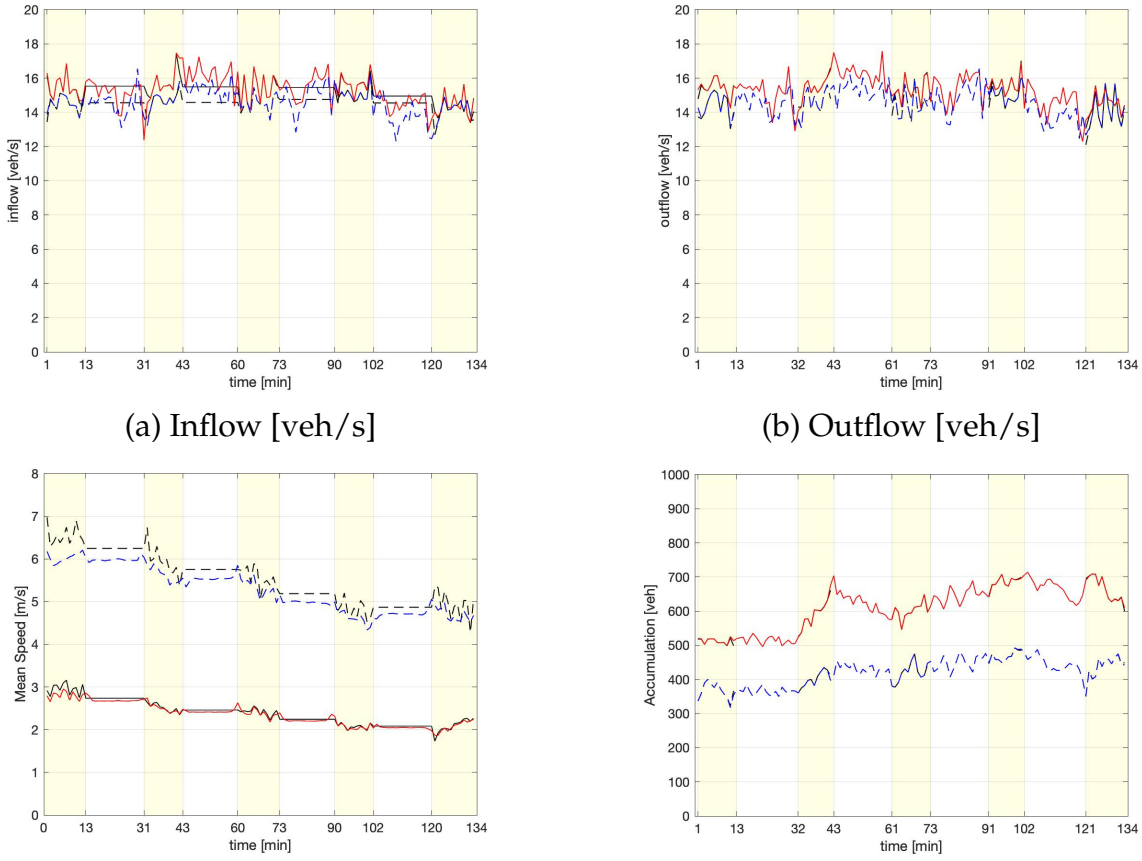

(a) Inflow [veh/s]

(b) Outflow [veh/s]

(c) Mean Speed [m/s]

(b) Accumulation [veh]

FIG. 4.14 – *Regional traffic state variables before and after data imputation (yellow zone: drone period, white zone: no-drone period, solid lines: in congested pocket, dashed lines: in less-congested pocket, black lines: using original data, red/blue lines: using the trip set after data imputation)*

During the no-drone period, the dynamics in both pockets are smoothly connected between the drone periods.

Regional trip length distribution and average trip length dynamics are shown in Figures 4.16 and 4.17. The regional trip length of each vehicle is calculated as the sum of the partial trip length in each pocket. In Figure 4.16, the black bars show the regional trip length distribution based on Type 1 vehicles, and the red bars in (a) and blue bars in (b) show that based on all the vehicles after data imputation in congested and less-congested pockets. The curves in Figure 4.16 show the fitted Weibull distribution, and the vertical lines show the average values of each distribution. After data imputation, the regional trip length distributions have a different peak, i.e., at around 100 to 400 m in the congested pocket and around 400 to 600 m in the less-congested pocket, and drop, i.e., over 400 m in the congested pocket and over 600 m in the less-congested pocket. The maximum trip length limitation of Type 5 vehicles to make the vehicles enter and exit the network during the no-drone period in our method affects the regional trip length distribution shapes besides the complete trip length distribution, with a peak point around 700 to 900 m, as shown in Figure 4.13 (a). Figure 4.17, shows that the regional average trip lengths have a constantly similar gap in two pockets,

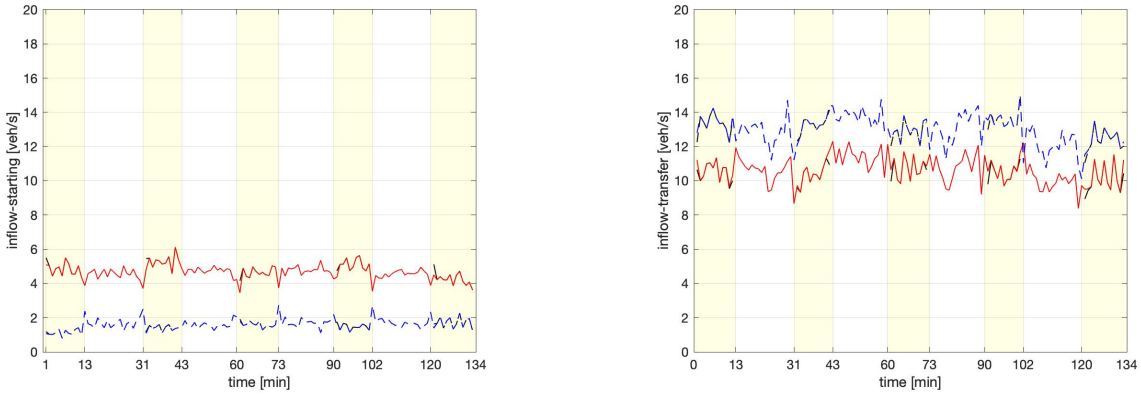

(a) Starting inflow [veh/s] (b) Transferring inflow [veh/s]

FIG. 4.15 – *Regional starting and transferring inflow before and after data imputation (yellow zone: drone period, white zone: no-drone period, solid lines: in congested pocket, dashed lines: in less-congested pocket, black lines: using original data, red/blue lines: using the trip set after data imputation)*

i.e., the trip length in less- congested pockets is around 150 to 200 m higher than in the congested pocket. In both the congested and less-congested pockets, the regional trip length dynamics during the drone period shows a small difference between before and after data imputation, especially at the beginning and end of the drone period because of Type 2 and 3 vehicles.

Thus, all the results correspond to the results of a whole network, and the parameters clearly show different characteristics in the two pockets. Therefore, like the regional traffic state variables in a whole network shown in Section 4.2.3, we use these variables after data imputation to assess the impact of MFD calibration.

4.3 MFD Model Formulation

The accumulation-based and trip-based models are the most common Macroscopic Fundamental Diagram (MFD) models. In this section, we first introduce the definition of MFD and describe the framework of both models in a single region setting. More advanced settings with two regions will be investigated in the next chapter. The indexes that appear in the following subsections are summarized in Table 4.3.

4.3.1 MFD

MFD is the relationship between average flow, density, and mean speed in a whole network. Its existence was initially verified with microscopic simulation studies by Mahmassani (1984) and Mahmassani (1987) and with real data by Geroliminis & Daganzo (2008).

The average flow Q[veh/s] and density K [veh/m] in the network can be calculated from total travel distance TTD [m], i.e., the sum of the distance traveled by all vehicles during the period dt [s], and total travel time TTT [s], i.e., the sum of the time spent by all the vehicles

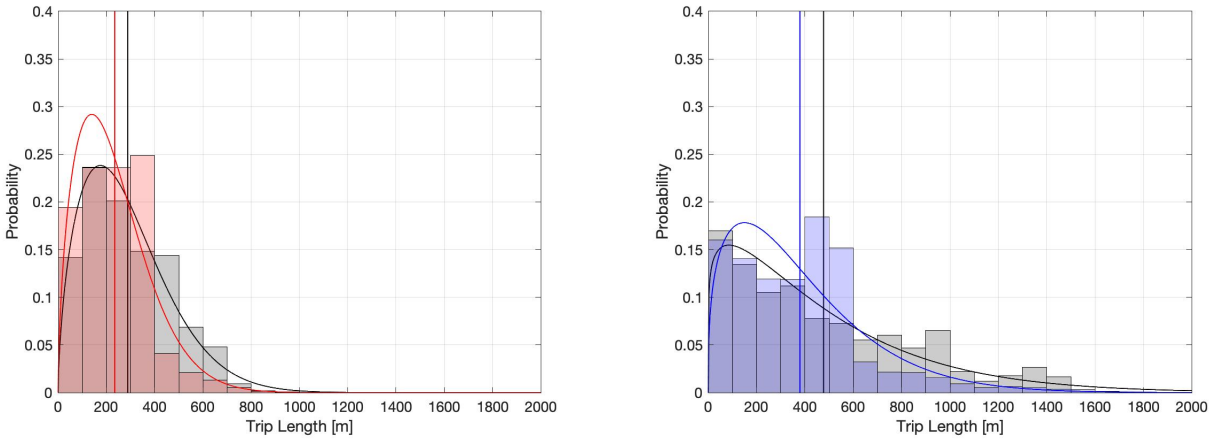

(a) Congested Pocket (b) Less-Congested Pocket

FIG. 4.16 – *Trip Length Distribution (black bars: calculated from original data, red/blue bars: calculated from the trip set after data imputation, curve lines: approximated Weibull distribution, vertical lines: average values)*

during the period dt as Eq. (4.3).

$$\begin{aligned} Q &= TTD/(l_r * dt) \\ K &= TTT/(l_r * dt) \end{aligned} \tag{4.3}$$

where l_r [m] is the total link length of the network R. The average mean speed of all the vehicles is denoted V [m/s], MFD can be expressed as $Q(K(t)) = V(t) * K(t)$, similar to the well-known FD formula, i.e., $q_l(k_l(t)) = v_l(t) * k_l(t)$ when q_l, v_l, and k_l are flow, mean speed and density of a link l at time t. Using the MFD formula, the average mean speed can be calculated as Eq. (4.4).

$$V = Q/K = TTD/TTT \tag{4.4}$$

The average flow and density can be easily transformed into regional variables such as production P [veh*m/s], i. e., the quantity of trips that can be performed during the period dt, and the accumulation n [veh], i. e., the number of vehicles in the network during period dt, by Eq. (4.5).

$$\begin{aligned} P &= Q * l_r = TTD/dt \\ n &= K * l_r = TTT/dt \end{aligned} \tag{4.5}$$

By using this transformation, MFD can also be transformed by Eq (4.6) and (4.7).

$$P(n(t)) = V(t) * n(t) \tag{4.6}$$

$$V(n(t)) = P(t)/n(t) \tag{4.7}$$

The relation between production and accumulation in Eq. (4.6) is called Production-MFD (P-MFD), and the relation between speed and accumulation in Eq. (4.7) is called Speed-MFD (V-MFD).

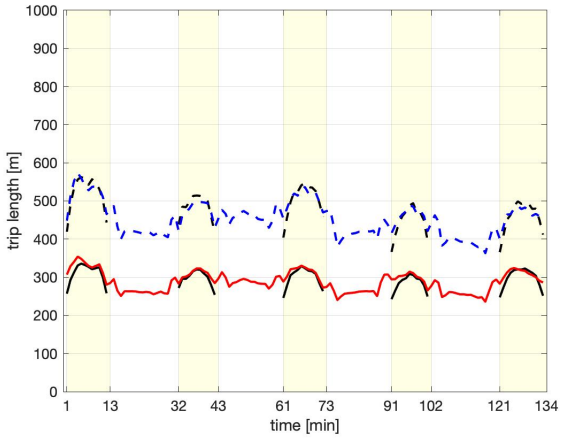

FIG. 4.17 – *Average Trip Length Dynamics (yellow zone: drone period, white zone: no-drone period, solid lines: in congested pocket, dashed lines: in less-congested pocket, black lines: using original data, red/blue lines: using the trip set after data imputation)*

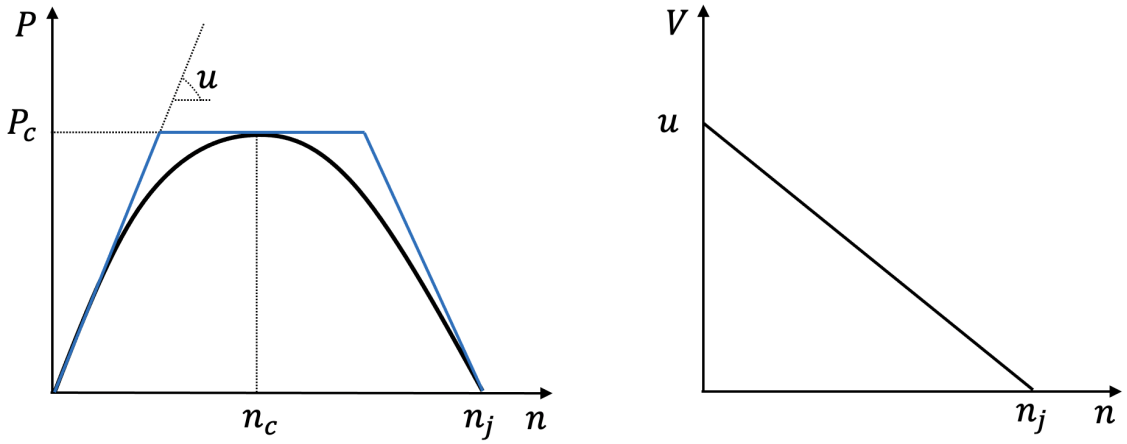

(a) Production MFD (b) Speed MFD

FIG. 4.18 – *Typical Simple Definition of Approximated MFDs*

P-MFD and V-MFD are often defined as a linear formation by approximating from the values of data. Figure 4.18 shows the typical simple definition of P-MFD (a) and V-MFD (b). To decide the shape of the approximated MFDs, several important variables are estimated that correspond to the MFD characteristics, as shown in Figure 4.18. The critical production P_c expresses the maximum throughput of the network, which corresponds to the network production capacity. The critical accumulation n_c is the border between the free flow state ($n < n_c$) and the congested state ($n > n_c$). In the definition, when the accumulation is n_c, the production reaches P_c. However, since a single value for n_c is often quite hard to estimate, P_c is sometimes defined from n_{c1}, the maximum accumulation limit of the free-flow state, to n_{c2}, which is the minimum accumulation limit of the congested state. At this time, the P-MFD has a trapezoidal shape as shown by the blue line in Figure 4.18 (a) instead of a parabolic shape as shown by the solid black line. The free flow speed u is the average maximum speed of all the vehicles in the network. In the parabolic P-MFD, u corresponds

Variables	Definition
Q	the average flow [veh/s] in the network
K	the average density [veh/m] in the network
TTD	the total travel distance [m] traveled by all the vehicles in the network during the period dt
TTT	the total travel time [s] traveled by all the vehicles in the network during the period dt
l_r	the total link length [m] of the network r
V	the average mean speed [m/s] in the network
P	the production [veh*m/s] in the network
n	the accumulation [veh] in the network
t	calculation time step
$P(n(t))$	the Production-MFD (P-MFD) at time t
$V(n(t))$	the Speed-MFD (V-MFD) at time t
L	the complete trip length [m] for all the vehicles
$Qout$	the outflow for exiting from a network or ending trips in a network
Qin	the inflow for entering a network or starting trips in a network
L_i	the complete trip length [m] of a vehicle i
tt_i	the travel time [s] of a vehicle i
Tin_i, $Tout_i$	the entry and exit time of a vehicle i
$time(t)$	time at the time step t
$dNin$, $dNout$	the number of vehicles entering and exiting the network at time t
P_c	the critical production
n_c	the critical accumulation. n_{c1} is the maximum accumulation limit of the free-flow state and n_{c2} is the minimum accumulation limit of the congested state.
u	the free flow speed
n_j	the jam accumulation

TAB. 4.3 – *Lists of Variables used in Section 4.3*

to the slope at the origin $n = 0$. The jam accumulation n_j corresponds to the maximum number of vehicles that can travel in the network simultaneously. In other words, we call this state a "gridlock" when the mean speed v becomes 0, and no vehicle can move since all the regions are jammed and block vehicles from entering them.

4.3.2 Accumulation based model

The Accumulation-based model is proposed by Daganzo (2007) and Geroliminis & Daganzo (2008). According to Geroliminis & Daganzo (2008), when the complete trip length L is defined as equal for all the vehicles, the outflow of a whole network $Qout(t)$, i.e, the flow of vehicles that exit the network or end their trips at time t, can be directly expressed by using P-MFD or V-MFD and the trip length in Eq. (4.8).

$$Qout(t) = \frac{P(n(t))}{L} = \frac{V(n(t)) * n(t)}{L} \tag{4.8}$$

This relation is sometimes called outflow-MFD $Qout(n(t))$ since the outflow can be expressed as the formulation of the accumulation.

The accumulation of a whole network n at the next time step $t + dt$ is calculated based on the conservation law, i.e., $dn/dt = Qin(t) - Qout(t)$, as Eq. (4.9).

$$n(t+1) = n(t) + (Qin(t) - Qout(t)) * dt \tag{4.9}$$

where $Qin(t)$ is an inflow of a whole network, i. e., the flow of vehicles that enter the network or start their trips, at time t. Thus, the traffic state, e.g., the outflow and the accumulation, can be simply calculated from Eq. (4.8) and (4.9) with input parameters such as V-MFD $V(n(t))$ or P-MFD $P(n(t))$, inflow dynamics $Qin(t)$, the initial accumulation $n(0)$ and the complete trip length L.

4.3.3 Trip based model

The initial idea of the trip-based model comes from the definition of trip length L_i of vehicle i based on the travel time tt_i and V-MFD $V(n(t))$ as shown in Eq. (4.10) by Arnott (2013)

$$L_i = \int_{Tin_i}^{Tin_i + tt_i} V(n(t))dt \tag{4.10}$$

where Tin_i is the entry time of vehicle i in the network. Daganzo & Lehe (2015), Lamotte & Geroliminis (2017) and Mariotte *et al.* (2017) proposed the resolution method of Eq. (4.10), by assigning to each vehicle a trip length and letting it travel at the global mean speed $V(n(t))$ until it completes the trip and exits the network. When the vehicles enter the network at time s, the proportion of the vehicles still in the network at time $t > s$ can be shown as $1 - F(\int_s^t V(n(t))du)$ according to Eq. (4.10). Therefore, when the inflow Qin is known for a whole time period from $t = 0$, the accumulation at time t can be calculated by Eq. (4.11).

$$n(t) = \int_0^t Qin(s)(1 - F(\int_s^t V(n(t))du))ds \tag{4.11}$$

The outflow is defined based on Eq. (4.11) and the conservation equation as Eq. (4.12).

$$Qout(t) = V(n(t)) * \int_0^t Qin(s)f(\int_s^t V(n(u))du)ds \tag{4.12}$$

Lamotte *et al.* (2018) mentioned that the trip-based model is equivalent to the accumulation-based model when trip length follows an exponential distribution with a constant coefficient under steady-state.

However, Eq. (4.11) and (4.12) are generally hard to solve analytically. Therefore, Daganzo & Lehe (2015) used time steps to perform the simulation. Lamotte & Geroliminis (2017) proposed event-based simulation that proceeds event by event, i.e., the departure or arrival of each vehicle, by keeping track of time and the cumulative distance traveled by each vehicle since the first departure. Based on the detailed process of the event-based model by Mariotte *et al.* (2017), our simulation process for the trip-based model of a whole network is given below:

Step 1. We assign the trip length L_i, the entry time Tin_i, and the exit time $Tout_i$ for vehicle i, which is already in the network at the beginning of the simulation $t = 0$ as shown below:

$$\begin{aligned} Tin_i &= Tin_{i-1} - 1/Qin(0) \\ L_i &= L \\ Tout_i &= L_i/V(n(0)) + Tin_i \end{aligned} \tag{4.13}$$

At this time, Tin_0 is the same as the time at the beginning of the simulation as $Tin_0 = time(0)$. $n(0)$, $Qin(0)$, and $V(n(0))$ are already known. L is assigned depending on the trip length setting, e.g., choosing from trip length distribution or average values. We repeat the calculation until the accumulation reaches $n(0)$. Tin_i, L_i, and $Tout_i$ for all the vehicles and construct the vectors for the vehicles inside the network as **Tin**, **L**, and **Tout**.

Step 2. The number of vehicles entering and exiting the network at time t is initialized as $dNin = 0$ and $dNout = 0$. At the first time, $t = 1$.

Step 3. We calculate the entry time of the following vehicle which enters the network after the latest Tin_i, i.e., $max(\mathbf{Tin})$, by

$$Tin_{next} = max(\mathbf{Tin}) + 1/Qin(t) \tag{4.14}$$

At this time, $Qin(t)$ is an input parameter.

Step 4(a). If the earliest time of the exit time vector is earlier than the next entry time such as $min(\mathbf{Tout}) < Tin_{next}$, the next event is that a new vehicle enters. Therefore, we add L_i, Tin_i, and $Tout_i$ of a new arrived vehicle i to the vector **L**, **Tin**, and **Tout**. At this time, L_i, Tin_i, and $Tout_i$ are calculated as below:

$$\begin{aligned} Tin_i &= Tin_{next} \\ L_i &= L \\ Tout_i &= L_i/V(n(t-1)) + Tin_i \end{aligned} \tag{4.15}$$

where $V(n(t))$ is an input parameter according to the calculated $n(t-1)$. Also, we update the number of entering vehicle as $dNin = dNin + 1$. The entry time of the next entering vehicle should be updated as $Tin_{next} = max(\mathbf{Tin}) + 1/Qin(t)$.

Step 4(b). If $min(\mathbf{Tout}) >= Tin_{next}$, the next event is that a vehicle inside the network exits. Therefore, we remove Tin_i, L_i, and $Tout_i$ of vehicle i whose $Tout_i = min(\mathbf{Tout})$ from **Tin**, **L**, and **Tout**. Also, we update the number of exiting vehicles as $dNout = dNout + 1$.

Step 5. Steps 3 and 4 are repeated until Tin_{next} exceeds $time(t)$. When $Tin_{next} > time(t)$, we calculate the accumulation and outflow at time t as:

$$\begin{aligned} n(t) &= n(t-1) + dNin - dNout \\ Qout(t) &= dNout/dt \end{aligned} \tag{4.16}$$

where dt is the time period between $t-1$ to t. Then, we update the simulation time as $t = t + 1$ and restart from step 2.

Step 6. Steps 2 to 5 are repeated until $time(t)$ reaches the end of the simulation.

4.4 Impact of Trip Length based on Real Speed

Trip length is an important parameter of MFD models. Yildirimoglu & Geroliminis (2014) and Kouvelas *et al.* (2017) showed that using a single mean trip length may lead to a huge error in the accumulation-based model. Also, Batista *et al.* (2019) and Paipuri *et al.* (2020) mentioned that the mean dynamics of trip length and the variance of trip length distribution play a significant role in the outflow in the trip-based model. However, as described in Chapter 3, it is difficult to obtain a good compromise of trip length estimation with limited data availability in practice. Therefore, it is essential to understand the effect of trip length aggregation granularity on prediction accuracy of classical MFD models.

This section considers several cases with different trip length aggregation granularities as input parameters of MFD models. Based on the MFD models described in Section 4.3, we compare the predicted traffic state, i.e., accumulation and outflow, to the original dynamics after the data imputation shown in Section 2. The latter is now considered as the ground truth. We use inflow dynamics and the initial accumulation after data imputation, as shown in Figures 4.10 (a) and (d). To focus on the effect of trip length aggregation, we use real values of the average mean speed dynamics V(t) for a whole network, as shown in Figures 4.10 (c) instead of V-MFD $V(n(t))$.

In MFD models, a single mean speed value is normally assigned for all vehicles while the speed is varied individually in the real data. Before analyzing the effect of trip length by comparing MFD model results and ground truth calculated from data, we verify the effect of speed aggregation in Section 4.4.1. In section 4.4.2, we analyze the effect of trip length variance numerically. Section 4.4.3 presents the prediction accuracy of both MFD models when using the constant average trip length for all vehicles and trip length distributions.

4.4.1 Numerical Analysis to Assess the Influence of Speed Variance

Before analyzing the effect of the trip length setting on the accuracy of traffic state prediction, we first verify the effect of using average speed for all vehicles at the same time while individual recorded speeds are different between vehicles.

Figure 4.19 shows the distribution and standard deviation (STD) dynamics of the individual mean speed from the original data (black bars in (a) and lines in (b)) and the trip set after data imputation (red bars in (a) and lines in (b)). While the average mean speed as the input parameter of the MFD model shown in Figure 4.10 (c) is around 3 m/s to 5 m/s, the individual mean speed distribution shown in Figure 4.19 (a) is in the range of 0 m/s to 12 m/s. After data imputation, the distribution has very high peaks around 3 m/s to 5 m/s since we assign the average mean speed value to vehicles during the no-drone period. For the same reason, the STD dynamics in Figure 4.19 (b) drop to 0 during the no-drone periods after data imputation. Thus, the speed can be very different from one vehicle to another, and using a single average value may affect the prediction results.

To verify the effect of variance of individual mean speed, we prepare test trip sets that have different STDs on the mean speed:

A1 All trips have the same speed as 4 m/s. The STD of the individual speed distribution is 0.

A2 Half of the trips have a fast speed of 5 m/s, and the other half of the trips have a slow

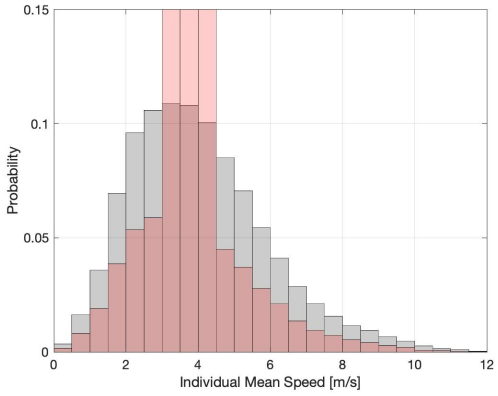

(a) Individual mean speed distribution

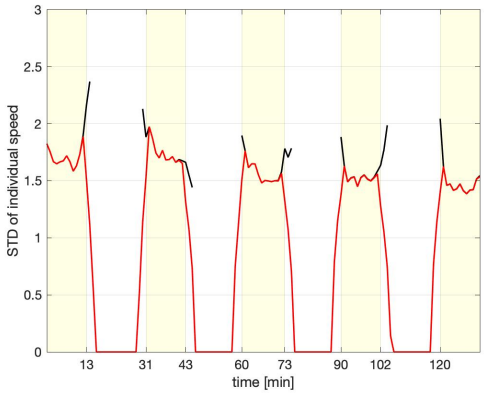

(b) STD dynamics of individual mean speed

FIG. 4.19 – *Individual speed variance of the original data (black) and the trip set after data imputation (red). (yellow zone: drone period, white zone: no-drone period) in (b)*

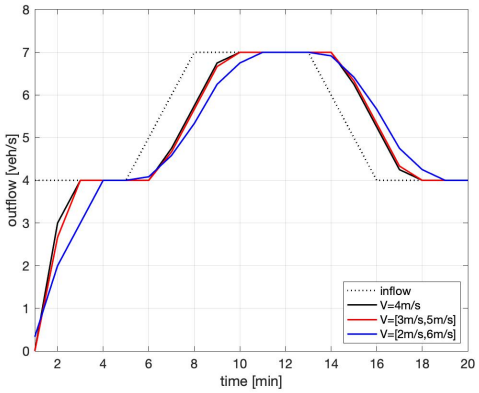

(a) Outflow [veh/s]

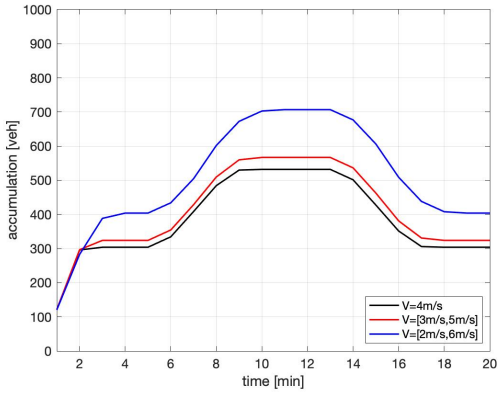

(b) Accumulation [veh]

FIG. 4.20 – *The effect of individual speed variance (black dashed line in (a): the inflow setting)*

speed of 3 m/s. These fast and slow speeds are assigned randomly, and the average speed of all vehicles is always 4m/s. The STD of individual speed distribution is 1.41

A3 Similar to case A2, but the fast speed is 6m/s, and the slow speed is 2 m/s. The STD of individual speed distribution is 2.82.

In case A1 represents the typical setting for MFD models when using a single speed value for all trips. Case A2 and A3 represent the real traffic state with different individual speed variances. Note that the individual speed STD of Athens' drone data is around 1.4 to 2, and the closest case is A2. The input inflow starts from the stable state as 4 veh/s for 10 minutes, increases up to 7 veh/s in 3 minutes, stays at 7 veh/s for 10 minutes, decreases until 4 veh/s in 3 minutes, and stays stable for 8 minutes, as shown by the black dashed lines in Figure 4.20 (a). Trip lengths are the same for all vehicles in all cases as 600m. Outflow and accumulation are calculated by the same method as the ground truth case, c.f., Section 4.2.3, based on the speed settings above.

In Figure 4.20, the solid black lines show the test case A1, which uses a single value of speed. The red and blue lines show the test cases A1 and A2 representing the ground truth case with different speed variances. Compared to case A1, the start time of increasing and decreasing outflow, i.e., around 12-13 minutes and 26-27 minutes, is the same in case A2, as shown in Figure 4.20 (a). However, the outflow in case A2 changes more gradually than in the case A1. For example, the outflow in case A2 reaches 7 veh/s at 17 minutes, while the one in case A1 reaches the same value at 16 minutes. For case A3, the increase and decrease of outflow begin earlier than in cases A1 and A2 at around 11 minutes and 25 minutes. The slope of the outflow change is much more moderate than for case A1, and the outflow in case A3 reaches 7 veh/s at 18 minutes. Thus, using a single-speed value for all the vehicles regardless of considerable speed variance leads to a steadier change of outflow. The outflow value may be predicted as higher, e.g., the difference is a maximum of 0.1 veh/s in case A2and 1 veh/s in case A3, after the inflow increases and is smaller, e.g., the difference is similar to when increasing, after the inflow decreases. For the accumulation in Figure 4.20 (b), the difference between cases A1 and A2 is around 70 veh after the inflow increases and around 50 veh after the inflow decreases. For case A3, the difference from case A1 is quite considerable with over 300 veh after the inflow increases and around 200 veh after inflow decreases. Since the outflow in case A1 is predicted as higher after the inflow increases and the value becomes stable after the outflow reaches 7 veh/s, the difference between each case is cumulated in the accumulation calculation, resulting in a lower accumulation in case A1 using a single speed value. After the inflow decreases, the difference in accumulation becomes smaller than for cases A2 and A3.

Thus, using a single-speed value may lead to higher and lower predictions than the ground-truth value for outflow. When the STD of the individual speed is less than 1.5, as in the A2 case, the error of the outflow prediction remains small, i.e., the maximum difference is less than 0.1 veh/s. However, these errors of outflow cumulate when calculating accumulation, and can lead to negligible errors, i.e., a difference of over 50 veh when the accumulation is around 1050 veh.

4.4.2 Numerical Analysis to Assess the Impact of Trip Length Variance

Here, we analyze the effect of using the average value of trip length without considering the variance. We prepare simple trip sets to compare the traffic state with a single trip length for all vehicles and various trip lengths before performing analysis using real data and MFD models.

B1 All the trips have the same average trip length value: L=600m. The STD of the trip length distribution is 0.

B2 Half trips have short trip lengths of 400m, and the other half have long trip lengths of 800m. These long and short trips occur alternately, and the average trip length is always 600m. The STD of the trip length distribution is 283.

B3 Similar to case B2, but the short trip length is 200m, and the long trip length is 1000m. The STD of the trip length distribution is 566.

Case B1 corresponds to using a single average value of trip length for all the vehicles in the accumulation model. Cases B2 and B3 represent the real traffic state with different trip

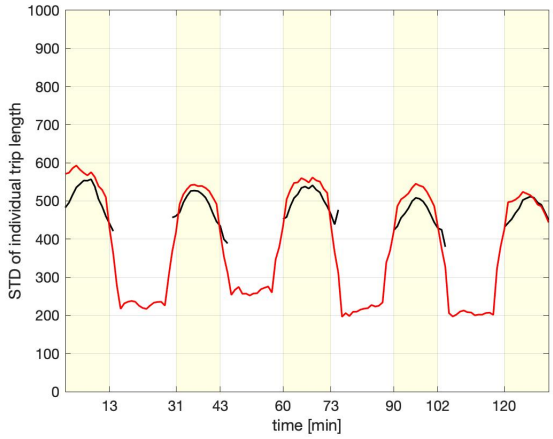

FIG. 4.21 – *STD dynamics of trip length calculated from the original data (black) and the trip set after data imputation (red). (yellow zone: drone period, white zone: no-drone period)*

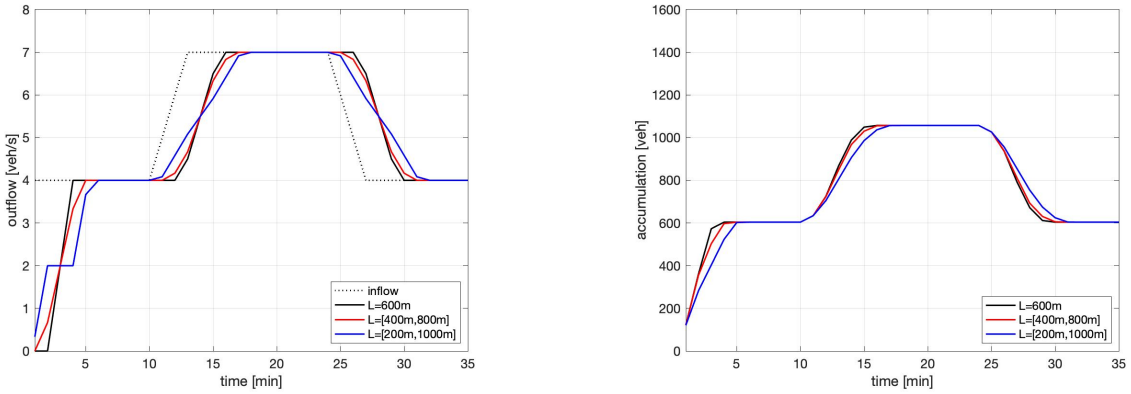

(a) Outflow [veh/s] (b) Accumulation [veh]

FIG. 4.22 – *The effect of trip length variance (black dashed line in (a): the inflow setting)*

length variances. Note that the trip length of the original data is distributed as black bars, and one of the trip sets after data imputation is distributed as red bars in Figure 4.13 (a). The STD of the trip length of the Athens' drone data is around 400 to 600 during the drone period, which is close to case B3. The STD of the trip length of the trip sets after data imputation is around 200 to 300, which is close to case B2. The inflow given is the same as in section 4.4.1. At this time point, all the vehicles drive at the same speed of 4 m/s.

The outflow and accumulation based on the three cases above are shown in Figure 4.22. The solid black lines show case B1, which uses the average trip length for all vehicles as the setting of the accumulation-based model. The red and blue lines show cases B2 and B3 representing the ground truth case with different trip length variances. The dashed black line in Figure 4.22 (a) shows the given inflow.

According to Figure 4.22 (a), while case B1 has a similar outflow and inflow slopes when the inflow changes, the outflow of cases B2 and B3 starts increasing and decreasing earlier, and the slopes are more moderate than for case B1. When the inflow increases for 10 - 13 minutes, the outflow of case B3 starts increasing from just after 10 minutes and stops at

around 18 minutes, while the outflow of case B1 increases for 13 to 16 minutes. For the accumulation, case B1 increases and decreases the value in shorter periods compared to cases B2 and B3. Therefore, when the inflow increases and decreases, the estimated accumulation using a single average value becomes larger and smaller than the ground truth. However, the accumulation errors appear only just after the inflow changes and do not cumulate.

Thus, using an average trip length value regardless of variance may make the outflow changes start later and more steadily. The dynamics change more steadily with the average trip length for accumulation prediction, but the error does not cumulate.

4.4.3 Experimental Investigation of Prediction Accuracy according to Trip Length Aggregation

To investigate the effect of trip length settings on prediction accuracy according to the MFD models, we compare the outflow and accumulation accuracy calculated by the accumulation-based model and the trip-based model described in Section 4.3 with different input trip length settings. In the literature, there are mainly two cases on input trip length setting for MFD models.

Case 1 We use the constant average value for all vehicles as the complete trip length input parameter $L =< L_i >$.

Case 2 We randomly choose the complete trip length of each vehicle from the distribution as $L \sim P(L_i)$.

The extension of Case 1, Yildirimoglu & Geroliminis (2014) suggests using the dynamic average trip length. However, since the average trip length of our data set is always around 600-900m for 2h30, as shown in Figure 4.13 (b) this extension makes the calculation complex, especially for the trip-based model. Therefore, at this time, we use only the constant trip length for a whole time period. Using the Athens' drone data, the average value of complete trip lengths and the complete trip length distribution are calculated by using the real trip length of all the vehicles in a whole network. The average value is $< L_i >= 613m$, and the distribution is shown in Figure 4.13 (a). As mentioned in the previous sections, it is quite challenging to adapt the trip length distribution instead of the average value in the accumulation-based model. Therefore, we use Case 2 only with the trip-based model.

Figure 4.23 shows the predicted outflow (a) and accumulation (b) according to the trip length setting of Case 1 for the accumulation-based model and both cases for the trip-based model. The black line shows the ground truth dynamics, which is the same as the dynamics from the trip sets after data imputation, as shown in Figure 4.10. In Figure 4.23 (a), the predicted outflow dynamics of case 1 have several deviations from the ground truth at around 14, 44, and 74 minutes. This stems from the fact that the outflow dynamics follow the inflow dynamics several minutes later when the trip length is constant for all vehicles, as we can see a similar shape of inflow dynamics at around 12, 42, and 72 minutes, c.f., Figure 4.10 (a). Compared to the accumulation-based and trip-based models of Case 1, the predicted outflow dynamics based on the accumulation-based model are changed more gradually and are more robust to adapt to the changing state. Using the same trip length distribution as in Case 2, the outflow suddenly changes from around 5.5 to 7 veh/s even when the inflow is constant, e.g., 13 to 31, 43 to 60, 73 to 90, 102 to 120 minutes, since the trip lengths are chosen

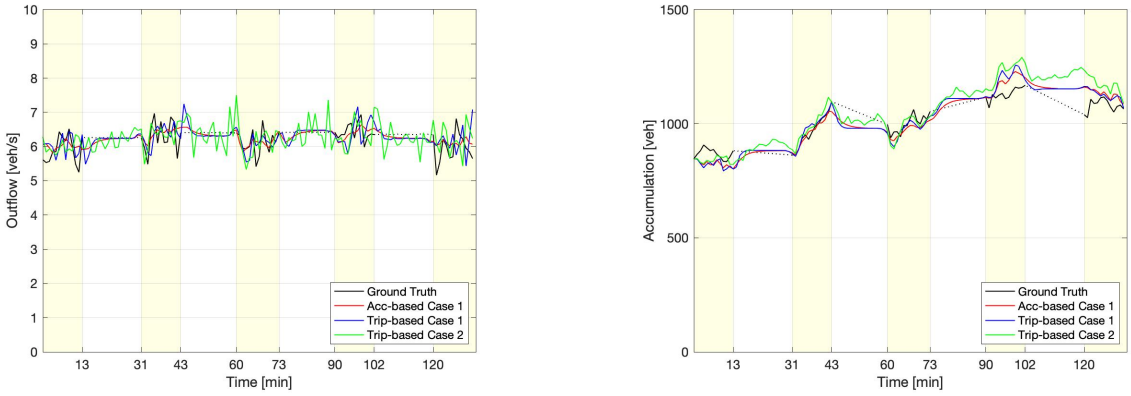

(a) Outflow [veh/s] (b) Accumulation [veh]

FIG. 4.23 – *Prediction results of a whole network according to MFD models (Acc-based: Accumulation-based model, Trip-based: Trip-based model) and trip length settings (Case 1: using average trip length, Case 2: using trip length distribution).(yellow zone: drone period, white zone: no-drone period)*

		Qout	*n*
Case 1	Acc	3.1	9.4
Case 1	Trip	4.0	8.8
Case 2	Trip	5.4	8.8

TAB. 4.4 – *Relative error [%] of the prediction results of the MFD models (Acc: Accumulation-based model, Trip: Trip-based model) with different trip length settings (Case 1: using average trip length, Case 2: using trip length distribution).*

randomly. For the Athens' drone data, the outflow prediction does not show a huge difference between Case 1 and Case 2 using the trip-based model even when the inflow dynamics change a lot. According to the predicted accumulation results shown in Figure 4.23 (b), all the cases show several significant gaps with the ground truth. At around 44 minutes, the predicted accumulation drops suddenly. These gaps may be caused by using a single speed regardless of the speed variance, as mentioned in section 4.4.1, since it happens just after the inflow increases at around 42 minutes. Compared to the accumulation-based and trip-based models of Case 1, the dynamics of the accumulation-based model changes more moderately than the outflow dynamics. In Case 2 in the trip-based model, the maximum gap is around 50 veh because of the sudden outflow changes.

To compare the accuracy of each model and case concretely, the relative error [%] is calculated as $\sum_t \sqrt{((x^*(t) - x(t))/x^*(t))^2}/T * 100$ where $x^*(t)$ and $x(t)$ show the ground truth dynamics and prediction results of each case and T denotes a whole time period of the simulation. The relative errors of all the cases are shown in Table 4.4. According to the table, all the relative errors are small, below 6% for outflow and below 10% for accumulation. The best case for the outflow prediction is when using the accumulation-based model with the average trip length, i.e., 3.1% of the relative error, since the accumulation-based model can predict robustly when the inflow changes suddenly. In Case 2 in the trip-based model, the relative error of the outflow prediction is the highest, i.e., 5.4%, since the value rises and drops suddenly, caused by the randomness of the trip length choice even when the values

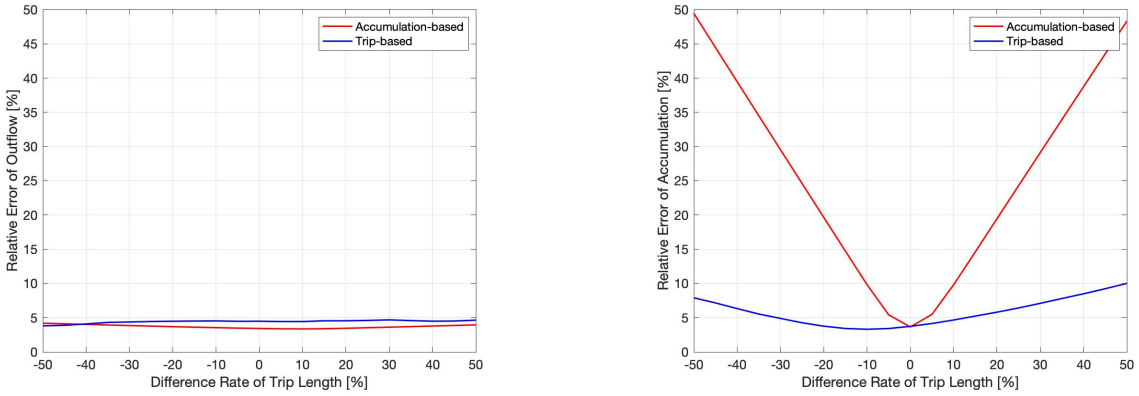

(a) Outflow (b) Accumulation

FIG. 4.24 – *The relative error of the prediction results in Case 1 according to the difference of the trip length from the average*

of the ground-truth and other cases are constant. On the other hand, for the accumulation, the best case is when using the trip-based model in both cases, i.e., the relative error is 8.8%.

For the calculation of Case 1 in Figure 4.23 and Table 4.4, we assume that the real average trip length value for all the vehicles is available. However, it is almost impossible to obtain the accurate trip length average value in practice because of two reasons: 1) typical data sources such as probe data provide only the trip lengths of a few sample vehicles, and 2) the average trip length can change with time. To analyze the errors according to the difference of the estimated average trip length from the real value, we compare for both models their relative errors of outflow and accumulation predictions. The difference between the estimated average trip length and the real value is described as the rate of rate of difference of the trip length, calculated as $(L - L^*)/L^*$ where L^* denotes the real average trip length and L denotes the estimated average trip length. The relative errors when the rate of rate of difference changes every 5% from -50% to 50% are shown in Figure 4.24. As shown in Figure 4.24 (a), the relative error of outflow does not change significantly along with the rate of rate of difference of the trip length for both models, i.e., below 7%. On the other hand, the rate of rate of difference of the trip length has a considerable effect on accumulation prediction, especially when using the accumulation-based model, as shown in Figure 4.24 (b). rate of difference The relative error of using the accumulation-based model falls below 5% only when the rate of difference of the trip length is close to 0%. However, the relative error rises immediately, and exceeds 10% when the rate of difference of trip length gets over around $\pm$10%. The accuracy of the trip-based model is also affected by the rate of difference of the trip length. When the rate of difference of the trip length is over 10%, the relative error reaches 6%, which is higher than when using trip length distribution. However, the impact is somewhat lower than the accumulation-based model, and the relative error is below 12% even when the rate of difference is around $\pm$50%.

Thus, we find that the accumulation-based model is efficient with high accuracy and a low parameter calibration requirement, e.g., estimating the constant average trip length compared to the trip-based model. However, the estimation accuracy of average trip length can significantly affect the prediction result. Also, for the trip-based model, prediction accu-

racy is affected by the average trip length estimation. However, the increase of the relative error according to the average trip length estimation error is more moderate than in the accumulation-based model. The accumulation-based model can provide more accurate results than the trip-based model only when the average trip length estimation error is less than $\pm 3\%$. Therefore, in the normal case in which only the probe data is available for average trip length estimation, a trip-based model can lead to better prediction results for accumulation. Furthermore, depending on data availability, in the case where there are not enough to estimate the average trip length within 10% difference, the trip length distribution can lead to better and more stable results than average trip length.

4.5 Impact of MFD approximation

MFD is another key parameter of MFD models besides trip length. In the literature, piecewise linear approximation (Leclercq *et al.* (2014), Mariotte *et al.* (2017)) and quadratic approximation (Geroliminis & Daganzo (2007), Lentzakis *et al.* (2016)) are often used for fitting P-MFD from data. However, since our data cover a limited observation time, i.e., the morning rush hour (8:00-10:30), only the traffic state close to saturation is available. In a very congested state, we need to pay attention to the setting of the MFD approximation since a small difference in MFD parameter estimation can significantly affect the prediction results.

Therefore, in Section 4.5.1, we first analyze the sensitivity to the MFD parameters of prediction accuracy. Because of our limited observation, a simpler linear approximation, i.e., described in Section 4.3.1, is used instead of a piecewise linear approximation. We focus our analysis on the P_c and n_c values, usually the hardest to define. The analysis is calculated based on the accumulation-based model using the average trip length for all vehicles (Case 1), which is a simple and stable case with good accuracy when using the real mean-speed in section 4.4, i.e., the relative errors are below 4% for the outflow and below 10% for the accumulation. Then, in section 4.5.2, the approximation validity of MFD with the best variable setting for the accumulation-based model is verified by trip-based models using two different trip length aggregation cases of Section 4.4.

4.5.1 The setting of characteristics variables for MFD approximation

P-MFD and V-MFD calculated from data every minute are shown as black plots in Figures 4.25 (a) and (b). The production of plots in Figure 4.25 (a) constantly scatter around 3000 to 4200 veh*m/s when the accumulation is from 800 to 1200 veh. Therefore, we can assume that we have only data related to the saturation state when the production value reaches the critical production. In the saturation state, the slight difference in production and mean speed setting can significantly affect the prediction results. Therefore, we need to choose the variable settings of the MFD approximation carefully. However, estimating n_c and P_c values is challenging for these data because of the wide scatter. Also, since the observed accumulation range is narrow, the n_j value cannot be calculated. Therefore, we first compare the prediction results with the different settings of P_c and n_{c1} for approximating a trapezoidal P-MFD to analyze the effect of the variable settings and to find the best variable combinations of these data. Since the n_j value cannot be estimated and it is not necessary to define the values far from the data range, we do not assign values to n_{c2} or n_j. Also, the predic-

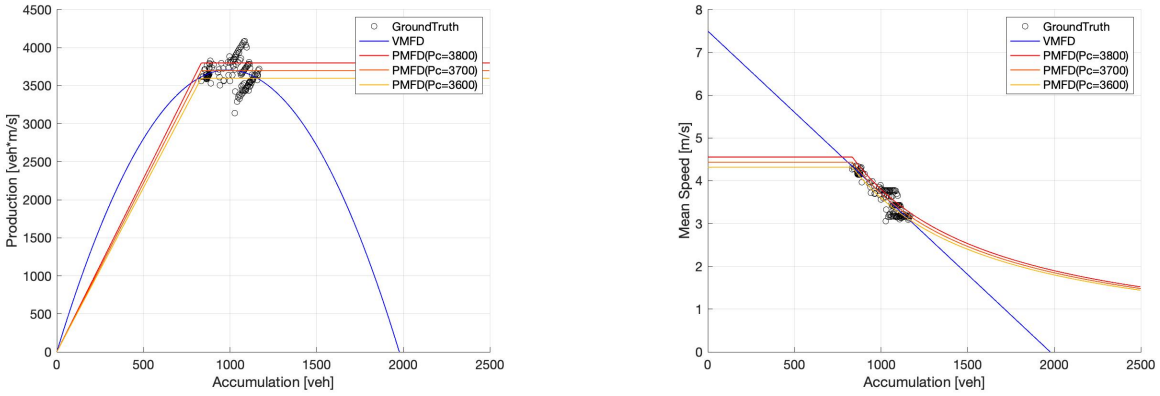

(a) P-MFD (b) V-MFD

FIG. 4.25 – *MFD approximation with different P_c.*

tion result is compared to the other approximation cases by using the linear approximation of V-MFD and the parabolic approximation of P-MFD corresponding to the approximated V-MFD.

To analyze the effect of the P_c values, we consider three cases according to the average production value from the data ($\bar{P} = 3670$[veh*m/s]) as shown in Figure 4.25 (a): 1) a little lower than the average $P_c = 3600$[veh*m/s], 2) a little higher than the average $P_c = 3700$[veh*m/s], and 3) somewhat higher than the average $P_c = 3800$[veh*m/s]. We use the minimum accumulation value of the data for the critical accumulation as $n_{c1} = 834$[veh] for all cases. V-MFD calculated by Eq. (4.7) corresponding to three cases of P-MFD is shown in Figure 4.25 (b). For the parabolic approximation of P-MFD, we first find the slope of V-MFD by linear regression based on data shown by the blue line in Figure 4.25 (b). Then, P-MFD is calculated by Eq. (4.6) corresponding to the linear approximated V-MFD. To avoid confusion, we call the MFD approximation based on P-MFD variables the "P-MFD-based approximation" and the approximation based on linear fitted V-MFD the "V-MFD-based approximation". For the effect analysis of the MFD variable settings, the outflow and accumulation are predicted by using the accumulation-based model with the average complete trip length (Case 1 in Section 4.2.3) since it is a simple method with good accuracy, described in Section 4.2.3, and the prediction accuracy is not subject to the effect of the randomness of the trip length choice.

Figure 4.26 shows the predicted outflow (a) and accumulation (b) according to three cases of the P-MFD-based approximation and the V-MFD-based approximation. For the P-MFD-based approximation, the difference of the outflow between three cases is small up to 31 minutes when the accumulation reaches n_{c1}. After 31 minutes, the outflow of the larger P_c case becomes higher than the others. However, the outflow values of the three cases are quite stable, and the difference does not increase. On the other hand, since the accumulation prediction error cumulates with time, the difference between the three cases becomes larger, as shown in Figure 4.26 (b). This is especially the case when we use a smaller P_c value, e.g., $P_c = 3600[veh * m/s]$), the estimated accumulation becomes relatively higher than in the other cases, and reaches over 2000 [veh] while the ground truth accumulation is around 1100 [veh] at the end of the time period. In Figure 23, the green line represents the true speed,

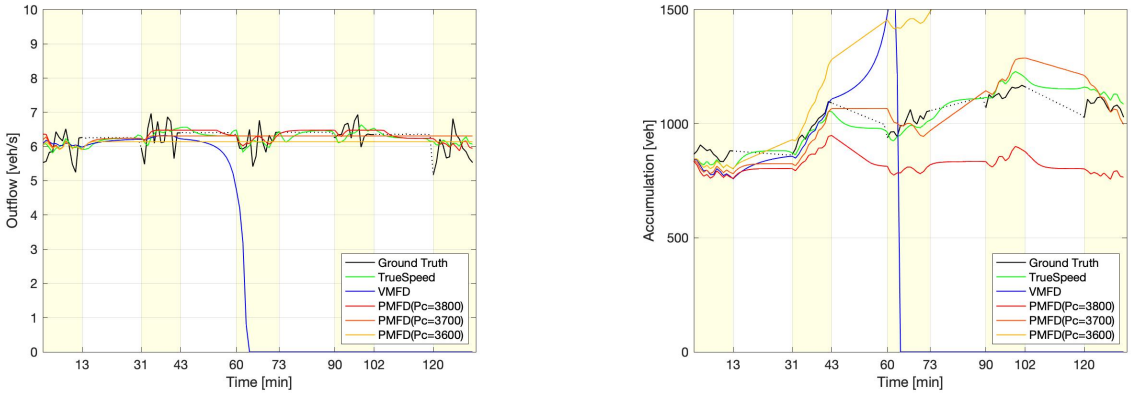

(a) Outflow [veh/s] (b) Accumulation [veh]

FIG. 4.26 – *Prediction results by the accumulation-based model according to different MFD approximation approaches and P_c settings (VMFD: V-MFD based approximation, PMFD: P-MFD based approximation, yellow zone: drone period, white zone: no-drone period)*

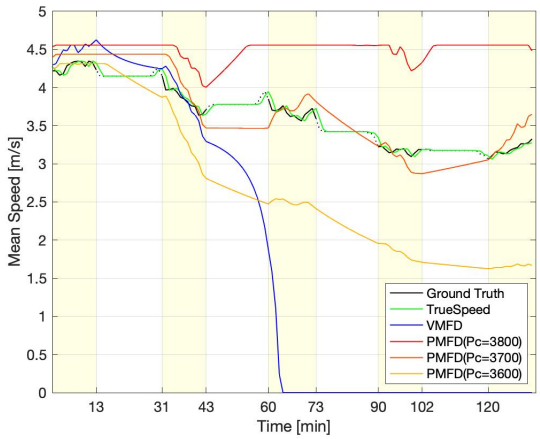

FIG. 4.27 – *Predicted speed dynamics of different MFD approximation approaches and P_c settings*

and the other colored lines show the mean speed dynamics of three P_c cases. According to Figure 4.27, when P_c is small, e.g., $P_c = 3600[veh * m/s]$, the mean speed drops significantly after 31 minutes. On the other hand, when P_c is very large, e.g., $P_c = 3800[veh * m/s]$, the traffic is in free-flow state with the maximum mean speed most of the time. For the V-MFD-based approximation, as shown in Figure 4.27, the mean speed suddenly drops when the accumulation increases after 43 minutes and reaches the gridlocked state at 65 minutes. Thus, the V-MFD-based approximation of these data is not sufficient to represent the mean speed when the accumulation is high. The relative errors of all the cases shown in Figure 4.26 are summarized in Table 5. According to Table 4.5, the relative errors of all parameters are less than 10% only when using P-the MFD-based approximation with $P_c = 3700[veh * m/s]$.

To analyze the impact of n_{c1} settings, we prepared three cases of P-MFD-based approximation based on the minimum accumulation value observed from the data ($n_{min} = 834[veh]$): 1) lower case $n_{c1} = 800[veh]$, 2) medium case $n_{c1} = 850[veh]$, and 3) higher case $n_{c1} = 900[veh]$. $P_c = 3700[veh * m/s]$ is used as the setting of the production capacity. P-MFD and

	n	$Qout$	V
True Speed	3.6	3.4	0
V-MFD based	57.5	56.1	58.6
P-MFD based ($P_c = 3800$)	18.8	3.2	25.3
P-MFD based ($P_c = 3700$)	6.3	3.5	5.4
P-MFD based ($P_c = 3600$)	46.4	4.6	28.2

TAB. 4.5 – *Relative Error [%] of the prediction results by the accumulation-based model according to V-MFD based approximation and different P_c settings of P-MFD based approximation*

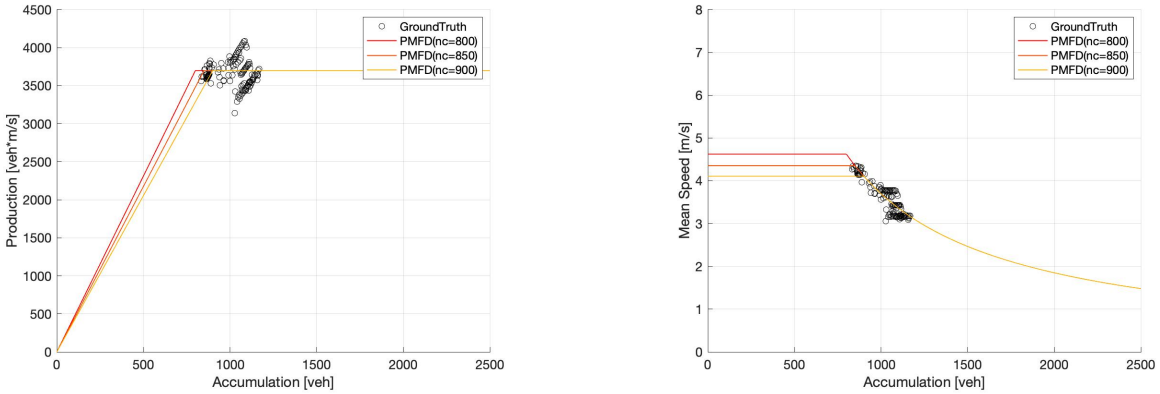

(a) P-MFD (b) V-MFD

FIG. 4.28 – *MFD approximation with different n_{c1}*

V-MFD based on three cases of the n_{c1} settings above are shown in Figure 4.28 (a) and (b).

The predicted outflow and accumulation according to n_{c1} settings are shown in Figure 4.29. The outflow of the three cases in Figure 4.29 (a) is slightly different only at the beginning of the time period. The difference gets smaller along with the increase of accumulation and takes the same value when the accumulation reaches around 800 [veh] at around 33 minutes. Because of the outflow difference at the beginning, the accumulation of larger n_{c1} cases takes a larger value than the others. However, the difference between the three cases does not increase after 10 minutes, as shown in Figure 4.29 (b). The relative errors of all cases also do not show large differences and are below 10%, as shown in Table 4.6. The best n_{c1} setting is $n_{c1} = 850[veh]$, and the relative errors of the accumulation and outflow predictions are 6.3% and 3.5% respectively.

Thus, we find that the P_c setting significantly affects the prediction results. In particular, estimating a lower P_c leads to a considerable error when the accumulation increases. On the other hand, the n_{c1} setting affects only free-flow. The best variables for the Athens drone data are $P_c = 3700[veh * m/s]$ and $n_{c1} = 850[veh]$. Therefore, we verify the validity of these settings for the trip-based model in section 4.5.2.

4.5.2 The effect of MFD approximation on each MFD model

To verify the validity of the MFD approximation settings on each model, we first calculate the traffic state prediction using the best MFD approximation settings for the accumulation-

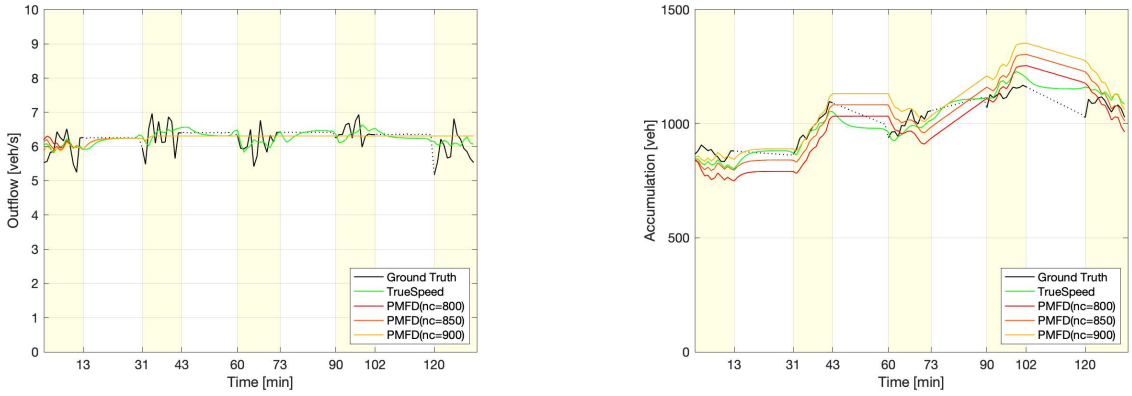

(a) Outflow [veh/s] (b) Accumulation [veh]

FIG. 4.29 – *Prediction results by the accumulation-based model according to n_{c1} settings of P-MFD based approximation (yellow zone: drone period, white zone: no-drone period).*

	n	$Qout$	V
P-MFD based ($n_{c1} = 800$)	7.3	3.5	6.8
P-MFD based ($n_{c1} = 850$)	6.3	3.5	5.4
P-MFD based ($n_{c1} = 900$)	7.4	3.4	6.0

TAB. 4.6 – *Relative Error [%] of the prediction results by the accumulation-based model according to n_{c1} settings of P-MFD based approximation.*

based model, i.e., $P_c = 3700$ [veh*m/s] and $n_c = 850$ [veh] by the trip-based model. The predicted outflow and accumulation by the trip-based model using average trip length (Case 1) and trip length distribution (Case 2) are shown in Figure 4.30. The outflow given by the trip-based model in both Cases 1 and 2 is lower than by the accumulation-based model. In Case 2, the outflow by the trip-based model oscillates around 1 veh/s because of the randomness of the trip length. For the accumulation shown in Figure 4.30 (b), the trip-based model in both cases overestimated the values compared to the accumulation-based model and ground truth. The errors of both trip length aggregation cases becomes quite considerable, e.g., the relative errors of Cases 1 and 2 are 28.8% and 64.0% for the accumulation, while the relative error of the accumulation-based model is 6.3%. Thus, using the same approximated MFD as the accumulation-based model leads to very large errors in the prediction by the trip-based model.

To investigate the difference between each model's prediction accuracy, we compare the relative error of the predicted outflow, accumulation and calculated mean speed from the approximated MFD according to P_c values. P_c takes every 50 [veh*m/s] from 3600 [veh*m/s] to 4200 [veh*m/s] and n_c is set constantly as 850 [veh]. We calculate the predicted traffic state for all cases and models. When $P_c >= 3750$[veh*m/s], the relative error of the outflow is almost constant, around 3.0%, for the accumulation-based model in Case 1. On the other hand, for the case of $P_c < 3750$[veh*m/s], the relative error increases until reaching around 5% when $P_c = 3600$[veh*m/s]. For the trip-based model in Case 1, the relative error decreases when P_c increases from around 5.0% at $P_c = 3600$[veh*m/s] until around 3.0% at $P_c = 4200$[veh*m/s]. Therefore, the error of the trip-based model in Case 1 is slightly

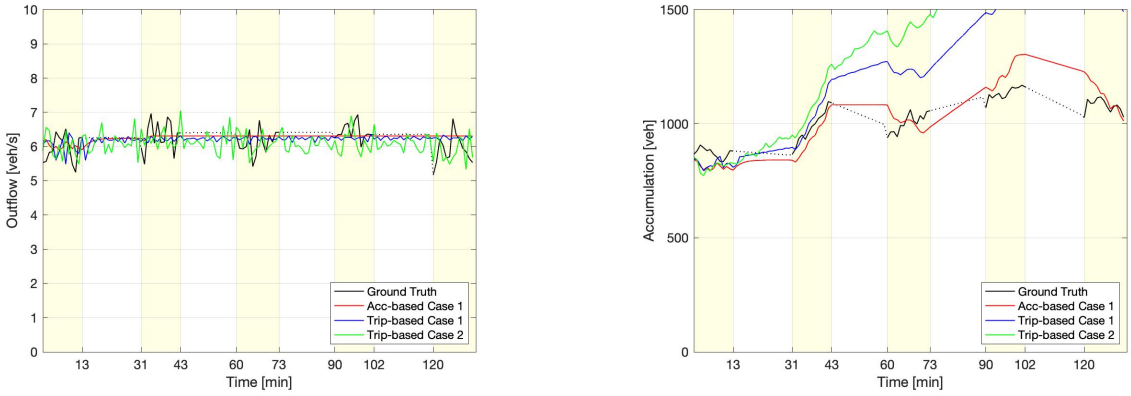

(a) Outflow [veh/s] (b) Accumulation [veh]

FIG. 4.30 – *Prediction results based on calibrated MFD settings for the accumulation-based model (yellow zone: drone period, white zone: no-drone period, Acc-based: Accumulation-based model, trip-based, trip-based model, Case 1: using average trip length, Case 2: using trip length distribution)*

higher, around 1.0%, than the accumulation-based model when $P_c = 3750$[veh*m/s]. For the trip-based model in Case 2, the relative error is constantly higher than the other cases as the error is always around 5.0 to 7.0%. For the accumulation, the relative error is the smallest, around 7%, at $P_c = 3700$[veh*m/s] for the accumulation-based model in Case 1. When P_c is over 3700[veh*m/s], the relative error increases logarithmically and exceeds 20% when $P_c >= 3900$[veh*m/s]. When P_c is less than 3700[veh*m/s], the relative error rises drastically and exceeds 45% at $P_c = 3600$[veh*m/s]. For the trip-based model in Case 1, the relative error of the accumulation is below 5% when P_c is around 4000 to 4150[veh*m/s]. When $P_c > 4050$[veh*m/s], the relative error increases gradually and reaches 5% when P_c is larger than 4200[veh*m/s]. Like the accumulation-based model, when P_c is small, e.g., $P_c < 4050$[veh*m/s], the relative error rises rapidly and exceeds 20% when $P_c < 3730$[veh*m/s]. However, the increase of relative error according to the smaller and larger P_c is more moderate than the accumulation-based model, and the largest relative error of the trip-based model at $P_c = 3600$[veh*m/s] is around 36%, while it is around 47% for the accumulation-based model. Except for when P_c is around 3650 to 3780[veh*m/s], the relative error of the accumulation obtained with the trip-based model is smaller than the accumulation-based model using the average trip length (Case 1). For the trip-based model in Case 2, the relative error rises and falls randomly, e.g., the relative errors are around 33% when $P_c = 3900$[veh*m/s] and around 6% when $P_c = 3950$[veh*m/s]. The trend shows that the average relative error decreases when P_c increases. However, the gap of the relative error when P_c changes 50[veh*m/s] is always around 20 to 30%. Since the trip length distribution of our data has a long tail, as shown in Figure 4.13 (a), the trip length values chosen randomly from the distribution greatly affect the prediction results when the traffic state is close to saturation. The mean speed prediction is the most accurate, e.g. around 5 to 6% relative error, at $P_c = 3700$ [veh*m/s] for the accumulation-based model and $P_c = 3900$ [veh*m/s] for the trip-based model in Case 1. For Case 2, the relative error for mean speed also changes randomly. Thus, the best setting of P_c shows some differences for both models in Case 1, and different settings can lead to very large errors, especially when the setting value of P_c is smaller than the best setting. For Case 2, the influence of P_c values on predic-

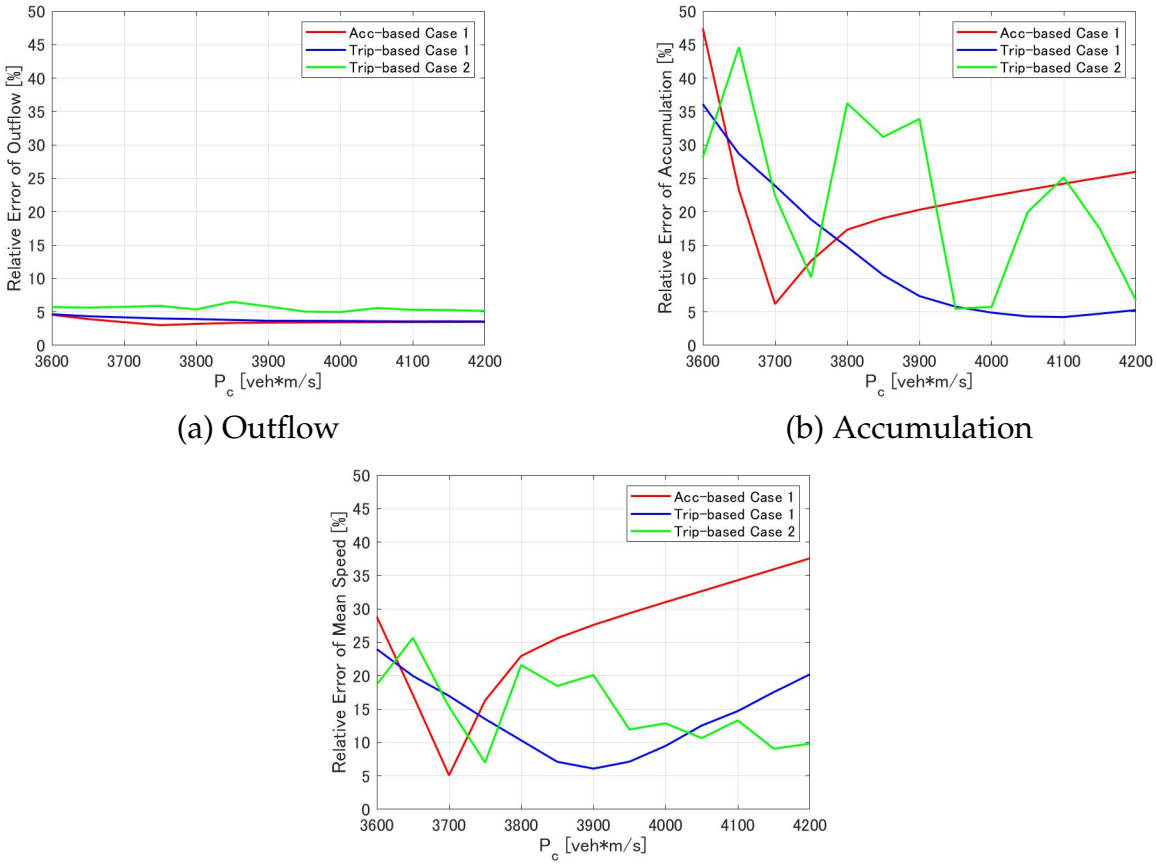

(a) Outflow

(b) Accumulation

(c) Mean speed

FIG. 4.31 – *Relative error of predicted traffic state variables according to P_c. (Acc-based: Accumulation-based model, trip-based, trip-based model, Case 1: using average trip length, Case 2: using trip length distribution)*

tion accuracy is somewhat smaller than in Case 1, and the relative error changes randomly because of the choice of trip length from the trip length distribution.

Finally, we confirm the prediction accuracy of the trip-based model using the average trip length and trip length distribution compared to the accumulation-based model with the best setting of P_c. We calculate the predicted traffic state by setting $P_c = 4050$[veh*m/s] for both cases of the trip-based model and $P_c = 3700$[veh*m/s] for the accumulation-based model in Case 1. The n_c value is 850[veh] for all cases. All the results are shown in Figure 4.32. The predicted dynamics of the outflow obtained by the trip-based model shown in Figure 4.32 (a) get closer to the ground truth and the accumulation-based model for both cases compared to the results before choosing the best P_c setting in Figure 4.26. Table 4.7 shows that the relative errors of all the cases are below 5.0% with the best settings of P_c. When using the trip-based model with the trip length distribution (Case 2) the relative error is slightly higher (5.0%) than the other cases, e.g., 3.5% for the accumulation-based model and 3.7% for the trip-based model in Case 1, because of the oscillation caused by the randomness of the trip length choice. For the accumulation, as shown in Figure 4.32 (b), the predicted accuracy of both cases in the trip-based model is much improved compared to Figure 4.26, especially after 30 minutes when the mean speed becomes lower than 4 m/s. According to

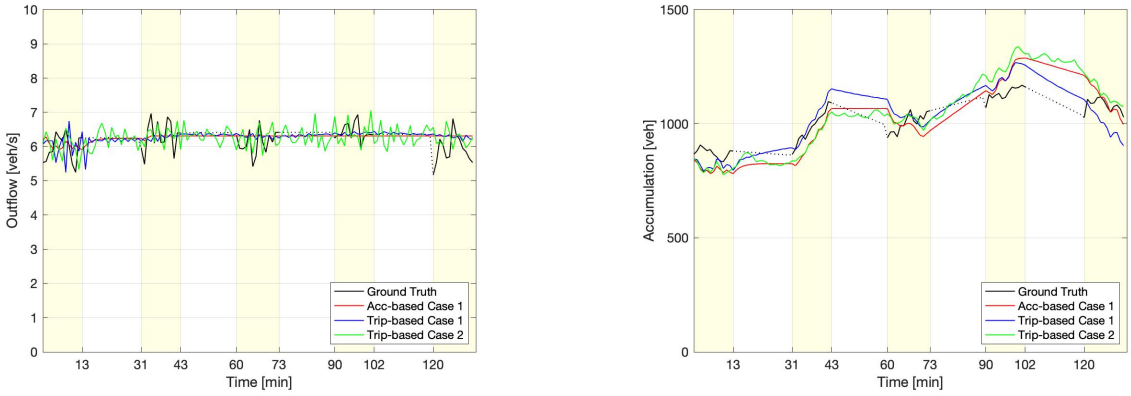

(a) Outflow [veh/s] (b) Accumulation [veh]

FIG. 4.32 – *Prediction results based on calibrated MFD settings for each model (yellow zone: drone period, white zone: no-drone period, Acc-based: Accumulation-based model, trip-based, trip-based model, Case 1: using average trip length, Case 2: using trip length distribution)*

	n	$Qout$	V
Accumulation-based model (Case 1, $P_c = 3700[veh * m/s]$)	6.3	3.5	5.4
Trip-based model (Case 1, $P_c = 4050[veh * m/s]$)	5.4	3.7	10.3
Trip-based model (Case 2, $P_c = 4050[veh * m/s]$)	6.8	5.0	8.5

TAB. 4.7 – *Relative Error [%] of the prediction results based on calibrated MFD settings for each model. (Case 1: using average trip length, Case 2: using trip length distribution)*

Table 4.7, the relative error for the accumulation prediction by the trip-based model in Case 1 are below 6% and better than the accumulation-based model with the best P_c setting. In Case 2, by the trip-based model, the accuracy is lower than in Case 1. As shown in Figure 4.31, the accuracy of Case 2 is changed randomly, and the gap between the small and very large errors reaches 20% for the accumulation prediction.

Therefore, we find that the difference of the P_c setting has a huge effect on the prediction result, thus we should calibrate the MFD variable setting separately for both models.

4.6 Conclusion

We investigated the effect of the two key calibration parameters, i.e., the trip length aggregation level and the variable settings of approximated MFD, on the prediction accuracy of traffic state dynamics based on a classical MFD model, i.e., accumulation-based and trip-based models, using full trajectory data obtained in a drone experiment (Barmpounakis & Geroliminis (2020)). To obtain the ground truth traffic states and input parameters, we first propose the temporal data imputation method to complete missing values during non-drone periods.

Based on the trip set after data imputation, the predicted outflow and accumulation were compared according to two MFD models with real mean speed and two different trip length aggregations, i.e., average trip length and trip length distribution. The accumulation-based

model using average trip length for all vehicles was an efficient method with high accuracy, low computational load, and few parameter calibration requirements compared to the trip-based model. However, the estimation accuracy of average trip length could significantly affect the prediction results of both models, especially for the accumulation-based model, small calibration errors of the average trip length can lead to a much larger prediction error than the trip-based model. Also, if the accuracy of the trip length estimation is not sufficient, e.g., the relative difference between estimation and the real value is more than 10%, using trip length distribution can lead to better and more stable results than using average trip length for the trip-based model.

To investigate sensitivity to the MFD parameters, we compared the prediction results according to the values of the critical production P_c and the critical accumulation n_c. P_c played an important role in the outflow and accumulation prediction results. In particular, a too-small P_c value led to huge errors. Also, the setting of P_c, which led to the most accurate prediction, was different in the accumulation-based and trip-based models. It was necessary to calibrate the MFD variables separately for both models.

5. Calibration of MFD Models Considering Multiple Regions and Path Sequences

5.1 Introduction

MFD models in multiple regions have received much attention recently, along with the development of network partitioning methods. Since MFD models are based on the assumption that the traffic state in a region is homogeneous and stable, efficient network partitioning methods are crucial for defining adequate regions where traffic states can be considered homogeneous, e.g., Ji & Geroliminis (2012), Saedi *et al.* (2020), and An *et al.* (2018). When predicting the traffic state in multiple regions by MFD models, it is necessary to consider both the flow transfer between regions and the trip patterns across them. For example, we need to consider the vehicular flows that move from one region to another besides the vehicles that pass in only one region considered in a single region model. Also, congestion spillback from one region to others should be considered. Thus, the MFD models for multiple regions are more complicated than the single region described in Chapter 4. Since the parameter settings, e.g., trip length and MFD, affect the prediction results by MFD models in a single region, c.f. Chapter 4, the regional parameter settings may also have a considerable impact on the prediction results in a multiregional setting.

While trip length is one of the key parameters of MFD models, estimating the regional trip length can be difficult according to the network partitioning. For example, since time and location information on individual vehicles in each region is required to estimate trip length accurately, typical data sources such as probe vehicles, which are generally sparse in time and space, may not provide enough trajectory data for a network divided into multiple smaller regions. Also, according to Chapter 3 and Paipuri *et al.* (2020), the regional trip length is more difficult to characterize as the path sequence, i.e., the order of the regions that the vehicle passes through on its trip, but it plays a major role. Therefore, the estimated trip length without sufficient trajectory data or path sequence information can lead to considerable errors in the prediction results by MFD models. Furthermore, trip length aggregation settings differ from one MFD model to another. For example, in the accumulation-based model, the average value of trip lengths is used in the literature. On the other hand, Batista *et al.* (2019), and Paipuri *et al.* (2020) recommended using the trip length distribution in the trip-based model since using the average value may lead to considerable errors. In Chapter 4, we showed that typical MFD models require different accuracies of trip length estimation in a single region, e.g., a relative error of less than 40% in the trip length estimation for trip-based model and less than 10% for the accumulation-based model are required to ensure that the relative error of the accumulation is below 10%. Using a single region model in Chapter 4 we examined another key parameter of MFD models, i.e. the MFD setting, which affects the prediction results, especially when the traffic state is close to saturation. Also, it was shown that we need different MFD settings for each MFD model to get accurate prediction results. Thus, the settings of trip length and MFD, and path sequence information, all affect the prediction results in single region models and may have a considerable and different impacts on the results in multiregional models.

Therefore, the comparative investigation of the effect of trip length, MFD settings and path sequence information on the predicted traffic state by obtained with multiple-region MFD models is important to further develop the practical application of the multiregional MFD models. Also, we showed in Chapter 3, how path sequence is important to properly describe trip length behavior but up to now no MFD model has been designed to consider this particular feature. While such an extension is trivial with the trip-based framework, in

this chapter we propose an extension of the accumulation based model to consider the path sequence in a multiregional setting.

5.1.1 Literature Review

The multiregional models developed at present are often based on the idea of Geroliminis & Daganzo (2007). They consider two types of flows for vehicles that start and end their trips in a region r (internal flow), i.e., q_{rr}, and for vehicles that start in the region r and end in another region r' (transferring flow), i.e., $q_{rr'}$ between two regions, i.e., the network's center and periphery. The flow from outside the network is not considered but is easy to take into account in their model. Under the constant regional trip length assumption, each flow is calculated based on the accumulation-based model proposed by Daganzo (2007). Accumulation n_r in region r is calculated separately according to the trip destination. For example, n_{rr} and $n_{rr'}$ are first calculated where n_{rr} shows the accumulation of vehicles in r that end their trips in r (internal accumulation) and $n_{rr'}$ shows the accumulation of vehicles in r that end their trips in r' (transferred accumulation). Thus, the regional accumulation n_r is calculated as the sum of the internal and transferred accumulation in region r, i.e., $n_r = n_{rr} + n_{rr'}$. The detailed model is explained in Section 5.2.1. Aboudolas & Geroliminis (2013) applied the two-region model by Geroliminis & Daganzo (2007) to multiple regions by implementing linearization. Hajiahmadi *et al.* (2013) proposed the multiregional model based on the model developed by Geroliminis & Daganzo (2007), considering accumulation separately according to the trip destinations under the constant regional trip length assumption.

Yildirimoglu & Geroliminis (2014) introduced the idea of the regional route from origin to destination regions in the partitioned network into connected several regions to develop routing strategies and establish the dynamic stochastic user equilibrium. They also revisited the constant trip length assumption in previous studies and replaced it with the dynamic average trip length defined for each regional route. The flows and trip length of each route were computed through aggregated and approximated dynamic traffic assignments. Mariotte & Leclercq (2019) extended this model to consider the spillback of congestion in each region and implement it in the trip-based model. Also, they assessed the accuracy of the accumulation-based and trip-based models in the Lyon network split into multi regions. By observing real trajectories, some vehicles return to regions they have already passed in their trips according to the shape of the partitioned regions. Especially when we consider the non-compact partitioning into small non-connected regions, e.g., the congested and less-congested pockets explained in Section 3 of Chapter 3, we observe that many trips go back and forth between the regions. However, an MFD model capable of considering the effect of such trajectories based on path sequence information, i.e., the order of the regions that a vehicle passes through, has not yet been proposed.

5.1.2 Research Objectives

In Chapter 4, we showed that trip length settings and estimation accuracy have a considerable impact on prediction accuracy obtained with classical MFD models in a single region. Also, as mentioned in Batista *et al.* (2019), Paipuri *et al.* (2020), and Chapter 3, path sequence information plays an important role in trip length estimation. Therefore, the settings and estimation accuracy of trip length and path sequence information may have a huge impact

on the prediction results by the multiregional MFD models. However, no study has assessed the impact of these settings using MFD models and real data because of the lack of enough data to give the ground truth of path sequence and regional trip length.

Our objectives in this chapter are: 1) to propose a simplified and mathematical multi-regional MFD model framework while considering path sequence information for calibration using real data, and 2) to investigate the effect of trip length estimation and path sequence information on the prediction accuracy of traffic state dynamics by using complete trajectory data. In this chapter we consider a test case with two interfaced regions, as described in Chapter 3, Section 3. These regions are labeled congested and less congested. In Section 5.2, we first present the multi-regional MFD model framework in the accumulation-based and trip-based models when the path sequence is not available. Then, we propose the extension method of these models to consider the path sequence. In Section 5.3, we assess the prediction results of MFD models according to the different trip length settings and whether the path sequence is available or not. In Section 5.4, the effect of MFD approximation is confirmed in the multi-region framework. The main conclusions of this chapter are summarized in Section 5.5. The complete trajectory set based on Athens drone data after data imputation described in Section 2 of Chapter 4 is used for all the calculations in this chapter.

5.2 MFD Model Design

When we consider more than two connected regions, MFD models should be extended to consider the interacting flow between each region. We denote the flow of the vehicles that move from region r to r' at time t as the transferred flow $Qtra_{rr'}(t)$. The flow of vehicles that end their trips in region r or exit the network from region r at time t is denoted the end flow $Qend_r(t)$. The regional outflow of region r can be expressed as the sum of transferred flow and the end flow. The regional inflow, i.e., the flow of vehicles that start their trip or entry into the network at region r, $Qin_r(t)$, is given as the input parameter of the model.

The multiregional MFD model considering regional routes was introduced by Yildirimoglu & Geroliminis (2014), and Mariotte *et al.* (2017) for the accumulation-based and trip-based models. The regional routes in the literature are often defined by dynamic traffic assignment, and the trips that return to the same region cannot be considered as these trips are observed in trajectory data according to network partitioning settings. Since path sequence information, including trips that return to the same region, can be calibrated from trajectory data, it may be possible to improve the prediction accuracy of MFD models. Additionally, Batista *et al.* (2019), and Paipuri *et al.* (2020) showed that multiregional models that do not consider path sequence information can lead to numerous errors in the prediction results. However, MFD models considering path sequence information have not been proposed yet. Therefore, to investigate the effect of path sequence information on the prediction results, we first need to extend the multiregional models to predict the traffic state using aggregated trip length and path sequence information calculated from data, e.g., path sequence distribution. The framework extended to consider the path sequence information for the trip-based model is quite straightforward. Since each individual trip is considered separately in this model, the path sequence can be assigned individually from the path sequence distribution. For the accumulation-based model, since the average trip length is generally

Variables	
$Qtra_{rr'}(t)$	the transferred flow of vehicles that move from region r to r' at time t
$Qend_r(t)$	the end flow of vehicles that end their trips in region r or exit the network from region r at time t
$Qout_r(t)$	the regional outflow of region r at time t
$Qin_r(t)$	the regional inflow of region r at time t
$n_r(t)$	the regional accumulation of region r at time t
PS	the path sequence, i.e., the vector of ordering regions that the vehicle passes through
n_r^{tra}	the accumulation of the vehicles that transfer from region r
n_r^{end}	the accumulation of the vehicles that end their trip in region r
$V_r(n_r(t))$	the regional V-MFD of the region r
l_r	the average partial trip length of region r
ρ_r	the trip end possibility of region r
$\bar{N}_r$	the average number of entering and returning regions r of the vehicle which ends its trip in region r'
$Tin_{i,s}$	the entry time of vehicle i at number s of the path sequence
$Tout_{i,s}$	the exit time of vehicle i at number s of the path sequence
Tin, **L**, **Tout**	the vectors of entry time, trip length, and exit time for the vehicles inside the network
$Exit_{i,s}$	exit type of vehicle i at number s of path sequence

TAB. 5.1 – *Lists of Variables used in Section 5.2*

used for all vehicles or vehicles with the same path sequence, path sequence information should be aggregated differently from the trip-based model to correspond to the average trip length. However, no study has yet proposed the accumulation-based model framework with aggregated path sequence information.

Therefore, in this section, we first explain the accumulation-based model for two regions without path sequence information in section 5.2.1. Then, we describe the new extension of the accumulation-based model for considering path sequence information in section 5.2.2. Then, the trip-based model with/without considering path sequence information is explained in section 5.2.3. The model explained above for two regions can be easily extended to a multi-region model. The notations of the variables in section 5.2 are listed in Table 5.1.

5.2.1 Accumulation-based Model without Path Sequence Information

First, we consider the simple case assuming that all vehicles follow the two types of trips: 1) passing through only one region r (internal trip), 2) entering r, moving from r to r', then exiting r' (transferred trip). The first trip shows the internal flow, and the second trip shows the transferred flow in the literature described in Section 5.1.1. When we denote the path sequence PS, i.e., the vector of ordering regions that the vehicle passes through, the path sequence of internal trips can be expressed as $PS = [r]$ or $[r']$ and one of transferred trips can be expressed as $PS = [r, r']$ or $[r', r]$. Note that the path sequence in this simple case does not include the trip that returns to the same region. Therefore, it is the same as the regional route in the literature. To consider the internal flow, we separate regional inflow Qin_r by the

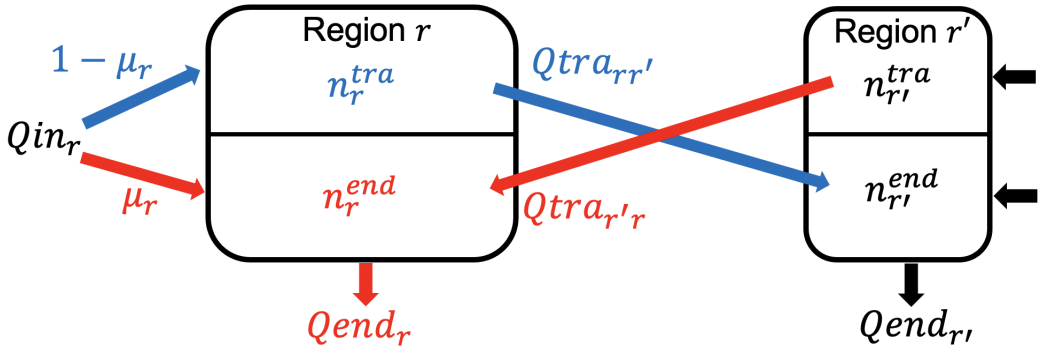

FIG. 5.1 – *Accumulation based model for two regions with a simple path sequence*

ratio μ_r that shows the number of vehicles that pass through only one region r over vehicles that start their trip in r. To consider the transferred flow separately from the end flow, we consider two types of accumulations: the accumulation of the vehicles that transfer from region r, i.e., n_r^{tra}, and the accumulation of the vehicles that end their trip at region r, i.e., n_r^{end}, as shown in Figure 5.1. This model is based on the model by Geroliminis & Daganzo (2008). The difference does not distinguish flows of vehicles that enter from outside into region r or exit from region r outside it and vehicles that start or end their trips in region r.

The transferred outflow and accumulation can be calculated in the same way as in the the single region model, c.f., Section 3.2 of Chapter 4. When $V_r(n_r(t))$ denotes the regional V-MFD according to the regional $n_r(t)$ at time t, and l_r shows the average partial trip length of region r, i.e., the trip length during the period a vehicle enters and exits the region, the transferred outflow and accumulation are expressed in Eq. (5.1).

$$\begin{aligned} Qtra_{rr'}(t+1) &= \frac{V_r(n_r(t)) * n_r^{tra}(t)}{l_r} \\ n_r^{tra}(t+1) &= n_r^{tra}(t) + (Qin_r(t+1) * (1-\mu_r) - Qtra_{rr'}(t+1)) * dt \end{aligned} \tag{5.1}$$

The end outflow and accumulation can be calculated by Eq. (5.2).

$$\begin{aligned} Qend_r(t+1) &= \frac{V_r(n_r(t)) * n_r^{end}(t)}{l_r} \\ n_r^{end}(t+1) &= n_r^{end}(t) + (Qin_r(t+1) * \mu_r + Qtra_{r'r}(t+1) - Qend_r(t+1)) * dt \end{aligned} \tag{5.2}$$

According to Eq. (5.1) and (5.2), the regional accumulation and the regional outflow can be calculated by Eq. (5.3).

$$\begin{aligned} Qout_r(t+1) &= Qtra_{rr'}(t+1) + Qend_r(t+1) \\ n_r(t+1) &= n_r^{tra}(t+1) + n_r^{end}(t+1) \end{aligned} \tag{5.3}$$

5.2.2 Accumulation-based Model with Path Sequence Information

When we consider the path sequence, it is necessary to consider the trips which exit the region once and return to the region later again. Here, two types of transferred outflow and accumulation are considered according to the destination: for the vehicles in region r which move to another region r' and end their trips in region r and end their trips in r'. The former

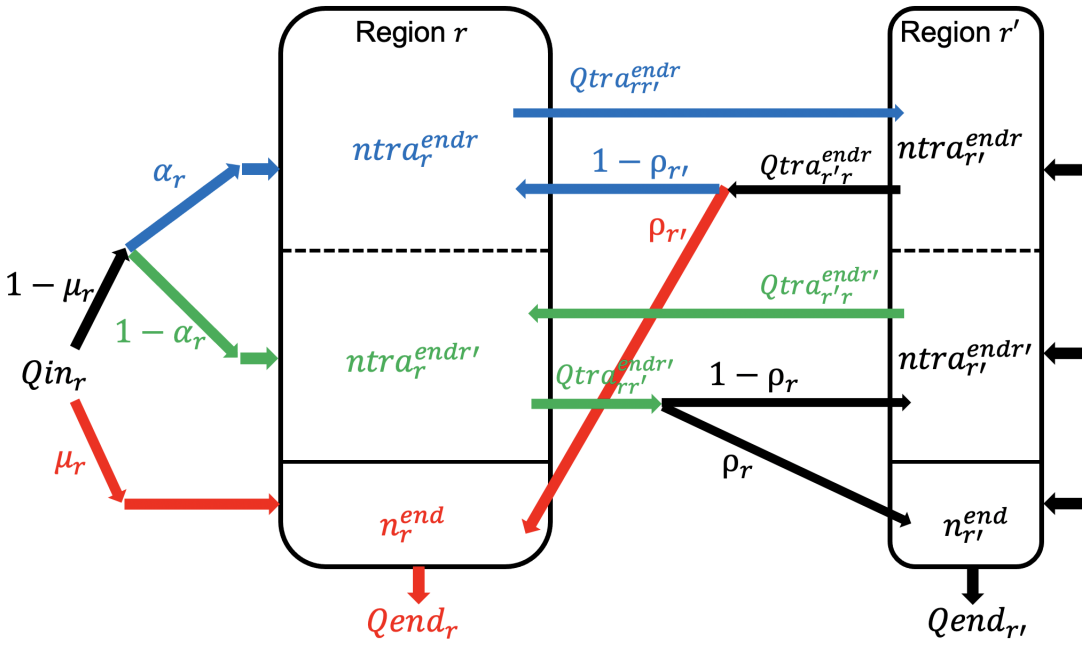

FIG. 5.2 – *Accumulation based model for two regions with path sequence information*

outflow and accumulation are labeled as $Qtra_{rr'}^{endr}$ and $ntra_r^{endr}$, and the latter ones as $Qtra_{rr'}^{endr'}$ and $ntra_r^{endr'}$. When ρ_r is the possibility that the vehicle in region r will not return to region r and end its trip in r', $1-\rho_r$ expresses the possibility that the vehicle returns to the region r. The probability of the path sequence which the vehicle passes through the region X times in total can be expressed by the binomial process as $P(X=s)=(1-\rho)^{s-1}*\rho$. According to the geometrical law, the expectation value of this binomial process can be calculated as $E(X)=1/\rho$. $E(X)$ represents the average number $\bar{N}_r$ of entry and return in region r by a vehicle, which finally ends its trip in region r'. For example, if the path sequence of vehicle i is $PS=[r',r,r',r,r']$ or $PS=[r,r',r,r']$, $N_{r,i}=2$. Thus, ρ_r can be calculated by deriving $\bar{N}_r$ from the path sequence information in the real data, i.e., $\rho_r=1/\bar{N}_r$.

Also, regional inflow Qin_r in region r has to be separated as for three types of trips: 1) passing through only region r, 2) moving to another region r' but ending in r, and 3) moving to another region r' and ending in r'. When μ_r is the ratio of the number of vehicles that pass through only one region r, i.e., $|PS|=1$, μ_r*Qin_r is the inflow of the vehicles that start and end at region r and never move to another region. On the other hand, the vehicle inflow that transfers from r to r' can be explained as $(1-\mu_r)*Qin_r$. Furthermore, we separate $(1-\mu_r)*Qin_r$ that pass through two regions into one that ends its trip in region r and another that ends its trip in the region r' by using the ratio α_r. α_r is the ratio of the vehicle that starts and ends its trip in region r, and $1-\alpha_r$ shows the ratio of the vehicle that starts in region r and ends in another region r'. For example, the vehicle inflow that starts the trip in region r, moves to another region r', and ends in region r is $\alpha_r*(1-\mu_r)*Qin_r$. All the connections between outflows and accumulations are shown in Figure 5.2.

Now, the transferred outflow and accumulation in region r, which ends the trip in region

r is written as Eq. (5.4).

$$\begin{aligned} Qtra_{rr'}^{endr}(t+1) =& \frac{V_r(n_r(t)) * ntra_r^{endr}(t)}{l_r} \\ ntra_r^{endr}(t+1) =& ntra_r^{endr}(t) + (\alpha_r * (1-\mu_r) * Qin_r(t+1) + (1-\rho_{r'}) * Qtra_{r'r}^{endr}(t+1) \\ & - Qtra_{rr'}^{endr}(t+1)) * dt \end{aligned} \tag{5.4}$$

The transferred outflow and accumulation in region r, which end the trip in another region r' is written as Eq. (5.5).

$$\begin{aligned} Qtra_{rr'}^{endr'}(t+1) =& \frac{V_r(n_r(t)) * ntra_r^{endr'}(t)}{l_r} \\ ntra_r^{endr'}(t+1) =& ntra_r^{endr'}(t) + ((1-\alpha_r) * (1-\mu_r) * Qin_r(t+1) + Qtra_{r'r}^{endr'}(t+1) \\ & - Qtra_{rr'}^{endr'}(t+1)) * dt \end{aligned} \tag{5.5}$$

The end outflow and accumulation in region r can be explained by Eq. (5.6).

$$\begin{aligned} Qend_r(t+1) =& \frac{V_r(n_r(t)) * nend_r(t)}{l_r} \\ nend_r(t+1) =& nend_r(t) + ((1-\mu_r) * Qin_r(t+1) + \rho_{r'} * Qtra_{r'r}^{endr}(t+1) \\ & - Qend_r(t+1)) * dt \end{aligned} \tag{5.6}$$

The regional outflow and accumulation can be calculated by Eq. (5.7).

$$\begin{aligned} Qout_r(t+1) &= Qtra_{rr'}^{endr}(t+1) + Qtra_{rr'}^{endr'}(t+1) + Qend_r(t+1) \\ n_r(t+1) &= ntra_r^{endr}(t+1) + ntra_r^{endr'}(t+1) + nend_r(t+1) \end{aligned} \tag{5.7}$$

5.2.3 Trip based model

Considering path sequence in the trip-based model framework is more straightforward than in the accumulation-based model since trip length and path sequence can be assigned individually. Based on the event-based model process by Mariotte *et al.* (2017), our simulation process for the trip based model of two regions is given below:

Step 1. We assign path sequence PS_i for vehicle i, which is already in the network at $t = 0$, as:

$$PS_i = PS \tag{5.8}$$

At this time, PS is assigned depending on the path sequence setting, e.g., choosing from the path sequence distribution or using the pattern chosen.

Step 2. When vehicle i is already in the network at $t = 0$, we assign the partial trip length $l_{i,s}$, the entry time $Tin_{i,s}$, and the exit time $Tout_{i,s}$ for vehicle i at number s of the path sequence as shown below:

$$\begin{aligned} Tin_{i,s} &= Tout_{i,s-1} \\ l_{i,s} &= l_{PS_i(s)} \\ Tout_{i,s} &= l_{i,s}/V_{PS_i(s)}(n_{PS_i(s)}(t)) + Tin_{i,s} \end{aligned} \tag{5.9}$$

At this time, the trip beginning at time $Tin_{i,1}$ can be calculated by using the trip beginning time of vehicle $i-1$ and the initial inflow of a whole network that is the sum of the regional inflow of all the regions as $Tin_{i,1} = Tin_{i-1,1} - 1/Qin(0)$. The trip beginning time of the first entry vehicle $Tin_{1,1}$ is the same as the time at the beginning of the simulation, i.e. $Tin_{1,1} = time(0)$. Partial trip length $l_{PS_i(s)}$ is assigned depending on the trip length setting. We repeat the calculation for a whole path sequence $s = 1 : |PS_i|$ until the accumulation inside each region reaches the initial accumulation $n_r(0)$. $Tin_{i,s}$, $l_{i,s}$, and $Tout_{i,s}$ for a whole path sequence of all the vehicles builds the vectors for the vehicles inside the network as **Tin**, **L**, and **Tout**. Also, we assign the exit type as "transfer" if s is not the end of the path sequence and as "end" otherwise, as shown in Eq. (5.10).

$$Exit_{i,s} = \begin{cases} 0 \text{ if } s = |PS_i| \text{ (”transfer”)} \\ 1 \text{ otherwise ("end")} \end{cases} \tag{5.10}$$

Step 3. The number of vehicles starting and ending their trips in region r at time t is initialized as $dNin_r^{sta} = 0$ and $dNout_r^{end} = 0$. Also, the number of vehicles coming from and going to the other regions is initialized as $dNin_r^{tra} = 0$ and $dNout_r^{tra} = 0$. The initial time is $t = 1$.

Step 4. We calculate the entry time of the following vehicle which enters the network after $Tin_{i,s}$, i.e., $max(\mathbf{Tin})$, by

$$Tin_{next} = max(\mathbf{Tin}) + 1/Qin(t) \tag{5.11}$$

Step 5(a). If the earliest time of the exit time vector is earlier than the next entry time as $min(\mathbf{Tout}) < Tin_{next}$, the next event is that a new vehicle enters. Therefore, we assign PS_i of a newly arrived vehicle i as Step 1. Then, we add $Tin_{i,s}$, $L_{i,s}$, and $Tout_{i,s}$ for a whole path sequence of a newly arrived vehicle i to the vector **Tin**, **L**, and **Tout**. At this time, L_i, Tin_i, and $Tout_i$ are calculated by Eq. (5.9). $Exit_{i,s}$ is calculated by Eq.(5.10). Then, we update the number of entering vehicles as $dNin_{PS_i(s)}^{sta} = dNin_{PS_i(s)}^{sta} + 1$. The entry time of the next entering vehicle should be updated as $Tin_{next} = max(\mathbf{Tin}) + 1/Qin(t)$.

Step 5(b). If $min(\mathbf{Tout}) >= Tin_{next}$, the next event is that a vehicle inside the network exits or transfers. If $Exit_{i,s} = 0$ for vehicle i whose $Tout_{i,s} = min(\mathbf{Tout})$, vehicle i moves to other regions at s. Therefore, we update $dNin_{PS_i(s)}^{tra} = dNin_{PS_i(s)}^{tra} + 1$ and $dNout_{PS_i(s)}^{tra} = dNout_{PS_i(s)}^{tra} + 1$. If $Exit_{i,s} = 1$, vehicle i exits the network at s. Therefore, we update $dNout_{PS_i(s)}^{end} = dNout_{PS_i(s)}^{end} + 1$. In all cases, we remove $Tin_{i,s}$, $L_{i,s}$, and $Tout_{i,s}$ of the vehicle whose $Tout_{i,s} = min(\mathbf{Tout})$ from **Tin**, **L**, and **Tout**.

Step 6. Steps 4 and 5 are repeated until Tin_{next} exceeds $time(t)$. When $Tin_{next} > time(t)$, we calculate the accumulation and outflow at time t by:

$$\begin{aligned} n_r(t) &= n_r(t-1) + (dNin_r^{tra} + dNin_r^{sta}) - (dNout_r^{tra} + dNout_r^{end}) \\ Qout_r(t) &= (dNout_r^{tra} + dNout_r^{end})/dt \end{aligned} \tag{5.12}$$

Then, we update the simulation time as $t = t + 1$ and restart from step 3.

Step 7. Steps 3 to 6 are repeated until the $time(t)$ reaches the end of the simulation.

5.3 Impact of Trip Length based on Real Speed

This section compares the ground truth of the regional outflow and accumulation and the prediction results using different trip length aggregation cases, e.g., average and distribution, according to MFD models with/without path sequence information, c.f., Section 5.2.

The Athens network is partitioned into congested and less-congested pockets when the partitioning weight on speed is $w = 6.7$, see, Section 3.1 in Chapter 3. The input variables such as regional inflow and the initial regional accumulation are calculated using the trip set after data imputation, see in Figures 12 (a) and (d) in Section 2 in Chapter 4. The ground truth regional outflow and accumulation are also shown in Figures 12 (b) and (d) in Chapter 4. To analyze the effect of trip length aggregation carefully, we use real values of the average regional mean speed dynamics $V_r(t)$, as shown in Figure 12 (c) in Chapter 4 instead of regional V-MFD $V_r(n_r(t))$.

Section 5.3.1 compares the prediction accuracy of different trip length aggregation cases of two models when the path sequence information is not available. In Section 5.3.2, we introduce the path sequence and repeat the assessment of the model.

5.3.1 Without Path Sequence Information

Two typical cases for trip length aggregation setting prediction accuracy are considered in this section:

Case 1 We use the constant average value of the regional trip length of each pocket as the input value $L_r =< L_{i,r} >$.

Case 2 We use the regional trip length distribution as the input value $L_r \sim P(L_{i,r})$.

At this time, the average value and distribution of regional trip lengths are calculated by using the real trip length of all the vehicles in each pocket. Since it is quite challenging to adapt trip length distribution instead of average values in the accumulation-based model, we assess Case 2 only with the trip-based model. μ_r is calculated by the number of vehicles that start trips in r with $|PS| = 1$ over the number of all vehicles that start trips in r. The values are $\mu_r = 0.08$ in both pockets. Initial regional accumulation $n_r(1)$ is given as the ground truth accumulation at 1 minute in Figure 12 (d) of Chapter 4. We calculate the ratio ν_r as the number of vehicles that end their trips in region r per the number of vehicles that pass through region r to divide $n_r(1)$ into the initial endand transferred accumulations. By using ν_r, initial end and transferred accumulations can be given as $n_r^{end}(1) = \nu_r * n_r(1)$ and $n_r^{tra}(1) = (1 - \nu_r) * n_r(1)$.

The regional outflow and accumulation according to the two cases and models are shown in Figure 5.3. The outflow dynamics of all cases are similar in both congested (Figure 5.3 (a)) and less-congested pockets (Figure 5.3 (c)) and much lower than the ground truth, i.e., around 6 [veh/s] in both pockets while the ground truth is around 12-18 [veh/s]. We compare end and transferred flows in Figure 5.4. In both pockets, the predicted end flows for all cases are stable and similar to the ground truth. In the congested pocket, the values in all cases are slightly smaller, i.e., the maximum difference is 1 veh/s compared to the ground truth at some time periods, as shown in Figure 5.4 (a). On the contrary, the values are slightly higher, i.e., the maximum difference is 1 veh/s compared to the ground truth. The main possible reason for these differences is that the return trips, e.g., vehicles start the trip in r, move

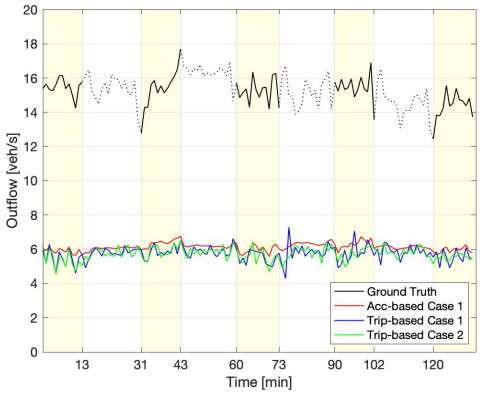

(a) Outflow [veh/s] in Congested Pocket

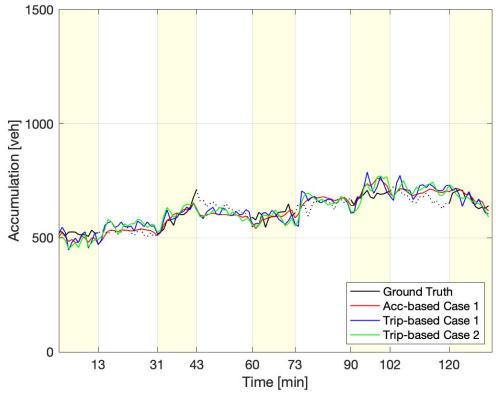

(b) Accumulation [veh] in Congested Pocket

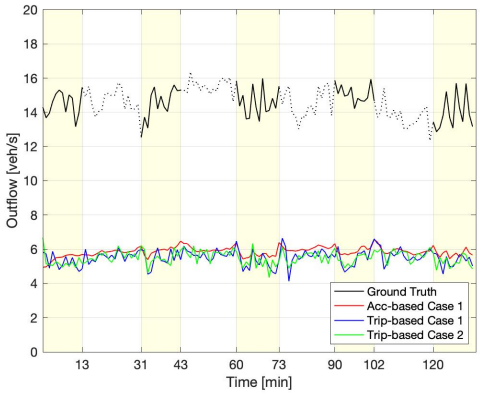

(c) Outflow [veh/s] in Less-Congested Pocket

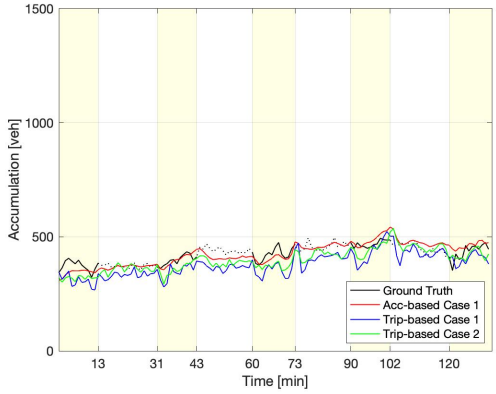

(d) Accumulation [veh] in Less-Congested Pocket

FIG. 5.3 – *Prediction results in each pocket without path sequence information (yellow zone: drone period, white zone: no-drone period, Acc-based: Accumulation-based model, trip-based, trip-based model, Case 1: using average trip length, Case 2: using trip length distribution)*

to r', and end in r, cannot be considered without path sequence information. For example, all vehicles that start in r are assumed to end in r' unless they are internal trips for vehicles that do not move to another region. Also, in both pockets, the results of the trip-based model are slightly lower than the accumulation-based model. The transferred flows in both congested (Figure 5.4 (b)) and less-congested pockets (Figure 5.4 (d)) are much lower than the ground truth, e.g., around 4-6 [veh/s] in the congested pocket and around 1-2 [veh/s] in the less-congested pocket while the ground truth values are around 10-14 [veh/s] and 8-12 [veh/s]. The errors of the end flow balance between two pockets and lower-estimated transferred flows are derived from a simple path sequence regardless of the path sequence. Figure 5.5 (a) shows the global outflow, which represents the network's outflow calculated by the sum of the end flows of both pockets. According to the figure, the global outflow has only small errors in the accumulation-based model, although the end flows in both pockets have errors. The trip-based model's global outflow is lower in both cases, around 1 veh/s lower than the ground truth, because of the cumulated small differences of end flows compared to the accumulation-based model.

For the regional accumulation in both pockets, as shown in Figure 5.3 (b) and (d), the

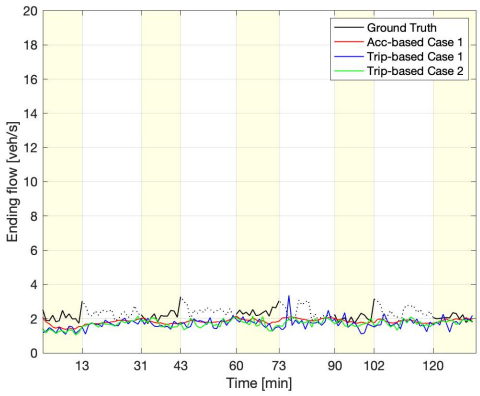

(a) End flow [veh/s] in congested pocket

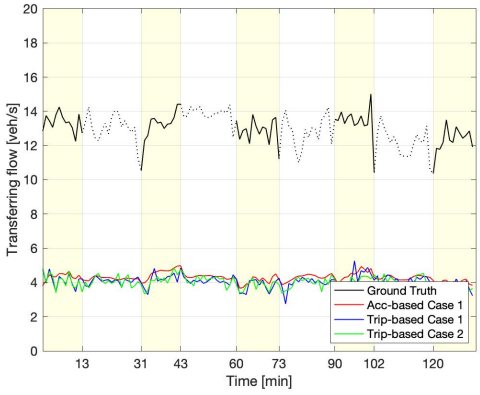

(b) Transferrde flow [veh/s] in congested pocket

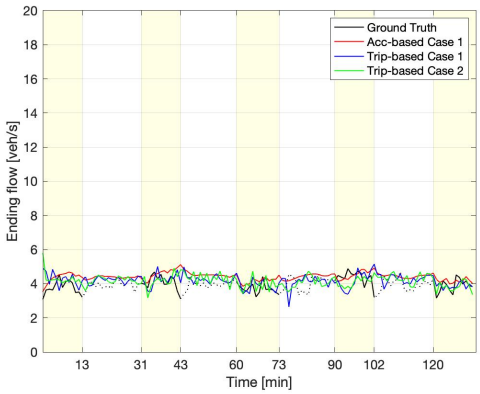

(c) End flow [veh/s] in less-congested pocket

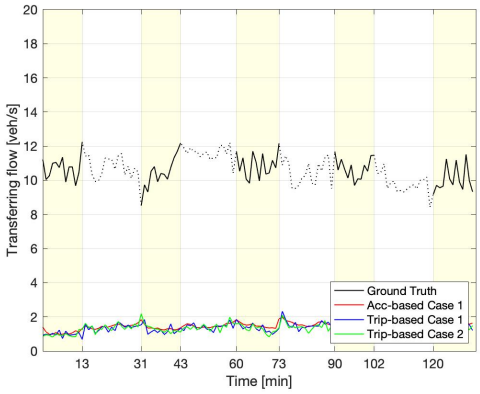

(d) Transferred flow [veh/s] in less-congested pocket

FIG. 5.4 – *Predicted flows in each pocket without path sequence information (yellow zone: drone period, white zone: no-drone period, Acc-based: Accumulation-based model, trip-based, trip-based model, Case 1: using average trip length, Case 2: using trip length distribution)*

dynamics of Case 1 with the accumulation-based model are slightly higher than in the other cases. For the global accumulation, which is the sum of the regional accumulation shown in Figure 5.5 (b), the error becomes more significant because of the aggregation of errors in both regions.

Table 5.2 shows the relative error of all the prediction results. The accuracy of the regional accumulation can be as good with errors below 10% when using the accumulation-based model with the average trip length (Case 1) and the trip-based model with the trip length distribution (Case 2) in the congested pocket. The regional outflow has significant errors in over 55% in all cases. On the other hand, the predicted global outflow and accumulation accuracy is comparatively high, with errors below 10% in all cases.

Thus, the regional accumulation and the global outflow and accumulation can be predicted with good accuracy even without the path sequence information. On the other hand, it is impossible to obtain an accurate regional outflow without the path sequence information, as we will show in the next section.

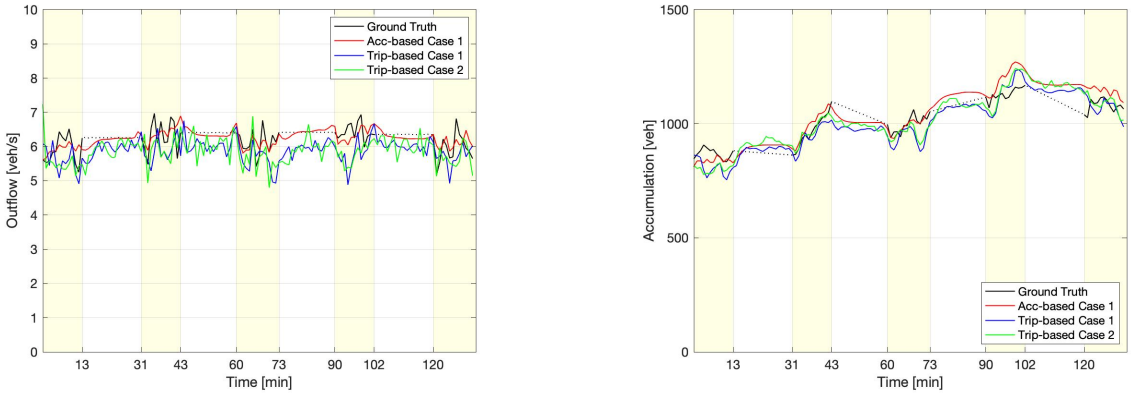

(a) Global Outflow [veh/s] (b) Global Accumulation [veh]

FIG. 5.5 – *Predicted global traffic state in each pocket without path sequence information (yellow zone: drone period, white zone: no-drone period, Acc-based: Accumulation-based model, trip-based, trip-based model, Case 1: using average trip length, Case 2: using trip length distribution)*

	Congested				Less-Congested				Global	
	$Qout_c$	n_c	$Qtra_c$	$Qend_c$	$Qout_u$	n_u	$Qtra_u$	$Qend_u$	$Qout$	n
Case 1 Acc	59.7	9.2	66.8	19.3	59.6	13.1	86.2	13.5	3.1	4.2
Case 1 Trip	62.3	10.0	68.9	25.9	62.0	8.8	87.1	11.9	7.4	4.1
Case 2 Trip	62.4	9.6	69.0	25.1	62.1	10.2	87.2	11.3	7.3	4.4

TAB. 5.2 – *Relative error [%] of the prediction results without Path Sequence Information (Acc-based: Accumulation-based model, trip-based, trip-based model, Case 1: using average trip length, Case 2: using trip length distribution)*

5.3.2 The case in which path sequence information is available

When the path sequence information is available, two cases of trip length aggregation settings in Section 5.3.1 are changed in the following:

Case 1 We use the constant average value of the partial trip length of each pocket as the input values $l_r =< l_r >$.

Case 2 We randomly choose the regional trip length from the joint distribution of regional trip length and path sequence as $L_r \sim P(L_r, PS_i)$. The input trip length is calculated from the regional trip length and path sequence as $l_r = L_r/|PS_{i,r}|$ where $|PS_{i,r}|$ denotes the number of times that vehicle i passes through region r in the chosen path sequence.

For the trip-based model, the path sequence is assigned randomly by path sequence distribution in Case 1 as $PS \sim P(PS_i)$. In Case 2, the path sequence is assigned by the joint distribution as $PS \sim P(L_r, PS_i)$ while choosing the regional trip length. We assess Case 2 only with the trip-based model since using trip length distribution in the accumulation-based model is quite difficult. Path sequence information in the accumulation-based model is considered as μ, ρ and α values, c.f., Section 5.2.2, calculated from the path sequence distribution.

PS	N_r	vehicle number [veh]
[c→ u]	1	5050
[u→ c → u]	1	2697
[c→ u → c → u]	2	6264
[u→ c → u → c → u]	2	2331
[c→ u → c → u → c → u]	3	6352
...	...	...

TAB. 5.3 – *Path sequence information sample (c: congested pocket, u: less-congested pocket)*

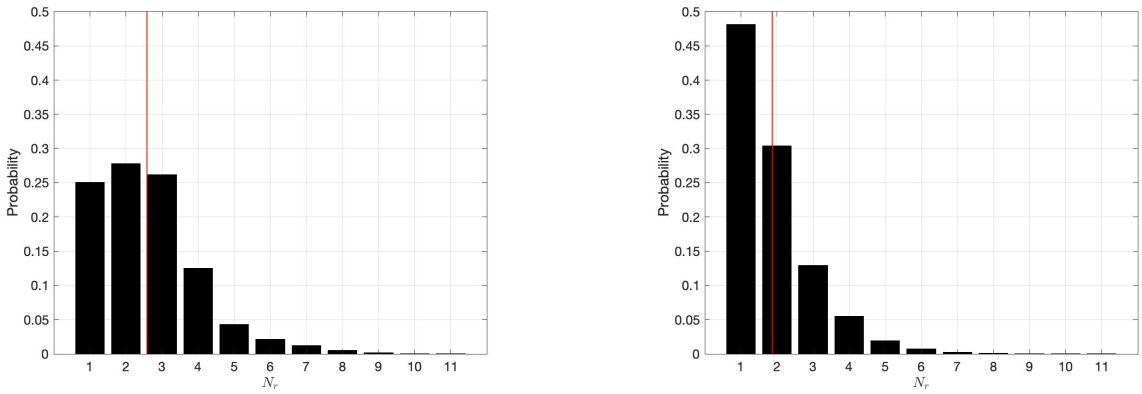

(a) Congested pocket (b) Less-congested pocket

FIG. 5.6 – N_r *distribution of the Athens data set after data imputation*

The average value of the partial trip length for Case 1 is calculated from the average trip length in a region since the vehicle enters the region until it moves to another region or exits the network. The joint distribution of regional trip length and path sequence is calculated by regional trip length for all vehicles with each path sequence. Path sequence information includes each path sequence, N_r value, i.e., the average number of entries and returns in regions r by a vehicle, and the number of vehicles of each path sequence, as shown in Table 5.3. Path sequence distribution is calculated from the number of vehicles of each path sequence. μ_r and α_r are calculated from the number of vehicles that $|PS_i| = 1$ and vehicles that $PS_{|PS_i|} = r$. μ values are 0.08, α values are 0.34 and 0.66 in congested and less-congested pockets respectively. The value of N_r is distributed as shown in Figure 5.6 for the congested pocket (a) and the less-congested pocket (b). The red vertical lines in the figures show the average value $\bar{N}_r$. According to $\bar{N}_r$, ρ values are 0.39 and 0.54 in the congested and less-congested pockets respectively. The initial regional accumulation $n_r(1)$ is given as the ground truth accumulation at 1 minute in Figure 12 (d) of Chapter 4. The initial transferred accumulation in region r for vehicles that end in another region; r' can be calculated in the same way in the model without path sequence in Section 5.3.1 by using ratio nu_r as $ntra_{rr'}^{endr'}(1) = n_r(1) * (1 - nu_r)$. The accumulation of vehicles in region r that end in r are simply divided into two for $nend_r(1)$ and $ntra_{rr'}^{endr}(1)$ as $nend_r(1) = ntra_{rr'}^{endr}(1) = 1/2 * n_r(1) * nu_r$.

The predicted outflow and accumulation results according to all cases are shown in Figure 5.7. The predicted outflows in both congested and less-congested pockets, as shown in

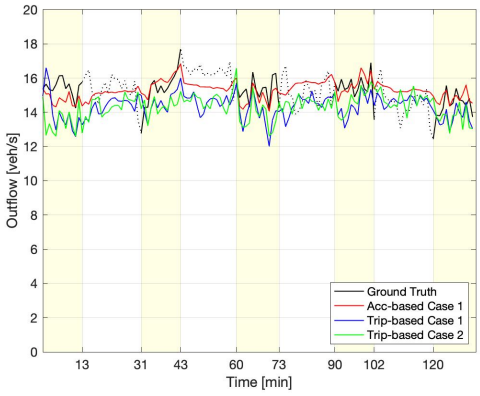

(a) Outflow [veh/s] in Congested Pocket

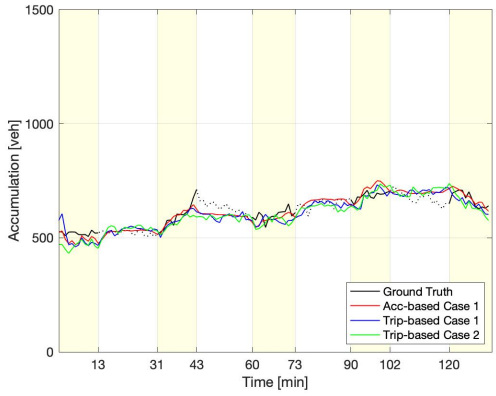

(b) Accumulation [veh] in Congested Pocket

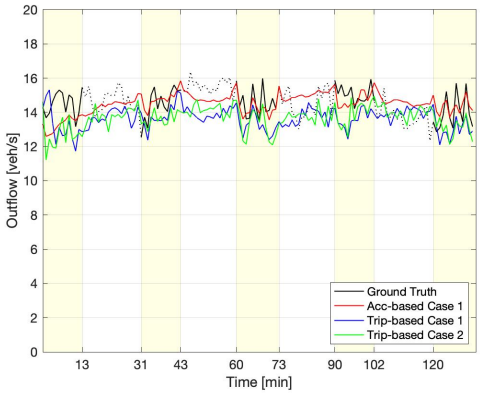

(c) Outflow [veh/s] in Less-Congested Pocket

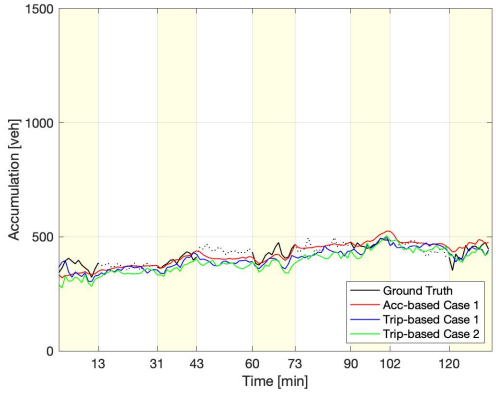

(d) Accumulation [veh] in Less-Congested Pocket

FIG. 5.7 – *Prediction results in each pocket with path sequence information (yellow zone: drone period, white zone: no-drone period, Acc-based: Accumulation-based model, trip-based, trip-based model, Case 1: using average trip length, Case 2: using trip length distribution)*

Figures 5.7 (a) and (c) are closer to ground truth values compared to the case without path sequence information in Figure 5.3. In particular, the proposed accumulation-based model provides fairly good results in both pockets as the relative errors are 4.8% and 5.4% in the congested and less-congested pockets according to Table 5.4 while the relative errors are over 55% in both pockets without path sequence information. The trip-based model in both cases predicts the outflow lower than the ground truth. The relative errors in Case 1 are 7.2% and 7.0%, and 8.1% and 7.7% in Case 2, for the congested and less-congested pockets respectively. Those errors are higher than the errors with the accumulation-based model. However, the accuracy improves significantly compared to the case without path sequence information, i.e., over 60% in both pockets in both cases. The end and transferred flows in both cases are shown in Figure 5.8. Transferred flows and end flows in all cases are improved compared to Figure 5.4 without path sequence information, i.e., the relative errors of the end flows are around 13% to 14% with path sequence information whereas they are around 19% to 26% without it. The relative errors of the transferred flows are around 5% to 10% with path sequence information whereas they are over 65% without it. In all cases, the end flow in the congested pocket is quite similar as the relative errors of all cases range

	Congested				Less-Congested				Global	
	$Qout_c$	n_c	$Qtra_c$	$Qend_c$	$Qout_u$	n_u	$Qtra_u$	$Qend_u$	$Qout$	n
Case 1 Acc	4.8	9.2	5.8	13.8	5.4	13.3	6.7	8.1	3.3	4.1
Case 1 Trip	7.2	9.4	8.0	13.1	7.0	8.6	7.8	10.9	7.8	3.8
Case 2 Trip	8.1	9.2	9.0	13.6	7.7	9.4	8.6	10.3	7.5	4.7

TAB. 5.4 – *Relative error [%] of prediction results with Path Sequence Information (Acc-based: Accumulation-based model, trip-based, trip-based model, Case 1: using average trip length, Case 2: using trip length distribution)*

	$Qout$			n		
	Single	Simple PS	PS info	Single	Simple PS	PS info
Case 1 Acc	3.1	3.1	3.3	9.4	4.2	4.1
Case 1 Trip	4.0	7.4	7.8	8.8	4.1	3.8
Case 2 Trip	5.4	7.3	7.5	8.8	4.4	4.7

TAB. 5.5 – *Relative error [%] of global outflow and accumulation by a single region model (Single), multi-regional model without path sequence information (Simple PS), and multiregional model with path sequence information (PS info). (Acc-based: Accumulation-based model, trip-based, trip-based model, Case 1: using average trip length, Case 2: using trip length distribution)*

between 13 and 14%. On the other hand, the transferred flow in the trip-based model with both cases is lower than for the ground truth and the accumulation-based model. The relative error of the accumulation-based model is 5.8% in the congested pocket, while the errors of the trip-based models are 8.0% in Case 1 and 9.0% in Case 2.

The predicted accumulation in all cases is shown in Figure 5.7 (b) for the congested pocket and (d) for the less-congested pocket. In the congested pocket, the predicted dynamics follow the ground truth in all cases and are not much different from the case without path sequence in Figure 5.3 (b), i.e., the relative errors are the same with and without path sequence in the accumulation-based model and the errors decrease from 0.4% to 0.6% in both cases of the trip-based model. In the less-congested pocket, the results of the trip-based model in both cases are slightly lower than those of the accumulation-based model (the maximum difference is 50 veh). In Table 5.4, the accuracy of predicted accumulation in the less-congested pocket is better for the trip-based model (the relative errors are 8.6% and 9.4% in Cases 1 and 2) than for the accumulation-based model (13.3%).

The predicted global outflow and accumulation dynamics in Figure 5.9 are quite similar to the results without path sequence in Figure 5.5. The relative errors of predicted outflow and accumulation over a whole network with a single region model in Chapter 4, a multiregional model without path sequence in Section 5.3.1, and with path sequence (global outflow and accumulation) are compared in Table 5.5. For the outflow, the accuracy of the single region model is the highest, i.e., the relative errors are 3.1% for the accumulation-based model and 4.0% and 5.4% in Cases 1 and 2 of the trip-based models. In particular, when using the average value for the trip-based model the relative error becomes higher in the multiregional models, for example, 7.4% without the path sequence and 7.8% with it. On the other hand, the predicted global accumulation accuracy is better when using a multiregional model (the relative errors from 3.8% to 4.7%) than using a single region model (from 8.8% to 9.4%). When using the accumulation-based model and the trip-based model

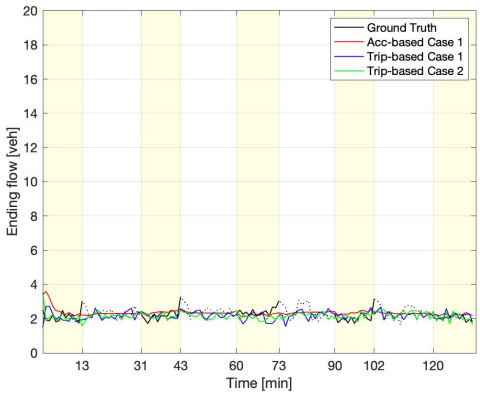

(a) End flow [veh/s] in congested pocket

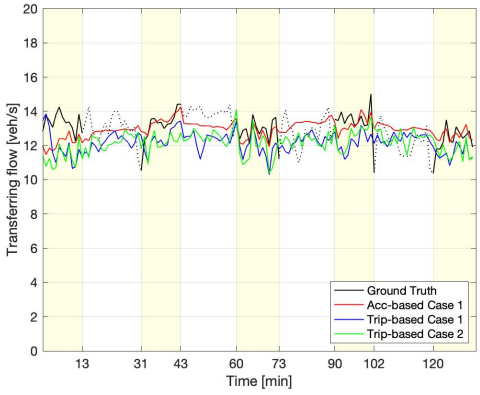

(b) Transferred flow [veh/s] in congested pocket

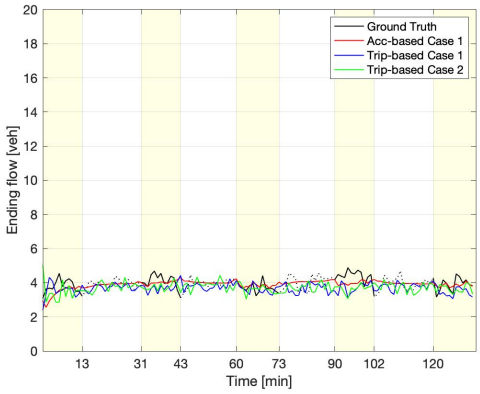

(c) Ending flow [veh/s] in less-congested pocket

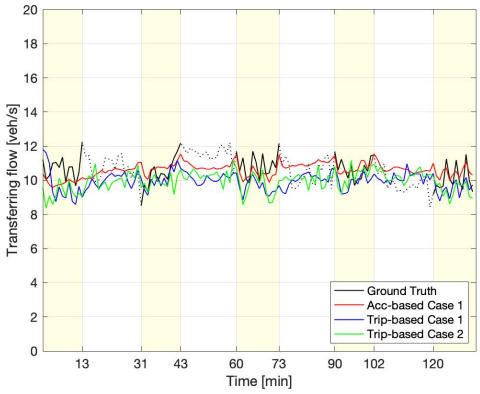

(d) Transferred flow [veh/s] in less-congested pocket

FIG. 5.8 – *Predicted flows in each pocket with path sequence information (yellow zone: drone period, white zone: no-drone period, Acc-based: Accumulation-based model, trip-based, trip-based model, Case 1: using average trip length, Case 2: using trip length distribution)*

with the average trip length value (Case 1), the best case is obtained using the multiregional model with path sequence information, i.e., the relative errors are 4.1% and 3.8%. Only when using the trip-based model with trip length distribution (Case 2), the relative error becomes slightly higher when using the path sequence (the relative error is 4.7%) than when without it (4.4%). As described in Section 5.4 of Chapter 3, it is necessary to have more data to obtain the joint distribution with good accuracy.

Thus, when we consider the path sequence in a multiregional MFD model framework, the accuracy of the regional outflow improves significantly by around 60% because of the improvement in the accuracy of the transferred flow prediction in all cases. The end flows in each region are also improved by around 10% with the path sequence. The regional accumulation is slightly better or almost the same with the path sequence. The accuracy of global outflow decreases when the model becomes more detailed as a single region model can follow the outflow dynamics more straightforwardly than the multiregional models. On the other hand, the prediction accuracy of accumulation improves when using the multire-

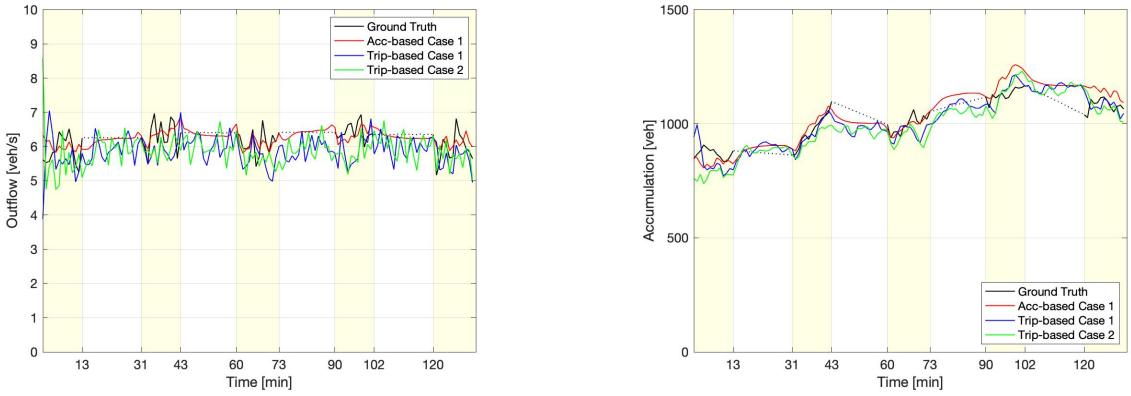

(a) Global Outflow [veh/s] (b) Global Accumulation [veh]

FIG. 5.9 – *Global Parameters*

gional model with the path sequence in line with the improved accuracy of the regional accumulation prediction.

5.4 Impact of MFD approximation

In Chapter 4, we found that MFD parameters should be calibrated separately depending on the MFD models concerned. In particular, the critical production settings have a considerable impact on the prediction results in a single region. This section analyzes the effect of regional MFD settings, especially the critical production settings, on the prediction results when we use the multiregional models with path sequence information, c.f., Section 5.2. We first find the proper critical production values for each pocket in Section 5.4.1. Then, in Section 5.4.2, we compare the prediction accuracy according to trip length aggregation, i.e., Cases 1′ and 2′ in Section 5.3.2, with the best MFD settings of each multiregional MFD model.

5.4.1 The settings of the critical production for MFD approximation

To find the best settings of the critical production Pc_r of the regional P-MFD $P_r(n_r)$ in region r, we compare the relative error of the predicted regional outflow and accumulation and calculated regional mean speed by using multiregional MFD models according to Pc_r values. The regional P-MFD is shown in Figure 5.10. According to the figure, Pc_r is set every 50 veh*m/s from 1350 to 1550 veh*m/s for the congested pocket and from 2200 to 2400 veh*m/s for the less-congested pocket. In the multiregional system, the settings in both pockets may affect their prediction results. Therefore, we calculate all the combinations of regional Pc_r settings. For the regional critical accumulation nc_r, we use the best settings calibrated as 550 veh for the congested pocket and 400 veh for the less-congested pocket using the accumulation-based model with the path sequence, c.f., see Section 5.2.2. The detailed calibration method for nc_r is similar to that in Section 5 of Chapter 4. Note that the nc_r values do not greatly affect the prediction results in the single region setting. According to the results in Section 5.3, the multi-region models without considering the path sequence lead to

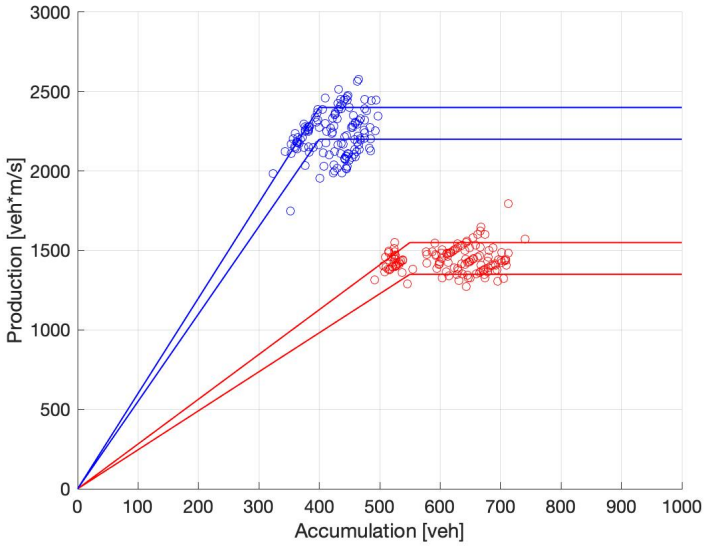

FIG. 5.10 – *Regional P-MFD (red plots: $P_r(n_r)$ in the congested pocket, blue plots:$P_r(n_r)$ in the less-congested pocket) and the maximum and minimum critical production settings (red lines: the settings for the congested pocket, blue plots: the settings for the less-congested pocket)*

considerable errors in the regional outflow prediction. Therefore, we use the accumulation-based and trip-based models considering the path sequence as described in Section 5.2.2 and 5.2.3 for this analysis. According to the results in Section 5.3.2, two cases of trip length settings, i.e., Case 1: using average partial trip length, and Case 2: using the joint distribution of regional trip length and path sequence, lead to only a slight difference. Also, since the trip length is randomly chosen in Case 2, the results may change randomly. Therefore, we calculate only with the average trip length (Case 1) to obtain the proper settings of Pc_r.

The results are shown in tables with the relative errors of the predicted outflow and accumulation with both models with all the combinations of the Pc_r settings shown in Figure 5.11. In the tables, the left side box in the column of a Pc_r setting shows the relative error of congested pockets, and the right side box shows the relative error of the less-congested pockets. The results are compared in each pocket and colored red when the relative error is higher and green when the relative error is lower.

For the result of the outflow with the accumulation-based model shown in Figure 5.11 (a), the relative errors are not much different in any combination, e.g., the maximum errors are 6.8% for the congested pocket and 7.2% for the less-congested pocket when $Pc_c = 1350$ veh*m/s and $Pc_u = 2200$ to 2500 veh*m/s where c and u represent the congested and less-congested pockets, and the minimum errors are 5.0% and 5.9% when $Pc_c = 1500$ veh*m/s and $Pc_u = 2350$ veh*m/s. The Pc_r setting in the congested pocket affects the relative errors in both pockets, and the relative error gets larger when Pc_c is both higher and lower than 1500 veh*m/s. On the other hand, the Pc_r setting in the less-congested pocket does not affect the relative errors for either pocket. The relative error of the accumulation with the accumulation-based model shown in Figure 5.11 (b) can become significant when the Pc_r values are small, e.g., the relative error exceeds 100% in the congested pocket when $Pc_c <= 1400$ veh*m/s and over 80% in the less-congested pocket when $Pc_u <= 2200$ veh*m/s. The error becomes smallest, around 10 to 13% in the congested

Outflow (Acc-based)		Less-Congested Pocket									
		Pc=2200		Pc=2250		Pc=2300		Pc=2350		Pc=2400	
Congested Pocket	Pc=1350	6,8	7,2	6,8	7,2	6,7	7,2	6,7	7,2	6,7	7,2
	Pc=1400	5,6	6,5	5,6	6,5	5,6	6,5	5,6	6,5	5,5	6,5
	Pc=1450	5,0	6,2	5,3	6,4	5,5	6,5	5,4	6,5	5,4	6,5
	Pc=1500	5,0	6,1	5,2	6,3	5,1	5,9	5,0	5,9	5,0	6,0
	Pc=1550	5,0	6,1	5,2	6,2	5,2	5,9	5,2	6,0	5,1	6,0

(a) Outflow with the Accumulation-based model

Accumulation (Acc-based)		Less-Congested Pocket									
		Pc=2200		Pc=2250		Pc=2300		Pc=2350		Pc=2400	
Congested Pocket	Pc=1350	223,9	11,3	224,1	12,6	224,3	14,0	224,4	15,5	224,6	17,1
	Pc=1400	102,2	8,5	103,9	10,8	104,0	12,1	104,1	13,4	104,1	14,9
	Pc=1450	11,3	88,2	10,2	19,4	12,8	9,9	12,9	11,5	12,9	12,9
	Pc=1500	15,1	94,1	13,9	18,9	13,0	9,2	13,0	11,4	13,0	12,8
	Pc=1550	17,6	94,2	16,6	19,1	16,5	8,7	16,5	11,4	16,5	12,8

(b) Accumulation with the Accumulation-based model

Outflow (Trip-based)		Less-Congested Pocket									
		Pc=2200		Pc=2250		Pc=2300		Pc=2350		Pc=2400	
Congested Pocket	Pc=1350	8,9	8,7	10,5	10,0	7,7	7,8	7,5	7,6	8,0	7,6
	Pc=1400	7,4	7,5	9,8	8,6	7,3	7,2	7,4	7,6	6,8	7,2
	Pc=1450	7,4	7,4	6,9	6,9	7,2	7,1	7,0	7,1	7,1	7,3
	Pc=1500	7,2	7,4	7,0	7,1	7,2	7,5	7,3	7,5	7,4	7,4
	Pc=1550	7,1	7,4	7,1	7,3	7,6	7,4	7,3	7,7	7,4	7,4

(c) Outflow with the Trip-based model

Accumulation (Trip-based)		Less-Congested Pocket									
		Pc=2200		Pc=2250		Pc=2300		Pc=2350		Pc=2400	
Congested Pocket	Pc=1350	99,8	10,7	100,2	13,8	48,4	10,7	32,0	11,2	46,6	12,5
	Pc=1400	48,7	11,3	89,7	21,9	18,1	11,7	42,5	19,9	9,3	15,3
	Pc=1450	51,8	16,6	22,9	16,4	11,9	13,0	11,3	20,2	10,9	14,2
	Pc=1500	15,0	8,9	11,6	13,8	17,5	11,7	16,2	12,4	15,8	16,5
	Pc=1550	16,1	12,3	12,8	17,1	15,2	14,4	13,9	19,4	15,4	20,6

(d) Accumulation with the Trip-based model

FIG. 5.11 – *Relative error [%] of predicted parameters according to P_c. The left and right side in the column shows the results in congested and less-congested pockets. When the error is high, the color is red and when the error is low the color is green.*

pocket, when $Pc_c = 1450$ veh*m/s. When Pc_c is larger than this value, the error in the congested pocket rises gradually until around 16 to 18% when $pc_c = 1550$ veh*m/s. Errors in the less-congested pocket are the smallest when $Pc_u = 2300$ veh*m/s, from 8 to 10%, unless $Pc_c >= 1400$ with significant errors in the congested pocket. When Pc_u is larger than 2300 veh*m/s, the error in the less-congested pocket gets larger gradually until around 13% when $Pc_u = 2400$ veh*m/s. According to both the outflow and accumulation results, the best settings of Pc_r for the accumulation-based model are $Pc_c = 1500$ veh*m/s and $Pc_u = 2300$ veh*m/s.

The relative outflow errors with the trip-based model are higher by from 2 to 5% than the accumulation-based model, as shown in Figure 5.11 (c), e.g., the maximum errors are 10.5% and 10.0% for the congested and less-congested pockets when $Pc_c = 1350$ veh*m/s and $Pc_u = 2250$ veh*m/s, and the minimum errors are 6.8% in the congested pocket when $Pc_c = 1400$ veh*m/s and $Pc_u = 2400$ veh*m/s and 6.9% in the less-congested pocket when $Pc_c = 1450$ veh*m/s and $Pc_u = 2250$ veh*m/s . When Pc_u is between 2250 to 2350 veh*m/s, the relative errors in both pockets are often the lowest values at around 7.0%, with $Pc_c = 1450$ veh*m/s. However, when $Pc_u = 2200$ and 2400 veh*m/s, different Pc_c settings lead to the smallest relative errors, e.g., when $Pc_c = 1550$ veh*m/s and $Pc_c = 1400$ veh*m/s. The Pc_r settings in the less-congested pocket are affected less than the settings in the congested pocket, similar to the accumulation-based model, and the relative errors increase and decrease regardless of the Pc_u settings. This variation of relative errors may be caused by choosing the path sequence randomly from the distribution in the trip-based model with path sequence information. As shown in Figure 5.11 (d), the relative errors of the accumulation with the trip-based model are significant over 45% in the congested pocket when Pc_r settings in both pockets are small, such as $Pc_c <= 1400$ veh*m/s and $Pc_u <= 2250$ veh*m/s. The relative errors are quite different in each pocket and the settings of Pc_c and Pc_u. The minimum relative error for the congested pocket is 9.3% when the $Pc_c = 1400$ veh*m/s and $Pc_u = 2400$ veh*m/s. On the other hand, the minimum relative error for the less-congested pocket is 8.9% when $Pc_c = 1500$ veh*m/s and $Pc_u = 2200$ veh*m/s. Also, high Pc_c values lead to better accuracy for the congested pocket but worse for the less-congested pocket regardless of the Pc_u values. When considering the accuracy of the balance between both the outflow and accumulation results in both pockets, the best settings of Pc_r for the trip-based model are $Pc_c = 1450$ veh*m/s and $Pc_u = 2300$ veh*m/s.

Thus, we find the settings of Pc_r, especially for the congested pocket, have a considerable impact on the prediction results in both pockets for both the accumulation-based and trip-based models. Using excessively low values for Pc_r, such as $Pc_c <= 1400$ veh*m/s and $Pc_u <= 2250$ veh*m/s, leads to poor accuracy for the accumulation prediction, i.e., the relative error is over 45%. The best settings for each model, i.e., $Pc_c = 1500$ veh*m/s and $Pc_u = 2300$ veh*m/s for the accumulation-based model and $Pc_c = 1450$ veh*m/s and $Pc_u = 2300$ veh*m/s for the trip-based model, are used to compare the prediction results for all the cases and models in Section 5.4.2.

5.4.2 The effect of MFD approximation on each MFD model

The regional outflow and accumulation are calculated using the average partial trip length (Case 1) with the accumulation-based and trip-based models and using the joint distribution of the path sequence and trip length (Case 2) with the trip-based model with the best settings

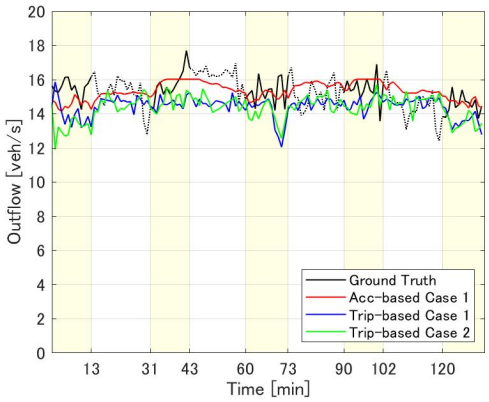

(a) Outflow in Congested Pocket

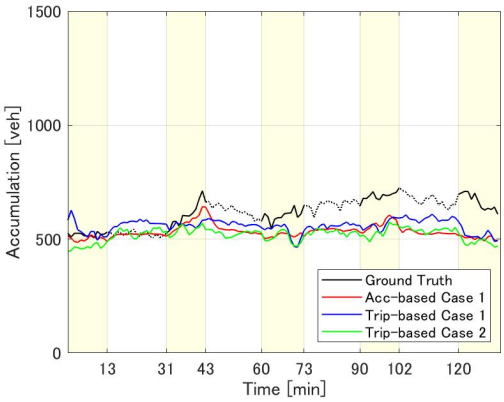

(b) Accumulation in Congested Pocket

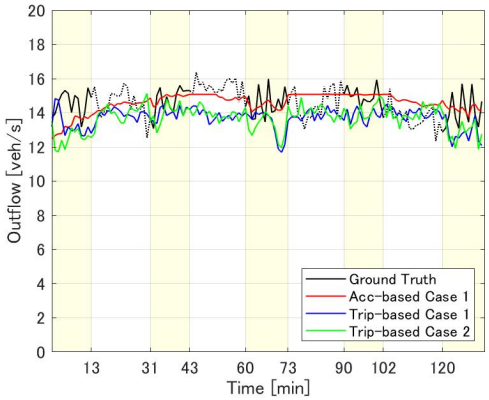

(c) Outflow in Less-Congested Pocket

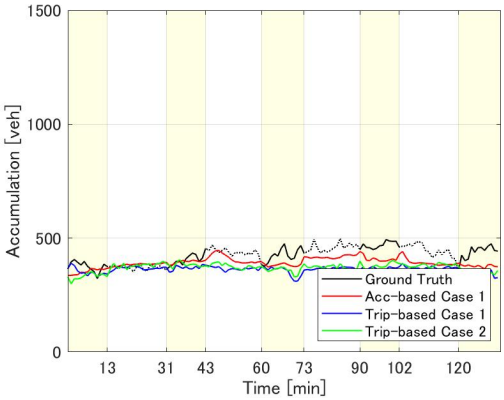

(d) Accumulation in Less-Congested Pocket

FIG. 5.12 – *Prediction results based on calibrated MFD settings for each model and each pocket (yellow zone: drone period, white zone: no-drone period, Acc-based: Accumulation-based model, trip-based, trip-based model, Case 1: using average trip length, Case 2: using trip length distribution)*

of Pc_r, i.e., $Pc_c = 1500$ veh*m/s and $Pc_u = 2300$ veh*m/s for the accumulation-based model and $Pc_c = 1450$ veh*m/s and $Pc_u = 2300$ veh*m/s for the trip-based model. The results are shown in Figure 5.12.

The accumulation-based model predicts the outflow dynamics gradually following the ground truth for both pockets, as shown in Figures 5.12 (a) and (c). However, the accumulation-based model cannot predict the sudden rise and drops of the ground truth dynamics. For example, the ground truth outflow dynamics decrease and increase from around 13 veh/s to 18 veh/s for 30 to 60 minutes in the congested pocket, while the predicted outflow stays at around 15 to 16 veh/s. Therefore, the accumulation prediction in the congested pocket shown in Figure 5.12 (b) becomes 100 veh smaller than the ground truth after 43 minutes. The accumulation error in the congested pocket cumulates and reaches a maximum value, around 200 veh, at the end of the calculation. As shown in Figure 5.12 (d), the predicted accumulation is around 100 veh smaller than the ground truth at the end in the less-congested pocket.

For the trip-based model in both trip length aggregation settings (Case 1 and 2), the predicted outflow is lower than the ground truth, e.g., the difference in the congested pocket

	Congested				Less-Congested				Global	
	$Qout_c$	n_c	$Qtra_c$	$Qend_c$	$Qout_u$	n_u	$Qtra_u$	$Qend_u$	$Qout$	n
Case 1 Acc	5.1	12.9	6.3	13.8	5.9	9.2	7.4	8.5	3.3	9.8
Case 1 Trip	7.4	12.0	8.2	13.8	7.6	14.6	8.5	9.9	7.5	11.7
Case 2 Trip	7.9	15.8	9.0	13.0	8.0	13.6	9.4	11.1	7.9	13.4

TAB. 5.6 – *Relative error [%] of the prediction results with the calibrated MFD Pc_r settings for each model and case. (Acc-based: Accumulation-based model, trip-based, trip-based model, Case 1: using average trip length, Case 2: using trip length distribution)*

reaches 3.5 veh/s at 43 minutes. Because of this difference, the regional accumulation is lower than the ground truth and the difference becomes larger with time, e.g., around 200 veh lower in the congested pocket and around 100 veh lower in the less-congested pocket at the end of the calculation. The predicted outflow and accumulation difference between Case 1 and Case 2 are quite significant in both pockets.

By comparing the relative errors of the prediction results using the best MFD settings in Table 5.6 and using the true mean speed in Table 5.4, the outflow results are quite similar. However, the relative errors of the regional accumulation are higher when using MFD, e.g., the relative errors in the congested pocket amount to 12.9% with the accumulation-based model and 12.0% and 15.8% in Cases 1 and 2 with the trip-based model when using MFD whereas they are 9.3%, 9.6%, and 12.1% when using the true mean speed.

Thus, the regional critical production settings largely affect the prediction results for both models. In particular, for the trip-based model, it is difficult to find the best settings since the results are also affected by the randomness of the path sequence and/or trip length depending on the trip length settings.

5.5 Conclusion

We investigated the effect of the parameter settings, i.e., trip length and MFD, on the prediction results using multiregional MFD models.

First, two types of typical trip length settings, i.e., the average and distribution, were compared using accumulation-based and trip-based models. Since the path sequence has a significant impact when characterizing trip length behaviors, we investigated the effect of path sequence information on the prediction results according to both the accumulation-based and trip-based models. We proposed the extended accumulation-based model framework that can consider the aggregated path sequence information as the input parameter. When the path sequence information was not available, the regional accumulation could be predicted with good accuracy, i.e., the relative errors were below 15% in the congested pocket, although the predicted regional outflows had significant errors, i.e., the relative errors were over 55% in all the models and trip length settings. On the other hand, when we considered the path sequence, the accuracy of the regional outflow improved significantly by around 60% in all the models. The accumulation accuracy was slightly better or not much different compared to the case without considering the path sequence when using the average partial trip length in both models. When using the joint distribution between the path sequence and trip length, the predicted accumulation accuracy could worsen by around 30%, since estimating joint distribution between the path sequence and trip lengths

requires more individual data than normal trip length distribution. Therefore, the overall calibration of different trip lengths par path sequences includes more errors that had clear impacts on the simulation results.

To confirm the effect of MFD settings, i.e., regional critical production values Pc_r, the best settings of Pc_r were first investigated by comparing all the combination of Pc_r values in each pocket in both models using average trip length. We found the settings of Pc_r, especially the congested pocket, had a considerable impact on the prediction results in both pockets with both models. Using excessively small values for Pc_r led to poor accumulation prediction accuracy, i.e., the relative error rose to over 45%. Finally, it was confirmed that the predicted outflow and accumulation dynamics for each case and model with the best settings followed the ground truth dynamics.

6. Calibration of MFD Models Considering Multiple Modes

6.1 Introduction

In urban areas, multiple modes such as cars, buses, and bicycles share the road network. Since driving behavior is quite different depending on the mode, previous studies suggested considering the effect of the interaction of other modes for traffic state estimation and prediction. This is another possible direction for improving model prediction accuracy compared to dividing the network into more homogeneous zones, and we want to explore this direction in this chapter. For example, buses stop more frequently regardless of the signals and traffic congestion to pick up and drop off passengers and have longer trip lengths to pass along road routes compared to cars. Several studies, e.g., Boyaci & Geroliminis (2011), Chiabaut *et al.* (2014), and Loder *et al.* (2017), showed that buses and cars have a different effect on the network dynamics in multimodal urban networks. Also, Barmpounakis *et al.* (2016) reported that motorcycles may have a different effects on network dynamics due to their smaller size and better maneuverability than the other modes. Gashaw *et al.* (2018) estimated the effect of traffic density of motorcycles on car flows by using a microscopic traffic mixed flow model. Paipuri *et al.* (2020) mentioned that it is essential to differentiate between the modes in MFD-based frameworks to have accurate traffic state predictions. Thus, the multimodal extension of MFD models has been required to improve the accuracy of traffic state prediction.

Compared to the other MFD models for a single mode, the multimodal extension of the MFD model has been developed quite recently, since Geroliminis *et al.* (2014) initially proposed bi-modal MFD (3D-MFD). Until now, empirical studies of multimodal MFD models have been limited by the availability of data since different modes of traffic and trip data in the same network are required. Therefore, these MFD models have often been used for control and operation applications based on numerical simulation rather than on real networks. On the other hand, since parameter settings such as trip length and MFD influence the prediction accuracy of single-mode MFD models, as the results in Chapters 4 and 5 showed, it is important to assess the prediction accuracy of each mode based on parameter settings. However, only a few studies, e.g., Paipuri *et al.* (2021), have addressed this investigation with sufficient quantities of data. In particular, trip length settings may have a huge impact on prediction accuracy according to the accuracy of the prediction assessments of single-mode models with different trip length settings in previous chapters.

Therefore, investigating the effect of the parameter settings of each mode on prediction accuracy is required to improve multimodal prediction accuracy and develop the application in the MFD framework. Also, comparing traffic state prediction between single-region and multimodal models with a known level of accuracy will provide good indications for MFD model applications with limited data.

6.1.1 Literature Review

Most MFD-based models in the literature consider two-dimensional MFD, which show the relation between the flow and density of a single-mode or the total flow and density of all vehicles. Geroliminis *et al.* (2014) initially proposed a 3D-MFD for the area of downtown San Francisco based on micro-simulation to consider traffic interaction between different modes. Ortigosa *et al.* (2015) analyzed the effect of bus lanes on the macroscopic traffic state based on 3D-MFDs with microscopic simulations on the city networks of Zurich and San

Francisco. 3D-MFD is used in the macroscopic traffic simulation based on the accumulation-based model by Ampountolas *et al.* (2017) and Dakic *et al.* (2019) for the perimeter control with a fixed bi-modal traffic composition.

The first empirical study of 3D-MFD was introduced by Loder *et al.* (2017) based on loop and taxi GPS data in Zurich, Swiss. They concluded that increasing the bus inflow to the network had a more negative impact on the state of car traffic, e.g., mean speed, than increasing car inflow. Loder *et al.* (2019) proposed a new functional form of 3D-MFD considering the structure and topology of car and bus networks and tested 3D-MFD calibration based on loop and taxi GPS data in Shenzen, China. Huang *et al.* (2019) and Fu *et al.* (2020) demonstrated 3D-MFD using the GPS data of probe cars, taxis, and public buses in Shenzen, China. The problem of data collection always limits the variety of modes to analyze the effect. Paipuri *et al.* (2020) proposed the 3D-MFD estimation method by using mobile phone data along with mode detection techniques. However, the penetration rate of the data was moderate, and the issues related to privacy and over-representation of specific modes limited the modes for analysis.

Quite recently, Paipuri *et al.* (2021) analyzed the 3D-MFD calibration of all the modes sharing a network by using complete trajectory data from pNEUMA drone experiments (Barmpounakis & Geroliminis (2020)) in Athens, Greece. The accuracy of prediction results based on two-fluid models were compared in a single-mode and multimodal framework, and they showed improved accuracy when using the multimodal model compared to the single-mode model. Also, they extended the classic trip-based model to consider the stop-and-go patterns of each mode. On the other hand, no study has yet investigated the effect of trip length calibration on the multimodal framework, while different trip behaviors in each mode shown in trip length may affect the prediction results differently. Also, empirical comparisons between the different MFD models according to parameter settings have not yet been investigated in the multimodal framework.

6.1.2 Research Objectives

Our objectives in this chapter are 1) to investigate the effect of parameter settings on the 3D-MFD model prediction accuracy of traffic state dynamics in different modes, and 2) to clarify the different properties and accuracy of single-mode and multimodal MFD models. The multiregional settings in the multimodal framework is not dealt with in this study as it is very complex to set up and calibrate. In Section 6.2, the calibration method of 3D-MFD and multimodal MFD models based on the 3D-MFD are presented based on the literature. In Section 6.3, multimodal data used for the investigation in this chapter are described, and calibrated parameters, i.e., the trip length of each mode and the 3D-MFD, are presented. In Section 6.4, the effect of trip length settings is first investigated in the multimodal framework by using real average speed instead of calibrated MFD. Then, the prediction results obtained by multimodal models with different 3D-MFD settings are compared with single-mode models described in Chapter 4. Finally, the main conclusions are summarized in Section 6.5.

Variables	
$m, m' \in M$	a target traffic mode m and another mode m' of all modes M in the network
n_m, $n_{m'}$	the accumulation of vehicles in traffic mode m and another mode m'
$V_m(n_m, n_{m'})$	the mean speed of vehicles in traffic mode m according to accumulation n_m and $n_{m'}$
vf_m	the constant free-flow speed of traffic mode m
$\beta_{m,m}$, $\beta_{m',m}$	coefficients between n_m and V_m and between $n_{m'}$ and V_m
$P(n_m, n_{m'})$	the total production of all modes according to each mode's accumulation n_m and $n_{m'}$ (3D P-MFD)
$V(n_m, n_{m'})$	the mean speed of all modes according to each mode's accumulation n_m and $n_{m'}$ (3D V-MFD)
$Pmax$	the critical production of all modes of vehicles
nc_m	the critical accumulation of vehicle mode m
$Qout_m(t)$	the outflow of traffic mode m at time t
L_m	the aggregated trip length of traffic mode m
$Qin_m(t)$	the inflow of traffic mode m at time t
dt	the unit time for the calculation
$Qout(t)$	the total outflow of all modes at time t
$Tin_{m,i}$	the entry time into the network of mode m vehicle i
$tt_{m,i}$	the travel time of mode m vehicle i
$Tout_{m,i}$	the exit time from the network of mode m vehicle i

TAB. 6.1 – *Lists of Variables used in Section 6.2*

6.2 Bi-Modal MFD Models in a Single Region

The main difference between models with single mode and multimodal frameworks is MFD calibration. In Section 6.2.1, the MFD calculation method used to consider the interaction of different modes is presented. The multimodal extension of classical models such as accumulation-based and trip-based models in a single region is quite straightforward. In Section 6.2.2 and 6.2.3, the simple extended methods of accumulation-based and trip-based models, as in Paipuri *et al.* (2020), are described. All the indexes that appear in this section are summarized in Table 6.1.

6.2.1 3D-MFD

3D-MFD shows the relation between modal accumulations and total production or mean speed considering the interaction between modes. An empirical MFD calculation proposed by Loder *et al.* (2017) is the simplest method in the bi-modal framework. Firstly, the modal mean speed of vehicles V_m in traffic mode $m \in M$ can be calculated by using the accumulation n of traffic mode m and another mode $m' \in M$, as Eq. (6.1).

$$V_m(n_m, n_{m'}) = vf_m + \beta_{m,m} * n_m + \beta_{m',m} * n_{m'} \tag{6.1}$$

where vf_m shows the constant free-flow speed value of mode m. $\beta_{m,m}$ and $\beta_{m',m}$ show the coefficients between n_m and V_m and between n'_m and V_m that represent the marginal effect of

mode m and m' on the mean speed of m. Total production of all modes M sharing the same network can be calculated by summing up modal production $P_m = n_m * V_m$ in Eq. (6.2).

$$P(n_m, n_{m'}) = \sum_{m \in M} (n_m * V_m) \tag{6.2}$$

The mean speed of all modes M can be calculated as Eq. (6.3).

$$V(n_m, n_{m'}) = \frac{\sum_{m \in M}(n_m * V_m)}{n} \tag{6.3}$$

where n denotes total accumulation calculated as $n = \sum_{m \in M} n_m$.

On the other hand, this linear approximation method based on V-MFD can lead to huge errors when the range of observed mean speed values is quite limited, c.f., Section 5.1 in Chapter 4. The calibration of the single-mode MFD in Chapter 4 shows a trapezoidal approximation of P-MFD is an another option that leads to better prediction results than the linear approximation method based on V-MFD. In the trapezoidal P-MFD approximation, the production value increases from 0 veh*m/s to critical production $Pmax$ when the accumulation n is less than the critical accumulation $nc1$, stays at $Pmax$ when n is between $nc1$ and another critical accumulation $nc2$, and decreases to 0 when $n > nc2$. Since we cannot observe the traffic state when the accumulation gets over $nc2$ from our data, $nc2$ value and decreasing production are not necessary to calibrate those values, same as Chapter 4. In this case, the mean speed V can be caluculated as a constant freeflow speed $vf = \frac{Pmax}{nc1}$ when $n <= nc1$, and $\frac{Pmax}{n}$ when $n > nc1$, c.f., the production $P = V * n$. When we extend this approximation into the 3D framework, the modal mean speed of vehicles in traffic mode m can be calculated as Eq. (6.4).

$$V_m(n_m, n_{m'}) = \begin{cases} \frac{\beta_{m,m}}{n_m} + \frac{\beta_{m',m}}{n_{m'}} \text{ if } V_m(n_m, n_{m'}) \leqq vf_m \\ vf_m \text{ otherwise} \end{cases} \tag{6.4}$$

Total production and the mean speed of all mode vehicles can be calculated based on Eq. (6.2) and (6.3).

We call the MFD calibration method based on Eq. (6.1) as "V-MFD based approximation" and one based on Eq. (6.4) as "P-MFD based approximation" in the following sections.

6.2.2 Accumulation-based Model

The accumulation-based model for multiple modes is quite similar to the single-mode framework described in Section 3.2 of Chapter 4 as it considers each mode's traffic state separately. The outflow $Qout_m(t)$ and accumulation $n_m(t)$ of traffic mode m at time t can be calculated by Eq. (6.5) based on 3D-MFD,

$$\begin{aligned} Qout_m(t) &= V(n_m(t), n_{m'}(t)) * n_m(t)/L_m \\ n_m(t+1) &= n_m(t) + (Qin_m(t) - Qout_m(t)) * dt \end{aligned} \tag{6.5}$$

where L_m and Qin_m show the aggregated trip length and inflow of mode m, and dt shows the unit time for calculation. The inflow $Qin_m(t)$ and initial accumulation $n_m(0)$ of each mode are variables obtained from the data.

The total outflow $Qout(t)$ and accumulation $n(t)$ of all modes M sharing the same network can be calculated by summing outflow and accumulation of each mode as Eq. (6.6).

$$\begin{aligned} Qout(t+1) &= \sum_{m \in M} Qout_m(t+1) \\ n(t+1) &= \sum_{m \in M} n_m(t+1). \end{aligned} \tag{6.6}$$

6.2.3 Trip-based model

The multimodal extension of the trip-based model is also quite simple and is done by considering each mode's traffic state individually. The only difference from the single-mode model described in Chapter 4 is using 3D-MFD instead of using the MFD of each mode. Mathematically, the trip length $L_{m,i}$ of mode m vehicle i can be calculated based on 3D V-MFD $V(n_m(t), n_{m'}(t))$ as in Eq. (6.7),

$$L_{m,i} = \int_{Tin_{i,m}}^{Tin_{m,i}+tt_{m,i}} V(n_m(t), n_{m'}(t)) \tag{6.7}$$

where $Tin_{m,i}$ and $tt_{m,i}$ are the entry time into the network and travel time of mode m vehicle i. The event-based model described in Section 3.3 of Chapter 4 can be used to predict the outflow and accumulation of each mode in the numerical calculation process by calculating individual entry time $Tin_{m,i}$, travel time $tt_{m,i}$ and exit time $Tout_{m,i}$ according to each mode's trip length L_m and inflow $Qin_m(t)$ in Eq. (6.8).

$$\begin{aligned} Tin_{m,i} &= Tin_{m,i-1} + 1/Qin_m(t) \\ tt_{m,i} &= L_m / V(n_m(t), n_{m'}(t)) \\ Tout_{m,i} &= Tin_{m,i} + tt_{m,i}. \end{aligned} \tag{6.8}$$

6.3 Traffic Variables and Model Parameters of Each Mode

To analyze the effect of trip length and 3D-MFD settings on prediction accuracy, we first need to calculate all the variables required from the ground truth state we have. Also, it is necessary to calibrate MFD model parameters such as the trip length and 3D-MFD based on the data. In Section 6.3.1, the data used to perform the prediction accuracy assessment according to the different model settings are presented, and the trip and traffic characteristics calculated from the data are compared between modes. In Section 6.3.2, the traffic state dynamics are calculated as the input variables and ground truth of the following accuracy assessment, and aggregated trip length is calibrated as a parameter for the multimodal MFD model. In Section 6.3.3, 3D-MFD is calibrated as another key parameter based on the calibration methods described in Section 6.2.1 using real data.

6.3.1 Multimodal Data

Drone data in Athens (Barmpounakis & Geroliminis (2020)), i.e., described in detail in Section 2 of Chapter 3, are distinguished as six modes, i.e., cars, taxis, buses, medium vehicles, heavy vehicles, and motorcycles. In Chapters 3, 4, and 5, since the travel time and distance

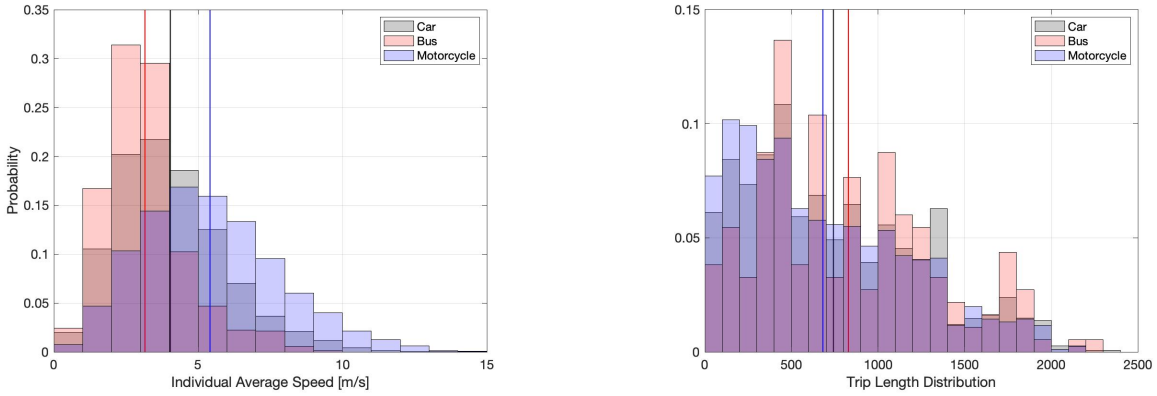

(a) Individual Speed Distribution (b) Trip Length Distribution

FIG. 6.1 – *Individual Trip Characteristics in Each Mode (vertical lines show the average values of each mode)*

of these modes are quite different from the other modes, we use trajectory data for 30237 vehicles in which buses and motorcycles are removed (see Section 2 of Chapter 3). Now, using the developments of Chapters 3, 4, and 5 we define the drone data set with car data, and we introduce the bus and motorcycle data which contain 898 buses and 16429 motorcycles. This provides the data of the other modes for multimodal simulation.

The mean speed and trip length difference of individual vehicles between modes are shown in Figure 6.1. The vertical black, red and blue lines show the average values of cars, buses, and motorcycles. As shown in Figure 6.1 (a), the individual speed of buses is lower than that of cars while that of motorcycles is higher, i.e., the average individual speeds are around 3.2 m/s for buses, 5.4 m/s for motorcycles, and 4.0 m/s for cars. Also, the speed range of motorcycles is larger than for cars, from 0 m/s to 15 m/s, while the speed range of cars is from 0 m/s to 10 m/s. The speed variance of buses is smaller than for other modes, as the speed range is from 0 m/s to 8 m/s. Trip length is calculated by the trajectories of each mode in which the trip start/end time in the network is available, c.f., see Section 5.1 in Chapter 3 for a detailed explanation. Figure 6.1 (b) shows that motorcycles have shorter trip lengths than cars, i.e., the average trip lengths are around 690 m for motorcycles and 740 m for cars. On the other hand, buses have longer trip lengths than other modes, i.e., the average trip length is around 810 m. The trip length distribution of motorcycles does not differ from cars. The trip lengths of buses vary from 100 m to 2400 m. The distribution shape is unclear because there are fewer data than for the other modes.

The P-MFD and V-MFD of each mode calculated from the data are shown in Figure 6.2. In Figure 6.2 (a), the production of motorcycles increases linearly when the accumulation is around 220 veh to 300 veh. When the accumulation is more than 300 veh, the production of motorcycles is constant, around 1600 veh*m/s to 2200 veh*m/s. The production of buses increases gradually when the accumulation is around 30 veh to 65 veh. Thus, the buses and motorcycles have a congested traffic state (non-saturated) while the cars have only a saturated traffic state according to the data, i.e., the production of cars is constant when the accumulation is around 800 veh to 1200 veh, since the buses have their own priority lanes and motorcycles can sometimes pass through roads regardless of the queues formed by other vehicles. As shown in V-MFD in Figure 6.2 (b), the mean speed of all modes decreases

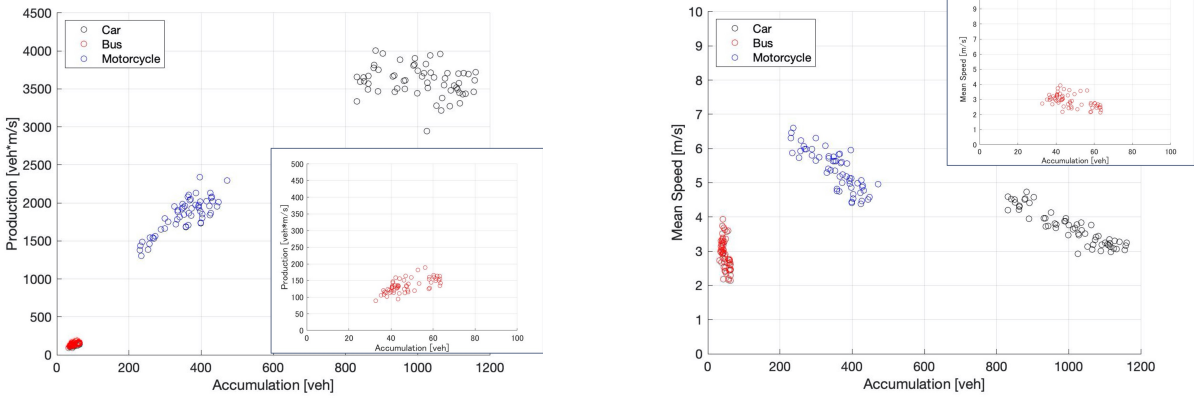

(a) Production MFD (P-MFD) (b) Speed MFD (V-MFD)

FIG. 6.2 – *Single-Mode(2D) MFD in Each Mode based on the original data*

linearly along with the increase of accumulation. The cars and buses have similar mean speeds, i.e., the mean speed of cars and buses are around 3 m/s to 5 m/s and 2 m/s to 4 m/s. On the contrary, the accumulation is quite different between cars and buses, i.e., the accumulation of buses is less than 100 veh, and that of the cars is around 800 veh to 1200 veh. The mean speed of motorcycles is higher than the other modes, from 4 m/s to 7 m/s, while the accumulation is lower than cars and higher than buses, i.e., around 200 veh to 500 veh.

Thus, motorcycles have higher individual speeds and shorter trip lengths than cars, and buses have lower individual speeds and longer trip lengths in the Athens' network. However, the trip length distributions, especially for buses, do not have a clear shape because of short data periods, i.e., 2.5 hours with four breaks for 10 to 15 minutes to change the drones' batteries, and a small amount of data, e.g., 898 veh for buses.

6.3.2 Traffic Variables and Trip Characteristics after Data Imputation

Since the Athens drone data lack trajectories for 10-15 minutes every 30 minutes due to the need to change the drones' batteries, i.e., called no-drone periods in previous chapters, it is necessary to complete the bus and motorcycle trajectories during the no-drone period to assess the prediction accuracy of the traffic state dynamics. Data imputation was carried out for bus and motorcycle trajectories by applying the same methods for cars described in Chapter 4 Section 2.

The traffic state variables calculated from complete trajectories after data imputation are shown in Figure 6.3. The inflow and outflow of motorcycles, shown in Figures 6.3 (a) and (b), are lower than for cars, i.e., the values are around 2.0 to 4.5 veh/s while the values for cars are around 5.0 to 7.0 veh/s, and stable during the no-drone period. The inflow and outflow of buses are also stable, but the values are quite small, at around 0.3 veh/s. The mean speed of all modes, shown in Figure 6.3 (c), decreases gradually and is stable during no-drone periods. The mean speed of motorcycles is around 1.5 to 2 m/s higher than for cars, and it begins at around 6 m/s and decreases by around 4.5 m/s. On the contrary, the mean speed of buses is around 0.5 to 1.0 m/s lower than for cars, and it begins at around 3.5

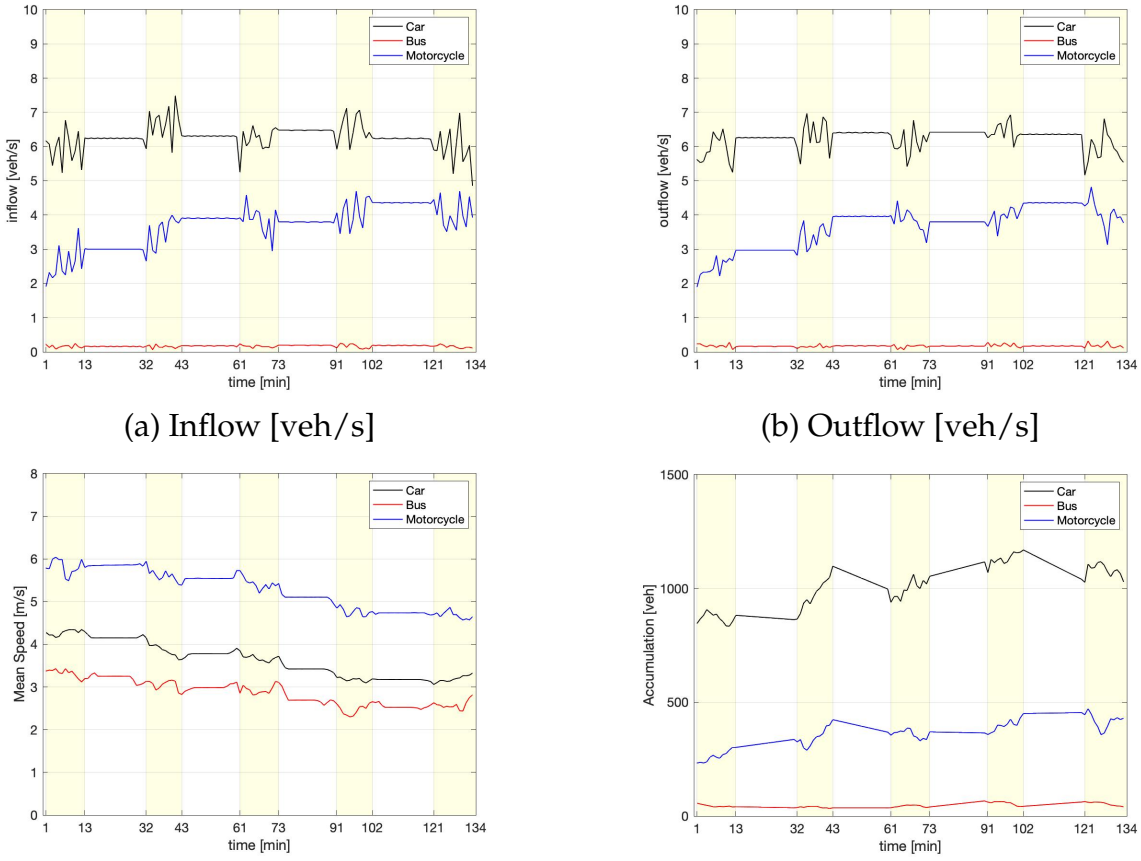

(a) Inflow [veh/s]

(b) Outflow [veh/s]

(c) Mean Speed [m/s]

(d) Accumulation [veh]

FIG. 6.3 – *Traffic variables in each mode after data imputation (yellow zone: periods with drone data, white zone: no-drone periods)*

m/s and decreases to 2.5 m/s. The accumulation of buses and motorcycles is significantly lower than for cars, as shown in Figure 6.3 (d). The accumulations are around 250 to 500 veh for motorcycles and less than 100 veh for buses while the accumulation of cars is over 800 veh. All the accumulation dynamics are stable during the no-drone periods. P-MFD and V-MFD calculated from complete trajectories after data imputation are shown in Figure 6.4. By comparing with MFD from original data shown in Figure 6.2, the shapes of both P-MFD and V-MFD for all modes are quite similar before and after data imputation. The plot number increases after data imputation by completing the no-drone periods. Thus, the traffic states for all modes are not changed due to the data imputation.

Figure 6.5 shows the average dynamics (a) and distribution (b) of the trip length of each mode. As shown in Figure 6.5 (a), the average trip length of motorcycles is around 100 to 200 m lower than for cars, and the values are stable without a sudden huge drop or rise, i.e., the maximum gap in 1 minute is less than 100 m. On the other hand, the trip length of buses is rather higher (around 200 to 300 m) than for cars except for between 43 to 55 minutes. Since the number of buses is generally fewer (less than 100 veh in all time periods) compared to the other modes, some short and long trip lengths considerably affect the average dynamics, which change suddenly from 600 m to 1000 m at 43 and 60 minutes.

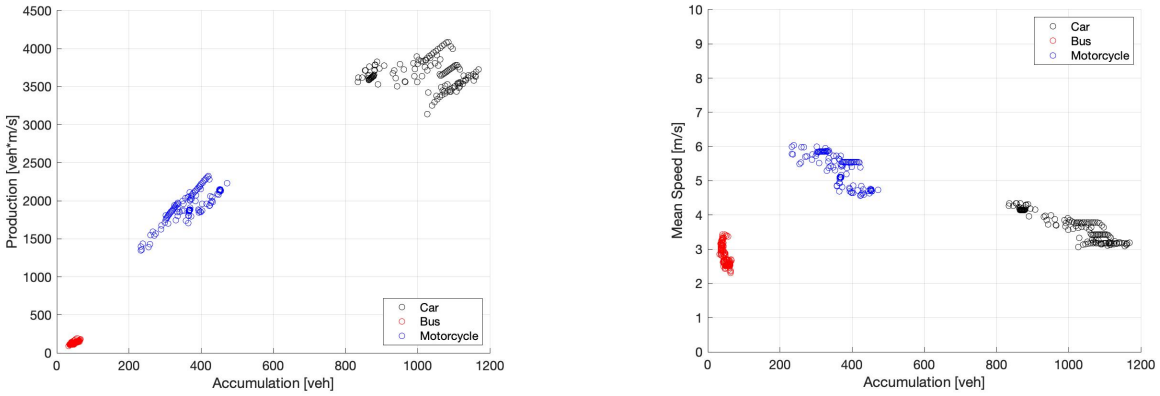

(a) Production MFD (P-MFD) (b) Speed MFD (V-MFD)

FIG. 6.4 – *Single-Mode (2D) MFD in Each Mode after Data Imputation*

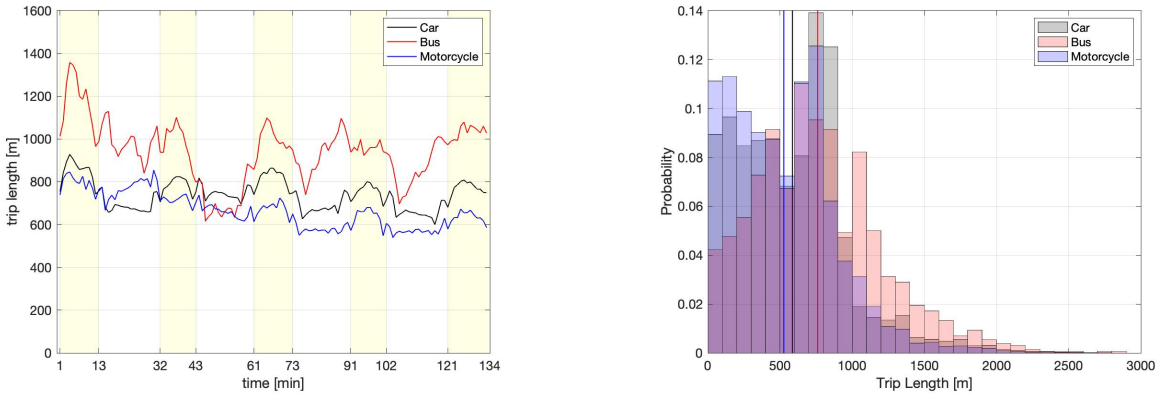

(a) Average Trip Length Dynamics (b) Trip Length Distribution

FIG. 6.5 – *Modal trip length after data imputation (Yellow zones in (a) show periods with drone data and white zones show no-drone periods. Vertical lines in (b) show the average values of each mode)*

In Figure 6.5 (b), the average trip length of motorcycles, i.e., a blue vertical line, is the lowest, and that of the buses, i.e., a red vertical line, is the highest, the same as the trip length before data imputation in Figure 6.1. Since obtaining both stable variable dynamics and trip length distribution is quite challenging, the trip length distribution after data imputation shows a considerable drop at around 500 m for all modes. The difficulty of obtaining a clear shape distribution after data imputation is the same as for cars, described in Section 2 of Chapter 4.

6.3.3 3D-MFD calibration

Based on two calibration methods of modal V-MFD $V_m(n_m, n'_m)$, i.e., V-MFD based and P-MFD based approximations, described in Section 6.2.1, we consider two options of 3D MFD settings. Since the data observation domain in speed and accumulation does not include oversaturated states, linear approximation on V-MFD leads to gridlock in simulation when

m\ m′	Vf_m [m/s]	Coefficient β_{mm} and $\beta_{m'm}$	
		car	motorcycle
car	7.3(7.1,7.5)	-0.0029(-0.0034,-0.0024)	-0.0020(-0.0028,-0.0012)
motorcycle	9.0(8.6,9.4)	-0.0028(-0.0036,-0.0021)	-0.0023(-0.0036,-0.0011)

TAB. 6.2 – *Parameters of V-MFD based approximation (Option 1) between cars and motorcycles. (.) shows values of 95% confidence limit*

m\ m′	Vf_m [m/s]	Coefficient β_{mm} and $\beta_{m'm}$	
		car	bus
car	7.5(7.3,7.7)	-0.0032(-0.0035,-0.0029)	-0.0122(-0.0151,-0.0093)
bus	5.6(5.4,5.7)	-0.0021(-0.0024,-0.0018)	-0.0117(-0.0144,-0.0090)

TAB. 6.3 – *Parameters of V-MFD based approximation (Option 1) between cars and buses. (.) shows values of 95% confidence limit*

accumulation values fall in oversaturated states. To avoid this problem and in absence of more data, we choose either to cap the speed with a minimum bound (Option 1: V-MFD based approximation with minimum speed limitation) or to use a rational functional shape for the speed related to a trapezoid P-MFD (Option 2: P-MFD based approximation). Here, we describe the detailed methods of calibration and present the calibrated parameters.

For Option1, the parameters are calibrated simultaneously by linear regression of the 3D relationship between accumulation of cars and another mode and mean speed of cars or another mode based on Eq. (6.1). The calculated parameters with 95% confidence limit for modal V-MFD approximation by Option 1 between cars and motorcycles are summarized in Table 6.2, one between cars and buses are in Table 6.3. The minimum speed bound is added on Eq. (6.1) to avoid gridlock in simulation as $V_m = Vmin_m$ when $V_m <= Vmin_m$. We assume $Vmin_m = 2.5$ m/s for all modes. Black plots in Figure 6.6 (a) and (c) show this 3D relationship for cars and motorcycles calculated based on data, and the surfaces show the fitted linear relationship. Figure 6.6 (b) and (d) show the contour of the fitted modal V-MFD. As shown in Figure 6.6 (b), the mean speed of cars decreases from over 7 m/s to below 6 m/s when the accumulation of cars increases from 0 veh to 500 veh, and to between 6 to 6.5 m/s when the accumulation of motorcycles increases from 0 veh to 500 veh. On the other hand, as shown in Figure 6.6 (d), the mean speed of motorcycles decreases from over 9 m/s to between 7.5 to 8 m/s when car accumulation increases from 0 veh to 500 veh, and similar for when motorcycle accumulation increases. Thus, car accumulation changes affect the mean speed of cars and motorcycles hugely. On the other hand, the changing of motorcycle accumulation affects mainly the mean speed of motorcycles.

For Option 2, we first calibrate the coefficient parameters from the relationship between accumulation of cars and another mode and mean speed of cars or another mode by exponential regression based on Eq. (6.4). The maximum speed limitation, i.e., free-flow speed, is calculated based on trapezoidal approximated single-mode P-MFD. The approximated single-mode P-MFD of cars and motorcycles are shown as lines in Figure 6.7 while the plots show the relation between accumulation and production of cars and motorcycles from data. Note that normally when the accumulation gets quite large, the production decreases. However, since the observed state of our data is quite limited, it is impossible to approximate the decreasing slope, and it is not necessary to calculate for prediction accuracy assessment. The

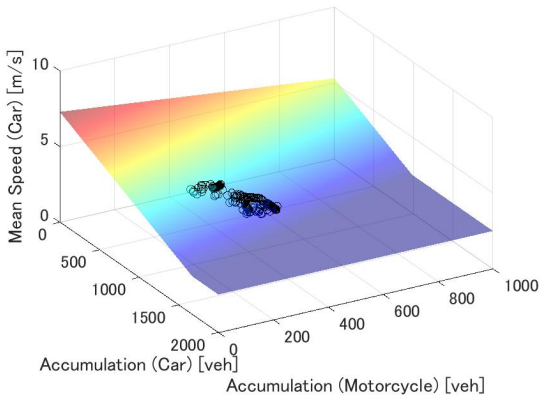

(a) Mean speed of cars (surface)

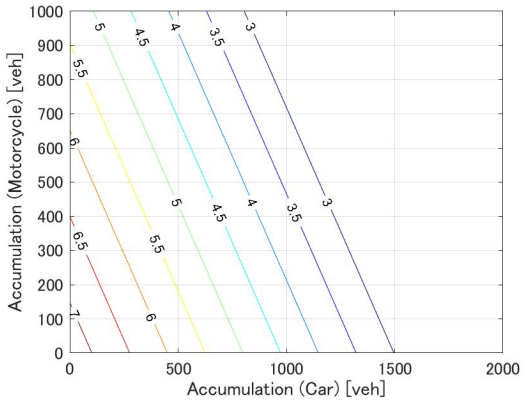

(b) Mean speed of cars (contour)

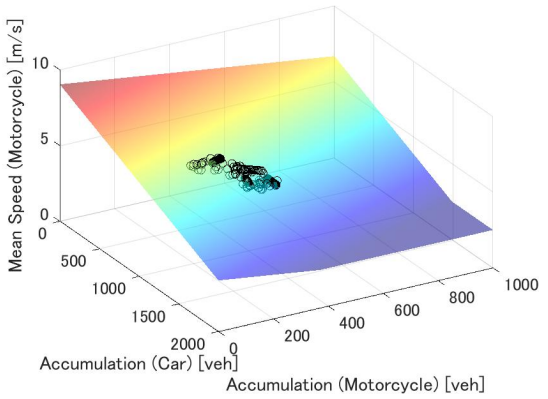

(c) Mean speed of Motorcycles (surface)

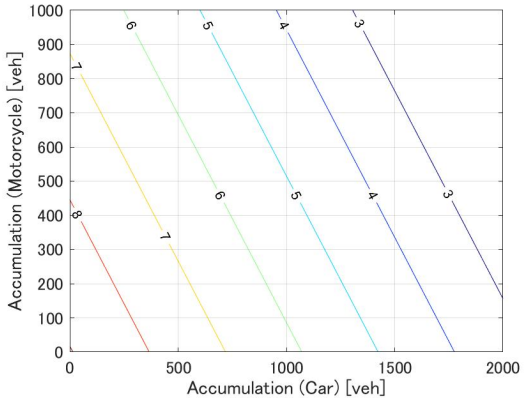

(d) Mean speed of Motorcycles (contour)

FIG. 6.6 – *3D Modal V-MFD between cars and motorcycles calculated based on linear V-MFD based approximation with minimum speed limitation (Option 1) (Black plots in (a) and (c) show the values directly calculated from data)*

critical production of each mode $Pmax_m$, i.e., the maximum production (network capacity), and critical accumulation $nc1_m$, i.e., the accumulation when the production achieves $Pmax_m$, are decided manually according to the plots in Figure 6.7. The calibrated $Pmax_m$ and $nc1_m$ values for cars, motorcycles, and buses are summarized in Table 6.4. According to the parameters in Table 6.4, the free-flow speed of each mode for Option 2 can be calculated as $Pmax_m/nc1_m$. Figure 6.8 (a) and (c) show the surfaces of the fitted modal V-MFD of cars and motorcycles from data, and (b) and (d) show the contours of modal V-MFD. The calibrated modal V-MFD shapes are quite different for cars and motorcycles. As shown in Figure 6.8 (b), the mean speed of cars is free-flow speed when the accumulation of motorcycles gets over 750 veh, and accumulation of cars get over 70 veh. Also, the contour of mean speed gets smaller, along with both accumulations of cars and motorcycles getting large. On the other hand, as shown in Figure 6.8 (d), the mean speed of motorcycles gets larger only when the accumulation of cars gets larger and is free-flow speed when the accumulation of cars is less than around 800 veh. The calculated parameters with 95% confidence limit for modal V-MFD approximation by Option 2 between cars and motorcycles are summarized in Table 6.5, one between cars and buses are in Table 6.6. Since the 95% confidence limit of coef-

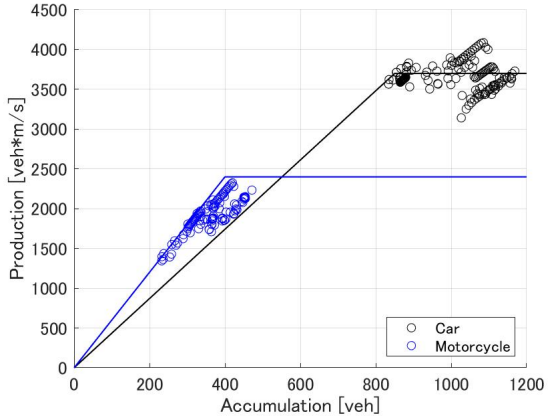

FIG. 6.7 – *Single mode P-MFD of each mode. (Plots show the values calculated from data and lines show the approximation)*

m	$Pmax_m$[veh*m/s]	$nc1_m$[veh]
car	3700	850
motorcycles	2400	400
bus	200	50

TAB. 6.4 – *Parameters of single mode MFD*

ficient of accumulation and mean speed of motorcycles is quite huge from -183,3 to 152.0, the fitting accuracy of the parameter calibration may not be high enough. Therefore, for the accuracy assessment in Section 6.4.2, we test all combinations of parameters within the 95% confidence limit values.

6.4 Prediction Accuracy Assessment of Multimodal MFD Models based on Parameter Settings

Like the investigation of the effect of parameter settings on prediction results in single-mode models, c.f., Chapters 4 and 5, we compare the prediction results obtained by the MFD models described in Section 6.2 with the ground truth traffic state calculated in Section 6.3.2. To analyze the effect of trip length settings, we first predict traffic state by accumulation-based and trip-based models based on the real mean speed of each mode instead of 3D-MFD in Section 6.4.1. Then, in Section 6.4.2, the prediction accuracy obtained by each MFD model based on 3D-MFD calibrated in Section 6.3.3 is compared with that of the single-mode model presented in Chapter 4.

6.4.1 Impact of Trip Length based on Real Speed

First, we compare the ground truth of each mode's outflow and accumulation and prediction results based on two MFD models, e.g., the accumulation-based model described in Section 6.2.2 and the trip-based model described in Section 6.2.3, using different trip length aggregation cases, e.g., average and distribution. To analyze the effect of trip length aggre-

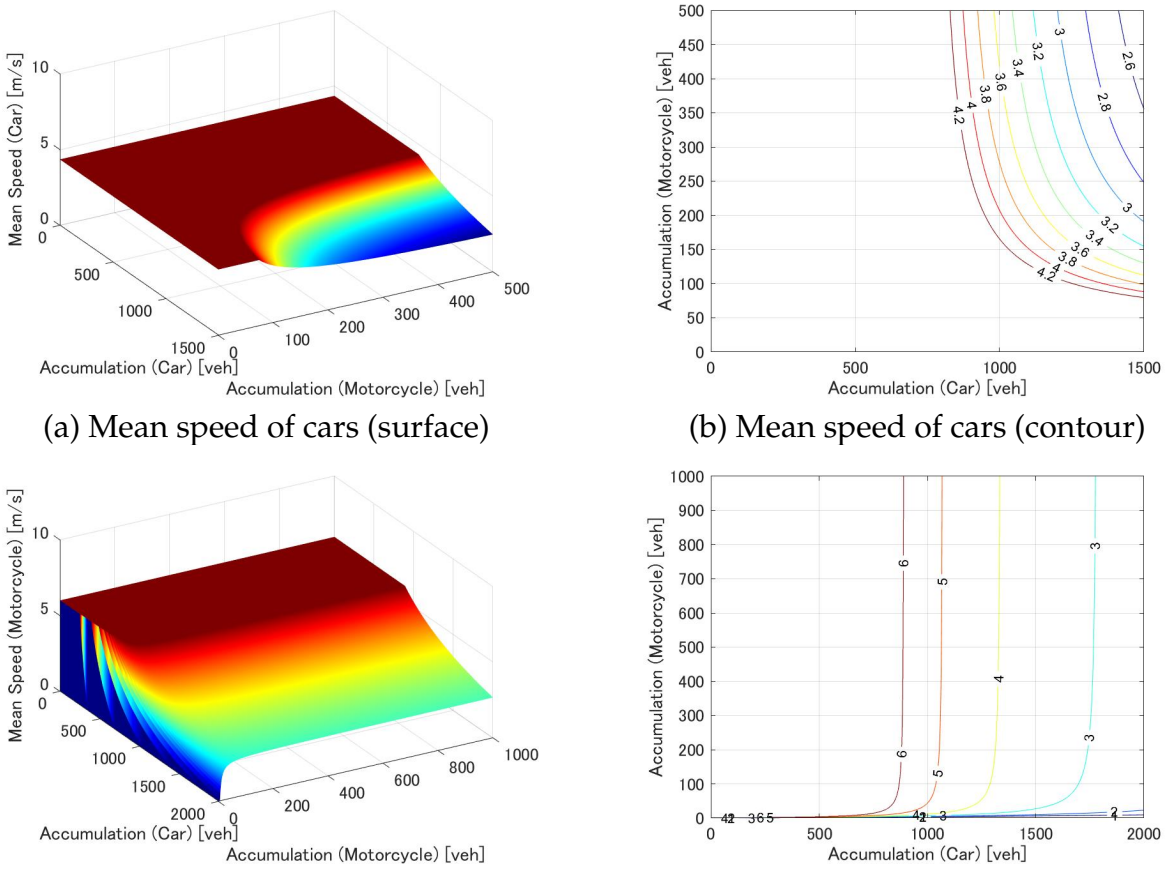

(a) Mean speed of cars (surface)

(b) Mean speed of cars (contour)

(c) Mean speed of motorcycles (surface)

(d) Mean speed of motorcycles (contour)

FIG. 6.8 – *Approximated 3D Modal V-MFD between cars and motorcycles calculated based on P-MFD based approximation (Option 2)*

gation on each mode's prediction results, we use the real values of the average mean speed dynamics of each mode $V_m(t)$ as shown in Figure 6.3 (c) instead of using 3D-MFD.

Two typical aggregation settings of trip length, the same as in Chapters 4 and 5, are considered in this section:

Case 1 We use the constant average value of the trip length of each mode as the input value $L_m =< L_{m,i} >$.

Case 2 We use the trip length distribution of each mode as the input value $L_m \sim P(L_{m,i})$.

The average trip lengths used for Case 1 and the trip length distribution for Case 2 of each mode are shown in Figure 6.1 (b) as vertical lines, i.e., 586 m for cars, 761 m for buses, and 527 m for motorcycles, and discrete distributions. Since it is challenging to adapt distribution on the accumulation-based framework, only Case 2 is tested for the trip-based model. We use the calculated inflow of each mode after data imputation, as shown in Figure 6.3 (a), as input values. Also, the initial accumulations are 846 veh for cars, 56 veh for buses, and 232 veh for motorcycles, as shown in Figure 6.3 (d).

Figure 6.9 shows the predicted outflow and accumulation of cars ((a) and (b)), buses ((c) and (d)), and motorcycles ((e) and (f)) by different trip length settings and models. Note that

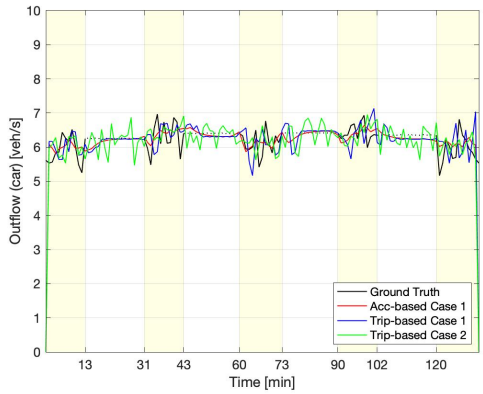

(a) Outflow [veh/s] of cars

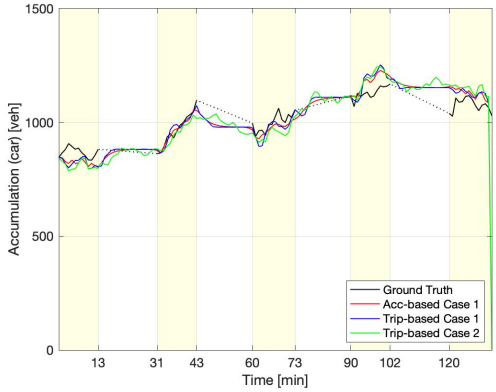

(b) Accumulation [veh] of cars

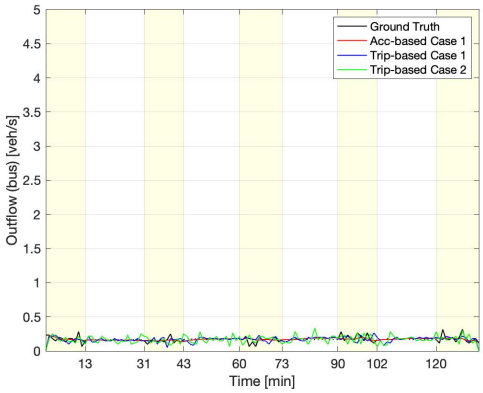

(c) Outflow [veh/s] of Buses

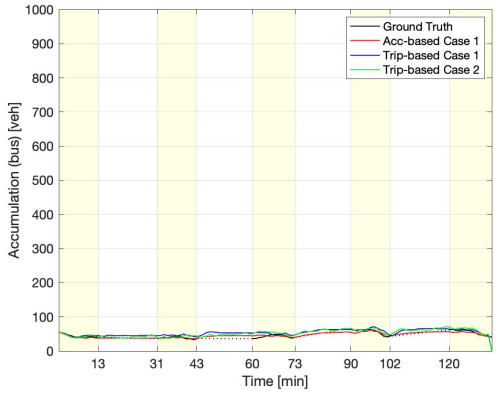

(d) Accumulation [veh] of Buses

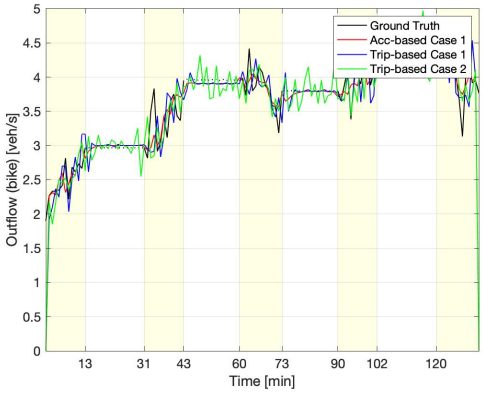

(e) Outflow [veh/s] of Motorcycles

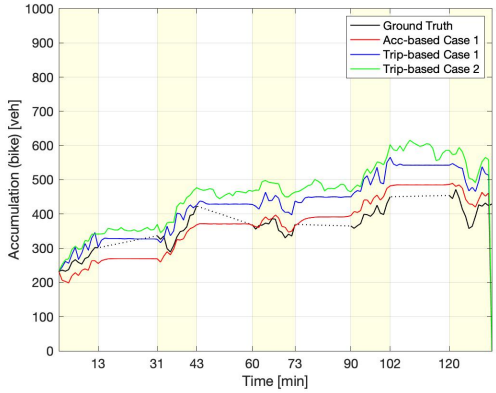

(f) Accumulation [veh] of Motorcycles

FIG. 6.9 – *Prediction results of each mode according to MFD models (Acc-based: Accumulation-based model, Trip-based: Trip-based model) and trip length settings (Case 1: Average trip length, Case 2: Trip length distribution) by using real speed (yellow zone: periods with drone data, white zone: no-drone periods)*

m\ m′	Vf_m [m/s]	Coefficient β_{mm} and $\beta_{m'm}$	
		car	motorcycle
car	4.4	3207(2956,3458)	164.2(75.12,253.20)
motorcycle	6.0	5356(4883,5829)	-15.47(-183.3,152.0)

TAB. 6.5 – *Parameters of P-MFD based approximation between cars and motorcycles. (.) shows values of 95% confidence limit*

m\ m′	Vf_m [m/s]	Coefficient β_{mm} and $\beta_{m'm}$	
		car	bus
car	4.4	3009 (2873,3145)	29.15(23.21,35.09)
bus	4.0	2263(2127,2399)	22.76(21.81,33.7)

TAB. 6.6 – *Parameters of P-MFD based approximation between cars and buses. (.) shows values of 95% confidence limit*

the results for cars are the same as those in a single-mode single-region model, as shown in Figure 21 and Table 4 in Chapter 4 since the only difference between single-mode and multimodal models is the way in which MFD is calibrated. Like the prediction for cars, when we use the accumulation-based model with the average trip length, the outflow dynamics change more gradually and are more robust to adapt to the changing state than when using the trip-based model. Using trip length distribution (Case 2) leads to sudden changes of maximum outflow 0.2 veh/s for buses and 1.0 veh/s for motorcycles since the trip lengths are chosen randomly. The accumulation is predicted as having higher values when using the trip-based model than when using the accumulation-based model in both modes. Notably, for motorcycles, the trip-based model overpredicts the accumulation, i.e., the maximum difference is around 150 veh in Case 2. This difference may be derived from the larger variance of individual speed for motorcycles than cars, as shown in Figure 6.1 (a). The relative errors are summarized in Table 6.7. The relative errors of buses and motorcycles, especially of buses, are larger than for cars, e.g., for the outflow, the errors of buses are over 16% while they are around 3 to 5% for cars, while for the accumulation the errors are 8.7% when using the accumulation-based model and over 19% when using the trip-based model. Since the outflow and accumulation values are quite small compared to cars, e.g., the outflows of buses and motorcycles are below 0.5 veh/s, and below 5 veh/s. However, those of cars are around 5 to 7 veh/s and the accumulations of buses and motorcycles are below 100 veh and 500 veh while that of cars is around 800 to 1300 veh. Small errors have considerably effects on buses and motorcycles. The accumulation-based model produces the most accurate prediction results in our data for both buses and motorcycles, e.g., the relative error of outflow for motorcycles is 4.3% when using the accumulation-based model while that when using the trip-based model is over 6%. The relative error of accumulation for motorcycles is 9.5% when using the accumulation-based model while that when using the trip-based model is over 16%.

Thus, when using real speed, the accumulation-based model can provide the most robust and accurate prediction results with low parameter calibration requirements, e.g., using average trip length. The prediction errors of buses and motorcycles can be somewhat higher than those of cars since individual speed varies over a larger range, and small errors can have a big effect when accumulation is small.

	car		bus		motorcycle	
Case and model	$Qout_m$	n_m	$Qout_m$	n_m	$Qout_m$	n_m
1(Average Trip Length) Accumulation-based	3.1	9.4	16.2	8.7	4.3	9.5
1(Average Trip Length) Trip-based	4.0	8.8	22.5	19.2	6.0	16.0
2(Trip Length Distribution) Trip-based	5.4	8.8	35.2	19.4	7.2	24.3

TAB. 6.7 – *Relative Error [%] of prediction results using real speed (the errors for cars are the same as in Table 4 in Chapter 4 for Case 1 and quite close for Case 2. Here, we use the same values as in Chapter 4.)*

	car			motorcycle		
Option	$Qout_m$	n_m	V_m	$Qout_m$	n_m	V_m
0 (Single mode MFD)	4.8	6.4	6.5	4.3	13.6	15.6
1 (V-MFD based approximation with limitation)	5.4	16.5	14.2	5.1	27.1	15.8
2 (P-MFD based approximation)	4.8	5.9	6.4	4.4	9.8	10.0

TAB. 6.8 – *Relative errors [%] of prediction accuracy based on calibrated 3D MFD between cars and motorcycles*

6.4.2 Comparison of Different MFD Calibration Methods

To analyze the effect of 3D-MFD calibration on the prediction results, we compare the prediction accuracy of three MFD calibration options described in Section 6.3.3. Since the observed traffic state from data is limited, the fitted parameters in Section 6.3.3 may not be the best values. Therefore, first, we compare the prediction results of each option with different combinations of all parameter values between 95% confidence limit. The best combination of parameters is used for the following investigation to compare the prediction accuracy of options. For comparing single-mode and multimodal models, we also prepare the case using a single-mode MFD based on the approximation parameters shown in Table 6.4 as Option 0.

Since the accumulation-based model is the simplest and stable method with the best accuracy in Section 6.4.1, we compare the prediction accuracy of Option 0 and three options in Section 6.3.3 based on the accumulation-based model. The input variables and trip lengths are the same as Section 6.4.1 when using Case 1 (average trip length) in the accumulation-based model. The predicted outflow and accumulation of cars and motorcycles are shown in Figure 6.10.

When using single-mode MFD (Option 0), the predicted outflow of cars and motorcycles, shown in Figures 6.10 (a) and (b), follow the ground truth dynamics. As shown in Table 6.2, the relative errors for both modes are below 5%. The predicted accumulation of cars in Figure 6.10 (c) also follows the ground truth, i.e., the relative error is 64%. The accumulation of motorcycles in Figure 6.10 (d) is predicted lower (the maximum difference is 100 veh) than ground truth since the mean speed of motorcycles in Figure 6.10 (f) is predicted as free-flow while the real mean speed value decreases. The relative error of motorcycle accumulation gets high as 13.6%. For V-MFD-based approximation with minimum speed limitation (Option 1), the best accuracy is provided when using calibrated parameters in Table 6.2. The mean speed of motorcycles does not achieve 2.5 m/s (the minimum bound), while the mean speed of cars achieves at the bound when $t = 89$ min. Accumulations of both modes are predicted quite higher, i.e., the maximum difference is 200 veh for cars and 270 veh for mo-

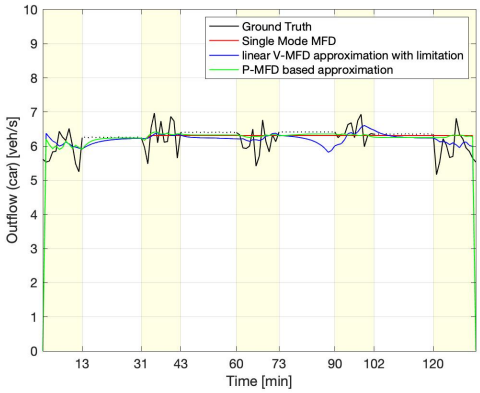

(a) Outflow [veh/s] of Cars

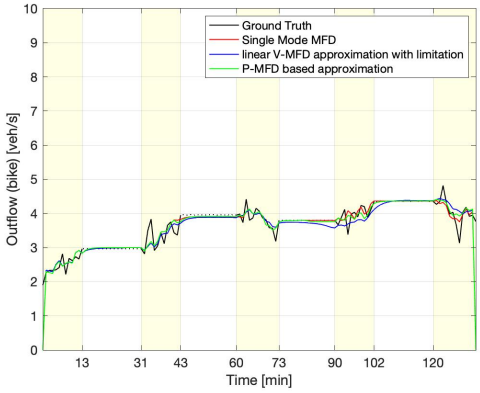

(b) Outflow [veh/s] of Motorcycles

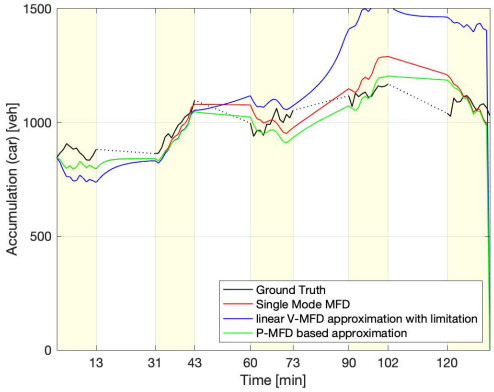

(c) Accumulation [veh] of Cars

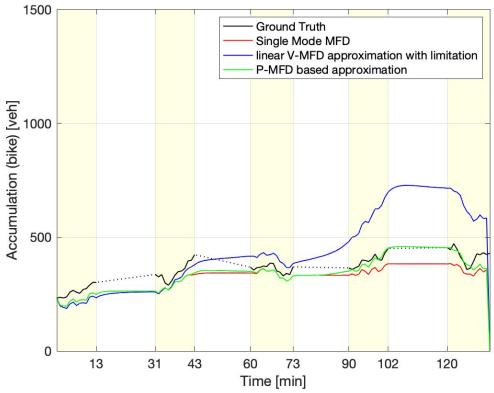

(d) Accumulation [veh] of Motorcycles

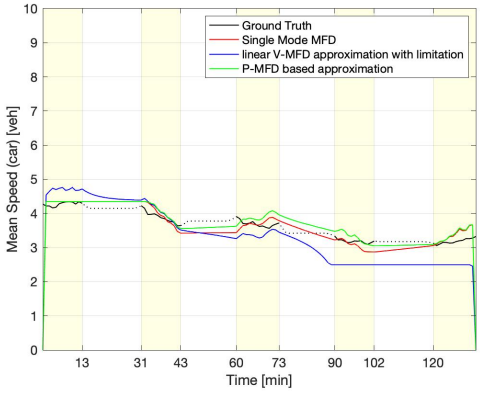

(e) Mean speed [m/s] of Cars

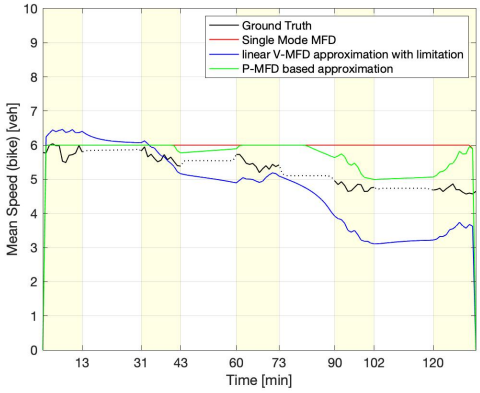

(f) Mean speed [m/s] of Motorcycles

FIG. 6.10 – *Results of 3D MFD model between cars and motorcycles based on the accumulation-based model using average trip length (yellow zone: periods with drone data, white zone: no-drone periods)*

torcycles. The relative errors of predicted accumulations are 16.5% for cars and 27.1% for motorcycles. On the other hand, the outflow of motorcycles has close accuracy to when using a single-mode MFD (Option 0), i.e., the relative error is 5.4%. The outflow of cars drops about 0.5 veh/s at around $t = 89$ min. However, it recovers in 20 minutes, and the outflow dynamics get similar to Option 0 after $t = 107$ min. The relative error is also close to Option 0 as 5.1%. For P-MFD based approximation (Option 2), the most accurate predictions are provided when we use $\beta_{car,car} = 3300$, $\beta_{motorcycle,car} = 140$, $\beta_{motorcycle,motorcycle} = 80$, and $\beta_{car,motorcycle} = 5800$. In this case, predicted outflow dynamics of both modes follow the ground truth in good accuracy, e.g., the relative errors are 4.8 % for cars and 4.4 % for motorcycles. Also, the predicted accumulations of both modes are closer to the ground truth than using single-mode MFD, e.g., the relative errors of Option 2 are 5.9% for cars and 9.8% for motorcycles, while the relative errors of Option 0 are 6.4% and 13.6%. As shown in Figure 6.10 (f), the mean speed of motorcycles does not stay in free-flow speed and follows the mean speed changing when using Option 2, and it leads to the better prediction accuracy of accumulation, especially after $t = 43$ min.

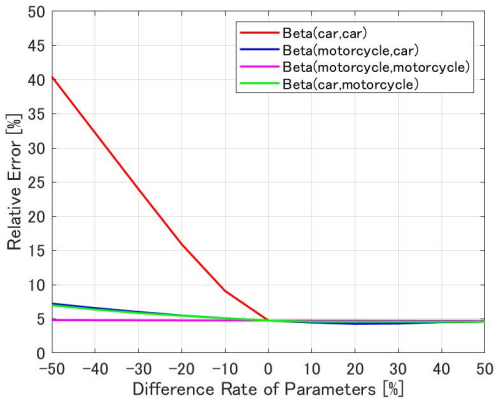

(a) Outflow [veh/s] of Cars

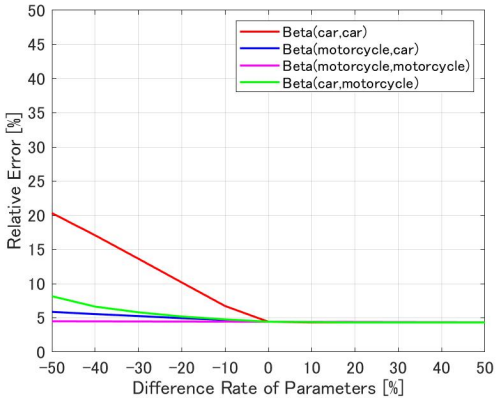

(b) Outflow [veh/s] of Motorcycles

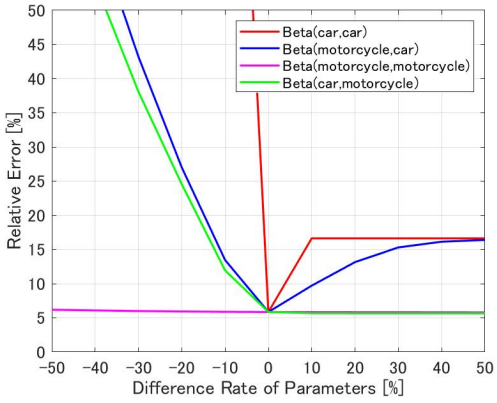

(c) Accumulation [veh] of Cars

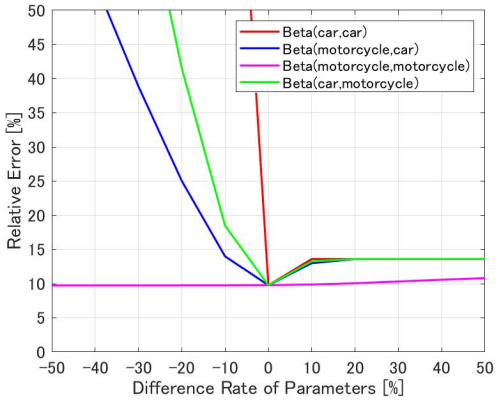

(d) Accumulation [veh] of Motorcycles

FIG. 6.11 – *Relative errors [%] according to difference rate [%] of calibrated parameters from the best values in Option 2 (using P-MFD based approximation)*

The effect of the parameter calibration errors is shown in Figure 6.11. The difference rate shows the relative difference of calibrated parameters from the parameters which lead to

the best accuracy. Especially, the calibration accuracy of $\beta_{car,car}$ value affect the prediction results of both mode traffic state hugely, e.g., 10% of positive difference leads to over 15% relative error and 1% of negative difference leads to over 50% relative errors for the accumulation of cars. $\beta_{motorcycle,car}$ and $\beta_{car,motorcycle}$ values also significantly affect the prediction accuracy of the accumulation of both modes. $\beta_{motorcycle,car}$ values affect the car accumulation stronger than $\beta_{car,motorcycle}$, e.g., 10% of the positive error of $\beta_{motorcycle,car}$ lead 10% of relative errors while the positive error of $\beta_{car,motorcycle}$ constantly give around 6% of the relative error. On the other hand, $\beta_{car,motorcycle}$ values affect the motorcycle accumulation stronger than $\beta_{motorcycle,car}$, e.g., 10% of the negative error of $\beta_{car,motorcycle}$ leads to around 18% of relative errors while 10% of the negative error of $\beta_{motorcycle,car}$ gives around 13% of the relative error.

Thus, we find that linear V-MFD-based approximation with minimum speed bound can avoid gridlock in simulation. However, it can still lead to considerable errors in the accuracy prediction. The P-MFD-based approximation can provide a more accurate prediction of the accuracy than using single-mode MFD. However, the parameters should be calibrated carefully since small calibration errors, especially of cars, may lead to significant prediction errors. Parameter calibrations, especially for Option 2, are quite challenging between cars and buses since data of buses are quite a few, i.e., the accumulation in a minute is less than 100 veh. Except for Option 2, the findings from the investigation results between cars and buses are quite similar to one between cars and motorcycles described above. We summarize the results in Appendix B.

6.5 Conclusion

The effect of the settings of two key parameters, i.e., trip length and MFD, on the prediction results were investigated in the MFD model framework with multi-mode vehicles. Drone data (Barmpounakis & Geroliminis (2020)) that include complete trajectories of all vehicles with different modes made it possible to carry out the empirical investigation described in this chapter. The accuracy prediction obtained by the accumulation-based and trip-based models was compared according to different trip length aggregations, e.g., average and distribution. Also, the effect of different calibration methods of 3D MFD is analyzed based on the accumulation-based model using average trip length.

The effect of trip length setting was compared between the cases with aggregation of the average value and distribution obtained by the accumulation-based and trip-based models for cars, buses, and motorcycles using real mean speed instead of MFD. As a result, the prediction results for buses and motorcycles could have larger relative errors than cars because individual speed had a larger range while only a single value was given for each vehicle mode. Also, since the accumulation of buses and motorcycles was somewhat smaller than for cars, small differences from the ground truth would lead to considerable relative errors.

For the 3D-MFD calibration, the linear approximation based on the relationship between accumulation of cars and another mode and the mean speed of cars or another mode, i.e., modal 3D V-MFD, with the minimum speed bound at 2.5 m/s can avoid gridlock in simulation, which occurs when using the linear approximation on V-MFD without the minimum bound. However, accumulation prediction errors of both modes are still huge, i.e., the relative errors are 16.5% for cars and 27.1% for motorcycles. The best option is the proposed "P MFD based approximation," which is a 3D extension of trapezoid approximation for P-MFD.

By using this option, we can achieve more accurate prediction than using single-mode MFD for each mode, i.e., the relative errors based on 3D-MFD are 5.9% for accumulation and 4.8% for outflow of cars while the relative errors based on single-mode MFD are 6.4% for accumulation and 4.8% for outflow. On the other hand, the small errors of parameter calibration may lead to significant prediction errors, e.g., 10% of positive errors of $\beta_{car,car}$ leads to over 15% relative error.

7. General conclusion

Empirical investigations of MFD model settings and parameter calibration based on real data provide valuable insights for the practical implementation of MFD models. In Chapter 1, the main research goal was formulated as:

Research Goal Investigating how to adjust the MFD model settings and calibration methods to achieve the best prediction accuracy.

This thesis focused on three challenges to address for the research goal: Challenge 1) Estimating the main model variables and defining the best calibration methods, including the proper resolution for the main parameters; Challenge 2) Assessing MFD model accuracy with respect to the model and parameter settings; and Challenge 3) Testing a new MFD model extension with heterogeneous trip length and path sequence descriptions. To overcome these challenges, six research questions were posed in Chapter 1 and addressed in Chapter 2 to Chapter 6. The main findings of each research question are discussed in Section 7.1. The main conclusion of this thesis is summarized in Section 7.2. Finally, Section 7.3 presents future recommendations to further develop the MFD model framework for real-time traffic control and management implementation.

7.1 Main Findings

To achieve the main research goal, two research questions on traffic state variable estimation and model parameter calibration were first raised (Research Questions 1 and 2). Then, four research questions on applying calibrated parameters in the MFD model were addressed. The answers to the associated questions are given below.

Research Question 1, stated below and answered in Chapter 2, targeted traffic density estimation, which is generally difficult using typical traffic data such as loop and probe data, while density is one of the important traffic state variables. Different methods have been proposed in the literature but never cross-compared to determine their accuracy with respect to data availability.

Research Question 1

What is the best method to estimate traffic density when the available data is limited? What is the level of accuracy for all the existing methods to estimate link and network density?

If trajectory data such as probe data are available in real-time, we can use the fishing rate, i.e., the ratio of probes that are detected at the loop locations over the loop flow, for both link and network-level estimation. If the probe and loop data observed at the same location are not available in real-time, we can still use the fishing rate calculated from historical data. If no trajectory is available, we can use the dynamic electric vehicle length (EVL), i.e., detected vehicle length calculated from the occupancy and link flow from the loop data and link mean speed.

The expected estimation error magnitudes were estimated by comparison with the ground truth traffic state calculated from real probe and loop data in Lyon. The results of the density estimation at the link-level showed that:

1. It is almost impossible to obtain accurate results, i.e., the relative error between ground truth and estimation is over 35%.

2. Exceptionally, when the historical fishing rate at each link at the moment concerned is available, we can achieve a relative error below 30%. Also, it is possible to obtain better accuracy when we reach a very high penetration rate, such as a fishing rate higher than 10%, which rarely happens.

The results of density estimation at the network-level showed that:

1. Using both the fishing rate and EVL can lead to better results, i.e., the highest relative errors are below 30% for the fishing rate and below 40% for EVL.

2. The most accurate result can be obtained by the new method by aggregating the link-level fishing rate, considering the covariance between the total travel time and the fishing rate of each link, i.e., the relative error is below 18% when loop coverage is over 30% in the network. However, this requires enough probe data (at least an average of 10% of fishing rate) and a loop coverage higher than 30%.

3. Using the network-level fishing rate calculated from links with loops to estimate all the links is a reasonable method to obtain as good accuracy as when using the link-level fishing rate to estimate the links with loops and the network-level fishing rate to estimate the links without loops, i.e., the difference is less than 3% relative error.

4. Day and/or time aggregation of the network-level fishing rate calculation leads to robust results for which the relative errors are below 20%, even when loop coverage is 10%.

5. Using a constant value for EVL leads to a considerable relative error higher than 30% even when the loop coverage is over 30%, although a constant EVL is often used in practice.

6. Using a relationship between occupancy and EVL is useful when no trajectory is available, i.e., the relative error is around 25% to 35% when loop coverage is 10% and below 25% when loop coverage is 30%.

Research Question 2, stated below and tackled in Chapter 3, targets the calibration of MFD model parameters, i.e., MFD and trip length, especially on the network partitioned into multiple small regions. It includes considering the effects of network partitioning with different degrees of network compactness on speed homogeneity, which is related to MFD shape and trip length estimation complexity, and the accuracy of the assessment of trip length estimation according to different trip length aggregation methods based on real data.

Research Question 2

How much does the network partitioning affect the MFD shape and trip length estimation accuracy? What is the appropriate trip length aggregation method in the partitioned network with limited data?

The effect of the compactness of the partitioned network on speed homogeneity and the complexity of trip length estimation is investigated by using the complete trajectory data

of all the vehicles provided by the Athens drone experiment (Barmpounakis & Geroliminis (2020)). The network is partitioned by the proposed simple static method into two traffic state pockets, i.e., congested and less-congested pockets, along with different degrees of network compactness. As a result, it is confirmed that the detailed partitioning with low network compactness significantly improves speed homogeneity, e.g., the standard deviation of link-mean speed decreases by around 30 to 40%, as the compactness of the network increases. On the other hand, the average pocket switching number (PSN), i.e., the average number of movements from one pocket to another by individuals, increases drastically from less than 1 to around 3 when partitioned with higher network compactness. Note that a higher PSN means trip length estimation is more complex since it requires trajectory data when the vehicle enters and exits each pocket, and it requires more detailed data when a vehicle passes through more pockets.

The estimation accuracies of two typical trip length aggregation settings, e.g., average trip length and trip length distribution, are assessed by comparing them with real average trip length and trip length distribution calculated from all the vehicles' trajectories. The cases where the regional trip length of each individual is available or not and where the path sequence information, i.e., ordering of the regions through which a vehicle passes, is available or not, are considered.

The results for the average trip length estimation show that:

1. If any information on the path sequence is unavailable, estimating reliable average trip length is quite difficult, e.g., the relative error between the true value and estimation is over 10%.

2. In particular, when only partial trajectories are available because of changing probe vehicle ID or missing data, it is almost impossible to obtain an accurate estimation, i.e., the relative error is between 20% to 45%.

3. If a few samples of the regional trajectories are available, the estimation accuracy improves significantly by partitioning with low compactness, i.e., the relative error is less than 1%.

The results for the trip length distribution estimation showed that:

1. Using joint distribution between the regional trip length of both pockets or between trip length and the path sequence is necessary to obtain an accurate estimation for regional and complete trip length, e.g., validated by T-test.

2. The volume of trajectory data affects the trip length estimation with the joint distribution. It is necessary to have a larger number of trajectories to obtain better results, e.g., at least 5000 trajectories are necessary to estimate distribution with less than 1% relative errors for the mean and variance.

3. Using the continuous fitted distribution, e.g., Weibull distribution, instead of the discrete distribution leads to more robust results with better estimation accuracy in most cases.

In Chapter 4, the effect of calibrated parameter settings on the prediction results by MFD models was investigated. Chapter 4 focused on classical single region models to tackle Research Question 3, stated below. It focused on the prediction accuracy of MFD models with

different trip lengths and MFD settings based on the trajectory data that can provide the ground truth traffic state and different trip length settings. The drone data of Athens (Barmpounakis & Geroliminis (2020)) include the most detailed trajectory information, which is enough to consider different trip length settings. However, there is break time without any data of around 15 minutes every 30 minutes. The trajectories are imputed for the periods without data using the proposed data imputation method.

Research Question 3

How much do parameter settings affect the prediction accuracy of classical MFD models in a single region?

By using the trip set after data imputation based on Athens drone data, the predicted outflow and accumulation were compared using two MFD models, i.e., the accumulation-based and trip-based models, with two different trip length settings, i.e., average and distribution. Firstly, the effect of trip length settings on the prediction results was analyzed based on real speed instead of using calibrated MFD. The analysis showed that:

1. The accumulation-based model using average trip length is an efficient method with high accuracy (the relative errors are 3.1% for outflow and 9.4% for accumulation), similar to the trip-based model (4.0% and 8.8% relative errors for outflow and accumulation) and a low parameter calibration requirement compared to using trip length distribution.

2. The estimation accuracy of average trip length can significantly affect the prediction results of both models. In particular, for the accumulation-based model, the small calibration errors of the average trip length can lead to much larger prediction errors than the trip-based model. The accumulation-based model can provide more accurate results than the trip-based model only when the average trip length estimation error is less than 3%.

3. If the accuracy of the trip length estimation is not sufficient, e.g., the relative error of the estimation is higher than 10%, using trip length distribution can lead to better and more stable results than using average trip length for the trip-based model.

The effect of MFD parameter settings, i.e., critical production (the maximum throughput of the network) and critical accumulation (corresponding accumulation), is investigated by comparing the outflow and accumulation prediction results with both models. The results show:

1. The critical production value plays an important role in the prediction results. In particular, calibrating the critical production too small leads to huge errors (over 45% relative errors) when accumulation increases.

2. The critical accumulation value only affects free flow.

3. The best setting of the critical production, which leads to the most accurate prediction, is different in the accumulation-based and trip-based models. It is necessary to calibrate the MFD variables separately for both models. In practice, we get a single best fit for the MFD calibration, so it may affect which model provides the best results.

Since the path sequence affects the trip length estimation accuracy, it may play an important role in the prediction accuracy using the multiregional MFD models. However, no study proposed MFD models considering path sequence information to improve prediction results. Research Question 4, stated below and addressed in Chapter 5, tackled this issue.

Research Question 4

How can we consider path sequence information in the classical MFD model framework?

The main issue of considering path sequence information is dealing with trips that return to the same regions.

For the trip-based model, the extension of considering path sequence information is straightforward since the path sequence corresponding to the trip length can be assigned for individual trips from the path sequence distribution, i.e., the number of trips with each path sequence.

For the accumulation-based model, since the average trip length is generally used for all vehicles or vehicles with the same path sequence, the path sequence information should be aggregated differently from the trip-based model. The probability of the number of times which the vehicle passes through the same region is expressed by the binomial process. The expectation value of this binomial process is calculated as the average number of times that vehicles return to the region based on path sequence information. Also, the regional inflow is considered separately as three types of trip: 1) passing through only a region, 2) passing through both regions and ending the trip in the region different from the region of entry, and 3) passing through both regions and ending the trip in the same region as entering. The ratios to separate the inflow into three are also calculated from the path sequence distribution.

Chapter 5 also tackles Research Question 5, stated below, which extends Research Question 3 in the multiregional framework. By using the proposed multiregional model, a similar investigation to address Research Question 3 is conducted for Research Question 5 based on drone data in Athens after data imputation.

Research Question 5

How much do the parameter settings affect the prediction accuracy of the multi-regional MFD model?

The new findings obtained by comparing the prediction results according to different trip length settings with and without considering the path sequence based on real speed instead of MFD are:

1. When the path sequence information was not available, the regional accumulation could be predicted with good accuracy, i.e., the relative errors are below 15%. However, the prediction errors increase significantly over 55% for both models and all the trip length settings for the regional outflows.

2. When considering the path sequence information, the accuracy of the regional outflow improves significantly by around 60% for all the cases. On the other hand, the accuracy of the regional accumulation is not much different when using the average trip

length in both models compared to the case where the path sequence information is not available.

3. When using the joint distribution between the path sequence and trip length, the prediction accuracy for the regional accumulation could worsen by around 30%, since joint distribution calibration requires more individual trajectory data than regional trip length distribution. The overall calibration of different trip lengths by path sequence can include more errors that clearly affect the simulation results.

4. The accuracy of global outflow in the multiregional framework is worse than the outflow calculated straightforwardly in the single region framework. On the other hand, the prediction accuracy of global accumulation using the multiregional model considering the path sequence is better than one using the single region model.

By comparing all the combinations of regional critical production values in each pocket, we confirm that setting the critical regional production, especially for the congested pocket, had a considerable impact on the prediction results in both models and all trip length settings. In particular, using smaller values leads to poor regional accumulation prediction accuracy, i.e., the relative errors are over 45%.

Research Question 6, stated below and tackled in Chapter 6, is the multimodal extension of Research Question 3. It requires a similar investigation of the effect of parameter setting on the prediction results, as Research Question 3 was based on trajectory data with several modes. Since the Athens drone data in also captured the trajectories of buses and motorcycles, the trip set of all modes after data imputation was used to address Research Question 6.

Research Question 6

How much do the trip length and MFD settings affect the prediction accuracy of the multi-modal MFD model?

We first compared the prediction results for several modes, e.g., cars, buses, and motorcycles, according to different trip length settings based on real speed instead of MFD. Note that this restricts this analysis to considering each mode independently as difference between the single-mode and multi-mode models lays on the MFD calibration. As a result, the accumulation-based model provides more robust results than a single-mode model prediction. The prediction errors of buses and motorcycles is larger than that of cars, i.e., the relative errors for the accumulation prediction are around 8.5 to 9.5% for cars, around 8.5 to 20% for buses, and around 9.5 to 25% for motorcycles since individual speeds have a wider range of variations.

For investigating the best calibration of 3D-MFD (bi-modal MFD) and effect of using the multi-modal model, we compare prediction results by using three options of 3D-MFD approximation based on data with the case using single-mode MFD for each mode. Results of this investigation between cars and motorcycles show that:

1. Linear approximations with minimum speed limitation for calibrating 3D modal V-MFD, e.g., the relationship between mean speed of cars or motorcycles and accumulation of cars and motorcycles, can avoid gridlock in simulation while linear approximation of

V-MFD tends to fall in gridlock. However, the relative errors of predicted accumulation are still quite high as 16.5% for cars and 27.1% for motorcycles.

2. 3D extension of trapezoid P-MFD approximation, e.g., the relationship between production and accumulation, can provide the most accurate prediction, which is better than using single-mode MFDs, e.g., the relative error of car accumulation is 5.9% while the relative errors of using single-mode MFD is 6.4%. However, the parameters should be calibrated carefully since the small calibration errors can lead to significant prediction errors, e.g., 10% of coefficient errors between accumulation and mean speed of cars can lead to over 15% relative errors.

7.2 Main Conclusion

The main conclusions of this thesis can be summarized as follows:

1. Accurate traffic density estimation is almost impossible at the link level except for when the real-time probe data and historical loop data capture probes at each link at the moment concerned. On the other hand, the traffic density estimation at the network level can lead to good accuracy, especially when using network-level fishing rates. When the real-time probe data is not available, using a historical relationship between occupancy and EVL is useful.

2. Network partitioning with low network compactness improves speed homogeneity, leading to a good MFD shape while also leading to greater complexity of trip length estimation, which requires more detailed data. If no information on the path sequence is available, estimating the average and distribution of trip length is challenging. On the other hand, a few samples of the regional trajectories can significantly improve the accuracy of average trip length estimation. Using joint distribution between the regional trip length of both pockets or between trip length and path sequence is necessary to estimate regional and complete trip length accurately. However, estimating joint distribution with good accuracy requires a larger number of trajectories.

3. The accumulation-based model with average trip length is an efficient method with similar accuracy to the trip-based model with lower computational time. However, the calibration accuracy of average trip length affects the accumulation-based model more significantly than the trip-based model, and the accumulation-based model requires more accurate trip length calibration. Using trip length distribution is more stable and better for the trip-based model if the trip length calibration accuracy is insufficient. For MFD parameter settings, critical production plays an important role in the prediction results, and it should be calibrated separately for models.

4. In the multiregional framework, regional accumulation can be predicted accurately without path sequence. However, the regional outflow prediction requires path sequence

information. The overall calibration of trip length distribution per path sequence can include more errors to introduce poorer prediction accuracy than when considering the path sequence separately from trip length. The global outflow calculated by the multi-regional model is worse than the single region model. On the other hand, the accuracy of predicted global accumulation is higher when using the multiregional models than when using the single region models. In the multimodal framework, the 3D extension of trapezoidal approximation based on P-MFD can provide more accurate predictions than using single-mode MFD and linear approximation of 3D V-MFD. However, small calibration errors of parameters can lead to significant prediction errors.

7.3 Future Works

This thesis broadens the perspectives for subsequent research. Some of them are presented below.

Investigation of the parameter setting effect on the prediction results obtained with the M-model

In Chapters 4 to 6, we focused on typical MFD models, i.e., accumulation-based and trip-based models. On the other hand, several MFD models that use trip length differently have also been developed in the literature. For example, the M-model proposed by Lamotte *et al.* (2018) is the new extension of the trip-based model but with better accuracy and shorter computation time acheived by calculating the average distance remaining to be traveled. Since the trip length is used differently from the classic models, the settings may affect the prediction results differently. Thus, the literature reviews of the new MFD models and the investigation of the parameter setting effect on the prediction results obtained by the new models will further develop in the MFD model framework.

Multimodal MFD model in the multiregional framework

In Chapter 6, we presented multimodal MFD models in a single region. Since we clarified that the multiregional models that consider path sequence improve the global accumulation prediction accuracy compared to using the single region model in Chapter 5, the multiregional extension of the multimodal MFD models may further improve prediction accuracy. On the other hand, since the multiregional extension requires more detailed trajectory data for trip length calibration, and the multimodal extension requires 3D-MFD calibration which is much more complicated than the MFD of a single mode, multiregional multimodal models may require much more data and calibration for parameter settings to predict accurate traffic states. Thus, the next step of this thesis is to propose the multiregional extension of the multimodal MFD and investigate the calibration of parameter setting for the multiregional multimodal MFD model.

Data assimilation for real-time traffic state prediction in the MFD model framework

In this thesis, we found that the parameter calibration significantly affects the prediction results obtained by MFD models. Data assimilation is often used to calibrate parameters including in real-time to improve prediction results. Figure 7.1 shows the real-time traffic state prediction flow in the MFD framework. The red arrows show the real-time updating (on-line) schemes, and the blue arrows show the off-line schemes. First, the network design

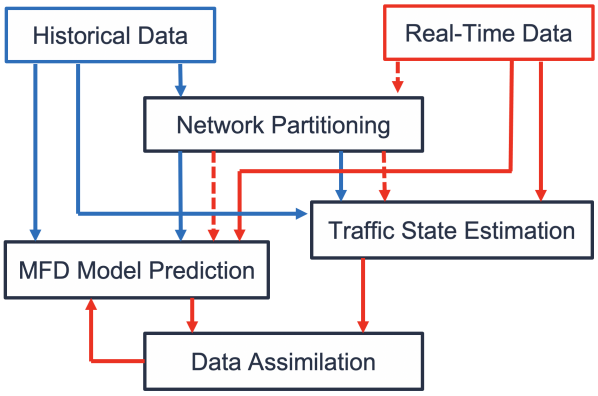

FIG. 7.1 – *Real-time traffic prediction framework*

is calibrated by static or dynamic partitioning based on historical or real-time traffic data as described in Chapter 3. Then, the real-time traffic state in the network designed is estimated based on real-time and historical data as described in Chapter 2. At the same time, the traffic state is predicted by MFD models based on parameters calibrated by historical data and real-time data, as described in Chapters 4 to 6. Finally, the traffic state predicted by MFD models and the estimated traffic state based on data is used for updating the MFD model parameters using data assimilation methods. Updated parameters are used for predicting the next time period by the MFD models. Real-time data assimilation in the MFD model frameworks has recently received a lot of attention from many researchers, e.g., Kouvelas *et al.* (2017), Saeedmanesh *et al.* (2019), Sirmatel & Geroliminis (2019). There is room for further developing this framework according to the findings of this thesis.

References

Aboudolas, K. & Geroliminis, N. (2013). Perimeter and boundary flow control in multi-reservoir heterogeneous networks. *Transportation Research Part B: Methodological*, 55:265–281.

Aljamal, M. A., Abdelghaffar, H. M. & Rakha, H. A. (2019). Developing a Neural–Kalman Filtering Approach for Estimating Traffic Stream Density Using Probe Vehicle Data. *Sensors*, 19(19):4325.

Ambühl, L., Loder, A., Zheng, N., Axhausen, K. W. & Menendez, M. (2019). Approximative Network Partitioning for MFDs from Stationary Sensor Data. *Transportation Research Record*, 2673(6):94–103.

Ampountolas, K., Zheng, N. & Geroliminis, N. (2017). Macroscopic modelling and robust control of bi-modal multi-region urban road networks. *Transportation Research Part B: Methodological*, 104:616–637.

An, K., Chiu, Y. C., Hu, X. & Chen, X. (2018). A Network Partitioning Algorithmic Approach for Macroscopic Fundamental Diagram-Based Hierarchical Traffic Network Management. *IEEE Transactions on Intelligent Transportation Systems*, 19(4):1130–1139.

Anuar, K., Habtemichael, F. & Cetin, M. (2015). Estimating traffic flow rate on freeways from probe vehicle data and fundamental diagram. pages 2921–2926.

Arnott, R. (2013). A bathtub model of downtown traffic congestion. *Journal of Urban Economics*, 76(1):110–121.

Astarita, V., Bertini, R. L., D'Elia, S. & Guido, G. (2006). Motorway traffic parameter estimation from mobile phone counts. *European Journal of Operational Research*, 175(3):1435–1446.

Ban, X. J., Hao, P. & Sun, Z. (2011). Real time queue length estimation for signalized intersections using travel times from mobile sensors. *Transportation Research Part C: Emerging Technologies*, 19(6):1133–1156.

Barmpounakis, E. & Geroliminis, N. (2020). On the new era of urban traffic monitoring with massive drone data: The pNEUMA large-scale field experiment. *Transportation Research Part C: Emerging Technologies*, 111(October 2019):50–71.

Barmpounakis, E., Vlahogianni, E. & Golias, J. (2016). Intelligent transportation systems and powered two wheelers traffic. *IEEE Transactions on Intelligent Transportation Systems*, 17(4):908–916.

Batista, S. F. A., Leclercq, L. & Geroliminis, N. (2019). Estimation of regional trip length distributions for the calibration of the aggregated network traffic models. *Transportation Research Part B*, 122:192–217.

Bekiaris-Liberis, N., Roncoli, C. & Papageorgiou, M. (2016). Highway Traffic State Estimation with Mixed Connected and Conventional Vehicles. *IFAC-PapersOnLine*, 49(3):309–314.

Boyaci, B. & Geroliminis, N. (2011). Estimation of the network capacity for multimodal urban systems. *Procedia - Social and Behavioral Sciences*, 16:803–813.

Buisson, C. & Ladier, C. (2009). Exploring the impact of homogeneity of traffic measurements on the existence of macroscopic fundamental diagrams. *Transportation Research Record*, (2124):127–136.

Chaudhuri, P., Stevanovic, A. & Martin, P. (2011). Assessing the accuracy and reliability of freeway traffic monitoring stations using gps probe vehicle speed data. *World Review of Intermodal Transportation Research*, 3:338 – 352.

Chen, C., Kwon, J., Rice, J., Skabardonis, A. & Varaiya, P. (2003). Detecting Errors and Imputing Missing Data for Single-Loop Surveillance Systems. *Transportation Research Record*, (1855):160–167.

Chiabaut, N., Xie, X. & Leclercq, L. (2014). Performance analysis for different designs of a multimodal urban arterial. *Transportmetrica B*, 2(3):229–245.

Coifman, B. (2001). Improved velocity estimation using single loop detectors. *Transportation Research Part A: Policy and Practice*, 35(10):863–880.

Daganzo, C. F. (2007). Urban gridlock : Macroscopic modeling and mitigation approaches. *Transportation Research Part B*, 41:49–62.

Daganzo, C. F., Gayah, V. V. & Gonzales, E. J. (2011). Macroscopic relations of urban traffic variables: Bifurcations, multivaluedness and instability. *Transportation Research Part B: Methodological*, 45(1):278–288.

Daganzo, C. F. & Lehe, L. J. (2015). Distance-dependent congestion pricing for downtown zones. *Transportation Research Part B: Methodological*, 75:89–99.

Dakic, I., Yang, K. & Menendez, M. (2019). Evaluating the effects of passenger occupancy dynamics on a bi-modal perimeter control. In *2019 TRB Annual Meeting Online*, pages 19–05589. Transportation Research Board, Washington, DC. 98th Annual Meeting of the Transportation Research Board (TRB 2019); Conference Location: Washington, DC, USA; Conference Date: January 13-17, 2019.

Edie, L. C. (1963). Discussion of traffic stream measurements and definitions. *Proceedings of the Second International Symposium on the Theory of Traffic Flow*, pages 139–154.

Fosgerau, M. (2015). Congestion in the bathtub. *Economics of Transportation*, 4(4):241–255.

Fu, H., Wang, Y., Tang, X., Zheng, N. & Geroliminis, N. (2020). Empirical analysis of large-scale multimodal traffic with multi-sensor data. *Transportation Research Part C: Emerging Technologies*, 118(October 2017):102725.

Gashaw, S., Goatin, P. & Härri, J. (2018). Modeling and analysis of mixed flow of cars and powered two wheelers. *Transportation Research Part C: Emerging Technologies*, 89(April 2017):148–167.

Gayah, V. V. & Daganzo, C. F. (2011). Clockwise hysteresis loops in the Macroscopic Fundamental Diagram: An effect of network instability. *Transportation Research Part B: Methodological*, 45(4):643–655.

Geroliminis, N. & Daganzo, C. F. (2007). Macroscopic modeling of traffic in cities. In *Transportation Research Board 86th Annual Meeting*. Washington DC.

Geroliminis, N. & Daganzo, C. F. (2008). Existence of urban-scale macroscopic fundamental diagrams : Some experimental findings. *Transportation Research Part B*, 42:759–770.

Geroliminis, N., Haddad, J. & Ramezani, M. (2013). Optimal perimeter control for two urban regions with macroscopic fundamental diagrams: A model predictive approach. *IEEE Transactions on Intelligent Transportation Systems*, 14(1):348–359.

Geroliminis, N. & Sun, J. (2011). Properties of a well-defined macroscopic fundamental diagram for urban traffic. *Transportation Research Part B: Methodological*, 45(3):605–617.

Geroliminis, N., Zheng, N. & Ampountolas, K. (2014). A three-dimensional macroscopic fundamental diagram for mixed bi-modal urban networks. *Transportation Research Part C: Emerging Technologies*, 42:168–181.

Godfrey, J. W. (1969). *The Mechanism of a Road Network*. Traffic Engineering and Control, vol 11 ed.

Haddad, J. & Mirkin, B. (2017). Coordinated distributed adaptive perimeter control for large-scale urban road networks. *Transportation Research Part C: Emerging Technologies*, 77:495–515.

Hajiahmadi, R., Knoop, V., De Schutter, B. & Hellendoorn, H. (2013). Optimal dynamic route guidance: A model predictive approach using the macroscopic fundamental diagram. In *Proceedings of the 16th International IEEE Conference on Intelligent Transportation Systems (ITSC 2013)*, pages 1022–1028. The Hague, The Netherlands.

Herring, R., Hofleitner, A., Abbeel, P. & Bayen, A. (2010). Estimating arterial traffic conditions using sparse probe data. *IEEE Conference on Intelligent Transportation Systems, Proceedings, ITSC*, pages 929–936.

Huang, C., Zheng, N. & Zhang, J. (2019). Investigation of bimodal macroscopic fundamental diagrams in large-scale urban networks: Empirical study with gps data for shenzhen city. *Transportation Research Record*, 2673(6):114–128.

Ji, L. J. . G. N., Y. (2014). Empirical observations of congestion propagation and dynamic partitioning with probe data for large scale systems. *Transportation Research Record: Journal of the Transportation Research Board*, 2422(1):1–11.

Ji, Y. & Geroliminis, N. (2012). On the spatial partitioning of urban transportation networks. *Transportation Research Part B: Methodological*, 46(10):1639–1656.

Kawasaki, Y., Hara, Y. & Kuwahara, M. (2018). Real-time traffic state estimation on a two-dimensional network by the state-space model. *Proceedings of the 21st International Conference of Hong Kong Society for Transportation Studies, HKSTS 2016 - Smart Transportation*, (March):183–190.

Keyvan-Ekbatani, M., Kouvelas, A., Papamichail, I. & Papageorgiou, M. (2012). Exploiting the fundamental diagram of urban networks for feedback-based gating. *Transportation Research Part B: Methodological*, 46(10):1393–1403.

Knoop, H. S. P., Victor & van Zuylen, H. (2009). Empirical differences between time mean speed and space mean speed. In C. Appert-Rolland, F. Chevoir, P. Gondret, S. Lassarre, J.-P. Lebacque & M. Schreckenberg,

eds., *Traffic and Granular Flow '07*, pages 351–356. Springer Berlin Heidelberg.

Knoop, V. L. & Hoogendoorn, S. P. (2013). Empirics of a generalized macroscopic fundamental diagram for urban freeways. *Transportation Research Record*, 2391(1):133–141.

Kockelman, K. M. (1998). Changes in flow-density relationship due to environmental, vehicle, and driver characteristics. *Transportation Research Record*, (1644):47–56.

Kong, Q. J., Li, Z., Chen, Y. & Liu, Y. (2009). An approach to Urban traffic state estimation by fusing multisource information. *IEEE Transactions on Intelligent Transportation Systems*, 10(3):499–511.

Kouvelas, A., Saeedmanesh, M. & Geroliminis, N. (2017). Enhancing model-based feedback perimeter control with data-driven online adaptive optimization. *Transportation Research Part B: Methodological*, 96:26–45.

Kwak, S. & Geroliminis, N. (2020). Travel time prediction for congested freeways with a dynamic linear model. *IEEE Transactions on Intelligent Transportation Systems*, pages 1–11.

Lamotte, R. & Geroliminis, N. (2017). The morning commute in urban areas with heterogeneous trip lengths. *Transportation Research Procedia*, 23:591–611.

Lamotte, R., Murashkin, M., Kouvelas, A. & Geroliminis, N. (2018). Dynamic modeling of trip completion rate in urban areas with MFD representations. *TRB annual meeting*.

Leclercq, L. (2005). Calibration of flow-density relationships on Urban streets. *Transportation Research Record*, (1934):226–234.

Leclercq, L., Chiabaut, N. & Trinquier, B. (2014). Macroscopic Fundamental Diagrams: A cross-comparison of estimation methods. *Transportation Research Part B*, 62:1–12.

Leclercq, L., Parzani, C., Knoop, V. L., Amourette, J. & Hoogendoorn, S. P. (2015). Macroscopic traffic dynamics with heterogeneous route patterns. *Transportation Research Part C: Emerging Technologies*, 59:292–307.

Lee, H. & Coifman, B. (2012). Quantifying loop detector sensitivity and correcting detection problems on freeways. *Journal of Transportation Engineering*, 138(7):871–881.

Lentzakis, A. F., Ware, S. I. & Su, R. (2016). Region-based dynamic forecast routing for autonomous vehicles. In *2016 IEEE 19th International Conference on Intelligent Transportation Systems (ITSC)*, pages 1464–1469.

Lighthill, M. & Whitham, G. (1955). On kinematic waves ii. a theory of traffic flow on long crowded roads. Proceedings of the Royal Society of London A: Mathematical. *Physical and Engineering Sciences*, 229(1178):317–345.

Lin, X. & Xu, J. (2020). Road network partitioning method based on canopy-kmeans clustering algorithm. *Archives of Transport*, 54(2):95–106.

Liu, H. X., Wu, X., Ma, W. & Hu, H. (2009). Real-time queue length estimation for congested signalized intersections. *Transportation Research Part C: Emerging Technologies*, 17(4):412–427.

Lloyd, S. P. (1982). Least squares quantization in pcm. *IEEE Trans. Inf. Theory*, 28:129–136.

Loder, A., Ambühl, L., Menendez, M. & Axhausen, K. W. (2017). Empirics of multi-modal traffic networks – Using the 3D macroscopic fundamental diagram. *Transportation Research Part C: Emerging Technologies*, 82:88–101.

Loder, A., Bressan, L., Dakic, I., Ambuhl, L., Bliemer, M., Menendez, M. & Axhausen, K. (2019). Modeling multi-modal traffic in cities using the 3d macroscopic fundamental diagram.

Lopez, C., Krishnakumari, P., Leclercq, L., Chiabaut, N. & van Lint, H. (2017a). Spatiotemporal Partitioning of Transportation Network Using Travel Time Data. *Transportation Research Record*, 2623(1):98–107.

Lopez, C., Leclercq, L., Krishnakumari, P., Chiabaut, N. & Van Lint, H. (2017b). Revealing the day-to-day regularity of urban congestion patterns with 3D speed maps. *Scientific Reports*, 7(1):1–11.

Lu, S., Knoop, V. L. & Keyvan-Ekbatani, M. (2018). Using taxi GPS data for macroscopic traffic monitoring in large scale urban networks: Calibration and MFD derivation. *Transportation Research Procedia*, 34:243–250.

Maghrour Zefreh, M. & Torok, A. (2018). Single loop detector data validation and imputation of missing data. *Measurement: Journal of the International Measurement Confederation*, 116(November 2017):193–198.

Mahmassani, W. J. C. . H. R., H. (1984). Investigation of network-level traffic flow relationships: Some simulation results. *Transportation Research Record: Journal of the Transportation Research Board*, 971:121–130.

Mahmassani, W. J. C. . H. R., H. S. (1987). Performance of urban traffic networks. *In 10th International Symposium on Transportation and Traffic Theory*, page 1–20.

Mariotte, G. & Leclercq, L. (2019). Flow exchanges in multi-reservoir systems with spillbacks. *Transportation Research Part B Methodological*, 122:327–349.

Mariotte, G., Leclercq, L. & Laval, J. A. (2017). Macroscopic urban dynamics: Analytical and numerical comparisons of existing models. *Transportation Research Part B: Methodological*, 101:245–267.

Mazaré, P.-e., Bayen, A. M. & Hall, S. D. (2012). Trade-offs between inductive loops and GPS probe vehicles for travel time estimation : A Mobile Century case study. *Transportation Research Board 91st Annual Meeting*,

Washington, DC, 61801(217):20.

Mazloumian, A., Geroliminis, N. & Helbing, D. (2010). The spatial variability of vehicle densities as determinant of urban network capacity. *Philosophical Transactions of the Royal Society A: Mathematical, Physical and Engineering Sciences*, 368(1928):4627–4647.

Nantes, A., Ngoduy, D., Bhaskar, A., Miska, M. & Chung, E. (2016). Real-time traffic state estimation in urban corridors from heterogeneous data. *Transportation Research Part C: Emerging Technologies*, 66:99–118.

Newell, G. (1993). A simplified theory of kinematic waves in highway traffic, part i: General theory. *Transportation Research Part B: Methodological*, 27(4):281–287.

Oh, S., Ritchie, S. G. & Oh, C. (2002). Real-time traffic measurement from single loop inductive signatures. *Transportation Research Record*, (1804):98–106.

Ortigosa, J., Zheng, N., Menendez, M. & Geroliminis, N. (2015). Analysis of the 3d-vmfds of the urban networks of zurich and san francisco. In *2015 IEEE 18th International Conference on Intelligent Transportation Systems*, pages 113–118.

Paipuri, M., Barmpounakis, E., Geroliminis, N. & Leclercq, L. (2021). Empirical observations of multi-modal network-level models: Insights from the pNEUMA experiment. *Transportation Research Part C: Emerging Technologies*, 131(May):103300.

Paipuri, M. & Leclercq, L. (2020). Bi-modal macroscopic traffic dynamics in a single region. *Transportation Research Part B: Methodological*, 133:257–290.

Paipuri, M., Xu, Y., González, M. C. & Leclercq, L. (2020). Estimating MFDs , trip lengths and path flow distributions in a multi-region setting using mobile phone data. *Transportation Research Part C*, 118(January):102709.

Qiu, T. Z., Lu, X. Y., Chow, A. H. & Shladover, S. E. (2010). Estimation of freeway traffic density with loop detector and probe vehicle data. *Transportation Research Record*, (2178):21–29.

Ramezani, M. & Geroliminis, N. (2015). Queue Profile Estimation in Congested Urban Networks with Probe Data. *Computer-Aided Civil and Infrastructure Engineering*, 30:414–432.

Richards, P. (1956a). Shock waves on the highway. *Operations Research*, 4(1):42–51.

Richards, P. (1956b). Shock waves on the highway. *Operations Research*, 4(1):42–51.

Rousseeuw, P. J. (1984). Least median of squares regression. *Journal of the American Statistical Association*, 79(388):871–880.

Rousseeuw, P. J. (1985). Multivariate estimation with high breakdown point. *Mathematical Statistics and Applications*, pages 283–297.

Saberi, M., Mahmassani, H. S., Hou, T. & Zockaie, A. (2014). Estimating network fundamental diagram using three-dimensional vehicle trajectories: Extending edie's definitions of traffic flow variables to networks. *Transportation Research Record*, 2422(November):12–20.

Saedi, R., Saeedmanesh, M., Zockaie, A., Saberi, M., Geroliminis, N. & Mahmassani, H. S. (2020). Estimating network travel time reliability with network partitioning. *Transportation Research Part C: Emerging Technologies*, 112(January):46–61.

Saeedmanesh, M. & Geroliminis, N. (2016). Clustering of heterogeneous networks with directional flows based on "Snake" similarities. *Transportation Research Part B: Methodological*, 91:250–269.

Saeedmanesh, M. & Geroliminis, N. (2017). Dynamic clustering and propagation of congestion in heterogeneously congested urban traffic networks. *Transportation Research Procedia*, 23:962–979.

Saeedmanesh, M., Kouvelas, A. & Geroliminis, N. (2019). A REAL-TIME STATE ESTIMATION APPROACH FOR MULTI-REGION MFD TRAFFIC SYSTEMS BASED ON EXTENDED KALMAN FILTER. *Transportation Research Board 98th Annual Meeting. January 12-16, Washington, D.C.*, 4346(January 2019):1–11.

Seber, G. A. F. (1984). *Multivariate observations*. New York, John Wiley & Sons, Inc.

Seo, T., Bayen, A. M., Kusakabe, T. & Asakura, Y. (2017). Traffic state estimation on highway: A comprehensive survey. *Annual Reviews in Control*, 43:128–151.

Seo, T. & Kusakabe, T. (2015). Probe vehicle-based traffic state estimation method with spacing information and conservation law. *Transportation Research Part C: Emerging Technologies*, 59:391–403.

Sirmatel, I. I. & Geroliminis, N. (2017). Economic model predictive control of large-scale urban road networks via perimeter control and regional route guidance. *IEEE Transactions on Intelligent Transportation Systems*, 19(4):1112–1121.

Sirmatel, I. I. & Geroliminis, N. (2019). MOVING HORIZON ESTIMATION FOR MODEL PREDICTIVE PERIMETER CONTROL OF MULTI-REGION MFD NETWORKS. *Transportation Research Board 97th Annual Meeting. January 7-11, Washington, D.C.*, 4346(January 2019):1–11.

Skabardonis, A. & Geroliminis, N. (2005). Real-time Estimation of Travel Times on Signalized Arterials.

Transportation and Traffic Theory, pages 387–406.

Skabardonis, A. & Geroliminis, N. (2008). Real-time monitoring and control on signalized arterials. *Journal of Intelligent Transportation Systems*, 12:64–74.

Tsubota, B. A. . C. E., T. (2014). Macroscopic fundamental diagram for bris- bane, australia: Empirical findings on network partitioning and incident detection. *Transportation Research Record: Journal of the Transportation Research Board*, 2421(1):12–21.

Van Erp, P. B., Knoop, V. L. & Hoogendoorn, S. P. (2017). Macroscopic Traffic State Estimation: Understanding Traffic Sensing Data-Based Estimation Errors. *Journal of Advanced Transportation*, 2017.

Wang, S., Xie, X. & Ju, R. (2019). A mesoscopic traffic data assimilation framework for vehicle density estimation on urban traffic networks based on particle filters. *Entropy*, 21(4).

Wu, X., Liu, H. & Geroliminis, N. (2011). An empirical analysis on the arterial fundamental diagram. *Transportation Research Part B: Methodological*, 45:255–266.

Xu, D. W., Dong, H. H., Li, H. J., Jia, L. M. & Feng, Y. J. (2015). The estimation of road traffic states based on compressive sensing. *Transportmetrica B*, 3(2):131–152.

Xue, Z., Chiabaut, N. & Leclercq, L. (2016). Evaluation of the effect of traffic modeling on the control of traffic networks. *Transportation Research Record*, page 18 p.

Yildirimoglu, M. & Geroliminis, N. (2014). Approximating dynamic equilibrium conditions with macroscopic fundamental diagrams. *Transportation Research Part B: Methodological*, 70:186–200.

Yildirimoglu, M., Ramezani, M. & Geroliminis, N. (2015). Equilibrium analysis and route guidance in large-scale networks with MFD dynamics. *Transportation Research Part C: Emerging Technologies*, 59:404–420.

Yuan, Y., Duret, A. & Van Lint, H. (2015). Mesoscopic traffic state estimation based on a variational formulation of the LWR model in lagrangian-space coordinates and Kalman filter. *Transportation Research Procedia*, 10(July):82–92.

Yuan, Y., Van Lint, J. W., Wilson, R. E., Van Wageningen-Kessels, F. & Hoogendoorn, S. P. (2012). Real-time lagrangian traffic state estimator for freeways. *IEEE Transactions on Intelligent Transportation Systems*, 13(1):59–70.

Zefreh, M. M., Török, Á. & Mészáros, F. (2017). Average vehicles length in two-lane urban roads: A case study in budapest. *Periodica Polytechnica Transportation Engineering*, 45(4):218–222.

Zhai, Y. (2013). Experiment based accuracy evaluation of traffic flow detectors data. *ICTIS 2013: Improving Multimodal Transportation Systems - Information, Safety, and Integration - Proceedings of the 2nd International Conference on Transportation Information and Safety*, pages 985–994.

Zhang, X. & Rice, J. A. (2003). Short-term travel time prediction. *Transportation Research Part C: Emerging Technologies*, 11(3-4):187–210.

A. Appendix for Chapter 4

A.1 Other Ideas for Data Imputation: Priority Placed on Trip Length Distribution

We applied several ideas to complete the entry and exit times and the trip length of trajectories during the no-drone period. Here, we present the ideas that prioritize keeping the shape of trip length distribution and inflow dynamics similar to that during the drone period. Like the method in Section 4.2.2, the accumulation, the entry and exit times and trip length during the drone period are not changed before or after data imputation. The reasons why the results of these ideas are not used for the MFD model calibration are also described. Each missing type of data is shown in Figure 4.2.

A.1.1 Idea 1: Assigning the exit time of Type 3,4 and 5 vehicles according to a trip length chosen from a distribution

The principle of this idea is as follows: we first assign the trip length for all vehicles without Type 1 (no data is missing). Then, we calculate the expected exit time corresponding to the trip length. According to the entry time and the expected exit time, we recategorize the missing type of data of the vehicles and assign the real and calculated exit times and trip length according to the types. For Type 1 vehicles, we keep the original trajectory information. To consider the other types of vehicles, we first calculate the inflow qin'_s and mean speed v'_s during no-drone periods using the same method as in Section 4.2.2, i.e., the average values over 3 minutes before the end of the drone period and after the beginning of the next drone period. Also, the entry time list of all the vehicles during the no-drone period $\mathbf{Tin}_s$ is calculated from qin'_s, c.f., see the detailed method in Section 4.2.2.

We first assign the trip lengths for the vehicles which start their trips during the drone period (Type 2 vehicles). The trip length L_i is chosen by the original trip length distribution calculated by Type 1 vehicles shown as black bars and lines in Figure 4.9 (b) under the minimum limitation $Lmin$ of the observed trip length L_i^* of each Type 2 vehicle during the drone period as $Li \sim P(Li|Li > Lmin)$. The exit times of these vehicles $Tout_i$ are calculated as $Tout_i = Tin_i + Lmin * Vi + (L_i - Lmin) * v'_s$, where Tin_i and V_i are the observed entry time and average speed of Type 2 vehicle i. As shown in Figure A.1, we can recategorize the data missing type according to the exit time calculated:

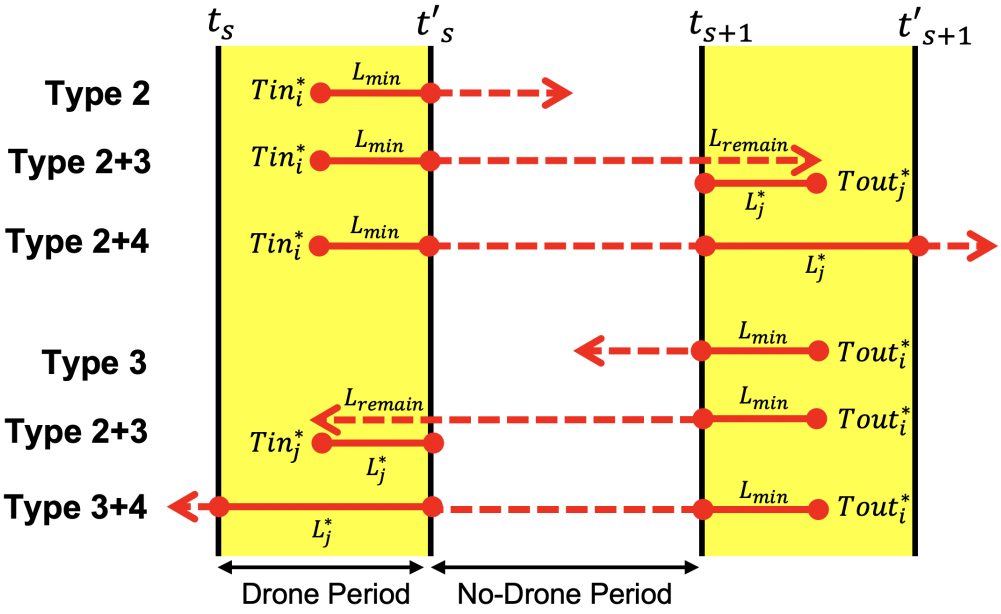

FIG. A.1 – *Recategorizing Type 2 and Type 3 vehicles according to the exit time calculated from the assigned trip length.*

1. Type 2 if the exit time is before the next drone period.
2. Type 2 and Type 3 simultaneously if the exit time is in the next drone period.
3. Type 2 and Type 4 simultaneously if the exit time is over the next drone period.

According to the trip length distribution, no trip exists over 3 drone periods. The vehicles categorized as Type 2 and 3 at the same time should be assigned to the observed exit time $Tout_j^*$ of Type 3 vehicle j. Therefore, we first calculate the remaining trip length $Lremain$ during the next drone period from the assigned trip length for Type 2 and 3 vehicles as $Lremain = L_i - (Lmin + v'_s * (t_{s+1} - t'_s)$ where $t_{s+1} - t'_s$ shows the duration of time of the no-drone period. The observed trip length L_j^* of the Type 3 vehicle closest to $Lremain$ is reassigned instead of $Lremain$. Now, the entry and exit times of vehicle k that are categorized as Type 2 and 3 simultaneously are $Tin_k = Tin_i^*$, which is the observed value of Type 2 vehicles, and $Tout_k = Tout_j^*$, which is the observed value of Type 3 vehicle. The trip length is $L_k = Lmin + v'_s * (t_{s+1} - t'_s) + L_j^*$. For vehicle k categorized as Type 2 and 4 at the same time, we assign the observed trip length of Type 4 vehicle j during the next drone-period and modify the exit time as $Tout_k = (L_i - (Lmin + v'_s * (t_{s+1} - t'_s) + L_j^*))/v'_{s+1}$. If the information of all Type 4 vehicles has already been assigned as the vehicle recategorized as Type 2 and 4 simultaneously, we assign the Type 3 vehicles with the latest exit time during the drone period by the same method as Type 2 and 3 at the same time.

For Type 3 vehicles that are not categorized as Type 2 and 3 simultaneously, the trip length L_i is assigned randomly from the trip length distribution under the minimum limitation $Lmin$ of the observed trip length of each Type 3 vehicle. The entry time is calculated according to the assigned trip length as $Tin_i = Tout_i - Lmin * Vi + (L_i - Lmin) * v'_s$. Then, we recategorize the data missing type in the same way as for Type 2 vehicles:

1. Type 3 if the entry time is during the former no-drone period.

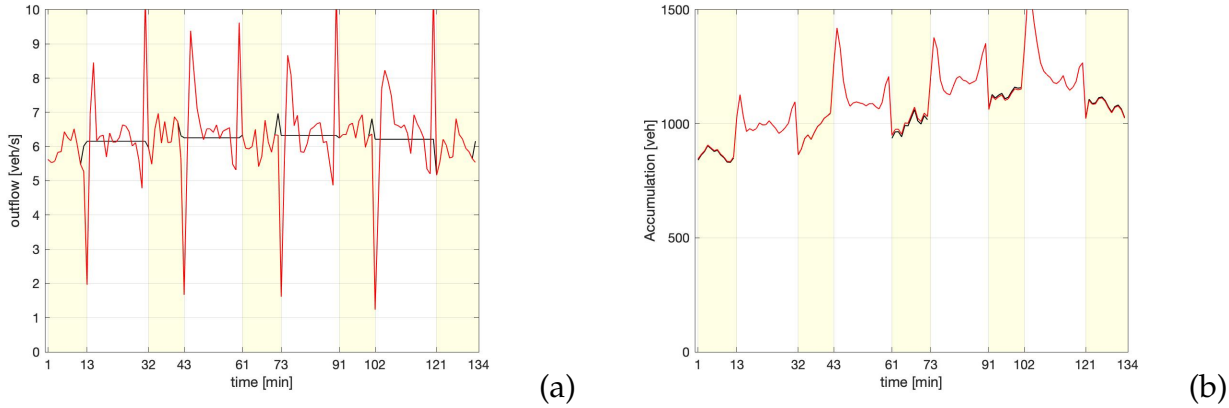

(a) Outflow [veh/s] (b) Accumulation [veh]

FIG. A.2 – *Parameter dynamics before (black) and after (red) data imputation by the method in the Appendix (Yellow zone: drone period, white zone: no-drone period)*

2. Type 2 and 3 at the same time if the entry time is during the former drone period.

3. Type 3 and 4 at the same time if the entry time is before the former drone period.

For the vehicle k recategorized as Type 3, the entry time Tin_k is calculated as $Tin_k = Tout_i^* - (Lmin/V_i + (L_i - Lmin)/v_s')$. The closest value to Tin_k is removed from $\mathbf{Tin}_s$. For the vehicle k recategorized as Type 2 and 3 at the same time, we calculate the remaining trip length $Lremain$ during the former drone period as $Lremain = L_i - (Lmin + v_s' * (t_{s+1} - t_s')$. The observed trip length L_j^* of the Type 2 vehicle closest to $Lremain$ is reassigned instead of $Lremain$ even if the trip length has already been assigned from the trip length distribution. For the vehicle recategorized as Type 3 and 4 at the same time, the entry time and trip length is calculated in the same way as for the vehicle categorized Type 2 and 4 at the same time as $Tin_k = (L_i - (Lmin + v_s' * (t_{s+1} - t_s') + L_j^*))/v_{s+1}' and L_k = Lmin + v_s' * (t_{s+1} - t_s') + L_j^*$ where j is a Type 4 vehicle. If the information of all Type 4 vehicles has already been assigned as the vehicle recategorized as Type 3 and 4 at the same time, we assign the Type 2 vehicle, which has the latest exit time during the drone period, using the same method as Type 2 and 3 at the same time.

If the observed Type 4 vehicles have not been assigned for the vehicles recategorized as Type 2 and 4 or Type 3 and 4 at the same time, We assign the trip length L_i by choosing from the trip length distribution under the minimum limitation $Lmin$ of the observed trip length of each Type 4 vehicle. The entry time Tin_i is chosen from $\mathbf{Tin}_s$ to obtain the exit time over the drone period according to the assigned trip length when the average speed is the same as the observation V_i^*. The exit time is calculated from $Tout_i = Tin_i + V_i^* * L_i$.

Finally, the entry time Tin_i of Type 5 vehicle i is assigned from the rest of $\mathbf{Tin}_s$, and the trip length is chosen randomly to avoid reaching the beginning of the next drone period as $L_i \sim P(L_i | L_i < (t_{s+1} - Tin_i) * v_s')$ where t_{s+1} is the beginning time of the next drone period. The exit time is calculated as $Tout_i = Tin_i + v_s' * L_i$.

The parameter dynamics after data imputation is shown in Figure A.2. The inflow and mean speed are not presented here since the inflow and mean speed follow the original dynamics during the drone period and the input value during the no-drone period, similar

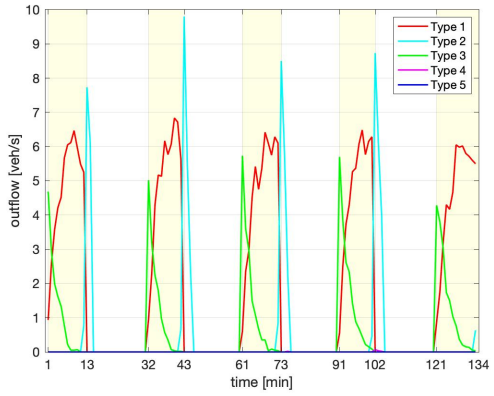

(a) original data

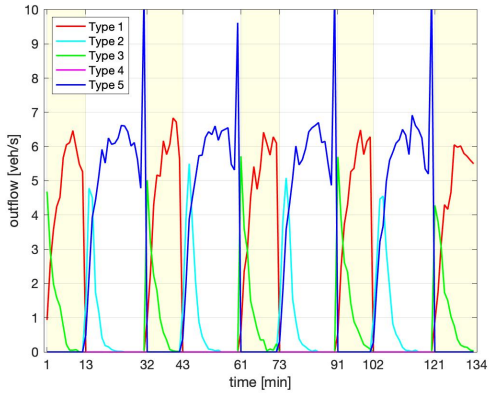

(b) after data imputation

FIG. A.3 – *Outflow of each data missing type (Yellow zone: drone period, white zone: no-drone period).*

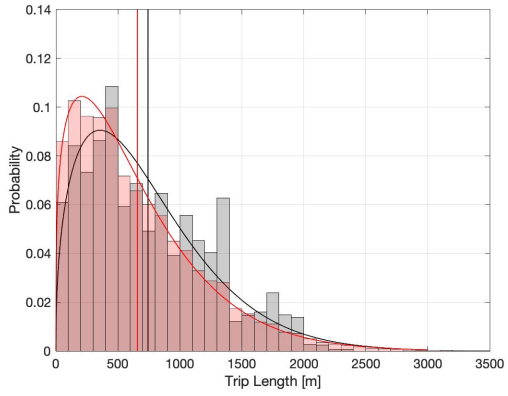

(a) Trip Length Distribution

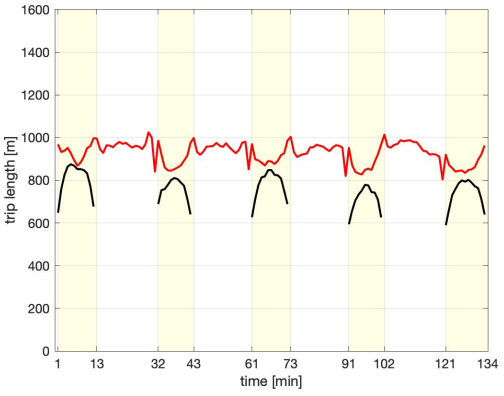

(b) Average Trip Length Dynamics

FIG. A.4 – *Trip length before (black) and after (red) data imputation by the method in the Appendix.*

to Figure 8 when using the method prioritizing inflow and outflow. However, as shown in Figure A.2 (a), the outflow after data imputation has huge decreases reaching 1 veh/s at the end of the drone period and huge increases reaching 10 veh/s at the end of the no-drone period. Figure A.3 shows the outflow dynamics of each missing data type before and after data imputation. The type category is used before recategorizing, e.g., the vehicle recategorized as Type 2 and 4 at the same time is denoted as a Type 2 vehicle here. According to Figure A.3, the decreases are caused because quite a few Type 2 vehicles end their trips at the beginning of the no-drone period with the assigned trip length from the original trip length distribution. When we use the modified trip length distribution shown as blue bars and lines in Figure 4.9 (b), c.f., see Section 4.2.2 for the description, these drops worsen. The rises at the end of the no-drone periods are caused by Type 5 vehicles because of the trip length limitation to exit by the end of the no-drone period. The accumulation dynamics also have huge increases of around 200 to 300 veh at the beginning and the end of the no-drone periods because of considerable gaps in the outflows. As shown in Figure A.4, the trip length distribution after data imputation has a slightly longer tail and the average dynamics

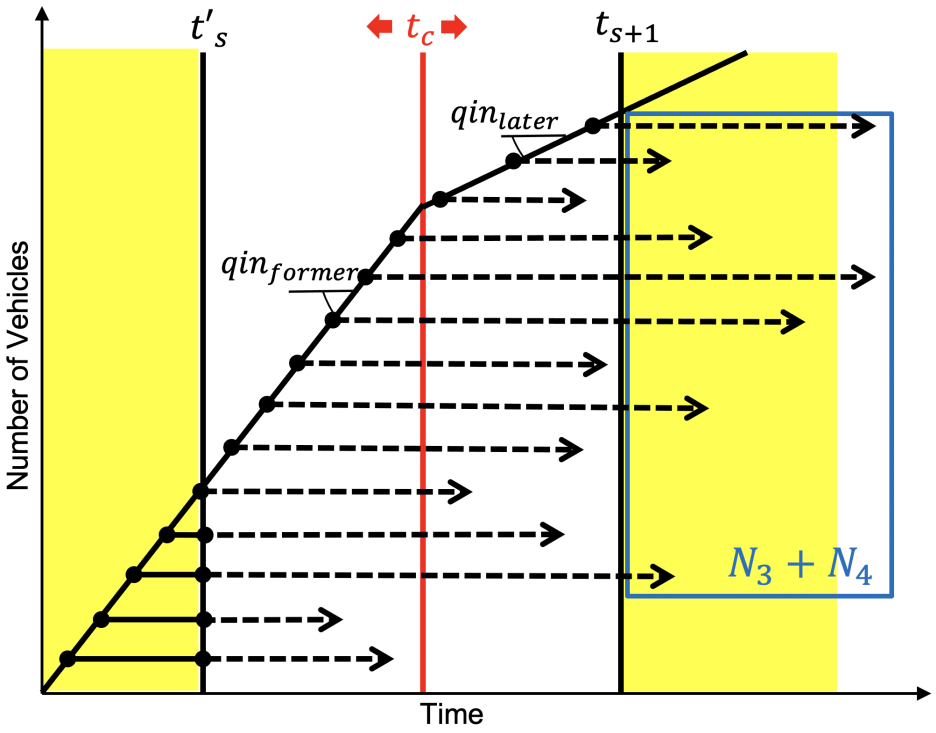

FIG. A.5 – *The changed times t_c of inflow and mean speed during the no-drone period.*

is higher by around 100 to 200 m than the original trip length distribution. However, the distribution has a good shape following the Weibull distribution, and the average dynamics is stable.

Although the trip length distribution and the average trip length dynamics are stable, the outflow and accumulation that are the ground truth of the MFD model calibration should not have such large oscillations. Therefore, this idea is not suitable in this study.

A.1.2 Idea 2: Changing inflow during the no-drone period correspond to vehicle accumulation of Type 3 and 4 vehicles

According to this idea, the no-drone period is separated into two parts, e.g., former and later, and we assume different inflows and mean speeds. The timing of these two parts is changed to fit the accumulation of the vehicles assumed as starting their trips during the no-drone period and ending after the no-drone period according to assigned entry time and trip length with Type 3 and 4 vehicle accumulation.

The former inflow qin_{former} and later inflow qin_{later} during the no-drone period are calculated as the average values over 3 minutes before the end of the drone period and after the beginning of the next drone period. The former mean speed v_{former} and later mean speed v_{later} are also calculated using the same method for the inflow. The inflow and mean speed are changed from the former to the later values at the changed times t_c. t_c is initially set as the middle of the no-drone period and is changed to forward time until the beginning of the no-drone period t'_s and backward time until the end of the no-drone period t_s, as shown in Figure A.5. The entry time list of all the vehicles during the no-drone period $\mathbf{Tin}_s$ is calculated from $1/qin_{former}$ before t_c and $1/qin_{later}$ after t_c.

To find the real times of t_c, trip lengths L_i are assigned for Type 2 vehicles and all the vehicles that start trips during the no-drone periods, i.e., the entry times of these vehicles are decided by $\mathbf{Tin}_s$, by choosing randomly from the modified trip length distribution, as shown in Figure 4.9. For Type 2 vehicles, the trip length is chosen with minimum limits imposed on the observed trip length L_i^*. The exit time $Tout_i$ of the Type 2 vehicle i is calculated as $Tout_i = t'_s + (L_i - L_i^*) * v_{former}$. The exit time of the vehicle that starts its trip during the no-drone period is calculated as $Tout_i = Tin_i + L_i * v'_s$ where $Tin_i \sim \mathbf{Tin}_s$. v'_s is v_{former} before t_c and v_{later} after t_c. The number of vehicles whose exit time is over the end of the no-drone period t_s should be equal to the sum of Type 3 and 4 vehicle accumulations. If the difference is more than 10 vehicles, we change t_c and recalculate.

We change t_c every 1 minute and repeat it 100 times by considering the randomness of trip length choice. However, the assigned accumulation of vehicles that start their trips during the no-drone period and end them after the no-drone period is overestimated by more than 300 veh for some periods. Also, when we use the original trip length calculated only by Type 1 vehicles, the accumulation is still overestimated by 50 veh, and there is no vehicle assigned as Type 4 during a whole drone period. Furthermore, even during the period in which we find the proper t_c, the calculated outflow decreases at the beginning of the no-drone period, as in the Appendix A.1.1. The average trip length dynamics also increases considerably at the beginning of the no-drone period because of the minimum limitation of trip length assignment for Type 2 vehicles.

Thus, this method requires much more calculation time for searching the proper t_c, and the calculated parameters have errors similar to those in the Appendix A.1.1.

B. APPENDIX FOR CHAPTER 6

B.1 Effect of 3D MFD Calibration between cars and buses

Parameter calibrations for all options described in Section 6.3.3 between cars and buses are quite challenging since the trajectory data of buses are few, e.g., less than 100 veh in a minute. Like the calibration between cars and motorcycles, we first test all combinations of parameters within 95% confidence limit to find the best parameters for getting the most accurate prediction. For Option 1 (linear V-MFD approximation with minimum speed limitation), we use the calibrated parameters in Table 6.3. For Option 2 (P-MFD based approximation), we use $\beta_{car,car} = 3100$, $\beta_{bus,car} = 24$, $\beta_{bus,bus} = 22$, and $\beta_{car,bus} = 2150$. The prediction results are shown in Figure B.1. Except for Option 2 which the parameter calibration accuracy is quite low, the results are quite similar to the investigation between cars and motorcycles described in Section 6.4.2. Relative errors of prediction accuracy of each option are summarized in Table B.1.

	car			bus		
Option	$Qout_m$	n_m	V_m	$Qout_m$	n_m	V_m
0 (Single mode MFD)	4.8	6.4	6.5	17.1	27.0	42.0
1 (V-MFD based approximation with limitation)	5.1	13.7	30.9	16.4	9.9	30.3
2 (P-MFD based approximation)	4.6	15.3	20.2	16.8	10.9	8.7

TAB. B.1 – *Relative errors [%] of prediction accuracy based on 3D MFD between cars and buses*

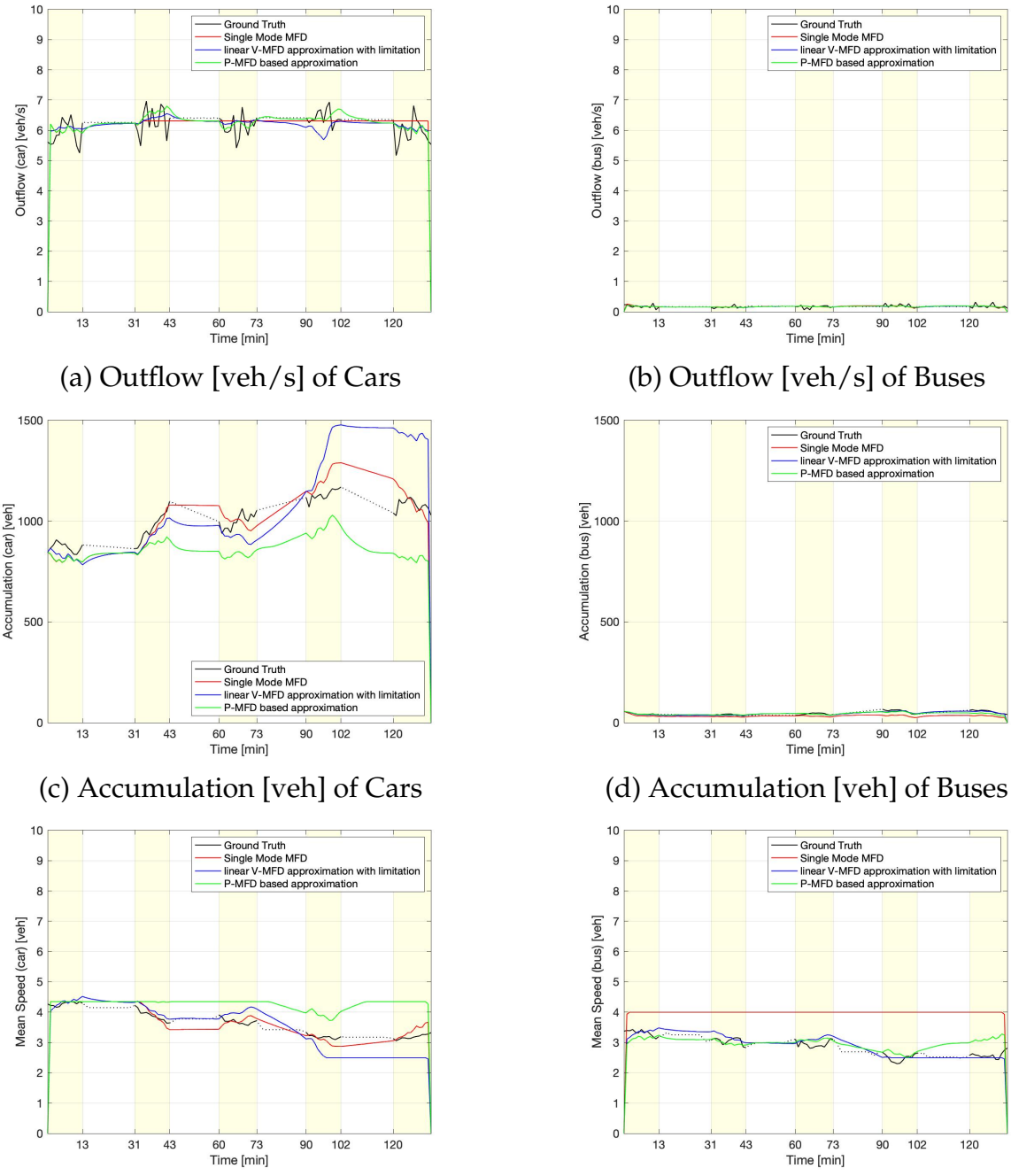

(a) Outflow [veh/s] of Cars

(b) Outflow [veh/s] of Buses

(c) Accumulation [veh] of Cars

(d) Accumulation [veh] of Buses

(e) Mean speed [m/s] of Cars

(f) Mean speed [m/s] of Buses

FIG. B.1 – *Results of 3D MFD model between cars and buses.*